DESIGN AND TESTING OF A NOVEL COMBINED ADHESION AND LOCOMOTION METHOD
FOR WALL CLIMBING VEHICLES

A Thesis

presented to

the Faculty of California Polytechnic State University,

San Luis Obispo

In Partial Fulfillment

of the Requirements for the Degree

Master of Science in Mechanical Engineering

by

James Roy Stefani

June 2016

COMMITTEE MEMBERSHIP

TITLE: Design and Testing of a Novel Combined Adhesion and Locomotion
                                Method for Wall Climbing Vehicles

AUTHOR: James Roy Stefani

DATE SUBMITTED: June 2016

COMMITTEE CHAIR: Thomas Mackin, Ph.D.
                                Professor of Mechanical Engineering

COMMITTEE MEMBER: John Ridgely, Ph.D.
                                Professor of Mechanical Engineering

COMMITTEE MEMBER: Joseph Mello, Ph.D.
                                Professor of Mechanical Engineering

ABSTRACT

Design and Testing of a Novel Combined Adhesion and Locomotion Method for Wall Climbing Vehicles

James Roy Stefani

The objective of this project was to design, construct and test a wall climbing vehicle which uses a novel vacuum tread system for both adhesion *and* locomotion. The design and manufacturing of this proof of concept vehicle is detailed with particular emphasis on the design decisions that proved most impactful to the performance of both the vehicle and the tread system. Adhesion performance was characterized by a series of tests that validate the concept, but also identify improvements and design recommendations for future embodiments of the adhesion/locomotion system.

ACKNOWLEDGMENTS

TABLE OF CONTENTS

APPENDICES

LIST OF TABLES

LIST OF FIGURES

Chapter 1: Introductory Material

1.1 Problem Statement

Climbing robots represent an important development for many different technical tasks which occur on vertical surfaces, ceilings or in areas which would be hazardous or inaccessible to people. These applications include, among others, inspection of structures, maintenance, construction and data acquisition. Climbing robots can be useful in several different ways. They can be more cost effective, accurate and efficient than human technicians because they can be run continuously and autonomously. They can access areas which would be difficult or impossible for a human technician, such as the interiors of ship hulls. They can also remove the need to have human technicians placed in dangerous or hazardous environments, such as nuclear reactors or chemical storage tanks. This makes them an attractive tool for many different industrial and scientific operations.

This is not to say that climbing robots do not have their draw backs. Many of the designs which have been developed can only be applied to a single application or subset of applications. The environments they can operate in are often limited by their adhesion and locomotion methods, as well as by their overall dimensions and load-bearing capacity. This ultimately means that, for any given application, a climbing robot must be specially designed, which reduces its cost effectiveness.

The purpose of this project is to introduce a novel combined adhesion and locomotion system, i.e. a tank tread which acts as a gasket for an active vacuum system, which has the potential to be applied to many different operating environments. The system also has the potential to be scaled easily, which means that it could be used for robots of many sizes and with a variety of carrying capacities.

1.2 Project Overview

As stated above, the purpose of this project is to produce and demonstrate a novel combined adhesion and locomotion system for climbing robots. This includes the design, manufacture and testing of the proposed system.

The proposed system uses two treads, similar to a tank, to locomote. Perforations are cut through the tread to create chambers through which a vacuum can be drawn, adhering the robot to a surface. These chambers are located along a central channel in the tread, surrounded by timing belt teeth to allow power engagement. The tread system is composed of three distinct layers, a timing belt made of stiff neoprene which interfaces with the drive and idler wheels, a soft neoprene layer used to create a seal between the vacuum chambers and the tread, and a layer of low friction fabric which covers the central channel.

A vacuum manifold with four separate vacuum chambers rides in the central channel of the tread and distributes vacuum to the holes cut into the tread. Each vacuum chamber is connected to a venturi vacuum generator, which produces the vacuum that adheres the robot to a climbing surface. A total of eight venturis are used in the system and all of the venturis are fed by a common positive air pressure source.

Three different wheels are used in the tread system. A drive wheel is used to transfer power from a gear motor to the tread. An idler wheel at the back of the robot is used to facilitate the smooth motion of the tread as it moves and to provide support to the tread system. A tensioning idler is used to tension the belt to ensure that no slipping occurs during operation and to allow the belt to be easily inserted and removed from the robot.

A full description of the design process used to create the robot, how the robot was manufactured and the testing procedures used to validate the robot's design can be found later in the report.

1.3 Background and Survey of Existing Systems

1.3.1 Common Applications for Climbing Robots

There are a wide variety of applications which currently use climbing robot, ranging from relatively mundane to extremely critical. Many of the industrial climbing robots are designed to perform cleaning tasks on vertical surfaces or in hazardous environments. The NERO II, for instance, is used to clean the interiors of nuclear reservoirs [1], while other robots, such as the SURF, are used to clean the exteriors of high rises without the use of scaffolding [4]. Still others are used to inspect and clean ships, such as the OCTOPUS, and airplanes [6].

Because climbing robots equipped with sensors produce repeatable and unbiased results with a high degree of accuracy, they are often used in inspection applications. Climbing robots are used to inspect bridges for corrosion and condition, both in concrete [5] and steel [7] bridges. They are also used to inspect oil tanks and pipes in chemical systems [6, 7], which tend to be both difficult to access and are hazardous to humans. One of the most critical and potentially hazardous inspection task climbing robots perform is in nuclear storage areas [1, 6].

Climbing robots can also be used to perform tasks which are not necessarily obvious. Welding is one such application which climbing robots are relatively well suited for because they can move at a constant rate and lay consistent welds over large seams, which can be difficult for human welders. For instance, engineers at the University of Canterbury have developed the TigBot, a robot which performs TIG welding on stainless steel structures [9]. Another interesting application is the use of climbing robots in search and rescue operation conducted by fire departments [6]. These robots are often used to scout potentially hazardous or difficult to reach areas, which allows fire fighters to both determine if the area is safe to enter and to locate any trapped or incapacitated people. Similarly, climbing robots have been developed to aid in military reconnaissance, allow soldiers to scout buildings before entering them [3].

Clearly, there are a wide range of applications which climbing robots are being applied to. Additionally, as climbing robot design becomes more sophisticated it will become more feasible to use climbing robots in a wider range of applications.

1.3.2 Major Design Principles of Climbing Robots in Non-Research Applications

To be effective at their designated tasks, climbing robots must meet certain design requirements. These requirements can be broken down into five major categories which can be applied to almost every climbing robot in some way or another [7]. This section contains a brief description of each of these categories based upon the list put forth by [7].

1.3.2.1 Velocity

The robot must be able to achieve a speed at which it can complete its required task in a reasonable amount of time, while remaining accurate and safe. This requirement depends upon several factors, such as the

dimensions of its work space, the maximum speed at which its chosen adhesion method can handle before the robot falls and the rate at which its work must be done. For instance, an inspection robot working on a bridge may be required to traverse relatively large distances between inspection areas, which means it need to move quickly between these points to remain efficient. Once it reaches an inspection point, it may need to move slowly for its inspection equipment to operate.

1.3.2.2 Mobility

The robot must be able to maneuver around its work environment efficiently and precisely, as well as be able to maneuver its tools or inspection equipment into the required location. This means that the robot must be able to position itself accurately on its work surface, maintain a desired trajectory, and move smoothly if its sensors or tools require smooth motion to operate. It must also be able to navigate over any obstacles it may encounter.

1.3.2.3 Payload

The robot must able to carry the tools and equipment which are required to complete its task. These can range from small and light weight systems, such as cameras, or larger and heavier systems, such as inspection equipment or tools. They must be able to accommodate these systems both in terms of carrying capacity, i.e. the weight they can hold while maintaining surface adhesion and locomotion, and of dimensional requirements, i.e. the space required to house the system.

1.3.2.4 Safety and Reliability

The robot system must be safe to use for both the human operator and bystanders, as wells as for the robot itself. It must also be robust enough to be usable, i.e. it must be able complete its desired task without frequent break downs and maintenance. They should have a high factor of safety for their given adhesion method and should also be capable of detecting and recovering from potentially hazardous conditions.

1.3.2.5 Usability

This is something of a catch all category dealing with the general usability of the robot, which can include everything from the weight of the system to the power requirements to how easy it is to operate. For the

system to be practical it should be at least as effective of the currently employed methods used to complete the desired task. This effectiveness can be defined in multiple ways, such as how effective the system is, if it is more powerful than the current method and if it is less dangerous than the current method. The system should be adaptable to multiple applications, i.e. it should be able to handle different payloads. It should also be easy to repair, maintain and trouble shoot, both in the field and when being serviced. It should not be too bulky or unwieldy so that its operators can easily handle it. There are a myriad of other factors which fall into this category and they are often specific to the required task or task which the robot is required to perform.

1.3.3 Existing Methods for Locomotion and Adhesion

A myriad of different climbing robots have been designed and implemented, many of which employ similar adhesion and locomotion in different combinations. The most common types of these adhesion and locomotion systems are discussed below [7]. A more comprehensive survey can be found in [7].

1.3.3.1 Locomotion methods

This section gives a brief description of the different types of locomotion methods used in wall climbing robots. It also discusses some of the advantages and disadvantages of each method.

1.3.3.1.1 Arms and Legs

The use of arms or legs is relatively common in wall climbing robots. These systems use multiple, often multi-degree of freedom, limbs to move. Generally, each of these limbs has an adhesive component on its tip which holds the robot to the wall. Because these limbs can be moved independently of one another and the robot can test the adhesion of the limb, limbed robots are quite adept at traversing relatively rough terrain and obstacles. But, because of the complex nature of the limbs, it is often difficult to control limbed robots and to operate them smoothly. Limbs also tend to be relatively slow when compared to other locomotion methods. This is because, generally, only a single limb can be moved at a given time to ensure the robot maintains contact with the wall. An example of a limbed robot can be found in Figure 1.
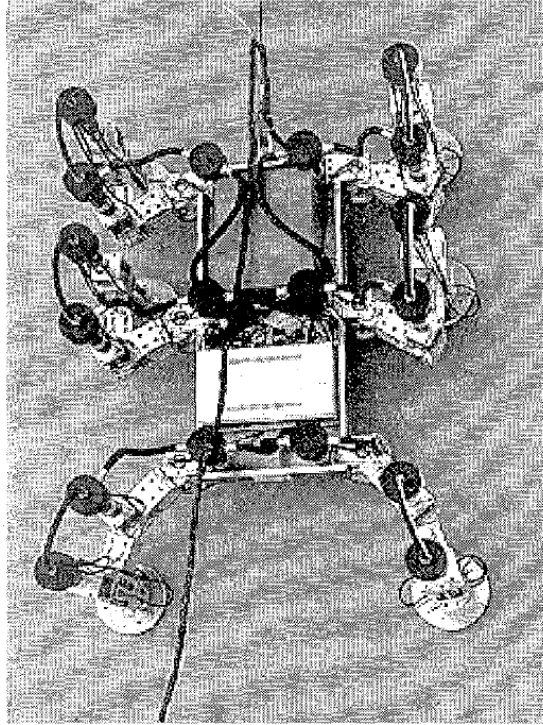
Figure 1: A six limbed climbing robot from [10].

1.3.3.1.2 Wheels and Tread

Wheels or treads are relatively common forms of locomotion for climbing robots, especially when the robot operates on a relatively smooth surface. Wheels and treads are relatively fast and provide smooth and continuous locomotion, which is desirable in many applications. They are also relatively simple to control and are also mechanically simple. The main disadvantage of wheeled or tracked robots is their inability to traverse steps and obstacles, which limits the application that they can be applied to. An example of a wheeled climbing robot can be found in Figure 2, while an example of a treaded climbing robot can be found in Figure 3.
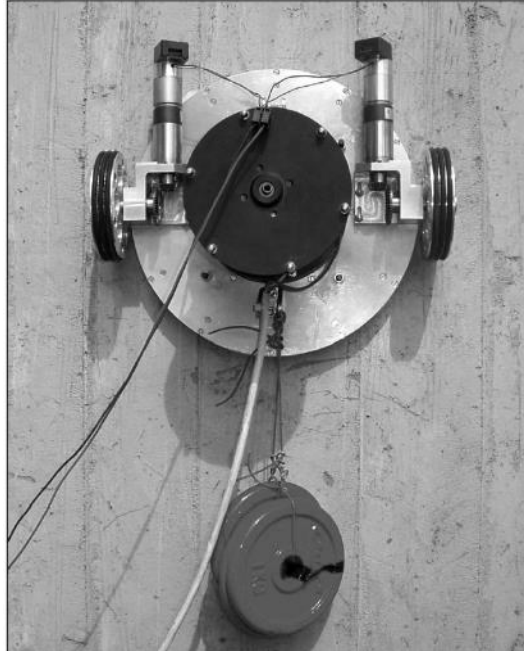
Figure 2: The Alicia II robot from [11] uses wheels to locomote.

Figure 3: An example of a treaded wall climbing robot from [8].

1.3.3.1.3 Sliding Frame

A fairly common form of wall climbing robot locomotion is the sliding frame. These systems generally employ two frames which can translate or rotate relative to one another, with each frame containing its own adhesion system. To move, the robot fixes one frame to the surface and then moves the second frame forwards or backwards. The second frame attaches itself to the surface and then the process repeats with the first frame moving. Sliding frames tend to be reliable because of their ability to test their footing. They are

also easy to control because of their relatively simple mechanical structure. However, like limbed robots, they tend to be slow and move in a discontinuous manner. They also tend to be bulky when compared to other designs. An example of a sliding frame climbing robot can be seen in Figure 4.
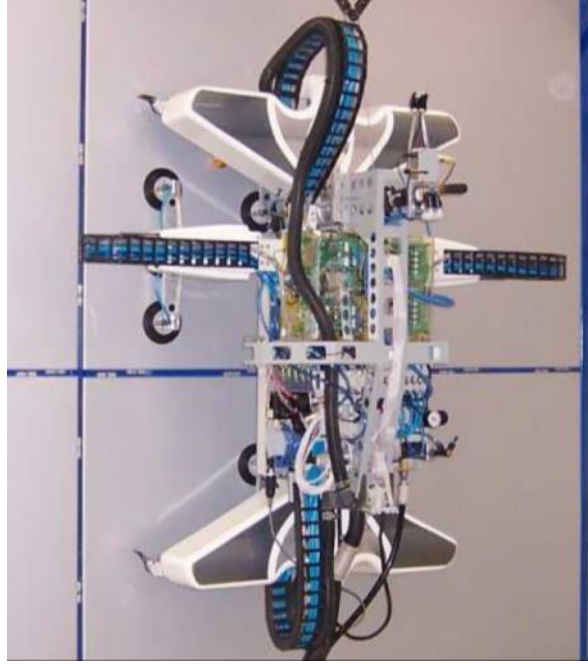
Figure 4: An example of a slibing frame climbing robot [12].

1.3.3.1.4 Rails and Wires

When the path of a climbing robot is well defined, wires or rails can be used as a method for locomotion. The robot travels along the guiding structure and uses its adhesion method only to fix itself in position on its work surface. Because the load is carried by the wire or rail, the adhesion method can be relatively weak and the robot itself can be quite heavy when compared to the other locomotion methods. Though the mechanisms used to move the robot along the rail or wire can be extremely simple and fast, the robot is restricted to use the given path, which means they must be highly specialized. An example of a wire driven climbing robot can be found in Figure 5.

Figure 5: An example of a wire climbing robot from [13].

1.3.3.2 Adhesion Methods

This section contains a brief description of the most commonly used adhesion methods in climbing robots. It also discusses the advantages and disadvantages of each method.

1.3.3.2.1 Magnetic

Magnets, both permanent and electromagnets, are commonly used as an adhesion method when a climbing robot works on ferromagnetic surfaces. A significant distinction can be made between the behavior, in application, of permanent magnets and electromagnets. The force generated by electromagnets can be controlled relatively easily by varying the current passing through the coils, which means that they can be positioned near the working surface without having to worry about generating too much attractive force or friction. However, electromagnets require power to operate, which reduces the electrical efficiency of the system as a whole. Permanent magnets can generate large attractive forces with a relatively small footprint and require no power, but they must be carefully placed. This is to ensure that they do not generate excessive force, which can damage the robot or cause excess friction. Because magnets can only work on ferrous surfaces, climbing robot design which employ them are limited in the types of applications in which they can be employed. Two examples of climbing robots which employ the magnet adhesion method are show in Figure 6.
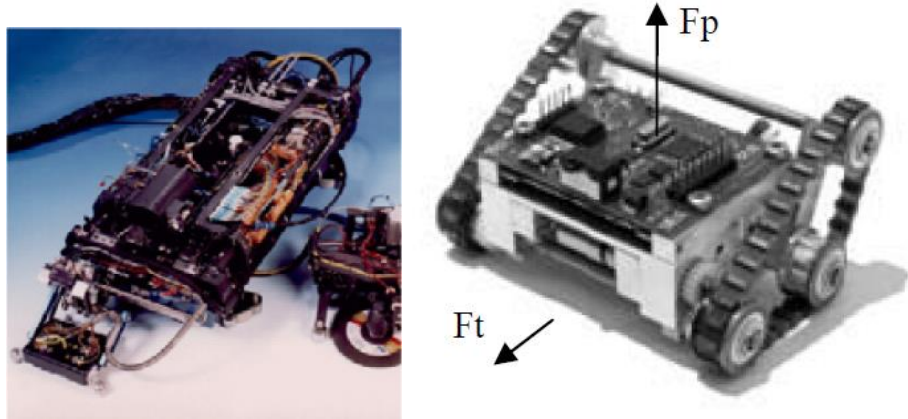
Figure 6: (Left) The Sadie robot, which combines a sliding frame with magnets [7]. (Right) The Tripillar robot which combines a tread system with magnets [14].

1.3.3.2.2 Pneumatic

Perhaps the most common adhesion methods used in climbing robots is the used of pneumatic adhesion. Pneumatic adhesion can be broken down into two major categories, active pneumatics and passive pneumatics. Suction cups are the most common, if not the only, form of passive pneumatics used in climbing robots. Suction cups have two major disadvantages associated with their use in climbing robots. The first is that they require a smooth surface to maintain negative pressure, which can be foiled by rough surfaces or particulates on a smooth surface. The second is that the cups must be reapplied to the surface relatively frequently because if the cups remain static for too long negative pressure is lost due to small leaks. This makes climbing robots which employ suction cups difficult or impossible to employ in most applications. An example of a robot which uses suction cups for adhesion can be found in Figure 7.
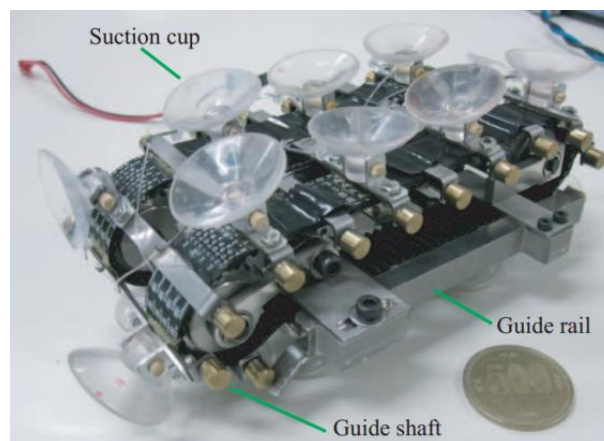
Figure 7: An example of a climbing robot which uses suction cups [20].

Active pneumatics can be broken down into two different major categories, true active vacuum adhesion and thrust or vortex adhesion. Active vacuum adhesion uses vacuum generators, generally pumps, to pull a vacuum in sealed, or semi-sealed, chambers to adhere the robot to work surface. Active vacuum adhesion is by far the most commonly employed of the pneumatic adhesion techniques, as it can be applied to a variety of surface types and the force generated can be controlled by the system using valves. The main disadvantage of active vacuum systems is the requirement of either on board or remote vacuum generators, which can add weight to the system or limit its operating range. Active vacuum systems also require a near perfect seal with the work surface so that the system does not lose suction, which limits the surfaces they can be used on as well as the size obstacles these robots can safely navigate. Vortex adhesion is an uncommon form of pneumatic adhesion which is still being researched. Robots which employ this method do so by creating a vortex with a high-speed fan. The main advantage of the vortex system is it does not require a seal to maintain adhesion like the other more common pneumatic methods. Thrust systems maintain adhesion by creating a thrust force, usually with fans, directed away from the wall, thereby pressing the climbing robot against it. Like vortex systems, thrust systems do not require a seal, but they tend to be unstable and difficult to control which makes them impractical. An example of a climbing robot which employs an active vacuum system and one which employs a vortex system can be found in Figure 8.

Figure 8: (Left) The ICM Climber which employs an active vacuum adhesion system [21]. (Right) The Alicia VTX robot which employs a vortex system [22].

1.3.3.2.3 Mechanical

Mechanical means of adhesion are quite diverse, though most can be broken down into two major categories, claws or grippers. Claws are used on surfaces which are rough enough for the claws to find purchase, while grippers are used to grasp portions of a structure. Once adhesion has been achieved in a mechanical system, there is often very little power required to maintain adhesion onto a surface. In fact, gripers can be designed in such a way that the system can lose power completely and still maintain adhesion. This makes mechanical adhesion methods relatively safe. However, mechanical adhesion tends to force the climbing robot to move slowly and carefully to ensure that adhesion has been achieved, while at the same time making it difficult to maneuver the robot. Figure 9 shows an example of the claw adhesion method and the gripper adhesion method. An example of gripper and claw adhesion systems can be seen in Figure 9.
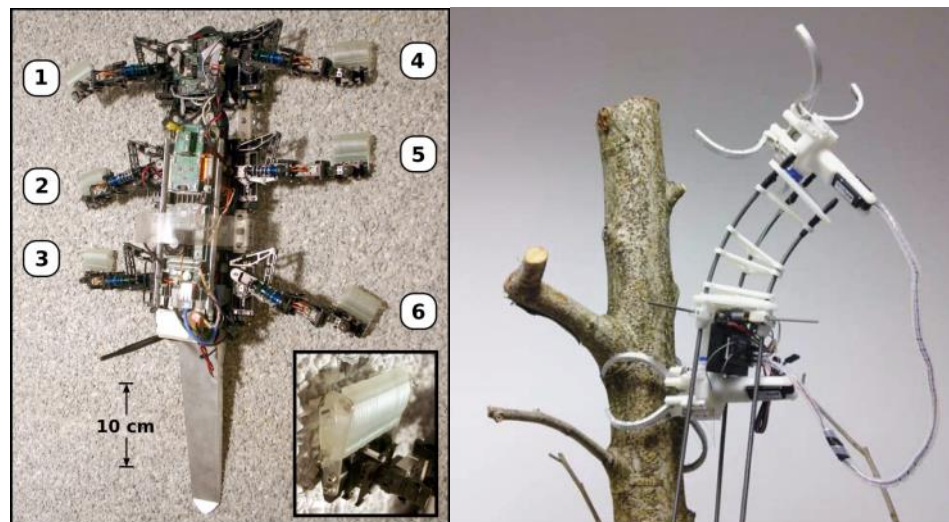
Figure 9: (Left) The RiSE robot which uses small claws to adhere to surfaces [16]. (Right) The Treebot which uses gripper to climb small trees [17].

1.3.3.2.4 Electrostatic

Although few robots employing this adhesion method exist, initial research shows that electrostatic adhesion offers a promising alternative to the more common adhesion methods used in industrial applications. In this adhesion method, pads comprised of electrodes and insulating substrate generate Van der Waals forces between the work surface and the robot. Because of the nature of the electrostatic force, a wide variety of surface, such as concrete, wood and glass, can be adhered to by robots employing this

adhesion method. It has also been shown that a low power to force ratio can be achieved, which means that it is also a relatively energy efficient method for adhesion. Currently, payloads for robots employing electrostatic adhesion are relatively low, but as the concept is developed further, it could very easily begin to compete with the currently employed adhesion methods. An example of a climbing robot which employs electrostatic adhesion is shown in Figure 10.
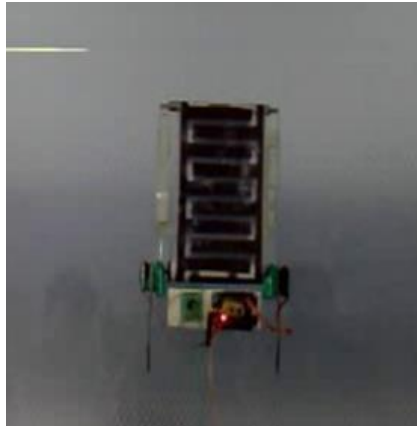
Figure 10: A climbing robot which employs an electroadhesive tread [18].

1.3.3.2.5 Chemical

Chemical adhesion is one of the least common adhesion methods and has, as of now, been confined to the laboratory. This category includes tapes, tacky elastomers and thermal glues. Each of these methods offers a low power adhesion solution, which is desirable. However, each method has its drawbacks. The glue and tape methods require frequent replacement, which can be cumbersome and difficult. The tack elastomer method requires relatively large forces to remove from the work surface once placed. Further research and development is required before any of these methods are capable of being applied in practical applications.

1.3.4 Designs Similar to the Proposed System

This section contains a brief description of climbing robot designs which are similar to the proposed system. It addresses why each design is similar to the proposed design and what differences exist between the proposed design and the existing design, focusing on the adhesion and locomotion method. It does not comment why one design might be superior to another.

1.3.4.1 Treaded Robot with Passive Vacuum Suction Cups

This design uses passive suction cups attached to treads to achieve both locomotion and adhesion. The system is relatively small and only weighs 0.3 kilograms. It uses a single DC motor to drive both belts, which means that the robot cannot be turned.

Once pressed onto a wall, which attaches the first set of suction cups, the robot attaches the suction cups to the wall using a torsion spring, which pushes the suction cups as they travel beneath the drive wheels. Once attached, pins on the suction cups mechanisms move into a guide rail, which distributes the attachment load evenly across all of the attached cups. To detach the cups, a wire is connected between the suction cups release tab and the neighboring suction cup such that the tab is pulled as the neighboring wheel moves around the back idler wheel. This means that the robot can only move forward. A more detailed description of the robot and its operating principle can be found in [20] and Figure 11 shows the completed robot.
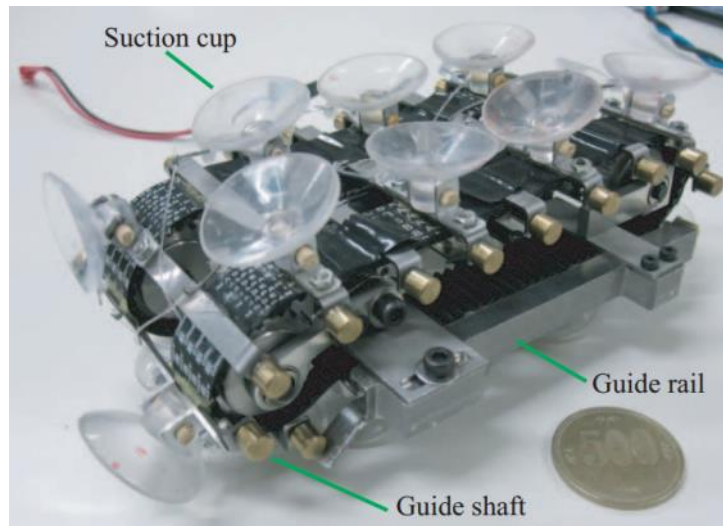
Figure 11: A climbing robot which uses passive suction cups attached to a continuous tread [20].

This design is similar to the proposed design in that it uses a combined adhesion and locomotion method. Like the proposed design it uses a pneumatic adhesion method and a tread for locomotion. However, the proposed design uses an active pneumatic system while this design uses passive suction cups. The proposed design will also be capable of turning 360 degrees, turning each tread independently and turning the treads both forwards and backwards.

1.3.4.2 The Tripillar

This Tripillar uses magnets embedded in a continuous tread to locomote on and adhere to ferrous surfaces. The system weighs 214 grams and uses power from a battery pack. Two DC motors are used to drive the treads, which allows the system to skid steer. It also contains a Bluetooth module to allow the system to be controlled remotely. Two IR sensors are used to align the robot with the surface it is going to climb.

The tread wraps around three wheels, which allows the system to transition between surfaces that are perpendicular to one another. A longitudinal cable is wired into the tread to ensure that it remains rigid when moving. The magnets are molded into the tread and the poles of the magnets are alternated. The operating principle is relatively simple; the magnets adhere to the ferrous surface which produces sufficient friction so that the robot can move without the tread slipping when it is driven by the motors. A full description of the Tripillar can be found in [14] and Figure 12 shows an image of the Tripillar system.
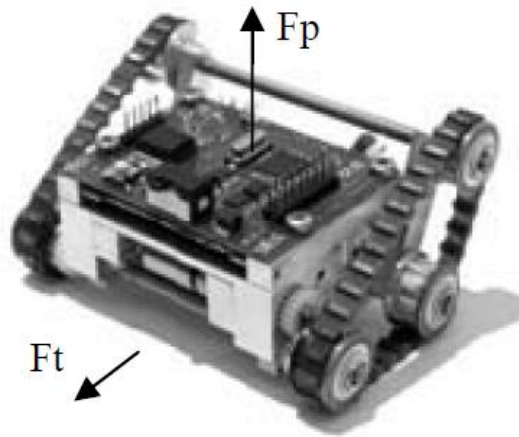
Figure 12: The Tripillar robot, which uses a continuous tread with embedded magnets [14].

Like the design discussed above, this design is similar to the proposed design in that it uses a combined adhesion and locomotion method. Like the proposed design, this system uses a continuous tread to locomote. Both the Tripillar and the proposed design are capable of skid steering. The main difference is that the proposed design uses a pneumatic adhesion method, while the Tripillar uses magnetic adhesion. This limits the Tripillar to operating on ferrous surfaces, but means that it does not require a tether, which the proposed design does require.

1.3.4.3 Treaded Robot with Active Vacuum Suction Cups

This design uses active suctions cups attached to a continuous tread for adhesion and locomotion. The system weighs about 14 kilo grams. It uses a single DC motor to drive the tread which means it is incapable of turning. The system contains an internal power supply and vacuum generator, which means it is not tethered.

The tread is a timing belt, which is driven by two sets of pulleys. Each of the pulley sets is composed of two pulleys which are separated to allow the suction cup assemblies to travel between them. The suction cup assemblies are bolted to the tread, with the cups on the outside of the tread and trigger mechanism on the insides. Each assembly is connected to a rotating manifold which connected to the vacuum generator. When an assembly is not in contact with the wall, the cup is cut off from the vacuum supply. As the cup comes into contact with the wall, the trigger mechanism enters a guide channel which depresses the trigger and exposes the cup to the vacuum. A full description of the system can be found in [8] and Figure 13 contains an image of the system.

Figure 13: A climbing robot which uses active suction cups attached to a continuous tread [8].

This climbing robots design is the most similar to the proposed design that could be found. Both designs use active vacuum adhesion which is incorporated into a continuous tread. Several differences separate the proposed design from this design. The most obvious of these differences is that the proposed design uses its treads perforations as suction chambers, while this design uses suction cups. Additionally, the proposed

16

design uses venturis and a positive pressure air supply to generate vacuum, while this design uses an electric vacuum generator. The proposed design is also capable of skid steering, which this design is not.

1.4 Proof of Concept Model

Before this thesis was started, the author and a graduate student from the Netherlands, Erik van Broekhoven, designed and built a proof of concept model. The purpose of this model was to demonstrate that a perforated tread was capable of being used as an adhesion and locomotion methods for wall climbing robot. It was also meant to determine any problems associated with the design, so that that information could be used in this project.

1.4.1 Design

The project began with a literature study to determine whether or not the proposed concept, i.e. the perforated tread acting as a suction cup, had been designed by another party. It was found that the concept was novel and so the project moved forward.

A model of the tread and manifolds was created to determine an optimized pattern for both parts which would allow the vacuum system to provide consistent force between the wall and the vehicle. This optimization was done using a Matlab script. The script analyzed images of different tread and manifold hole patterns overlaid with each other to determine the area exposed to vacuum as the manifold was moved across the tread. An image of the types of images used in the program can be found in Figure 14.
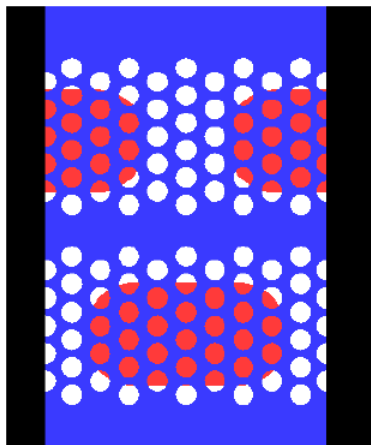
Figure 14: Sample of the images used to determine exposed tread hole area.

Once the hole patterns of the tread and manifold were finalized, the material of the tread and manifold were chosen. The material for the tread was chosen to be fabric reinforced neoprene because it was compliant in the direction of the thickness of the tread but stiff longitudinally and laterally. The manifolds material was chosen to be acrylic with a thin sheet of Teflon were the manifold contacted the tread to reduce friction.

To shorten the time to manufacture the vehicle a radio controlled tank chassis was purchased from Taigen Tanks. The tank offered many components which could be used directly in the project such as its motor system, its drive and idler wheels, its frame and its tensioning system. The model of the vehicle was based on the dimensions of this chassis and components were added as necessary to complete the design. An image of the final model can be found in Figure 15.
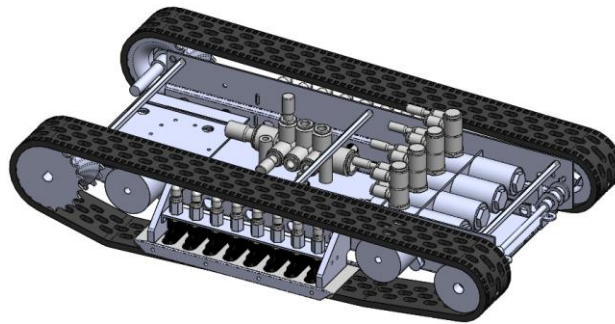
Figure 15: Solidworks model of proof of concept model.

1.4.2 Manufacturing

The manufacturing of the vehicle itself was relatively straight forward. The tank chassis was stripped down to its sheet metal frame and the superfluous components were removed. Struts were added to in interior of the frame to stiffen it and holes were drilled in its base to mount the venturi system. Lipped delrin wheels were machined to replace the idler and tensioner wheels that came with the tank to help retrain the tread during operation.

The tread and manifold plates were laser cut as their geometries were complicated. The treads were then stitched together using Kevlar thread to form continuous belts. Silicone paste was then used to seal the stitched area. Guide rails were then attached to the manifold plates to guide the tread as it passed under the manifold plates.

1.4.3 Testing and Observations

The first test which was conducted was a pull off force measurement test performed on different surfaces. The test involved adhering the vehicle to different surfaces then pulling the vehicle off the surface using a force scale. The results of this test can be found in Table 1.

Table 1: Pull-off force on different surface types.

Material	Force [N]
Acrylic	35-40
Wall	75-80
Wood	45-50
Painted door	55-60
Painted steel closet	55-60
Glass	80-85

The second test which was conducted was to see if the vehicle was able to drive under its own power. This test was unsuccessful as the friction between the tread and manifold was too great for the stock motors on the tank chassis to handle. As an alternative, the drive wheels were rotated by hand and forward motion was achieved without the vehicle dropping from the wall, though it was extremely difficult to move.

A myriad of observations were made about the vehicles performance during testing. These ranged from problems in the tread system to difficulties with the vehicles frame. Table 2 lists the significant observations which were made during the testing of the vehicle.

Table 2: Observations made about the conceptual model during testing.

Observation	Description
Motor Torque	The motor torque was insufficient to drive the vehicle up the wall. The cause of this problem was a combination of friction between the manifold and the tread and the weight of the vehicle.
Tread/Manifold Friction	The amount of friction between the tread and the manifold was far more significant than initially predicted.
Deflection of the drive and Tensioner shafts	Significant deflections were observed in the drive and idler wheel shafts when the belt was tensioned. This cause the tread to slip when the wheels of the vehicle were turned.
Frame Deflections	Deflections in the frame were observed after the belt was tensioned.
Tread Stiffness Problems	A significant amount of stretch and deformation was observed in the tread when the wheels were turned. This included deformation at the hole where the drive wheel engaged with the tread, warping of the vacuum through holes and buckling when the tread was pushed under the manifold.
Venturi clogging	Several instances of venture clogging were observed during the testing.
Adhesion Failures	Several instances of adhesion failure between the wall and the vehicle were observed. Each instance of failure was the result of a single failed vacuum section.

Low Adhesion Force	The adhesion force between the wall and vehicle was lower than expected.
Peel Off	The motors at the front of the vehicle created a moment which caused the treads to peel off the wall.

1.4.4 Results and Conclusions

Despite the fact that the vehicle could not locomote under its own power, the ultimate results of the proof of concept model were promising and provided information which was applied to the next iteration of the design. A list of improvements to future designs that was developed during the course of the proof of concept phase of the project follows.

- Create a detailed model of the vehicle to determine the motor torque required and ensure a sufficient factor of safety is used when selecting the motors.
- Use professionally manufactured belts as treads to ensure the tread is stiff enough to handle the loads it will be subjected to.
- Use a brace between the drive ad idler wheels and stiff shafts to minimize deflections in the wheel system.
- Use material combinations for the tread and manifolds which have a low coefficient of friction.
- Have a means of measuring the vacuum pressure in the manifolds directly to make characterizing the vehicles adhesion performance easier.
- Try to ensure that the center of gravity of the vehicle is near the center of the manifolds to reduce peel off forces.
- Ensure that the frame is stiff enough to handle the tension and operation loads it will be subjected to.
- Ensure that the tread is unable to slip off of the wheels during operation.
- Ensure the wheels are well aligned.

The most significant outcome during the design of the project was that a rubber tread could be used to seal a vacuum system and hold the vehicle to a wall. Figure 16 shows the first proof of concept model adhering to a wall.

Figure 16: Proof of concept model adhering to a vertical surface.

Chapter 2: Design

2.1 Design Criteria

This section details the criteria that were used to guide the design of the climbing robot. These criteria are

described in detail in Table 3.

Table 3: The criteria used to design and test the climbing robot system.

Criteria	Numerical Value	Description
Maximum System Weight	15 lbf	The system should be a reasonable weight so that the user can easily and safely carry it and apply it to surfaces.
Minimum Payload Capacity	1.5 lbf	The minimum payload which the system should be able to carry.
Minimum Drive Speed	0.5 ft/s	This is the minimum drive speed which the robot should be able to achieve during forward motion.
Maximum Required Input Air Pressure	100 psi	The maximum pressure which the input to the system should require. Set by the maximum possible pressure output from testing station in Mustang 60.
Minimum Pull Off Force Factor of Safety	2.0	This is the minimum force which should be required to remove the robot from a surface when it has payload.
Minimum Number of Failed Vacuum Sections for Continued Adhesion	2	This is the minimum number of vacuum sections which can be exposed to the atmosphere or have failed and still allow the robot to maintain adhesion.
Minimum Surface Roughness	0.005 in.	The minimum surface roughness which the robot should be able to operate on.
Maximum Voltage Input	120 VAC	The system should be able to be powered using a standard wall outlet.

2.2 Component Selection

This section details the selection of the major system components. These components drove much of the

rest of the systems design. These components include the selection of the motors, the power supply, the

venturis and the belt system.

2.2.1 Motor Selection

The motors were a critical portion of the design. This was because they ultimately control both the total

weight that the system can carry and the speed at which the system can travel. The inability of the proof of

concept model to locomote under its own power also demonstrated the importance of the using sufficiently

powerful motors in the new system.

2.2.1.1 Selection Criteria

It was decided early in the project that the motors would be direct current (DC). This was because the controller which was to be created for the robot would be simpler to design and program if the motors it was driving were DC. The controller, more specifically the motor driver chips, also determined the maximum allowable input voltage and current for the motors. The allowable electrical parameters of the motors can be found in Table 4. These parameters were used as a guide when selecting the motors which would be used to drive the motors.

Table 4: Maximum allowable electrical characteristics of the motors. Values taken from the VNH5019A-E data sheet.

Parameter	Value
Current Type	Direct
Maximum Voltage	40 Volts
Maximum Current	30 Amps
Maximum Power	1.2 Kilowatts

The physical requirements of the motors were determined next. The output torque and speed of the motor shaft were the most important physical parameters of the motors. To calculate the required torque output, a simple conceptual model of the system was created. This model was based on the predicted physical parameters of the final system, using the proof of concept model as a guide. The model was then symbolically analyzed to determine the required torque for the motor. The results of this analysis were used to create a calculator which would take in known or projected system parameters and output the motor torque. This calculator was used throughout the design process to ensure that the selected motors would be able to meet the torque requirements of the final design. The symbolic calculations used to create the calculator can be found in Appendix A, as well as an outline of the calculator and sample results.

The speed requirements of the motors were calculated next. This was a relatively simple calculation. It involved back calculating the motors RPM from the desired minimum speed of the robot and the projected drive wheel radius, and assumed that the speed of the robot could be calculated as if the drive wheels were placed directly on a surface rather than on treads. Again, this calculation was updated as the design of the robot was iterated. The calculation used to determine the required output RPM of the motor can be found in Appendix A.

The other physical parameters of the motor were also considered. This includes the weight of the motor, the motors size and how easily the motor could be mounted. To ensure that the motors did not expend a large amount of their output power lifting themselves, it was determined that they should not be a large fraction of the systems overall weight. With this in mind, was decided that the motors should each contribute less than 10% of the overall mass of the system. To allow for as much room as possible for the other components in the robot, a compact overall package for the motors was desired. Based on preliminary sizing of the system, motors which fit with in a 4"x3"x3" space would be considered ideal, though this was a flexible requirement and motors which fell outside this space by +0.5" on any of the parameters would be considered. A list of all of the physical requirements for the motors can be found in Table 5.

Table 5: Physical requirements used to select the drive motors for the climbing robot.

Physical Parameter	Value
Required Output Torque From Calculator	26.7 in-lb
Output Angular Velocity	40 RPM
Maximum Motor Weight	1.75 lb
Desired Motor Dimensions	4"x3"x3"

2.2.1.2 Selected Motors

Using the above parameters, a search for DC gear motors was conducted. This search turned up two different motors which satisfied most of the conditions required for the project. These two motors, one from Molon motors and the other from Maxon motors, were compared. Table 6 contains a comparison of the relevant specifications for each of the motors which were considered.

Table 6: Specifications for the two motors which best satisfied the projects requirements.

Parameter	Molon Motor	Maxon Motor
Maximum Torque	50 in-lb	60 in-lb
Torque Factor of Safety	1.87	2.25
Max Angular Velocity	25 RPM	50 RPM
Required Voltage	24 VDC	24 VDC
Max Current	1.08 A	2.73 A
Dimensions	4.17"x2.75"x3"	1.26" dia. x 4.65" long
Weight	1.2 lb	1.12 lb
Cost per Motor	$53.16	$744.88

While the Maxon motor better satisfied the speed and torque requirements above, the Molon motor was chosen for several reasons. The first and most significant was cost. The Maxon motor was almost fifteen times the cost of the Molon motor, which put it far outside the budget of the project. Also, two of the

Maxon motors required a relatively large current which would make them less safe to use. The length of the Maxon motors also made it difficult to fit them easily in the space available.

The Molon motors, while not able to match the Maxon motor in output speed or torque, do satisfy most of the projects requirements. The only area which they do not satisfy is desired output speed, but this is acceptable because with the finalized drive wheel size they can move the robot at approximately .29 feet per second, which is reasonable. The Molon motors torque output also has a low factor of safety when compared with the initial torque requirement predictions, but the final weight of the system and final wheel size reduce the projected torque requirement significantly, making them more than powerful enough. They have a relatively low current draw, meaning they will not over tax the controller or the power supply when running near their maximum current draw. Their compactness also means that they were easy to integrate into the space that was available for them. Images of the Molon motors selected for the project can be seen in Figure 17 and Figure 18.
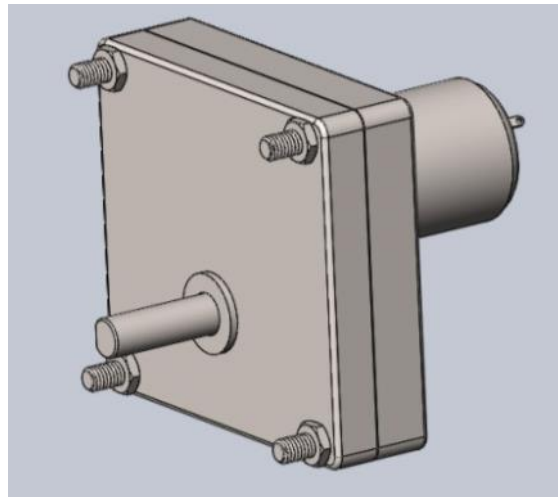
Figure 17: Solid model of the selected motor.

Figure 18: Molon motor chosen for the vehicle.

2.2.2 Power Supply Selection

The power supply was an important factor to consider in the design of the vehicle, as it provided the vehicle with electrical power for the controller, the motors and the sensors. Three parameters were considered in the selection process for the power supply used. These were the weight contributed to the vehicle by the power supply and its cables, the power requirements of the motors and the controller and the amount of space the power supply occupied in the vehicle.

2.2.2.1 Selection Criterion

The criteria used to select the power supply used in the project were relatively strait forward. The first and most critical of these criterion was the ability of the power supply to meet the electrical power requirements of the vehicles. This requirement was determined by summing the current draw of the motors and the controllers and by finding the maximum voltage that the motors could safely operate at. The weight requirement for the power supply was based on its total contribution to the overall weight of the vehicle. It was decided that the power supply and its cabling should not weigh more than 10% of the total weight of the vehicle. To maximize the space inside the vehicle, a limit was placed on the foot print dimensions. Table 7 contains the criterion used to select the power supply.

Table 7: Criteria used to select the vehicle power supply.

Criteria	Value
Minimum Voltage Output	24 V
Minimum Current Output	2.75 Amps
Minimum Power Output	66 Watts
Maximum Allowable Weight	1.5 lbf
Maximum Foot Print Dimensions	3 in. x 4 in.
Maximum Height	3 in.

2.2.2.2 Selected Power Supply

Three different types of power supplies were proposed for the system. These were a battery pack, an on vehicle AC/DC converter and an off vehicle AC/DC converter. The battery pack option was quickly dismissed because while a battery pack would eliminate the need of an electrical tether for the vehicle, they are extremely heavy and has large foot prints at the required voltage and power needs of the vehicle.

Ultimately, the power supply type chosen was the off vehicle AC/DC converter because it offered several advantages over the on vehicle AC/DC converter. The most significant of these advantages was the fact that the off vehicle converter contributed almost no weight to the vehicle, with only the weight of the lines between the converter and the vehicle contributing to the vehicles overall weight. The off vehicle converter also did not require any space in the interior of the vehicle, which would make it easier to work inside the robot after assembly. The off vehicle converter was also much safer, as an on vehicle converter would require an AC line to be run to the vehicle. This meant there would be significant risk of electrocution if the line or the converter were grounded to the vehicle. Figure 19 shows the off vehicle AC/DC converter that was used as the projects power supply.

Figure 19: Agilent N5747A power supply used to power the vehicle.

2.2.3 Venturi Selection

The selection of the venturis used in the robot was a critical portion of the design because they generate the vacuum used to adhere the system to surfaces. Three major parameters were used in determining which venturis would be employed in the design. These were the maximum vacuum which could be generated by the venturis, the required input pressure for the venturis and the rate at which the vacuum can evacuate the required volume. Other considerations which were taken into account, but were less critical, were the dimensions and weight of the venturis. Because the proof of concept model used venturis from Vaccon and they proved to be of high quality, it was decided that the venturis for this project would also be purchased from Vaccon.

2.2.3.1 Selection Criterion

To minimize the required area exposed to the vacuum, and thereby reduce the size of the tread, to ensure safe adhesion venturis which could generate high vacuum were desired. It was found that the maximum pressure achievable by Vaccon's venturis was 13.75 psi. This maximum pressure was shared by all of their miniature and midsized venturis. This was also true of the required input pressure for each of the venture models. They all required an 80 psi input to achieve maximum suction.

The weight and the dimensions of the miniature venturis were also all standard, with no variation between models. The exception to this was in the different silencers which could be used with the venturis. Three different silencers were available, a closed end silencer, a straight-through silencer and hybrid silencer. The closed end and straight-through silencers were similar in their overall weight, but the closed end silencer was shorter by about .4 inches. The hybrid silencer was quite a bit larger than the other two options both in increase in length and weight of the venture system. To keep the length of the venturis to a minimum, the closed end silencers were selected.

This left the evacuation rate to determine which should be used in the project. To determine the required evacuation rate, the volume that the venturis were first estimated. This calculation was based on the estimated volumes of the manifold chamber, the connecting tubing and the tread perforation volumes. The estimated volume was determined to be 9.4×10^{-4} ft^3. The desired time to evacuation was determined based on the rate that the pressure sensors measuring the vacuum could operate at. The time to evacuation

was selected as 0.01 sec, which allowed the pressure sensors to take around 5 measurements during the evacuation. The required evacuation rate was then calculated and found to be about 10 sec per ft^3. All of the calculations related to estimating the evacuation rate can be found in Appendix A. Table 8 contains the requirements for determining which model of venturi would be used.

Table 8: Parameters used to select the venturi models used in the robot.

Parameter	Value
Input Pressure	80 psi
Maximum Vacuum	13.75 psi
Evacuation Rate	10 s/ft^3
Length (Including Silencer)	4.20 in
Diameter	0.75 in

2.2.3.2 Selected Venturi

Because most of the parameters for each of the venturi models were similar, the selection process was relatively quick. The decision was made by comparing the evacuation rate between each of the miniature venturi models offered by Vaccon. Cost was also factored into the decision, as well as the fact that venturis from the proof of concept model were available.

Using the estimated volume of a single section of the vacuum system and the evacuation rates provided by Vaccon, the time to evacuation was calculated for each of the miniature venturi models. The costs of each of the venturi models with the closed end silencer were also gathered. This information can be found in Table 9.

Table 9: Evacuation rate, evacuation time for the estimated volume of a single vacuum section and the cost of each of the different venturi models in Vaccon's miniature venturi line.

Parameter	JS-60M	JS-90M	JS-100M	JS-150M
Evacuation Rate	28.24 s/ft^3	10.05 s/ft^3	8.99 s/ft^3	4.46 s/ft^3
Evacuation Time	0.027 s	0.009 s	0.008 s	0.004 s
Cost	$65.00	$71.50	$78.25	$84.75

The venturi model which was ultimately selected was the JS-90M, for several different reasons. The JS-90M allowed for a sufficient number of readings during the re-evacuation process. The shorter evacuation time also allows the robot to recover more quickly when sections of the vacuum system are exposed to the atmosphere and also allows the vacuum system to deal with minor leaks which may occur during operation. The cost of each of the different models were all similar, but the JS-90M falls at the lower end of the cost spectrum. This, coupled with the fact that four of the JS-90M models were available from the proof of

concept model meant that it was the most cost effective option. An image of the JS-90M model can be found in Figure 20, which shows both the venturi's main body and the closed end silencer.
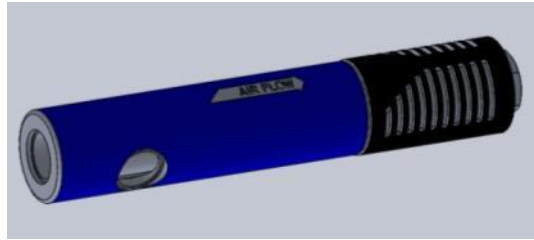
Figure 20: Solidworks representation of the JS-90M-AA4.

2.2.4 Tread Selection and Design

The treads which drive the robot and act as the gasket for the vacuum system are perhaps the most critical portion of the design. The design of the new tread system was begun by looking at the problems associated with the proof of concept models tread. With this insight, criteria were set forth for the design of the new tread, both in terms of the materials used in the tread and the shape that the tread would take.

 The proof of concept model suffered from several different problems associated with its treads, which this design seeks to address. The first of these problems was buckling of the tread when under vacuum, which was caused by high friction between the tread and the manifold, as well as the low stiffness of the tread material. The second problem which the proof of concept models tread had was a large amount of deflection in the tread when it was under tension and when driven. The perforations in the tread which interacted with the drive wheels warped significantly, which caused damage to the edges of the belt. The third problem with proof of concept tread was that it was not initially continuous and had to be stitched to attach the free ends. The stitched area suffered from small tears each time the belt was tensioned, which would eventually cause failure. This tearing also meant that the stitched area was difficult to seal effectively and that leaks caused by the tears would eventually become great enough to cause the vacuum system to fail. The stitched area was also raised on both sides of the tread, which cause the manifold to be pushed away from the tread as it moved over the stitched area dethatching the robot from the wall.

2.2.4.1 Selection and Design Criterion

It was decided early in the projected that using timing belts as the basis of the treads would offer several advantages over other potential designs, such as the sprocket driven belt in the proof of concept model. Timing belts are generally stiff and can be tensioned without causing any deflection or stretching in the belt. This stiffness also means that they are less likely to buckle during operation, which is especially important for the robot to function properly. The teeth of timing belts also do not suffer from the deflections seen in the proof of concept models drive holes at even relatively high torques. Teeth also help to ensure that no slipping around the drive pulley, even at high speed or torques.

Timing belts also allow for the tread to be flat against the wall for its entire length between the drive wheels and the back idlers. This was not possible in the proof of concept model because the drive sprocket and

back idler would contact the wall before the tread. Having the tread leaving the wheels parallel to the wall allows for the drive and idler wheels to take a portion of the reaction loads from the wall that would otherwise be carried by the manifold. It also means that the manifold does not need to force the tread flat against the wall, which the manifold in the proof of concept model had to do.

Another advantage of using timing belts is the fact that several companies exist which produce custom belts. By using an outside manufacturer, belts of greater complexity could be produced for much less effort and time than if they were machined on site. A survey of different custom belt companies was conducted and it was found that F.N. Sheppard had the widest variety of customization options available. These options included the removal of teeth in a given area of the belt, the application of low friction material on belt surfaces, the application of backing material on the outside of the belt and perforations of the belt. Each of these capabilities was important for the design of the tread. Their website included a design catalog which contains a large amount of information which was used to design the belts used in the robot.

Several different belt materials were available from F.N. Sheppard. These included urethane, various neoprene rubbers and silicone. The most common materials used in the construction of their belts were urethane with a durometer of 90 shore-A and neoprene with a durometer of 70 shore-A. Each of these materials could be reinforced with different types of internal fibers, the urethane with steel or Kevlar and the neoprene with fiberglass. These reinforcement fibers allow for the belts to be tensioned without stretching. F.N. Sheppard also offered a variety of different tooth patterns, each with different dimensions. These patterns were common between the different available belt materials.

To determine which belt material and dimensions should be used in the project, two different factors were considered. The tension in the belt was perhaps the most critical because if the belt were too lose it could jump teeth on the wheels or buckle, while if it were too tight the shafts, bearings or the belt itself might fail. Using an equation found in a timing belt catalog, the minimum required tension of the belt was estimated. This equation uses the design torque acting on the belt, the diameter of the drive pulley, the mass per unit length and the speed of the drive pulley. The calculation used to determine this estimate and the belt factor of safety can be found in Appendix A. Table 10 contains the estimated values for the minimum required belt tension.

Table 10: Minimum tread tension for the robots treads to function properly and the factor of safety estimated for the tread.

Parameter	Value
Minimum Belt Tension	55 lb
Factor of Safety	16

The next important criterion for the design of the tread was the area of the perforations that the vacuum would be pulled through. Using the projected weight of the system and the desired factor of safety, a required vacuum force was calculated. This calculation was performed assuming for two cases, when the robot is attached to a vertical surface and when the robot is attached to the ceiling. Using this vacuum force and the vacuum pressure which could be generated by the venturis, the perforation area was calculated. Table 11 contains the values for the required vacuum and for the required area of the perforations, and the calculations used to obtain these values can be found in Appendix A.

Table 11: Expected required vacuum forces for both vertical operation and operation upside-down and the tread perforation area which is required to achieve the greater of the two force values.

Parameter	Value
Vacuum Force – Vertical Surface	33 lb
Vacuum Force – Ceiling	33 lb
Perforation Area	2.4 in^2

Another important factor which was considered was the friction between the manifold and the tread. One of the main reasons which the proof of concept model could not drive itself and the models treads buckled was due to the friction between the treads and the manifolds. In the model, Teflon was added to the bottoms of the manifold plates but the rubber of the tread still caused a large amount of friction. To determine the desired coefficient of friction between the tread and manifold, a short calculation was performed. First, it was decided that the friction force between the tread and the manifold should not exceed twenty percent of the force output of the motors. From this number, the maximum allowable friction force was calculated. This force value was then used to determine the maximum allowable coefficient of friction by dividing the frictional force by the vacuum force determined above. The calculated maximum coefficient of friction value is the static coefficient of friction, because the static coefficient of friction is always greater than the dynamic coefficient of friction. Table 12 contains the maximum friction force allowed between the tread
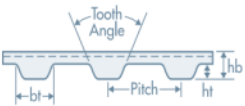
and the manifold, as well as the maximum static coefficient of friction allowable. Appendix A contains the calculations used to determine these two values.

Table 12: Maximum friction force allowable between the tread and the manifold and the resulting maximum allowable coefficient of static friction between the tread and the manifold.

Parameter	Value
Maximum Friction Force	10.5 lb
Maximum Desired Coefficient of Friction	.5

2.2.4.2 Selected Belt Design

The first step which was taken in the design of the belt was the determination of which of the materials offered by F.N. Sheppard, urethane or neoprene, should be used, as well as the tooth pattern which should be used. This was accomplished using both the design catalog provided by F.N. Sheppard and recommendations by one of their support staff. The design catalog contained detailed design information for both urethane reinforced with steel and urethane with Kevlar. This information included the stiffness, allowable tension, weight and tensile strength for different tooth pitches. The catalog did not contain any of this information for the neoprene timing belts, except for the durometer of the neoprene. This made the urethane belts more attractive initially, as their properties could be directly compared to the requirements above. The tooth pattern of the belt was selected next and Figure 21contains a table from the catalog which contains the dimensional information for each of the available tooth patterns. Three of these patterns were considered for the project. These were the XL, L and H patterns.

Belt Section	Construction Urethane/ Neoprene	Pitch (in.)	hb (in.)	ht (in.)	Tooth Angle (Degree)	bt (in.)
40 DP	Urethane	0.0816	0.048	0.018	60	-
MXL	Urethane & Neoprene	0.080	0.045	0.018	40	0.045
XL	Urethane & Neoprene	0.200	0.090	0.050	50	0.101
L	Urethane & Neoprene	0.375	0.140	0.075	40	0.183
H	Urethane & Neoprene	0.500	0.160	0.090	40	0.241
XH	Urethane & Neoprene	0.875	0.440	0.250	40	0.495
XXH	Neoprene	1.250	0.620	0.375	40	0.750

Figure 21: A table containing the dimensions of the different belt patterns taken from F.N. Sheppard's design catalog. The highlighted belt sections are those which were considered for the tread of the robot.

Based on the design criterion from the previous section, each of the tooth patterns which were considered would be able to handle the projected minimum tension and tooth loading, even if the width of the belts was relatively thin. Several different factors ultimately lead to the selection of the type H belt pattern. The first was that it was the stiffest of the options and could carry the greatest tension. This meant that the tread would be less likely to buckle when driven and would allow a wider range of tensions to be tested. The type H pattern also had the strongest teeth of the three options, again meaning that a wide range of tensions could be tested without fear of damaging the belt teeth. The height of the teeth in the type H pattern also meant that the belt would be less likely to slip off the wheels during skid steering.

Urethane reinforce with Kevlar was initially chosen as the material for the tread because, as stated above, little information was given about the neoprene belt material beyond its durometer. This choice was reconsidered and ultimately changed after consulting with F.N. Sheppard. Although a neoprene belt would be less stiff than a urethane belt, it was found that neoprene would ultimately work better for the robot for several different reasons. Firstly, after describing the parameters of the robot and the expected loading on the belt, the representative was confident that a neoprene belt would more than meet the projects requirements. The cost of the neoprene belts was significantly lower than that of a urethane belt. The production time for the neoprene was also significantly shorter than that of the urethane belt, as the neoprene belts were prefabricated and only required modification. The neoprene belt offered by the company was molded, and so did not require any welding to make it continuous, which the urethane belt would. This weld interferes with the continuity of the perforation pattern for the vacuum system, causing a dead spot at the welded section. So, based on the advice of the F.N. Sheppard representative, the neoprene reinforced with fiber glass was chosen.

The next step in designing the treads was the selection of the backing material which would be on the outside of the tread and the selection of the low friction material which the manifold would contact on the inside of the tread. The backing material was a relatively simple selection. The neoprene belt used in the proof of concept models tread, which was 70 Shore A durometer, showed that even relatively stiff neoprene could form a sufficient seal. A brief survey was conducted to determine the standard durometer of neoprene used in suction cups and it was found the between 40 and 60 Shore A durometer neoprene is commonly

used. This information, coupled with a backing selection chart from F.N. Sheppard, lead to the selection of quarter inch thick 40 Shore A durometer neoprene being selected for the backing.

One of the services which F.N. Sheppard provided was the application of the Teflon coating on belts and the application of low friction fabrics. Initially, Teflon coating was chosen for the area were the tread and manifold would come into contact because the bottom of the manifold would also be coated in Teflon. This would have made the coefficient of friction between the tread and manifold around 0.04, which is extremely low. After consulting with the F.N. Sheppard representative it was discovered that the Teflon coating could not be applied to the area of the belt were the manifold would be traveling. This meant that a low friction fabric would be applied to this area instead. No specific data was given for the properties of the low friction fabric, but the F.N. Sheppard representative was confident that the fabric would ensure that the friction between the manifold and tread would be lower than the maximum allowable force.

With all of the belt materials and tooth pattern chosen, the final portion of the belt system that was designed was the physical design of the belt. This included the width of the belt, the length of the belt, where the belt teeth should be removed, if an indented channel should be cut in the belt for the manifold and the perforation pattern layout. The first and easiest of these was the determination of where in the belt the teeth should be removed. Because the tread would undergo lateral forces during skid steering, it made sense that the teeth should be removed in the center of the tread. This left teeth on both sides of the tread which could then be used to align the tread with the wheels, align the manifold with the perforations in the tread and allow the wheels to carry the lateral loads of the skid steering through the teeth.

To determine the width of the area where teeth were removed, and by extension the width of the tread itself, the next physical parameter determined about the tread was the pattern of perforations. Initially, a slotted pattern similar to the proof of concept models pattern was designed. Slots were chosen in an attempt to increase the area exposed to the vacuum while also ensuring that the area of the tread exposed to the vacuum was minimized. An image of the initial slotted pattern can be found in Figure 22. After consulting with F.N. Sheppard it was discovered that using a slotted pattern would increase the cost of the belts dramatically. So the slotted perforations were abandoned in favor of circular perforations. F.N Sheppard offered several different standard circular hole patterns, with various diameters and pitches, which were

more cost effective than the slotted pattern. To determine which pattern would provide the most consistent

vacuum force at the proper magnitude, a test assembly was created in Solidwoks. Using this assembly,

different potential hole patterns were tested against each other. The full details of this test assembly and the

methods used to determine the final hole pattern can be found in Appendix A. The final pattern which was

decided upon three rows of the quarter inch holes at a half inch pitch along the rows. The rows were

staggered relative to one another to allow for the overall width of the pattern to be minimized. Table 13

contains the projected performance information gathered from the Solidworks test assembly. Figure 23

contains an image of the final perforation pattern selected for the tread and a detailed drawing of the treads

perforation pattern can be found in the drawing package which accompanies this report.
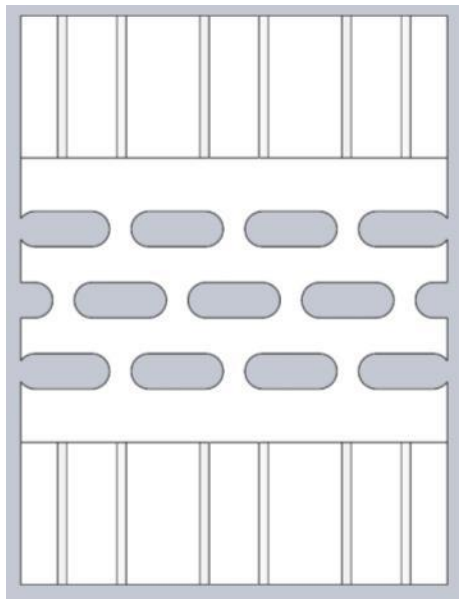
Figure 22: Original slotted pattern chosen for the tread.

Table 13: Hole pattern dimensions of the final tread design and the projected area of the wall exposed to the treads.

Parameter	Value
Hole Diameter	0.25 in
Number of Rows	3
Pitch in Row	0.5 in
Projected Average Area of Wall Exposed to the Manifold	2.24 in^2
Projected Vacuum Force	30.3 lb
Maximum Pattern Width	0.75 in^2
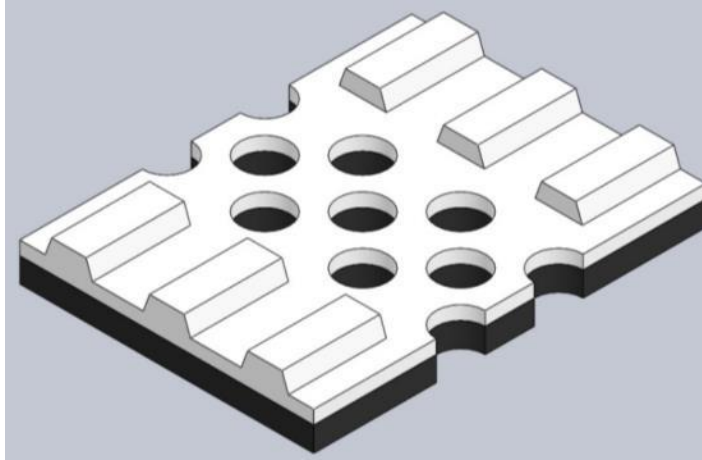
Figure 23: Solidworks model of the final tread hole pattern.

With the width of the perforation pattern determined, the width of the area where the teeth were removed from the belt could be determined. It was decided that an eighth of an inch gap should be left on either side of the tread pattern. This was to both ensure that the perforations in the tread were completely covered by the manifold, even if the manifold shifted relative to the tread, and to allow for continuous reinforcement fibers to remain in the area where teeth were removed. This meant that the section where the teeth were removed would be one inch wide. It was decided that the overall tread width would be two inches wide. This was to ensure that the teeth of the tread and wheels would have a large are over which to contact.

The determination of the belts length was relatively easy. After a Solidworks layout of the drive and back idler wheel was created, the belt tool in Solidworks was used to determine the pitch length of the belt which would snuggly fit around the wheels. With this number in hand, the standard neoprene belt lengths produced by F.N. Sheppard were consulted. A belt that was slightly longer than the Solidmodels predicted length was then chosen to allow the tread to be placed around the wheels without difficulty. The belt length also determined the number of teeth on the belt. Table 14 contains the predicted required belt length by Solidworks, as well as the selected length of the final belt and number of teeth on the final belt.

Table 14: Predicted and actual pitch length of the final tread design, as well as the number of teeth on the final tread design.

Parameter	Value
Solidworks Minimum Predicted Length	33.8 in.
Final Belt Length	34.0 in
Number of Teeth	68

2.3 Subassembly Design

This section contains descriptions of the design process of the subassemblies of the vehicle and their components. This includes the criterion used to design each component, the process used to select the final design of each component and the process used to validate the final design of the components. A complete solid model package of all components manufactured at Cal Poly, as well as their respective drawings, can be found in files which accompany this report

2.3.1 Frame Subsystem

The frame subassembly was key to the functionality of the vehicle as a whole. It provided attachment points for all of the other major subsystems of the design and gave the vehicle its rigidity. Therefore it neededmust be strong enough to withstand the forces of operation as well as light enough to allow for the other subsystems weight. Figure 24 shows the frame subsystem.
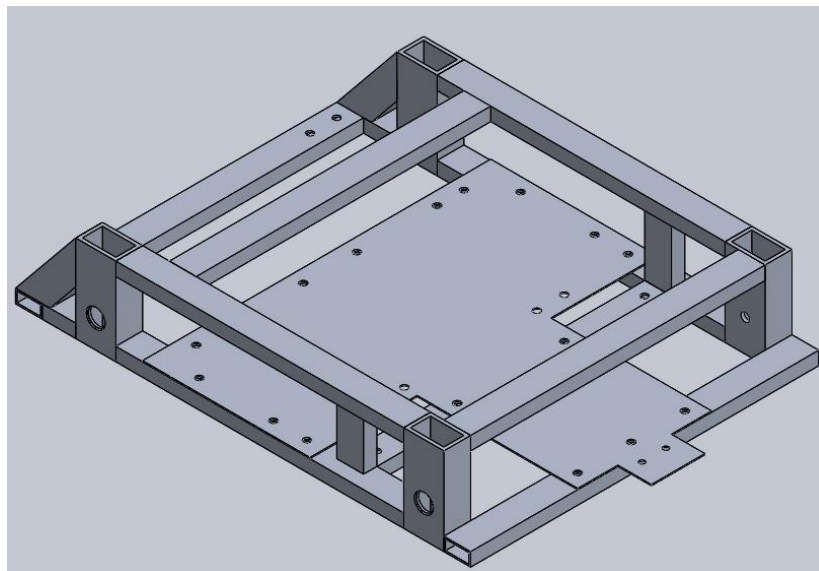
Figure 24: Solidworks model of the frame subsystem.

2.3.1.1 Frame

The frame of the vehicle was required to be both rigid and light weight, while providing sufficient space and attachment points for the other subassemblies. The first step in the design of the frame was determining what type of material the frame would be made of. Three different possibilities where conceptualized. These were: a sheet metal frame, an aluminum tubular frame and an aluminum t-slot frame. Each of these

concepts was compared to the others to determine which would best suit the projects requirements. This comparison can be found in Table 15.

Table 15: Decision matrix used to determine the frame material used in the project.

Criteria	Criteria Description	Criteria Multiplier	Sheet Metal	Tubular	T-Slot
Weight	The overall weight of the frame.	6	2	3	1
Manufacturability	How easy to manufacture the frame is.	2	1	2	3
Precision	How precisely the frame can be manufactured.	4	1	2	3
Stiffness	How stiff the final frame could be made.	5	1	2	3
Cost	How little the frame would cost to make.	1	3	2	1
Attachment	How easy attachment of other systems to the frame would be.	3	1	3	2
Total			29	51	46

As seen above the tubular frame was superior to the other two concepts. With the general material of the frame chosen, the specifics of the frame were then designed. The tubing selected to make up the frame can be found in Table 16. To ensure that the internal components of the vehicle would fit into the frame, the first thing that was designed for the frame was the internal dimensions. The height of the frame needed to accommodate the motors and the banks of venturis with enough room to make adjustments to the internal components easily. The width was chosen to accommodate both the controller and attached pressure sensors as wells at to allow for different motors to be used if the chosen motors did not perform as expected. Finally, the length was chosen based on the theoretical length of internal component layout.

Table 16: Tubing selected to make up the vehicle frame.

Location Used	Material Type	Outside Dimensions	Wall Thickness
Wheel Uprights	6061-T6 Aluminum	1" x 0.5"	0.125"
All Other Frame Members	6061-T6 Aluminum	0.5"x 0.25"	0.0625"

An assembly of the frame was created using the above tubing dimensions and the required internal dimensions of the frame. This layout was refined to the final design in two different ways, the first being the creation of an assembly in Solidworks which allowed different components to be placed in the frame. This allowed measurements between components to be taken and adjustments to be made to ensure that there was sufficient room in the frame to accommodate all of the components and that those components

could be easily interacted with when in the frame. This was also the point at which the locations for the bolts holes on the frame were determined.

The second refinement method employed was the use of Solidworks Simulation Tools to perform finite element analysis on the frame to ensure that it would be able to withstand the expected loading that would be applied to it during operation. This step did not result in any major changes to the design of the frame, but did serve to validate the frames final design. The methodology and the detailed results of this analysis can be found in Appendix A.

One concern that was raised during the design of the frame was the method of joining to be used to attach the frames struts together. Two methods were proposed, the first of which was the use of brackets at the frame's joints. This method was not selected as it would increase the overall weight of the frame dramatically. The second method, and the method chosen, was to weld the frames components together. This would add relatively little weight to the frame while providing solid connections between the frames struts. The main drawback to welding aluminum is degradation of strength at the welded sites, but this was accounted for in the analysis found in Appendix A. The final design of the frame can be seen in Figure 25. The final dimensions of the frame, the weight of the frame and the summary results of the finite element analysis of the frame can be found in Table 17.

Table 17: Final dimensions, weight and the simulation results for the frame.

Parameter	Value
Dimensions (L x W x H)	17.0 in. x 13.0 in. x 3.25 in.
Predicted Weight	3.44 lbs
Maximum Von Mises Stress	4436.5 psi
Maximum Displacement	0.002 in.
Minimum Factor of Safety	7.4
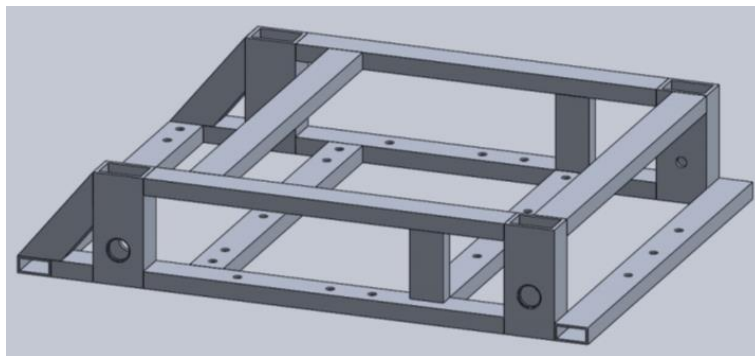
Figure 25: Solid model of the final frame design.

2.3.1.2 Base Plate

The base plate provides attachment points and support for some of the interior components of the vehicle. These included the controller, pressure sensors and vacuum components. The base plate was designed after the frame design was finalized, which meant that most of the dimensional constraints of the plate were already set. This also dictated the hole pattern that was required for the plate. This meant that the only major design decisions that were made for the base plate was the material used in its construction and the thickness of the plate. To keep the overall weight of the plate lower while keeping the plate relatively stiff, 6061-T6 aluminum was chosen as the material for the design. The plate was assumed to carry low loads when the vehicle was assembled. This meant that the weight of the plate was the primary driver in the selection of the thickness of the plate. The final design of the Base Plate can be seen in Figure 26. The final dimensions of the plate, the weight of the plate and the summary results of the finite element analysis of the plate can be found in Table 18.

Table 18: Final dimensions and weight of the base plate.

Parameter	Value
Length	13.5"
Width	13.0"
Thickness	0.4"
Weight	0.44 lbs
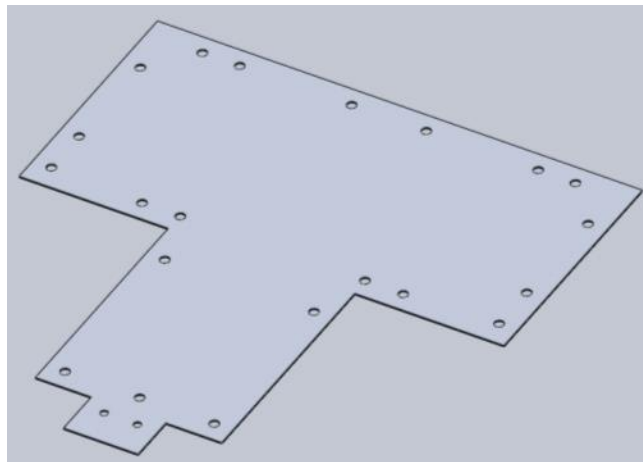
Figure 26: Solid model of the final base plate design.

2.3.2 Motor Subsystem

The motor subassembly served several different functions for the vehicle. These functions are the alignment of the motors shafts with the drive wheel shafts, the attachment of the motor to the vehicle and the coupling of the motor shafts to the drive wheel shafts. There are three components which make up the motor assembly excluding the motor itself. These components are the motor mounting bracket, the motor base plate and the shaft coupler. An image of the motor subsystem including the motor can be found in Figure 27.
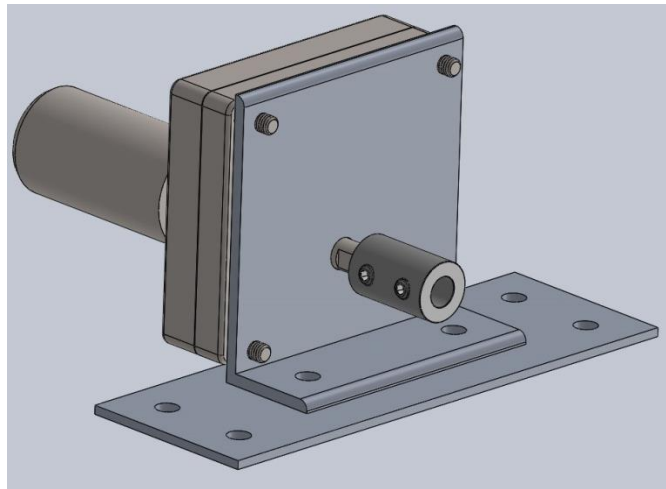
Figure 27: Solid model of the final motor subsystem.

2.3.2.1 Motor Mounting Bracket

The motor mounting bracket attaches directly to the motor. There were several factors that were taken into consideration when designing the bracket such as the stiffness of the bracket, the weight of the bracket, the ability of the bracket to withstand the operating loads applied to it by the motor and the precision required in the alignment of the motor and drive shafts.

Because 6061-T6 aluminum is lightweight, stiff and easy to machine it was chosen as the material for the bracket. An L-Shape was chosen for general shape of the bracket as this would allow for convenient mounting of both the motor to the bracket and the bracket to the mounting plate, as well as allowing easy access to the shafts after assembly.

With the shape and material of the bracket selected, the dimensions of the bracket were then determined. A hole pattern corresponding to the mounting bolts and shaft of the motor was laid out on the upright portion of the bracket. This pattern dictated the height of upright leg as well as the brackets width. The final step in the design of the mounting bracket was performing a simulation to verify that the final design would be able to handle the forces applied to it during the operation of the motor. The methodology and the detailed results of this simulation can be found in Appendix A. Figure 28 contains an image of the final design of the motor mounting bracket. The final weight, dimensions and verification results of the mounting bracket can be found in Table 19.

Table 19: Final dimensions, weight and simulation results of the motor mounting bracket.

Parameter	Value
Width	3.00"
Thickness	0.125"
Motor Leg Length	3.00"
Base Leg Length	1.125
Weight	0.14 lbs
Maximum Von Mises Stress	6390 psi
Maximum Displacement	0.0035 in.
Minimum Factor of Safety	6.2
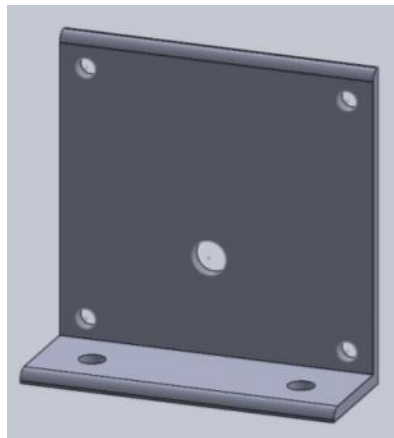
Figure 28: Solidworks model of the final motor mounting bracket design.

2.3.2.2 Motor Base Plate

The motor base plate acts as the attachment point between the motor mounting bracket and the vehicles frame. It also serves to align the motor shafts and the drive wheel shafts along the length of the vehicle. The main considerations for the plate were its mass, its stiffness and the precision of the shaft alignment.

The length of the attachment plate as well as the bolt hole positioning for the frame to plate attachment points were dictated by the frame. The width of the plate was chosen to allow two bolts to be used to attach the plate to the frame without the bolts interfering.

Because the motors chosen did not perfectly mirror one another when flipped, two versions of the motor base plate were designed. The only difference between these two designs was the position of the bracket to plate bolt holes along the length of the plate, which were positioned in such a way that the motor shafts and drive shafts on both sides of the vehicle were aligned. The holes for attaching the motor bracket to the plate were positioned along the width of the plate to ensure that there was not interference between the motor shafts and the drive shafts when the motors were installed.

The thickness of the plate was determined by simulating the pate under operating conditions to ensure that a small amount of deflection occurred in the plate. This also served as the verification of 6061-T6 aluminum as the material choice and as the verification of the final design. The methodology and the detailed results of this simulation can be found in Appendix A. The final design of the Motor Base Plate can be seen in Figure 29. The final dimensions of the plate, the weight of the plate and the summary results of the simulation of the plate can be found in Table 20.

Table 20: Final dimensions, weight and simulation results for the motor plates.

Parameter	Value
Dimensions (L x W x T)	5.75 in x 2.00 in x 0.094 in
Weight	.1025 lbs
Maximum Von Mises Stress	11,525 psi
Maximum Displacement	0.005 in.
Minimum Factor of Safety	3.5
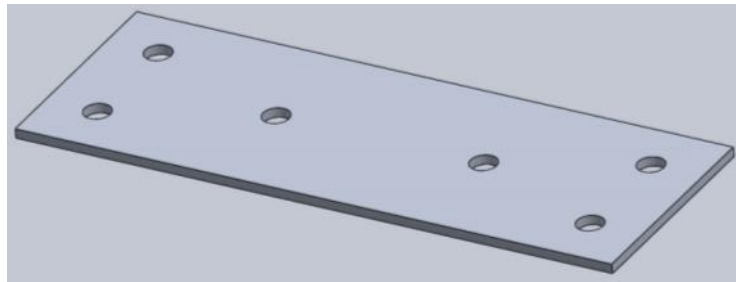
Figure 29: Final design for the left side motor plate.

2.3.2.3 Shaft Coupler Selection

A shaft coupler was required to connect the motor's shaft with the drive wheel shaft. Several major factors contributed to the selection of the coupler for the final design, which were the size of the coupler, the diameter of the shafts being coupled, the shaft type being coupled and the loading the coupler would be likely to experience.

The length and outer diameter of the coupler was a concern, because there was limited space in the area designated for the coupler. Additionally, a smaller coupler was desired to minimize mass and the moment of inertia that was driven by the motor.

The output shafts of the chosen motors were 5/16" in diameter and were D-shaped. In an effort to simplify the selection process of the couplers, the portion of the drive shaft that coupled to the motors was designed to be 5/16" in diameter and D-shaped. Because the shafts were D-shaped, a coupler which used set screws was ideal, as set screws would provide good grip on the flats of the shafts and be easy to tighten and loosen when the shaft coupler was installed.

The coupler used in the final design was a black-oxide steel set screw rigid shaft coupler from Mcmaster Carr. This coupler met all of above criterion and was cost effective. The detail of the coupler can be found in Table 21.

Table 21: Parameters associated with the selected coupler.

Parameter	Value
Outer Diameter	5/8"
Length	1"
Max Torque	86 in.-lbs
Factor of Safety	1.7

2.3.3 Vacuum Subsystem

The vacuum system is used to generate the vacuum used to adhere the vehicle to different surfaces. In addition to the venturis and the manifolds which are discussed in the separate sections, several different components make up the vacuum system of the vehicle. These are the vehicle inlet manifold and the brackets which hold the venturis.

2.3.3.1 Vehicle Inlet Manifold

The purpose of the vehicle inlet manifold is to take in positive air pressure and distribute it to the inlets of the venturis. It consists of four different parts: a straight push-to-connect fitting, two 4 outlet swivel push-to-connect manifolds, a nylon manifold and a hex head plug. All of these components were required to handle the 80 psi that the venturis required to operate.

The push-to-connect fittings were chosen to make assembly and disassembly of the vehicle easier. The straight push-to-connect fitting is used to connect the inlet of the manifold with the incoming positive pressure supply line. The two 4 port push-to-connect manifolds were chosen because each would be connected to four of the venturis. The details of both of the push-to-connect chosen can be found in Table 22.

Table 22: Information on the fittings used in the inlet manifold.

Parameters	Four port push-to-connect manifold	Single Port push-to-connect straight adaptor
Number of Ports	4	1
Tubing OD	1/4"	3/8"
Thread Type	1/8" NPT Male	1/4" NPT Male
Maximum Pressure	145 psi	290 psi

The nylon manifold served to securely connect the main air supply line to the outputs for the venturi. Several material options were available such as aluminum and steel, but nylon was chosen to reduce weight. The manifold had two outlet ports and two inlet ports, and was chosen such that the ports matched the threads for the push-to-connect fittings. The hex head plug was used to block the unused inlet of the nylon manifold. The details about the nylon manifold can be found in Table 23, and an assembled view of the inlet manifold can be found in Figure 30.

Table 23: Information on the nylon manifold.

Parameter	Value
Dimensions	1.75" x 1" x 1"
Max Allowable Pressure	200 psi
Inlet Pipe Size	1/4" NPT
Outlet Pipe Size	1/8" NPT
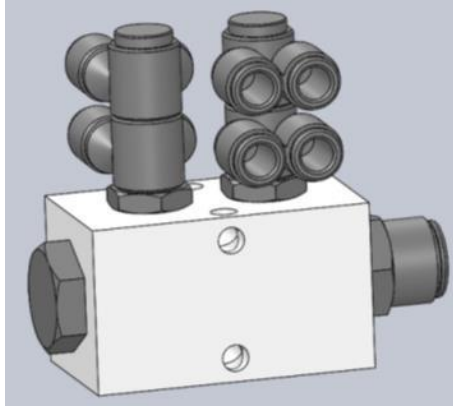
Figure 30: Inlet manifold of the vehicle.

2.3.3.2 Venturi Mounting Brackets

The purpose the venturi mounting bracket was to hold the venturis rigidly, while still allowing access to the inputs and outputs of the venturis. Each bracket was designed to hold four venturis which would feed into the same manifold. The bracket consisted of a sheet of 6061-T6 aluminum bent into an L-shape. The long leg of the bracket was used as the mounting point for the venturis, with a square pattern of tightly grouped holes which allowed the bracket to be relatively small while allowing the venturis to be easily manipulated and attached. The short leg had two mounting holes so that he brackets could be attached to the frame. Table 24 contains details about the brackets. Figure 31 shows and image of the venturi mounting bracket without the venturis installed.

Table 24: Final dimensions and weight of the venturi mounting bracket.

Parameter	Value
Width	1.725"
Plate Thickness	0.0625"
Base Leg Length	1.00"
Venturi Leg Length	2.0625"
Weight	0.03 lbs
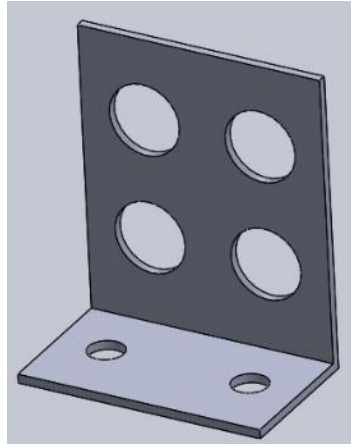
Figure 31: Solid model of the venturi mounting bracket.

2.3.4 Vacuum Manifold Subsystem

The vacuum manifold subsystem's purpose was to distribute vacuum across the tread to adhere the vehicle to a surface. This subsystem also included the means by which the manifold is held firmly to the tread during operation and the means by which the manifold is attached to the vehicle body. An image of the manifold subsystem can be found in Figure 32.
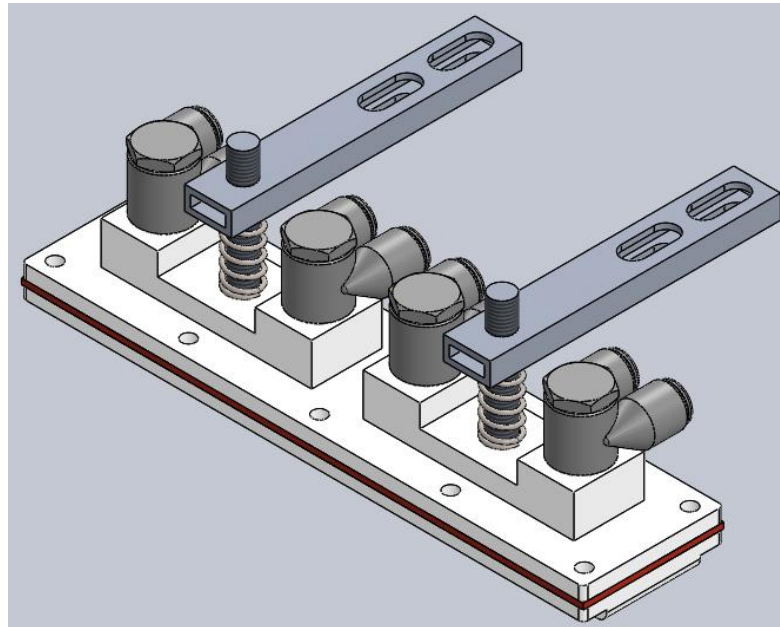
Figure 32: Solid model of the vacuum manifold.

2.3.4.1 Lower Manifold

The lower manifold was the portion of the manifold subsystem which directly contacts the tread. The lower manifold contains four chambers which are connected to one of the four venturis on a given side. Slots are cut at the bottom of each chamber to allow for the vacuum to pass between the manifold and the wall.

The first step in designing the lower manifold was choosing its material. The chosen material needed to be lightweight and have a low coefficient of friction when in contact with the tread. Initially, Teflon was chosen as it is extremely lightweight and slick, but it proved extremely difficult to machine and was prone to warpage. This led to Delrin being chosen because it is lightweight, easy to machine and is generally stronger that Teflon.

The next step in designing the lower manifold was to determine the basic shape and dimensions that it would need to take. The length of the lower manifold was chosen so that the manifold would both cover as much of the tread as possible while also not interfering with the tensioning system or the drive wheel. Because the lower manifold needed to be in contact with the tread at all times, a two tiered shape was chosen and can be seen in Figure 33. The lower tier was designed to ride in the channel cut into the treads teeth. This meant that the width of the lower tier was smaller than that of the width of the channel in an attempt to prevent any contact between the teeth of the tread and the lower manifold. The thickness of the lower tier was chosen to give the higher tier clearance above the tread's teeth, as the upper tier is flared over the tread teeth. The upper tier is flared to allow for tapped holes to be placed along its outer edge without interfering with the gasket placed between the upper and lower manifold. The thickness of the upper tier was chosen to allow for good thread engagement of the bolts which hold the upper and lower manifold together.
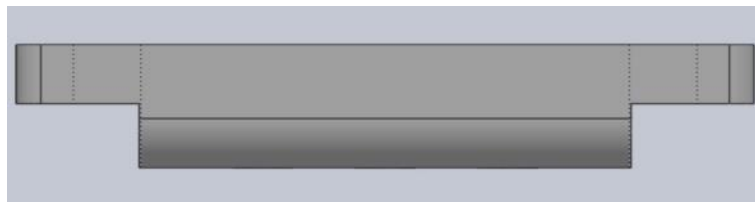
Figure 33: View of the tiered shape of the lower manifold.

The next step in design of the manifold was the layout of the vacuum chambers and their dimensions. It was important that each of the vacuum chambers remained independent of one another to prevent the failure of one chamber from affecting the others. Because the diameter of the holes in the tread was known, the minimum distance between chambers was calculated to ensure that no hole could be engaged by more than one chamber at a time. This value would also ensure a hole could not be in contact with the atmosphere and engaged with the first or last chamber in the manifold. A margin of error was included into this distance for added insurance and this value was used to section the lower manifold to determine the length of the chambers. The width of the chambers was chosen such that a wall thickness of a tenth of an inch was between both sides of the chambers and the outside atmosphere. The depth of the chambers was chosen to ensure that the material between the slots in the manifold would not crack or warp when in use.

The final portion of the design was the design of the slotted pattern in the bottoms of the vacuum chambers. Because there were three rows of holes in the tread three slots along the width of the vacuum chambers. These slots were laid out along the width such that their center lines corresponded to the center lines of the rows of holes on the tread. The width of the slots was chosen to be smaller than the diameter of the holes in the tread. This was to minimize the amount of the tread exposed to the vacuum in the manifold in an effort to reduce tread-manifold friction. The length of the slots was chosen such that at any given time the number of holes exposed to the vacuum remained relatively constant and that enough holes were exposed to the vacuum that the minimum force between the wall and the vehicle was always met. Details on the method used to determine the length of the slots can be found in Appendix A. The final design of the lower manifold can be found in Figure 34. Table 25 contains details about the lower manifold such as the weight, final dimensions and calculation results.

Table 25: Major dimensions and weight of the lower manifold.

Parameter	Value
Over All Dimensions (L x W x H)	6 in x 1.5 in x .25 in
Chamber Dimensions (L x W x D)	1 in x .75 in x .15 in
Slot Dimensions (L x W)	0.825 in x .125 in
Weight	0.06 lb
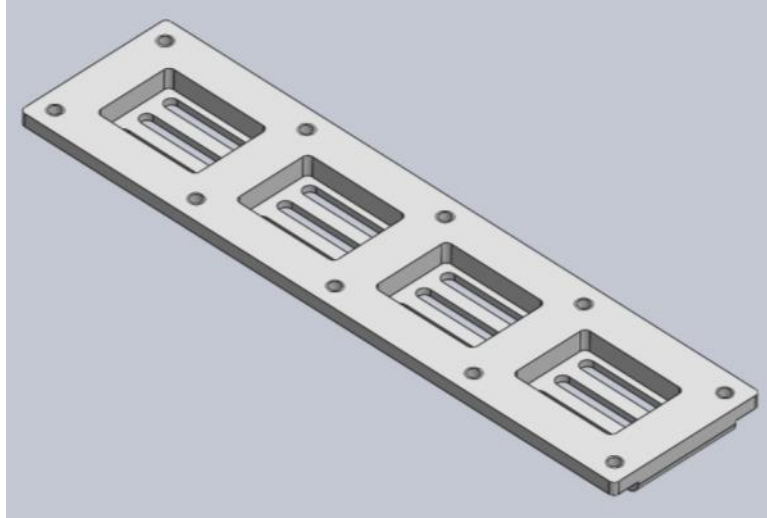
Figure 34: Solid model of the final lower manifold design.

2.3.4.2 Upper Manifold Section

The upper manifold sits on top of the lower manifold. The purpose of the upper manifold was to act as a connection between the lower manifold and the vacuum system, provide attachment points for the mounting structure and to help create a seal with the lower manifold and the gasket.

The material chosen for the upper manifold was chosen based on two criterions. These were the mass of the final product and the ease with which the material could be machined. The two materials considered were aluminum and Delrin. Delrin was chosen because it weighs about half as much as aluminum does and is also easier to machine than aluminum.

The upper manifold had a three tiered design. The first and lowest tier provided a series of through holes corresponding to the threaded holes on the lower manifolds upper tier which allows the two halves of the manifold to be joined. The second tier provides a threaded hole for the uprights used to attach the manifold to the mounting structure. The third tier had NPT threaded holes to allow for the fittings that connect the manifold and the vacuum system to be attached.

The width and length of the first tier are the same as the upper tier of the lower manifold. This made aligning the holes between the upper and lower manifold easier and also simplified the design of the gasket. The thickness of the first tier was to reduce the amount of material required in the upper manifold and to reduce the length of the bolts required to hold the upper and lower manifold together.

The second tier was raised off the surface of the first tier such that a sufficiently deep hole could be drilled and tapped to accommodate the upright which connected the manifold to the mounting structure. The length of the second tier was chosen such that neither the upright nor the adjustment nut for the upright would interfere with the third tier or the manifold fittings. The width of the second tier was chosen to match that of the third tier to simplify machining.

The third tier was broken up into four separate platforms, with each platform corresponding to a vacuum chamber in the lower manifold. Each platform has a tapped NPT through hole at its center. The third tier's height was chosen to allow for a fully tapped NPT hole to be placed in on each of the four surfaces. The height was also chosen to ensure that the manifold fittings connection points would stand above the surface of the base plate. The width and length of the platforms was chosen to allow for NPT threads to be drilled and tapped without risking cracking any of the platforms. The final design of the upper manifold can be found in Figure 35. Table 26 contains details about the upper manifold such as the weight, final dimensions and calculation results.

Table 26: Dimensions and weight of the final design of the upper manifold.

Parameter	Value
Over All Dimensions (L x W x H)	6 in x 1.5 in x 0.6 in
First Tier Thickness	0.15 in
Second Tier Dim. (L x W x H)	5.05 in x 0.75 in x 0.21 in
Third Tier Dim. (L x W x H)	.6 in x .75 in x 0.45 in
Through Hole Diameter	.1495
Upright Hole Call Out	1/4-20
Fitting Hole Callout	1/8 NPT
Weight	.1 lb
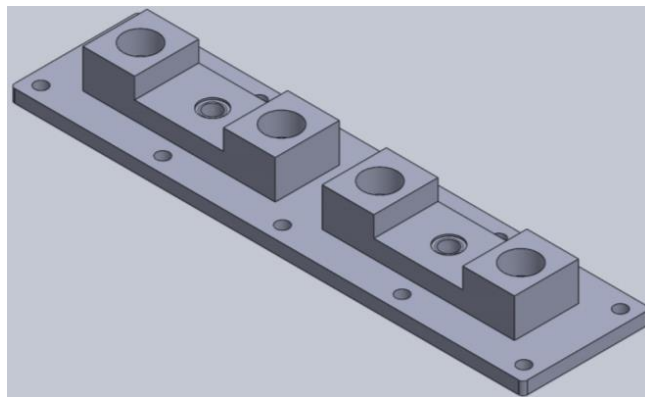
Figure 35: Solid model of the final upper manifold design.

2.3.4.3 Manifold Gasket

The manifold gasket was designed to help create a seal between the upper and lower manifold halves. Its dimensions were based on the length and the width of the lower manifolds upper tier. Holes positioned at each of the vacuum chamber locations on the lower manifold were cut slightly smaller than the camber dimensions to allow for some overhang into the chambers.

Fiberglass reinforced silicone rubber was chosen as the material for the gasket because silicone provides a good seal and the fiberglass ensures that the sheet does not get squeezed out of place during assembly. The thickness of the sheet was chosen to reduce the amount of additional height added to the manifold by the gasket. The final design of the manifold gasket can be found in Figure 36. Table 27 contains details about the manifold gasket such as the weight, final dimensions and calculation results.

Table 27: Information on the final gasket design.

Parameter	Value
Dimensions (L x W x T)	6 in x 1.5 in x 0.0625 in
Hardness	40D
Weight	.02 lb
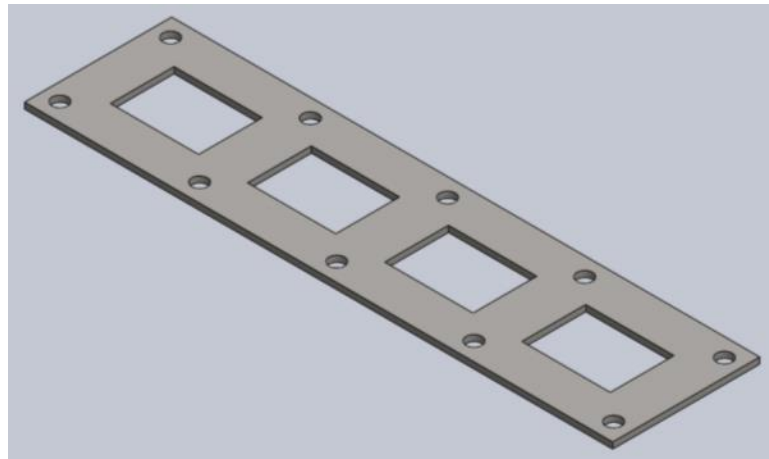
Figure 36: Solid model of the final gasket design.

2.3.4.4 Mounting Structure

The purpose of the mounting structure was to connect the manifold to frame of the vehicle. This structure consisted of two parts, the adjustable struts and the threaded uprights. The adjustable struts were attached directly to the frame of the vehicle and positioned the manifold relative to the channel in the tread. The

threaded uprights connected the manifold to the struts and position the manifold vertically relative to the tread.

2.3.4.4.1 Adjustable Struts

The adjustable struts consisted of two rectangular tubes. These tubes had a trough hole which the threaded uprights could be placed in to at one end and a pair of slots at the other. The purpose of the slots was to allow the struts to be connected to the frame and be adjusted to align the manifold with the channel in the tread. The position of the upright hole relative to the slots was determined using a Solidworks assembly of the vehicle.

A stock aluminum rectangular tube was chosen as the base material for the struts for ease of manufacturing and to reduce weight. The design and material selection were validated by performing a simulation using the expected loading on the struts. The methodology and detailed results of this simulation can be found in Appendix A. The final design of the adjustable struts can be found in Figure 37. Table 28 contains details about the adjustable struts such as the weight, final dimensions and simulation results.

Table 28: Information on the final design of the mounting struts.

Parameter	Value
Overall Dimensions (L x W x H)	3.1 in x 0.5 in x 0.25 in.
Wall Thickness	0.0625 in.
Hole Diameter	.25 in.
Slot Dimensions (L x W)	.6 in. x 0.25 in.
Weight	.007 lbs
Maximum Von Mises Stress	11,550 psi
Maximum Displacement	0.004 in.
Minimum Factor of Safety	3.5
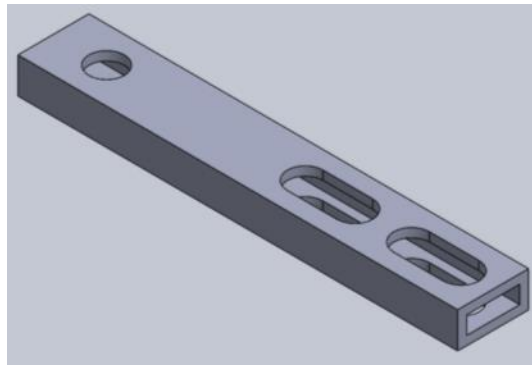
Figure 37: Solid model of the final mounting strut design.

2.3.4.4.2 Threaded Uprights

The threaded uprights were aluminum 1/4-20 threaded rods. These rods were cut a length which would allow the manifold to be pressed firmly against the tread, while remaining short enough to not interfere with the assembly of the vehicle. Table 29 contains details about the threaded uprights such as their weight, final dimensions and simulation results.

Table 29: Information on the threaded upright.

Parameter	Value
Length	1.5 in.
Thread Type	¼-20
Weight	0.01 lbf

2.3.4.4.3 Spring

A spring was placed around the threaded uprights and between the adjustable struts and the upper manifold. This was done to give the manifold subsystem the ability to recover more effectively from losses in vacuum pressure and to give it more compliance to prevent any shocks the vehicle might encounter during operation from causing damage to the manifold or the mounting struts. The spring which was chosen offered a good amount of compressible length combined with a high spring constant. Table 30 contains the details on the spring which was chosen.

Table 30: Information on the suspension spring.

Parameter	Value
Uncompressed Length	0.75 in.
Maximum Load	11.10 lbf
Spring Rate	24.3 lbf/in.

2.3.4.5 Fittings

The fittings that were chosen to connect the manifold to the vacuum system were push-to-connect double ninety degree swiveling elbows. These fittings were chosen because they met the vacuum requirements of the system; they rotated which allowed for easy assembly and were push-to-connect which also made assembly easy. A two port version was chosen so that an inlet line to the manifold and a line for the pressure sensors could be run from the same fitting.

2.3.5 Wheel Subsystem

The purpose of the wheel subsystem was to translate motor torque to the tread and to allow the tread to smoothly translate. Two distinct wheel assemblies where used in this system, the drive wheel assembly and the idler wheel assembly. The similarities and differences of these two assemblies will be discussed in this section. Four major components make up the wheel subassembly. These are the bearings, the drive and idler shafts, the drive and idler wheels and the brace. An image of the wheel subsystem can be found in Figure 38.
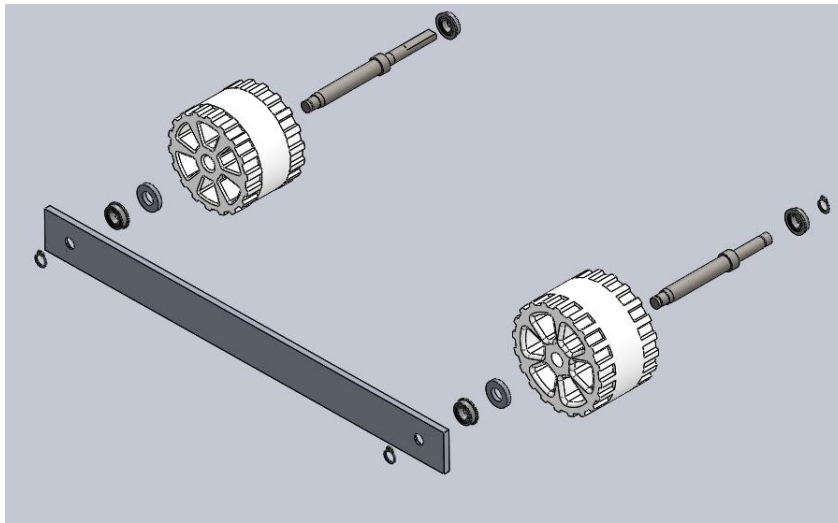
Figure 38: An exploded view of the wheel subsystem.

2.3.5.1 Bearing Selection

The bearings served an important purpose in the wheel subsystem, which was to carry the loading of the shafts while reducing friction. Two different types of bearings were chosen for the system. These were flanged roller bearings capable of taking thrust loads and low friction thrust bearing in the shape of a washer.

2.3.5.1.1 Flanged Bearing

The flanged roller bearings were selected for several different reasons. The first and most significant of these reasons was their ability to carry the predicted loads that would be applied to them during operation. This loading was calculated using the predicted belt tension that the system would require to operate. This calculation can be found in Appendix A. The second was its dimensions and shape. The bearing was

chosen because its shaft diameter was 8mm which is close to the diameter of the output shaft of the motor. This simplified the dimensions of the drive shafts and the selection of the coupler between the drive shaft and the motor. The flange on the front of the bearing allowed the bearing to be located precisely, which was required for proper belt alignment.

The bearings mounting holes in the frame and the wheel brace were designed so that the bearings could be easily and securely mounted. An inner hole was sized to snuggly fit the body of the bearing while still allowing the bearing to be pressed into place by hand. A circular indent centered on this hole was cut to a depth and diameter that would allow the flange of the bearing to be recessed making the bearings surface flush with the surface of the frame up rights or of the brace. A retaining compound was used to secure the bearings once they were installed. Figure 39 shows an image of the selected bearing. Table 31 contains details about the chosen flange bearing such as its dimensions, the results of the loading calculation and performance specifications. Table 31 also contains information on the retaining compound used to hold the bearings in place.

Table 31: Information on the selected flange bearing and the retaining compound used.

Parameter	Value
Inner Dimeter	0.315 in.
Outer Diameter	0.707 in.
Thickness	0.197 in.
Loading Capacity	280 lbf
Maximum Predicted Loading	63 lbf
Safety Factor	4.4
Retaining Compound	Loctite 609
Primer	7649 Primer for Loctite
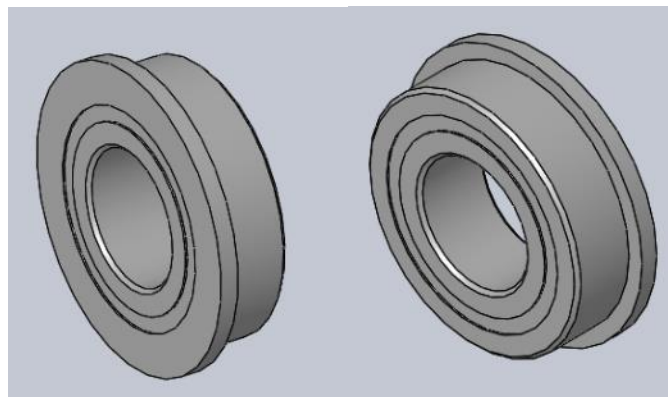
Figure 39: Solidworks model of the chosen flange bearing.

2.3.5.1.2 Thrust Washer

The second bearing that was used in the wheel subassembly was a low friction brass thrust washer. This

bearing was chosen for two reasons. The first and most significant reason for its use in the design was to act

as a spacer between the wheels of the vehicle and the cross brace of the wheels. This ensured that the

tensioning system would not interfere with the cross brace during tensioning and it ensured that the belt

would not rub against the cross brace. The second reason that the thrust washer was chosen was to prevent

the shafts of the vehicle from rubbing the flange bearings in the cross brace during operation while

providing low contact friction. Table 32 contains details about the washer chosen.

Table 32: Information on the chosen thrust washer.

Parameter	Value
Inner Diameter	0.379 in.
Outer Diameter	0.75 in.
Thickness	0.125 in.
Load Capacity	70.0 lbf

2.3.5.2 Drive and Idler Shafts

The drive and idler shafts provided rigid attachment points for the wheels for their respective wheels. The

drive shafts also transferred torque from the motors to the drive wheels. Several key factors were

considered during the design of the shafts. These were the strength of the shafts, the required dimensions of

the shafts set by other components, the ease with which the wheels could be attached and positioned on the

shafts and the manufacturability of the shafts. As the drive and idler shafts are identical in many respects,

the similar features in their designs will be discussed together. A labeled image of the common end of the

shafts can be found in Figure 40. Subsections later in this section will discuss their differences.
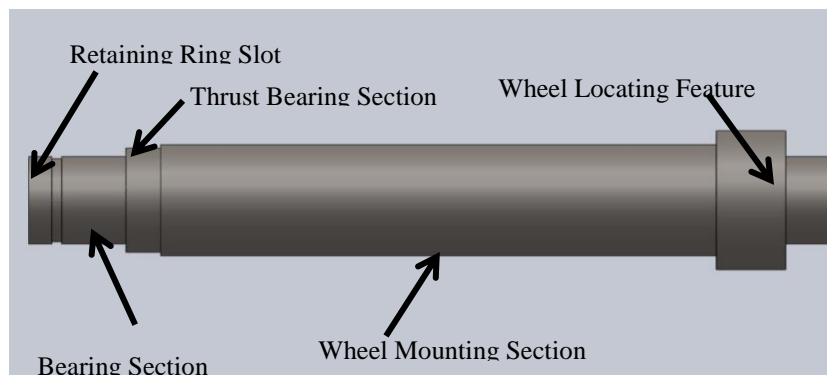
Figure 40: Labeled common shaft end.

2.3.5.2.1 Common Shaft End

The first step taken in designing the common end of the drive and idler shafts was the determination of the dimensions of the shafts and the placement of features on the shafts. Several of these dimensions were already determined by other components in the design. The brace bearing section's diameter was determined by the inner diameter of the flanged bearings and its length was chosen to all for different retaining methods to be used to hold the cross brace in place. The diameter and length of the thrust washer section of the shafts was determined by the thickness and the inner diameter of the thrust washers. The length of the wheel mounting section of the shaft was determined by the width of the wheels. The width of the wheel locating feature was chosen to be similar to that of the thrust washers and its diameter was chosen to extend past the inner running of the flanged bearing.

With most of the common end dimensions selected, the final dimension which needed to be determined was the diameter of the wheel mounting section. This was done by creating shafts with a range of different diameters and simulating the performance of each shaft under the expected loading conditions the shafts would be subjected during operation. The primary parameter which was looked at during this study was the deflection of the shaft under load. The methodology and detailed results of these simulations can be found in Appendix A. The final diameter was chosen because it resulted in small deflections under load while allowing for well-defined steps in the shaft that would be relatively easy to machine.

The material that the shafts would be made from was determined during same simulation that the diameter of the wheel mounting section was determined. This was done by running each simulated diameter with both 6061-T6 aluminum and 1045 medium carbon steel as the material of the shaft. It quickly became apparent that the 6061-T6 aluminum would result in very shaft diameters and so the 1045 steel was chosen. The detailed results and methodology of the simulations can be found in Appendix A.

The final step in the design of the common end of the shafts was to determine the attachment method which would be used to hold the cross brace in place on the shafts. Several different options were considered, but the use of retaining rings was the ultimate choice for several reasons. Retaining rings offered good strength and were easily added to and removed from the shafts without the need to disassemble the vehicle. They also require the least amount of machining on the shafts to install. To ensure the selected ring would work

in the vehicle, a calculation was performed to determine the rings maximum allowable thrust load. This

load was compared to the expected loads that the rings would be subjected to. The details of this calculation

can be found in Appendix A. The position of the slot for the retaining ring on the common end was

determined by simply measuring the thickness of the cross brace when the flanged bearings were installed.

The slot dimensions were based on the manufactures recommendations. Table 33 contains details about the

final design of the common shaft end such as the final dimensions of the common end, the final results of

the retaining ring calculations.

Table 33: Dimensions of the common shaft end and the results of the retaining ring calculations.

Parameter	Value
Wheel Mounting Section Dimensions (L x Dia.)	2.0 in. x 0.4 in.
Thrust Bearing Section Dimensions (L x Dia.)	0.125 in. x 0.375 in.
Brace Bearing Section Dimensions (L x Dia.)	0.231 in. x 0.315 in.
Retaining Ring Slot Dimensions (W x Dia.)	0.035 in. x 0.299 in.
Wheel Locator Dimensions (L x Dia.)	0.25 in. X 0.5 in.
Retaining Ring Factor of Safety	10.7

2.3.5.2.2 Drive Shaft

The design of the non-common end of the drive shaft was relatively simple. It required a portion of the

shaft that would fit into the flange bearing and a portion to be coupled to the drive motor.

The length of the non-common end of the drive shafts was determined by the distance from the outside

edge of the frame flange bearing to the front end of the motors output shaft. This length was reduced

slightly to ensure that the drive shaft would not interfere with the motor shaft and to allow for easy

installation and removal of the shaft and motor.

The diameters of these two sections were easily determined as they were set by components which had

already been selected. The diameter of the first three quarters of an inch of shaft after the wheel locating

feature was 8mm in diameter so the shaft would fit snuggly into the flange bearing. The remaining length

of shaft was 5/16" in diameter so that it could be inserted into the motor to shaft coupler. An inch at the end

of the shaft was D-shaped to ensure the coupler could be attached to the shaft securely. Table 34 contains

the details about the final design of the non-common end of the drive shaft and of the final design of the

drive shaft such as overall length and weight. Figure 41 shows the final design of the drive shaft.

Table 34: Final dimension, weight and simulation results for the drive shaft.

Parameter	Value
Frame Bearing Section Dimensions (L x Dia.)	0.25 in. x 0.315 in.
Motor Attachment Section Dimensions (L x Dia.)	1.465 in. x 0.313 in.
Weight	.131 lb
Maximum Von Mises Stress	17,960 psi
Maximum Deflection	0.002 in.
Minimum Factor of Safety	4.3
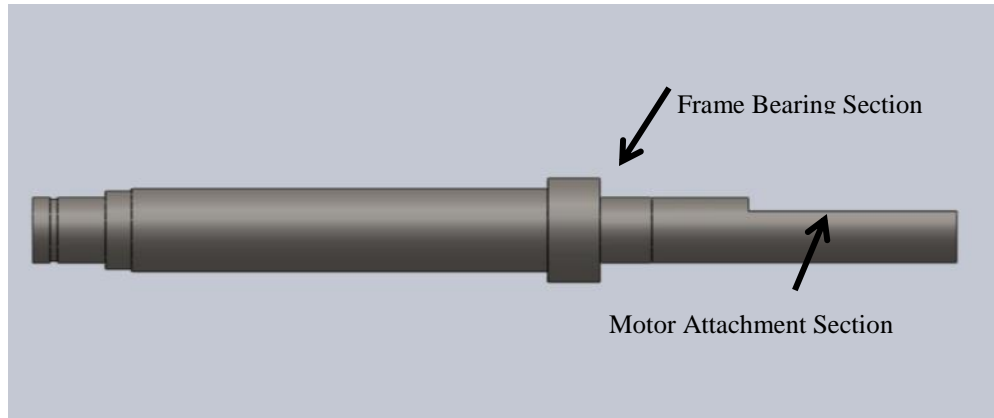
Figure 41: Solid model of the drive shaft.

2.3.5.2.3 Idler Shaft

The design of the non-common end of the idler shaft was straight forward. The length of the non-common end was chosen such that, when it was installed, the end of the shaft would protrude past the idler upright. This was to allow for a retaining ring to be installed to hold the shaft in place during operation. This retaining ring was the same ring as was used on the common end of the shafts. Finally the diameter of the shaft was chosen to be 8mm so that it would fit snuggly into the flange bearing in the upright. Table 35 contains the details about the final design of the non-common end of the idler shaft and of the final design of the idler shaft such as overall length and weight. Figure 42 shows the final design of the idler shaft.

Table 35: Final dimensions and weight of the idler shaft.

Parameter	Value
Idler End Section Length Dimensions (L x Dia.)	1.0 in. x 0.315 in.
Retaining Ring Slot Dimensions (W x Dia.)	0.035 in. x 0.299 in.
Weight	.124
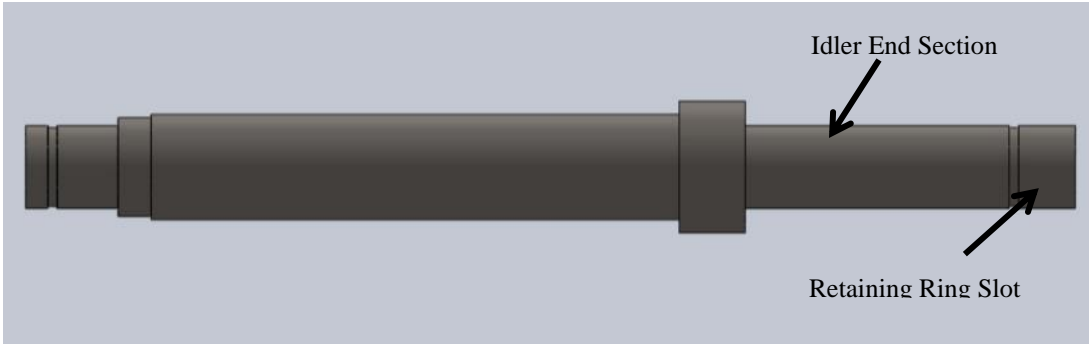
Figure 42: Solid model of the idler wheel shaft.

2.3.5.3 Drive and Idler Wheel Design

The drive and idler wheels were both critical portions of the design. They needed to be light weight, rigid, capable of handling the operating loads they would be subjected to and to be easy to manufacture. The only real difference between the drive wheels and the idler wheels is their diameter and consequently the number of teeth on each wheel.

2.3.5.3.1 Common Drive and Idler Wheel Design Elements

The first step in the design of the wheels was to determine if the wheels would be modified pulleys provided by FN Sheppard or if they would be custom designed. Ultimately it was decided that the wheels would be custom designed for several reasons. The pulleys that FN Shepard could provide were solid aluminum. This posed two major problems. The weight of these pulleys would be significant in terms of their contribution to the vehicles overall weight and to the amount of inertia which the motors would need to overcome to move them. The pulleys would also require a significant amount of machining to be usable.

Because of the complex geometries that the wheels would have, 3D printing was determined to be the most time efficient and cost effective option for the manufacturing method of the wheels. This limited the material which could be used to construct the wheels. As the 3D printer most readily available to the project printed in ABS plastic, ABS was chosen as the final material of the wheels.

The next step in the design of the wheels was to determine the dimensions of the teeth. This was relatively simply to determine because FN Sheppard provided detailed dimensions of the belt teeth found on the treads. The only change in dimension between the belt tooth geometry and the wheel tooth geometry was a

slight reduction in the base thickness of the wheel teeth. The number of teeth on each wheel was determined by the diameter of the wheels and this number was provided by FN Sheppard.

A central band of material was designed between the toothed sections of the wheels. This band rode in the manifold channel of the tread and acted as a stop for the teeth of the tread. This assisted in the initial installation of the tread onto the wheels and prevented the belt from slipping off the wheels while the vehicle was operating. It also helped to transfer the loads on the tread during turning onto the wheels and away from the manifold.

The overall width of the wheels was chosen to exactly match the overall width of the tread. The width of the toothed sections of the wheels was chosen to be slightly larger than the width of the toothed sections on the tread. This was done to prevent rubbing between the wheels and the tread during operation. The width of the center band on the wheels was slightly smaller than that of the channel in the tread, again to reduce the amount of rubbing between the wheels and the tread.

The bodies of the wheels were designed with spokes that ran between the outer portions of the wheels, where the teeth and central band were located to the wheels hubs. These spokes were designed to reduce the weight of the wheels while still allowing them to carry the loads they would be subjected to during operation.

The wheels were designed to press fit directly onto the drive and idler shafts. Press fitting was chosen over the use of set screws, pins or adhesives to reduce the complexity of manufacturing and assembly, maintain the integrity of the wheels geometry, and to ensure that the wheels could be replaced easily. The diameter of the shaft hole was determined by performing a press fit calculation to determine the amount of interference between the wheel and the shaft was required to hold the wheels in place, the details of which can be found in Appendix A.

2.3.5.3.2 Drive Wheel Design

The diameter of the drive wheel was selected based upon the theoretical wheel radius used to calculate the motor requirements. FN Sheppard's design catalog was used to determine which of the standard pulley

diameters was closest to the ideal diameter. This then determined both the diameter of the drive wheel and the number of teeth on the drive wheel.

The final design of the drive wheel was validated by simulating the drive wheel under expected operating conditions. The loading in used in the simulation were calculated and then applied to a model of the wheel. The detailed results, methodology and loading calculations can be found in Appendix A. Table 36 contains details on the final drive wheel design, such as weight, general dimensions and simulation results. Figure 43 shows the final design of the drive wheel.

Table 36: Final dimensions, weight and simulation results for the drive wheel.

Parameter	Value
Outer Diameter	2.64 in.
Hub Diameter	0.399 in.
Number of Teeth	17
Weight	.26 lbs
Maximum Von Mises Stress	1030 psi
Maximum Displacement	0.001 in.
Minimum Factor of Safety	4.5
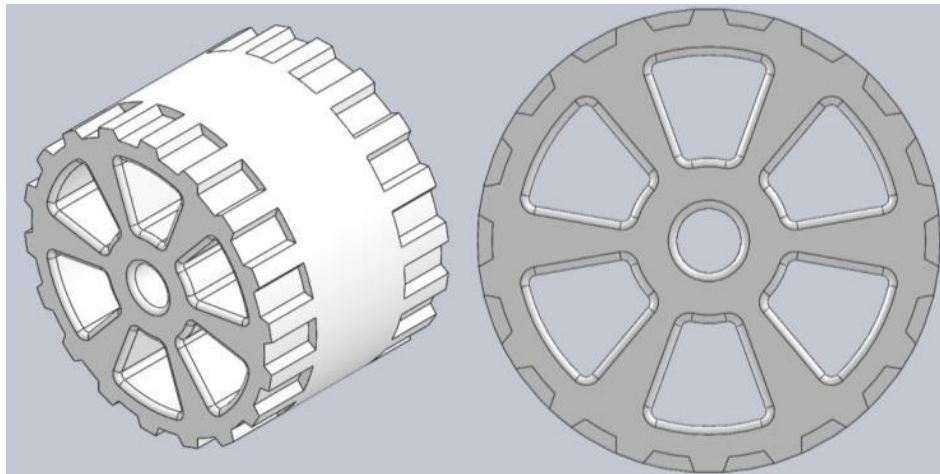
Figure 43: Solid model of the drive wheel.

2.3.5.3.3 Idler Wheel Design

The diameter of the idler wheels was chosen based on the suggestion of FN Sheppard. A minimum tensioning idler diameter was required for the tread system to function properly. This requirement was based upon the belt geometry used in the tread. The minimum diameter possible was used to reduce the weight of the idler wheel and to prevent interference between idler wheel and the tensioning system. This diameter also dictated the number of teeth on the idler. The drive wheels were subjected to more loading

than the idler. Because the drive wheels simulation was successful, it was assumed that the idler wheels would be able to handle the loading it was subjected to and so no simulation of the idler wheel was conducted. Table 37 contains details on the final idler wheel design, such as weight, general dimensions and simulation results. Figure 44 shows the final design of the idler wheel.

Table 37: Final dimensions and weight of the idler wheel.

Parameter	Value
Outer Diameter	3.31 in.
Hub Diameter	0.392 in.
Number of Teeth	20
Weight	.36 lbs
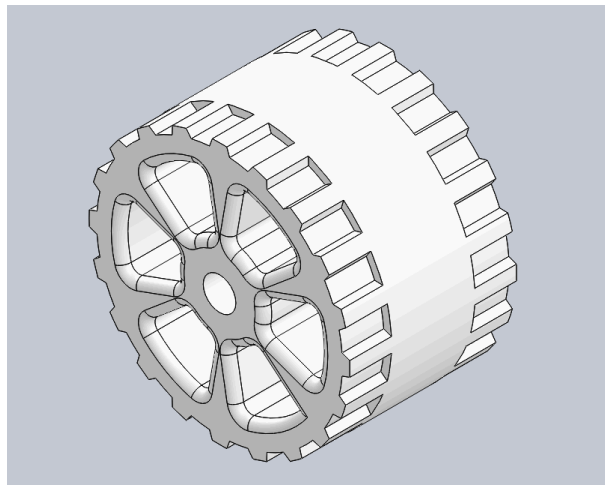
Figure 44: Solid model of the idler wheel.

2.3.5.4 Brace Deign

A major problem encountered in the proof of concept model was deflection of the drive and idler wheels of the model when the tread system was tensioned. To prevent this from happening in the new prototype, a brace between the drive and idler wheels was designed. This brace also carried a portion of the tension load in the wheel subsystem which increased the factor of safety on the flange bearings.

The design of the brace was relatively simple. The distance between the centers of the drive and idler wheel shafts was determined. This was the distance that the flange bearings in the brace would be separated by. The length of the brace was then determined by adding the radius of the bearings plus and additional quarter of an inch to both ends of the brace. The width of the brace was chosen to be the diameter of the flange of the bearing plus three quarters of an inch.

The mounting points for the bearings in the brace were designed with a through hole and a blind hole. The through hole was sized to allow the end of the shaft to be inserted through the brace. The blind hole was designed such that the bearing could be inserted into the brace until the flange contacted the surface of the brace. The hole was chosen to be blind to leave a relatively thick portion of the brace material between the bearing and the retaining ring on the shaft. This gave the retaining rings a surface to contact without potentially damaging the bearings. This blind hole and the wall it left were used to determine the required thickness of the brace.

The design of the brace was validated by simulating the loads which would be applied to it during the operation of the vehicle. The detailed results and methodology for this simulation, as well as the loading calculations, can be found in Appendix A. Appendix A also contains a buckling calculation for the brace. Table 38 contains details on the final brace design, such as weight, general dimensions and simulation results. Figure 45 shows the final design of the brace.

Table 38: Final dimensions, weight and simulation results for the brace.

Parameter	Value
Brace Dimensions (L x W x T)	14.0 in. x 1.25 in. x 0.187 in.
Hole Separation	12.25 in.
Weight	0.31 lbs
Maximum Von Mises Stress	4,319 psi
Maximum Displacement	0.002 in.
Minimum Factor of Safety	9.2
Buckling Factor of Safety	114
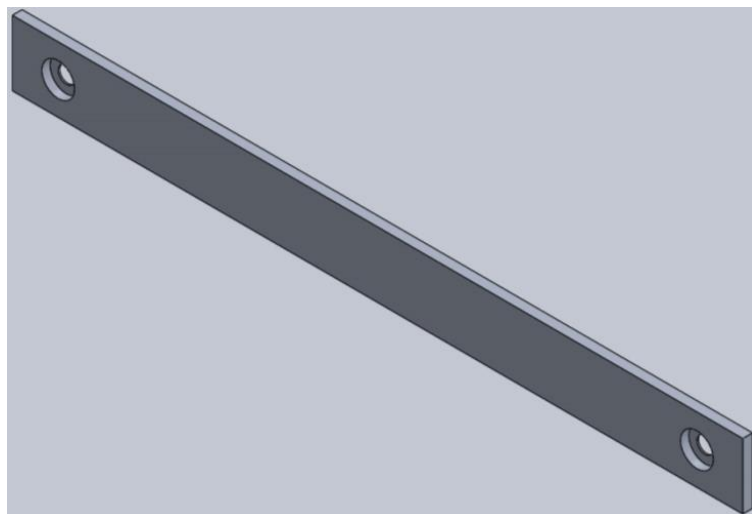
Figure 45: Brace solid model.

2.3.6 Tensioner Subsystem

The purpose of the tensioner subassembly was to provide a means by which the vehicle's tread could be easily tensioned and un-tensioned while the vehicle was fully assembled. To do this, a screw driven mechanism was designed to raise and lower a toothed wheel, similar to the drive and idler wheels. When the wheel was raised into position it would engage with and begin to tension the tread. Once the desired tension in the tread was achieved, the tensioner mechanism was locked into place.

This screw driven mechanism consists of four major components. These are the tensioner wheel assembly, a clamping mechanism, a shaft and a screw assembly. The assembled mechanism can be seen in Figure 46 and Figure 47.
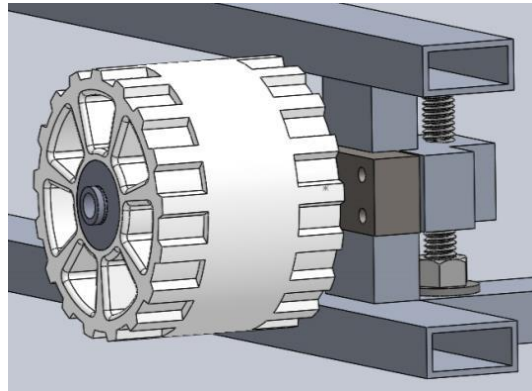
Figure 46: Front view of the tensioner subassembly.
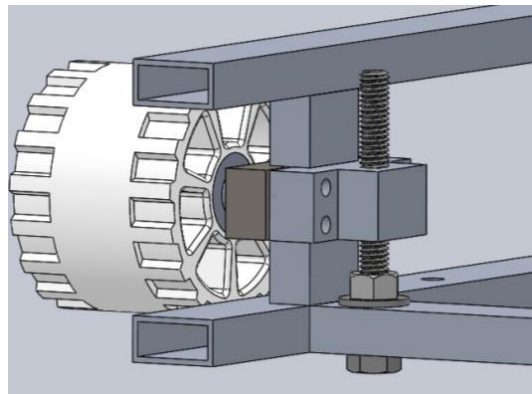
Figure 47: Rear view of the tensioner subassembly.

2.3.6.1 Tensioner Clamp

The tensioner clamp served several different purposes in the tensioner subsystem. It provided rigid support for the tensioner wheel, allowed the tensioning subsystem to be locked into place and acted as part of the

mechanism which raised and lowered the tensioning wheel. It consisted of an interior half and an exterior half. These two halves were placed around the frames tensioner upright and were connected using bolts.

2.3.6.1.1 Tensioner Clamp – Interior

The half of the tensioner clamp which was placed on the interior of the frame was designed primarily to interact with the drive screw of the tensioner mechanism. It was also designed to fit onto the frame's tensioner upright to prevent the tensioner from slipping during the tensioning process. Figure 48 shows an image of the interior half of the tensioner clamp.
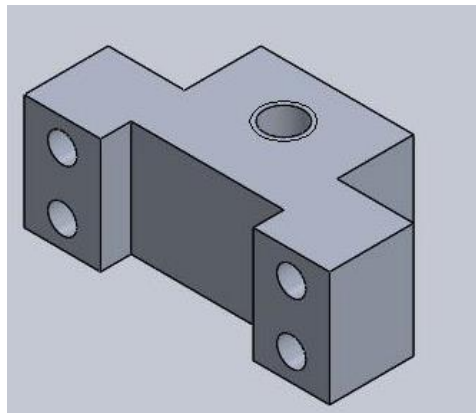
Figure 48: Solid model of the interior half of the tensioner clamp.

The overall width of the interior clamp half was chosen to accommodate the slot that allowed the clamp to be placed onto the tensioner upright and the four through holes for the bolts which hold the two clamp halves together. These through holes also determined the height of the clamp. The thickness of the clamp half was chosen to accommodate the depth of the slot and the threaded hole used for the drive screw. To reduce the length of screws required to hold the two pieces of the clamp together, the thickness of the clamp half around the bolt holes was reduced.

The width of the slot in the interior clamp half was chosen such that the clamp could slide freely on the tensioner upright, but still prevent the tensioner mechanism from shifting during vehicle operation. The depth of the slot was chosen such that the two halves of the clamp do not make contact when they are fully tightened. The slot was positioned along the center line of the part.

The tapped drive screw hole was positioned on the part such that when the clamp was in place in the vehicle the threaded hole aligned with the hole in the frame for the drive screw. The through holes for the

clamping bolts were positioned so that the heads of the bolts would not interfere with each other or with the interior clamp half's body.

Aluminum was chosen as the material of the interior clamp half to reduce its weight contribution to the vehicle. Table 39 contains details on the final interior clamp half design, such as weight, general dimensions and calculation results.

Table 39: Final dimensions and weight for the interior clamp half.

Parameter	Value
Interior Clamp Dimensions (L x W x H)	1.05 in. x 2.0 in. x 0.75 in.
Slot Dimensions (W X H x D)	1.0 in. x 0.75 in. x 0.2 in.
Threaded Hole Callout	¼-20 THRU
Attachment Through Hole Diameter	0.19 in.
Weight	0.09 lbf

2.3.6.1.1 Tensioner Clamp – Exterior

The exterior half of the clamp holds and positions the tensioner shaft and design of the exterior half of the tensioner clamp was driven by the need to hold the tensioner wheel rigidly in place during operation. Like the interior half of the clamp, the exterior half used a slot to fit securely onto the tensioner upright.

The basic shape of the exterior half of the clamp was that of a rectangle. The height and width of the exterior half of the clamp were chosen to be the same as the interior half of the clamp to simplify the design. The thickness of the exterior clamp half was chosen to accommodate the depth of the slot cut into it while maintaining sufficient material for the clamping bolts and the tensioner shaft to be secured in place without risk of striping the threads. The slot cut into the exterior half of the clamp is identical to the slot cut into the interior half of the clamp.

The threaded holes used to secure the clamping bolts in place were positioned so that they corresponded to the through holes in the interior half of the clamp. The hole for the tensioner shaft was centered on the width of the width of the clamp, but offset from the center of the height of the clamp. This was done to allow the tensioner wheel to be given an offset relative to the clamp to compensate for any welds in the frame which would prevent the tensioner clam from reaching the top of the tensioner upright. Because the tensioner shaft was chosen to be steel the material that was chosen for the exterior clamp half was steel. This was done to allow the shafts to be welded into place.

The design of the exterior half of the clamp was validated using a simulation which included the tensioner shaft and the exterior half of the clamp. The methodology and detailed results of this simulation can be found in Appendix A. Table 40 contains details on the final exterior clamp half design, such as weight, general dimensions and calculation results. Figure 49 shows the final design of the exterior clamp half.

Table 40: Final dimensions, weight and simulation results for the exterior clamp half.

Parameter	Value
Interior Clamp Dimensions (L x W x H)	0.5 in. x 2.0 in. x 0.75 in.
Slot Dimensions (W X H x D)	1.0 in. x 0.75 in. x 0.25 in.
Shaft Hole Diameter	0.38 in.
Attachment Through Hole Callout	#10-24 THRU
Weight	0.14 lbf
Maximum Von Mises Stress	11,850 psi
Maximum Displacement	0.003 in.
Minimum Factor of Safety	6.5
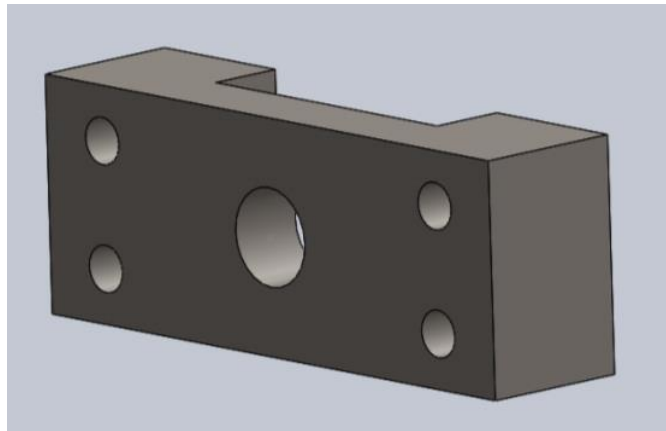
Figure 49: Solid model of the exterior half of the tensioner clamp.

2.3.6.2 Tensioner Wheel Assembly

As stated above, the tensioner wheel was very similar in design to the drive and idler wheel of the vehicles. The tooth geometry used in the tensioner wheel is the same as the tooth geometry used for the drive and idler wheels. Like the drive and idler wheels, 3D printed ABS plastic was chosen as the material that would make up the tensioner wheel. Like the drive and idler wheels, the design of the tensioner wheel consisted of an outer band which held the teeth and alignment band which was connected to a central hub by spokes. The width of the tensioner wheel was also the same as the width of the drive and idler wheel.

The diameter and number of teeth on the tensioner wheel were determined using the FN Sheppard design catalog and Solidwork's belt length tool. The details of this process can be found in Appendix A. The wheel diameter that was chosen provided enough potential belt extension without interfering with other subsystems.

Because the tensioner shaft was fixed, the tensioner wheel was required to rotate freely on the shaft. This was accomplished by including bushings in the design of the tensioner wheel assembly. The bushings that were chosen were selected to operate at the projected speeds and loads experienced by the tensioner wheel during vehicle operation. They also had flanges, which made them easy to insert and position in the tensioner wheel.

To accommodate the bushings, the hub of the tensioner wheel was designed differently than the hubs of the idler and drive wheels. The flange of the bushings required the diameter of the tensioner wheel hub to be increased significantly. Additionally, the diameter of the through hole of the hub was increased to accommodate the outer diameter of the bushing. A recess was added to the hub to allow the bushing to be pressed flush with the face of the tensioner wheel. Table 41 contains details on the final design of the tensioner wheel. Figure 50 shows the final design of the tensioner wheel.

Table 41: Final dimensions and weight for the interior clamp half.

Parameter	Value
Outer Diameter	2.64 in.
Hub Diameter	0.625 in.
Number of Teeth	17
Weight	.26 lbs
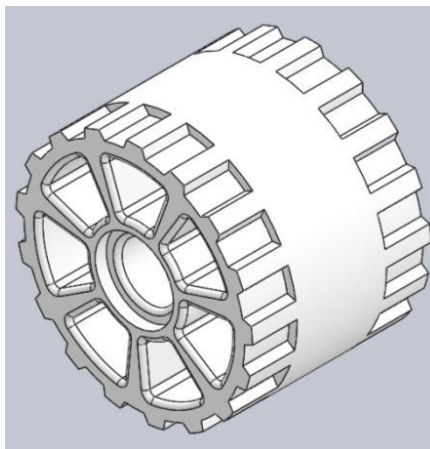
Figure 50: The solid model of the Tensioner wheel.

2.3.6.3 Tensioner Shaft

The purpose of the tensioner shaft was to provide a rigid surface that the tensioner wheel could be both positioned on and allowed to rotate freely on. It would also need to be attached to the exterior tensioner clamp half.

The dimensions of the tensioner shaft were relatively straight forward to design. The portion of the shaft on which the tensioner wheel rested was chosen to have a length equal to the width of the tensioner wheel plus the length required to accommodate the retention ring which kept the wheel on the shaft. The diameter of this section was chosen to allow the bushings in the tensioner wheel to rotate freely on shaft. The next portion of the tensioner shaft acted as a spacer and prevented the tensioner wheel from slipping into contact with the frame and to help align the tensioner wheel with the drive and idler wheels. To make welding the tensioner shaft to the exterior clamp half easier a short section was added to the shaft that would slip into the exterior clamp half's central hole.

Like the drive and idler shafts, 1045 medium carbon steel was chosen as the material for the tensioner shaft. Steel was chosen to reduce the amount of deflection in the shaft when it was loaded, which was especially critical for the tensioner shaft because it was cantilevered from the tensioner clamp exterior half. The final design of the tensioner shaft was validated using the same simulation used to validate the design of the tensioner clamp exterior half. Again the details of this simulation can be found in Appendix A. Table 42 contains details on the final design of the tensioner shaft such as weight and major dimensions. Figure 51 shows the final design of the tensioner shaft.

Table 42: Final dimensions, weight and simulation results for the interior clamp half.

Parameter	Value
Wheel Mounting Section Dimensions (L x Dia.)	2.0 in. x 0.38 in.
Wheel Locating Section (L x Dia.)	0.5 in. x 0.5 in
Mounting Section Dimension (L x Dia.)	0.25 in. x 0.38 in.
Retaining Ring Slot Dimensions (W x Dia.)	0.029 in. x 0.351 in.
Weight	0.1 lbf
Maximum Von Mises Stress	11,850 psi
Maximum Displacement	0.003 in.
Minimum Factor of Safety	6.5
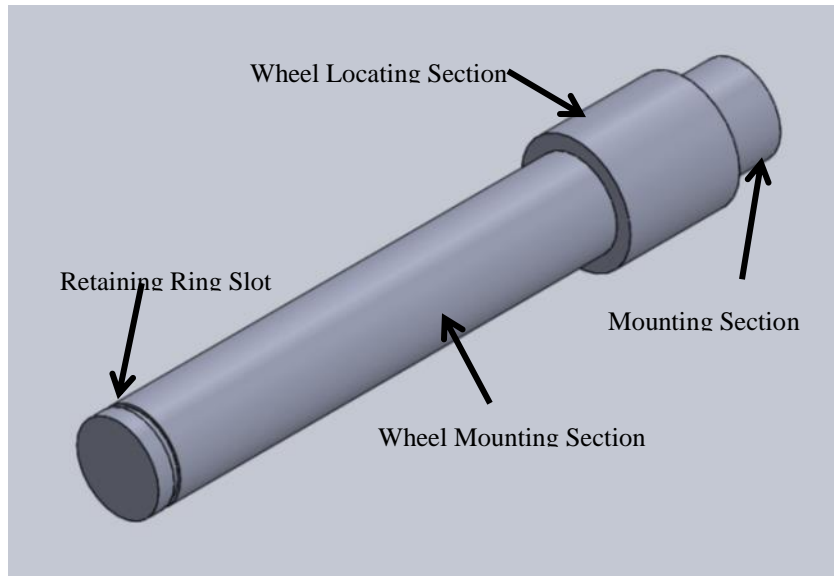
Figure 51: Tensioner shaft solid model.

2.3.6.4 Tensioner Screw Assembly

The purpose of the tensioner screw assembly was to drive the tensioner clamp up and down to tension and un-tension the treads. This assembly was made up of three components, a bolt, a lock nut and two nylon washers. Figure 52 shows the screw assembly in place in the tensioner assembly.
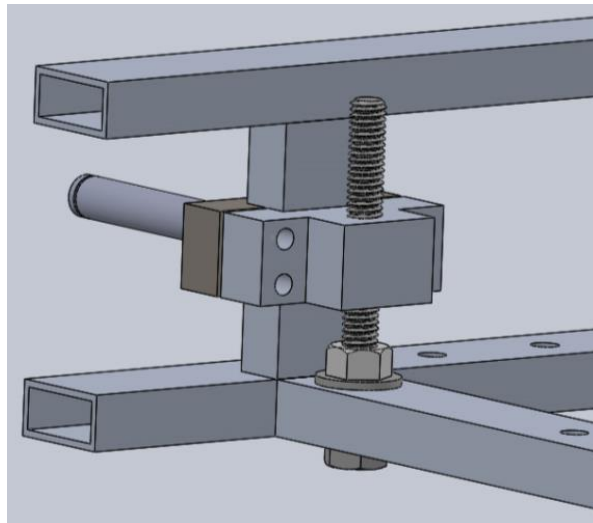
Figure 52: Tensioner screw assembly solid models.

The operation of the screw assembly was relatively simple. The bolt was placed into the hole in the frame and held in place using the lock nut. The bolt was then screwed into the interior clamp half. Because the bolt was held in place, when it was turned the interior clamp was raised or lowered. The nylon washers

were placed between the frame and the bolt head and the frame and the lock nut to reduce friction and
prevent the mechanism from binding.

2.4 Final Design Assembly

Figure 53 shows the final assembled Solidworks model of the vehicle and Table 43 contains details on the
final assembled vehicle such as its overall dimensions and estimated final weight. This estimated weight
does not include the fasteners used in the project, nor does it include the mass of the treads.

Table 43: Overall dimensions and weight of the assembled vehicle.

Parameter	Value
Final Assembly Dimensions (L x W x H)	19.1 x 18.45 in. x 3.945 in.
Solidworks Estimated Weight	12.4 lbf
Estimated Total Weight	13.4 lbf
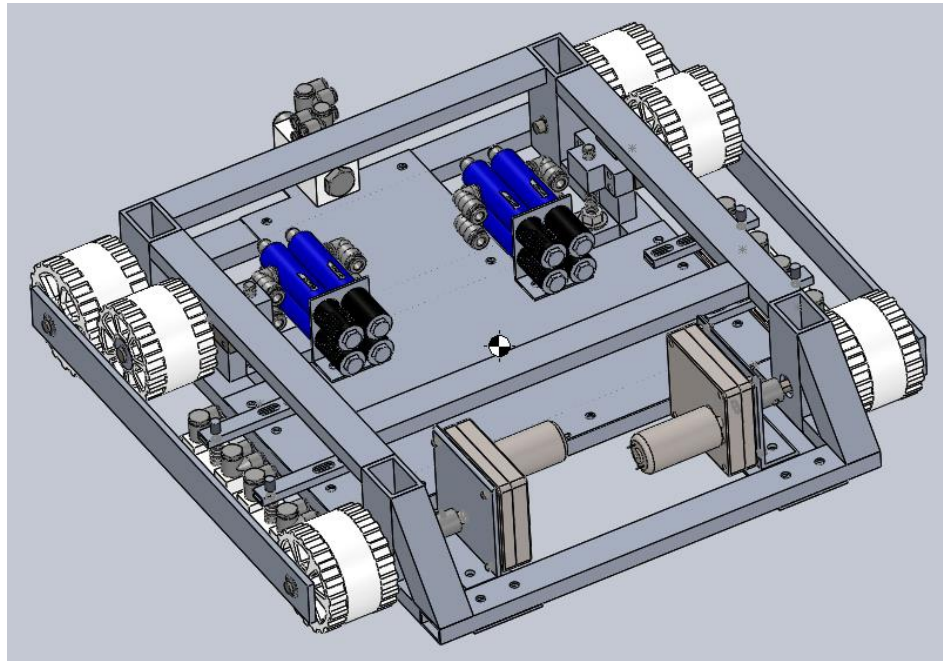
Figure 53: The final assembled model of the vehicle.

Chapter 3: Manufacturing and Assembly

3.1 Bill of Materials

This section gives an overview of the total cost of the project. Table 44 gives a breakdown of the cost of the vehicles by subsystem as well as the total cost of the vehicle. A detailed bill of materials can be found in Appendix B and gives a per item cost break down for the entire vehicle, the quantities of each item used and the supplier of each item.

Table 44: Cost breakdown by subsystem for the vehicle.

Vehicle System	Cost
Frame Subsystem	$130.22
Motor Subsystem	$150.03
Vacuum Subsystem	$670.83
Manifold Subsystem	$226.48
Wheel Subsystem	$390.74
Tensioner Subsystem	$155.68
Tread Subsystem	$611.16
Total	$2,335.14

3.2 Component Manufacturing

This section give brief descriptions of the processes used to manufacture the various components of the design. Each section will deal with a different subsystem and will discuss the manufacturing method, anomalies or tolerance issues encountered in the manufacturing process and any modifications made to the designs during the manufacturing, assembly and testing processes. Each subsection will show the final product of the manufacturing process. A weight break down by part can be found in Appendix C.

3.2.1 Frame Subsystem

Figure 54 shows an image of the manufactured and assembled frame subsystem.
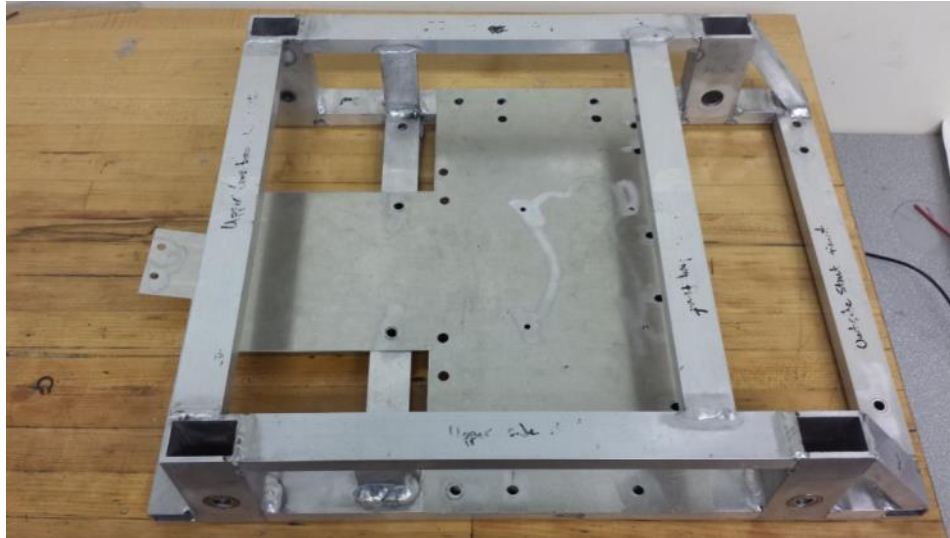
Figure 54: Manufactured and assembled frame subassembly.

3.2.1.1 Frame

The manufacturing of the frame was relatively straight forward. Sections of 6061 aluminum square tubing was rough cut on an aluminum chop saw. These tubing sections were then milled and deburred to create blank struts of the required lengths. The hole patterns were then drilled into each of the struts using a mill to ensure tight tolerances could be kept.

Once all of the individual struts were created, they were handed over to a shop tech at Cal Poly's machine shop for welding. A TIG welder was used to weld each strut into place in the frame and 4043 Aluminum filler rod was used during the welding process. Because of the complexity of the frame, no special fixtures were used during the welding process. This resulted in slight misalignments in some of the frames components, though none drastic enough to make the frame unusable. Some examples of these misalignments can be seen in Figure 55 and Figure 56 and the effects of these misalignments are discussed in Chapter 4.
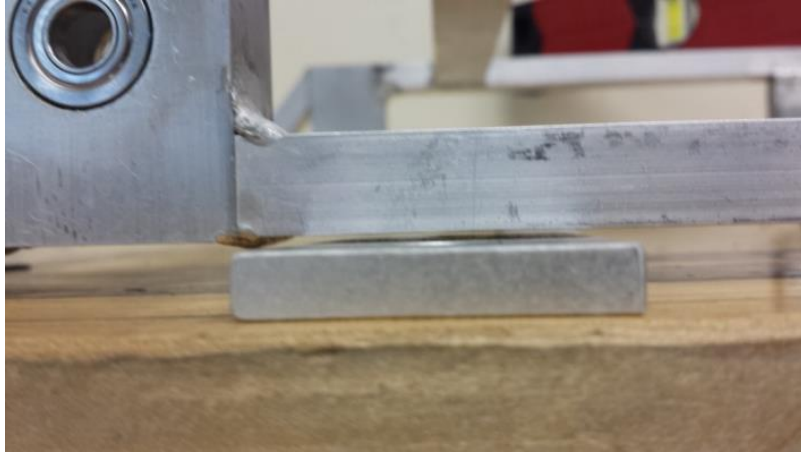
Figure 55: Misalignment of the frame at the right corner. The corner was raised by 1/32nd of an inch.
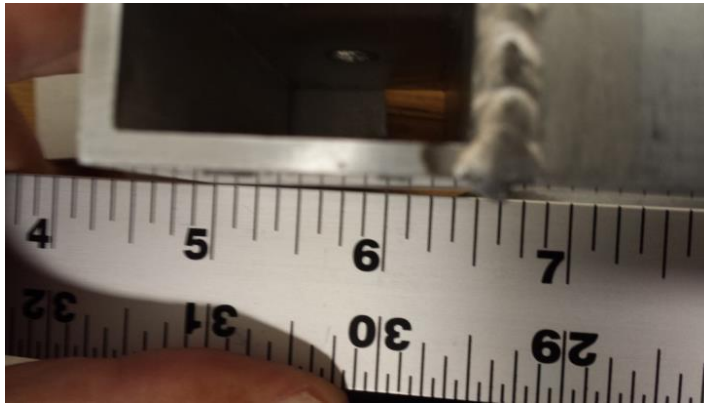
Figure 56: Angular misalignment of the idler strut on the left side of the vehicle.

Once the frame was completely welded, a dremel tool was used to smooth out some of the weld beads. This served to both improve the look of the frame and to prevent the weld beads from interfering with the other subsystems as they were attached to the frame.

Finally, the bearings were installed into the frame. The bearings and frame were thoroughly cleaned and then the retaining compounds catalyst was painted on to the outer race of the bearing and the bearing holes in the frame. The retaining compound was then applied to the bearing and the frame and the bearings were pressed into place by hand until the bearing and frame strut faces were flush. The excess retaining compound was then removed .An image of the bearing inserted in the frame can be found in Figure 57.
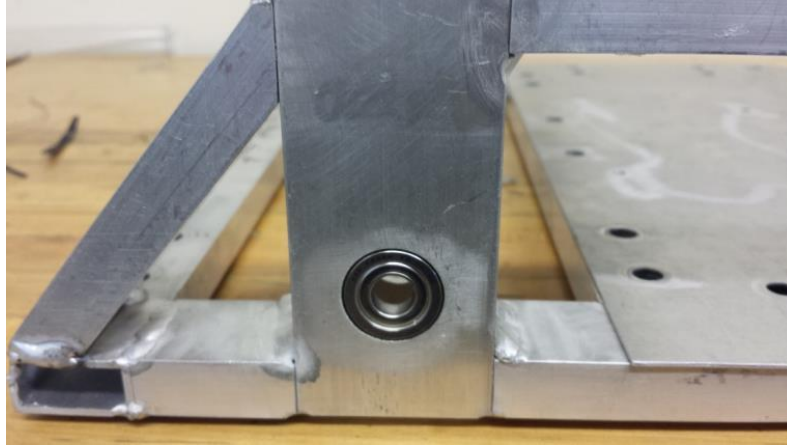
Figure 57: One of the bearings in place in the frame.

During the initial testing of the tensioner system, the tensioner on the right side of the vehicle jammed. In the process of unjamming it the frame was cracked. A patch of 6061 aluminum was welded between the struts were the crack occurred to cover the crack and provide the struts with additional support. The patched area of the frame can be seen in Figure 58
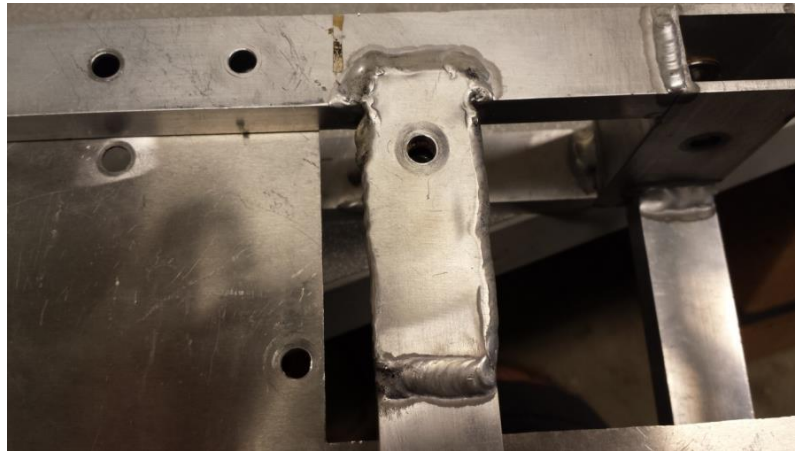
Figure 58: The patch used to fix the frame.

3.2.1.2 Plate

The base plate for the frame was manufactured from a sheet of 6061 aluminum. The basic shape and dimensions of the plate were marked out on the aluminum sheet. The sheet was then cut to shape using a vertical band saw. The sharp edges left by the cutting process were smoothed using a polishing wheel. The hole pattern was then laid out on the plate and the holes were drilled using a drill press. The holes in the

plate were intentionally oversized to help with alignment with the frame. The final base plate can be seen in Figure 59.
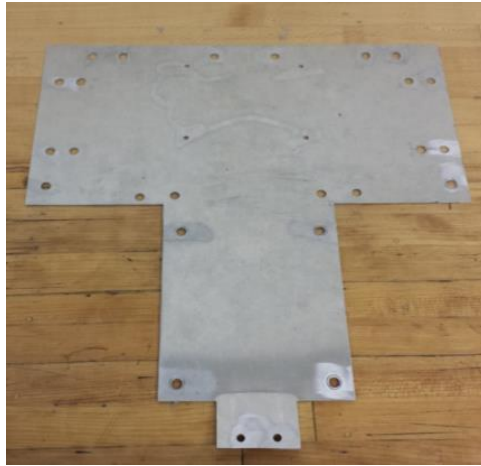
Figure 59: Manufactured base plate.

3.2.2 Motor Subsystem

Figure 60 shows an image of the manufactured and assembled motor subsystem. The final subsystem weight was 1.66 lbf for both of the assembled motor subsystems.
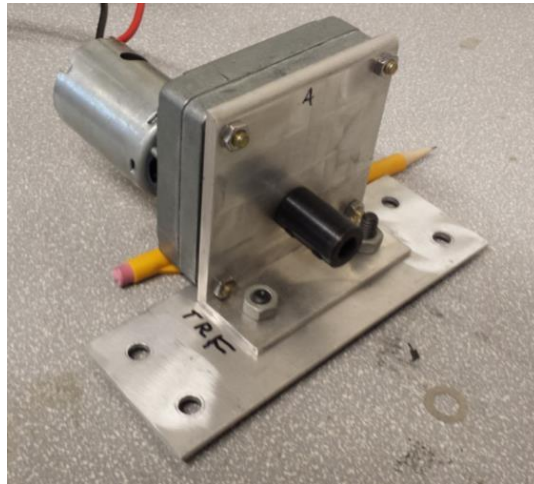
Figure 60: Motor subassembly fully assembled.

3.2.2.1 Motor Mounting Brackets

The first step in creating the motor mounting bracket was rough cutting the L-shaped stock using a band saw. These rough cuts were then milled to the final width that the brackets would have. Next, one leg of the brackets was milled to reduce its length. The face of each leg of the bracket was then milled until they were

the desired thickness. The hole patterns for both legs were then drilled using a mill to ensure precision. The bracket was then polished on a polishing wheel to remove any burrs left by the machining process and to improve the surface finish.

The only difficulty encountered during the manufacturing of the mounting brackets was the fact that the motor's mounting screws were not positioned correctly. This resulted in motors not being able to be mounted on the bracket. This was solved by increasing the hole diameters of the motor mounting points on the brackets. Figure 61 shows both of the final mounting brackets.

Figure 61: Left and right motor mounting brackets.

3.2.2.2 Motor Base Plate

The motor base plate was relatively simple to manufacture. The plates were rough cut from stock aluminum plates using a band saw and then milled to size. The hole patterns for the left and right side plates were then drilled into the plates using a mill to ensure the patterns precision. The plates were then deburred using a polishing wheel. Images of the final motor base plates can be seen in Figure 62 and Figure 63.

Figure 62: Left side motor mounting plate.

Figure 63: Right side motor mounting plate. Note the slots cut so the motor could be adjusted.

Two difficulties were encountered with the machined plates. The first was misalignment between the frame holes and the plate holes which prevented the plates from being attached to the frame. This was corrected by increasing the plate's frame mounting holes diameter until the plates could be attached to the frame.

 The second problem was that while the left side plate aligned the motor shaft with the drive shaft, the right side motor shaft had significant misalignment laterally with its drive shaft. To correct this, slots were cut in the plate to allow the motor to be adjusted into the correct position.

3.2.3 Vacuum Subsystem

Figure 64 shows an image of the manufactured and assembled vacuum subsystem after it was installed in the frame subsystem. The final weight of the subsystem was 1.68 lbf in total.
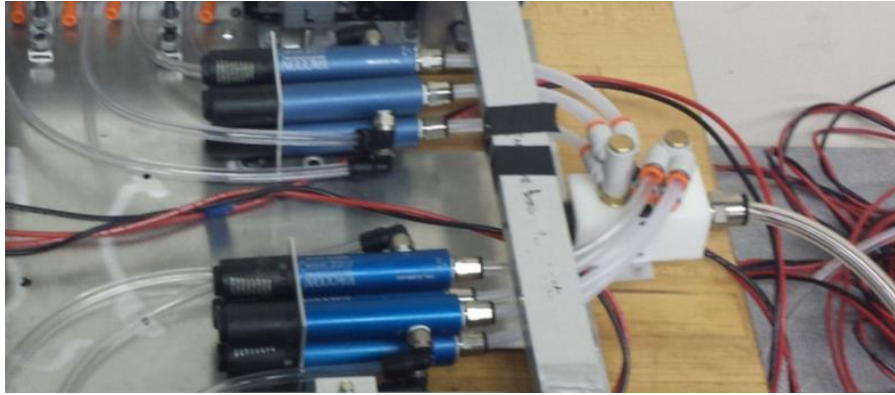
Figure 64: Vacuum subassembly installed in the vehicle.

3.2.3.1 Venturi Mounting Brackets

Stock aluminum sheeting was cut the desired size using a band saw and the edges were deburred. The hole

pattern was then marked on the plate and then drilled out using a drill press. The bend point of the bracket

was marked and then the bracket was bent to ninety degrees using a sheet metal bender. An image of the

final venture mounting brackets can be seen in Figure 65 and the right bracket with venturis in position can

be seen in Figure 66.
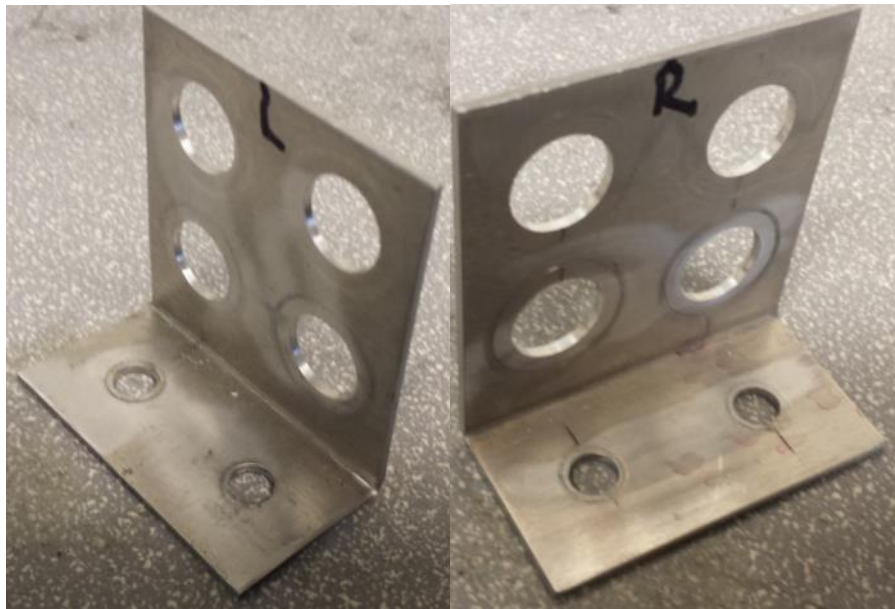
Figure 65: Left and right venture mounting brackets.

Figure 66: Venturi mounting bracket with the venturis installed.

3.2.3.2 Inlet Manifold Assembly

The inlet manifold assembly was easy to assemble. Teflon tape was added to the threads of each

component and then they were screwed into the nylon block. Figure 67 shows the assembled Inlet manifold

assembly.

Figure 67: Inlet manifold assembly.

3.2.4 Vacuum Manifold Subsystem

Figure 70 shows an image of the manufactured and assembled manifold subsystem. The weight of the manifold subsystems was 0.55 lbf each.
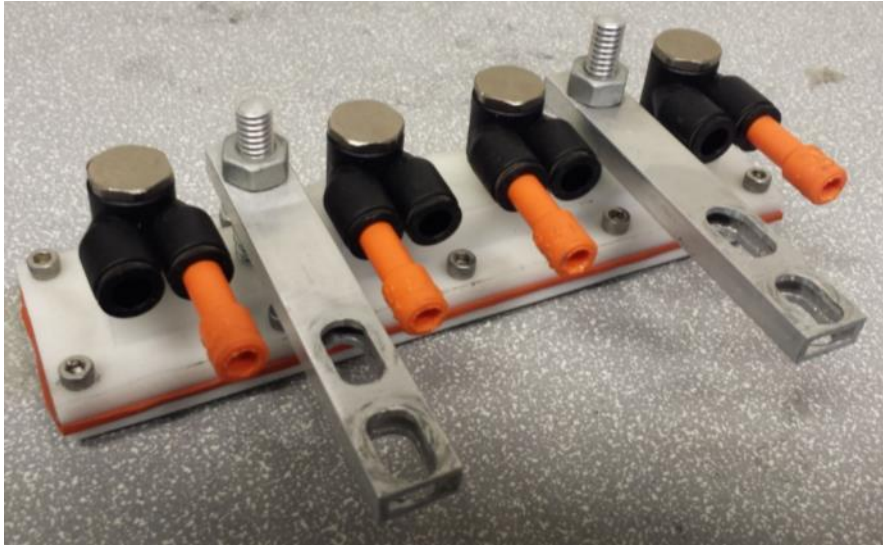
Figure 68: Assembled left side manifold.

3.2.4.1 Lower Manifold

The lower half of the manifolds was difficult and time consuming to machine. Stock delrin bars were rough cut to size using a table saw and miter saw. These bars were then machined down on a mill to the final length, width and thickness dimensions of the lower manifold half. The thickness of the outside edges was then reduce to form a tiered shape. The individual chambers and their corresponding slots were then milled into each of the lower manifold halves. Finally, the attachment hole pattern along the outside edge of the lower manifold were drilled on a mill and the tapped by hand. During the milling processes, large amounts of coolant were used to prevent heat from building up in the manifold and causing warpages. An image of the lower half of the manifold can be seen in Figure 69.
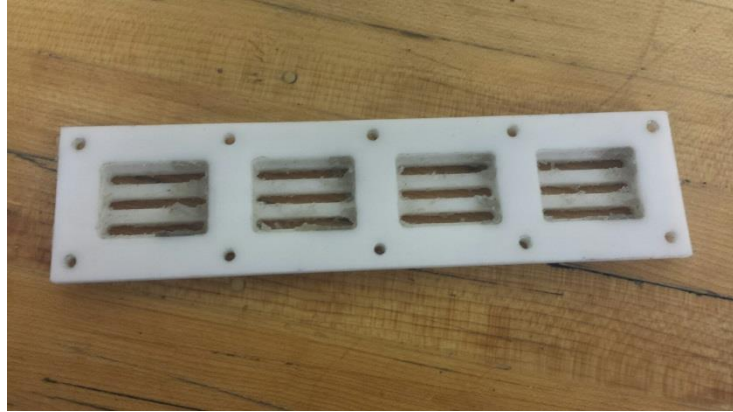
Figure 69: Lower manifold half.

Because the stock that was purchased came slightly warped and the cutting of the stock on the saws caused

further warping, it was difficult to machine the lower manifolds to be perfectly flat. To account for this

warp, the bars which would become the lower manifolds were machined flat before they were machined to

the lower manifolds final dimensions. This significantly reduced the amount of warping in the final

product, but did not eliminate it. Figure 70 shows the warpage in the final lower manifold and the effects of

this warpage are discussed in Chapter 4.

Figure 70: The bending seen in the right lower manifold half.

3.2.4.2 Upper Manifold

The process used to machine the upper half of the manifolds was identical to that of the lower manifold

halves. Stock delrin bars were rough cut and the milled into the desired shape. The through holes for

assembling the manifolds were drilled but not tapped and the hole for the vacuum fittings and mounting

holes for the uprights were drilled then tapped. Teflon sealant tape was then applied to the vacuum fittings

and they were then screwed into place. Images of the upper half of the manifold can be seen in Figure 71.
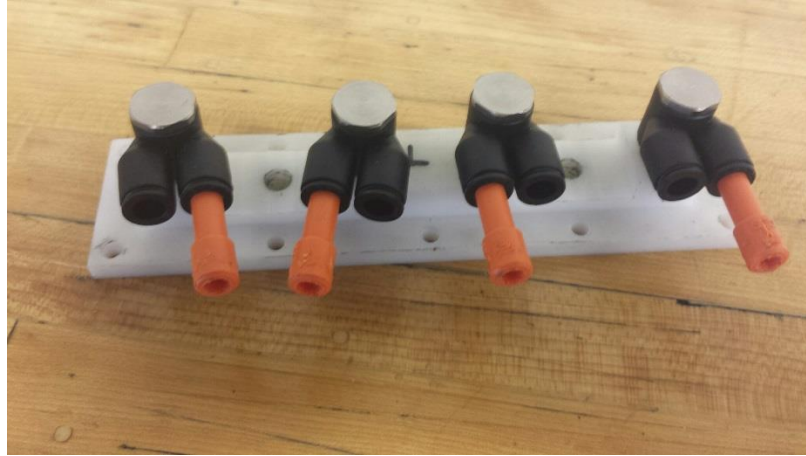
Figure 71: Upper half of the manifold with the fittings installed.

There was the slight misalignment between the attachment holes between the lower and upper halves of the manifolds. This was corrected by slightly oversizing the through holes in the upper manifold halves.

3.2.4.3 Manifold Gasket

The manifold gasket was relatively easy to manufacture. The pattern for the gasket was printed out and tapped to a sheet of silicone rubber. The pattern was then cut out by hand using a razor blade. Care was taken to clean the screw through holes to prevent binding during assembly. An image of the manifold gasket can be seen in Figure 72.

Figure 72: Manifold gasket.

3.2.4.4 Manifold Mounting Structure

The manufacturing of the manifold mounting structure occurred in two parts. The first part was the machining of the mounting struts. Stock aluminum tubing was rough cut on a band saw and then machined

to the desired length on a mill. The hole for the threaded upright was then drilled on the mill. The slots for

the frame mounting points were then cut on the mill. Each of the struts was then deburred and polished. An

image of the mounting struts can be seen in Figure 73.

Figure 73: One of the manifold mounting struts.

The threaded uprights were extremely easy to manufacture. Stock threaded rods were rough cut to the

required lengths using a band saw. The cut ends were then polished and deburred on a polishing wheel. A

nut was run over each rod clean and deburr the threads. An image of the threaded uprights can be seen in

Figure 74.

Figure 74: One of the threaded uprights.

3.2.5 Wheel Subsystem

Figure 75 shows an image of the manufactured and assembled wheel subsystem. The final weight of the

wheel subsystems was 0.98 lbf each.

Figure 75: Assembled wheel subassembly.

3.2.5.1 Drive and Idler Shafts

The drive and idler shafts were extremely complicated and time consuming to manufacture. Steel stock was rough cut to length on a grinding saw. Each rod was then inserted into a lathe and a carbide tipped tool was used to machine common shaft end onto the end of each rod. Once the steps of the common end were machine, a parting tool was used to cut the slot to hold the retaining ring.

At this point, the dimensions of each common end were compared and the most similar shafts were paired up. The common ends of each rod were then chucked into the lathe and the unmachined ends were turned down to a diameter of 8mm and cut to the correct length. The drive shaft of each pair was then turned down further to 5/16 in. and a flat was ground on each shaft. A slot for the interior retaining ring was then cut into the idler shafts. Finally, the portion of each shaft that a wheel would be pressed onto was sanded until the desired diameter was achieved. An image of the drive and idler shafts can be seen in Figure 76.

Figure 76: A set of drive and idler wheel shafts.

Several difficulties were encountered during the manufacturing of the drive and idler shafts. The most significant of these was the lack of precision in the lathe used to manufacture the shafts. It was extremely difficult to achieve consistent diameters across the length of the shafts. This resulted in some amount of slop when the shafts were fitted into the bearings.

Another difficulty encountered during the machining of the idler and drive shafts was the jamming of a parting tool when cutting one of the idler shafts to length. This caused a significant bend in the back end of the shaft. A considerable amount of time was spent straightening out the shaft and, while the shaft was made significantly straighter, it was stilled slightly bent.

3.2.5.2 Drive and Idler Wheels

The drive and idler wheels were both 3d printed. This first required the creation of .STL files from the Solidwork models of the wheels. These files were then inserted into the 3D printer software and the printer was run. Once the wheels were completed they were placed in a bath of acetic acid to remove the support material used in the printing process.

Once the wheels had dried, the interior of the hubs were sanded until their diameters fell within the desired range for press fitting onto the shafts. The wheels where then pressed onto their respective shafts using a hand press. An image of the drive and idler wheels after they were pressed onto their shafts can be seen in Figure 77 and Figure 78.

Figure 77: The idler wheel pressed onto its shaft.

Figure 78: The drive wheel pressed onto its shaft.

The only difficulty encountered during the manufacturing of the drive and idler wheels was during a reprint one of the idler wheels. The reprinted wheel came out of the printer warped at one set of teeth. An image of this warpage can be seen in Figure 79. This was caused by the tray on which the wheel was printed shifting during the printing process due to heat expansion. This problem was corrected and a replacement wheel was produced.

Figure 79: Warpage in the idler wheel.

In an effort to improve grease distribution on the tread, channels were machined into the central band of the drive and idler wheels. These channels were cut into the wheels by placing the wheels in a lathe and filing down the desired areas. The depth of the channels was chosen to such that the tread did not contact the bottoms of the channels but that enough material was left on the wheels that they would not break. The results of this modification to wheels are discussed further in Chapter 4.

3.2.5.3 Brace

The manufacturing of the braces was relatively straight forward. Aluminum stock bar was rough cut to length on a band saw and the machined to length on a mill. The drilling of the mounting holes for the bearings came next and proved to be very difficult. Initially, an end mill with the same nominal diameter as the outer race of the bearing was used to create a blind hole for the bearing to be mounted in. The problem was that the actual end mill diameter was smaller than its nominal diameter, so the bearings could not be pressed in without being damaged. The solution was to drill a through hole in the brace using a drill bit, which had enough wobble to expand the hole to the desired size. A recess was then milled around the hole to accommodate the bearings flange.

The final step in manufacturing of the brace was the instillation of the bearings. The bearings and braces were thoroughly cleaned and then the retaining compounds catalyst was painted on to the outer race of the bearing and the bearing holes in the brace. The retaining compound was then applied to the bearing and the brace and the bearing was pressed into place by hand until the bearing and brace faces were flush. The excess retaining compound was then removed. An image of the braces can be seen in Figure 80.
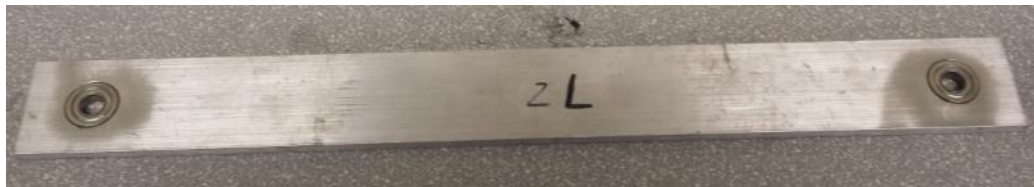
Figure 80: Brace with the bearings pressed into place.

3.2.6 Tensioner Subsystem

Figure 81 shows an image of the manufactured and assembled tensioner subsystem after it as assembled onto the frame. The final weight of the tensioner systems was 0.57 lbf each.
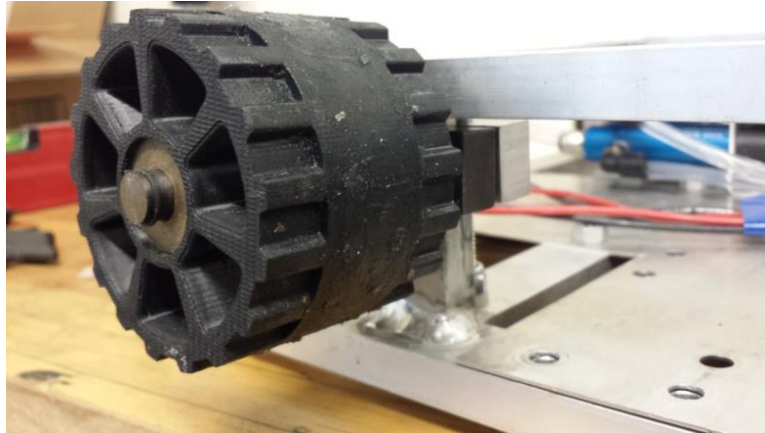
Figure 81: Tensioner subassembly attached to the wheel.

3.2.6.1 Tensioner Clamp Exterior Half

Stock steel bar was rough cut using a steel chop saw and then milled to the desired dimensions of the exterior clamp half. The slot was then milled in to the face of the clamp half and the tensioner shaft mounting hole drilled out. The holes for the attachment bolts were drilled out and tapped. The part was then deburred and polished, with special attention given to the slot. The tensioner shaft was then inserted into its mounting hole and the two parts were welded together. An image of the tensioner clamp exterior clamp half with the tensioner shaft welded in place can be seen in Figure 82.

Figure 82: Exterior clamp half with the shaft in place.

The only anomalies encountered in the manufacturing of the tensioner clamp exterior half was that during assembly it was noted that the left side tensioner upright was sloped outward. This caused the tensioner wheel to be at a sever angle relative to the drive and idler wheels on that side. To correct this, two part

putty epoxy was used to create an angled spacer on the exterior clamp half used on that side. This seemed

to completely correct the issue. An image of the space on the exterior clamp half can be seen in Figure 83.
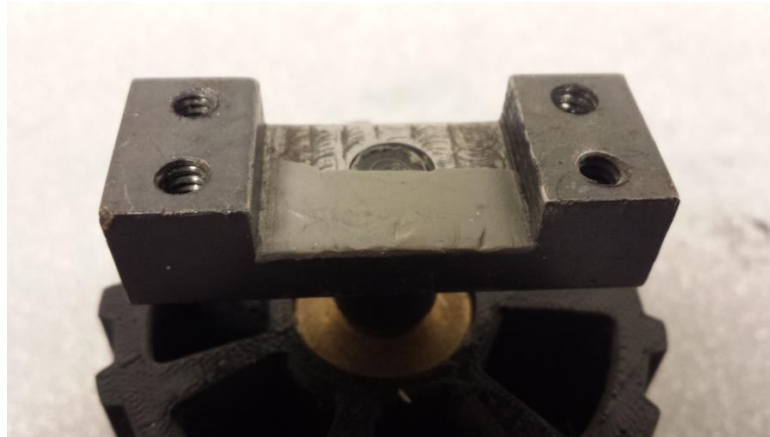
Figure 83: Spacer used to correct the misalignment of the left side tensioner wheel.

3.2.6.2 Tensioner Clamp Interior Half

Stock aluminum bar was rough cut on a band saw and then milled to the desired outer dimensions of the

interior clamp half. The slot was then milled into one face of the parts and then flipped over and the

exterior cuts were milled out. The through holes for the attachment bolts were then drilled out on the mill.

The hole for the drive screw was then drilled and tapped. Finally the parts were deburred and polished, with

special attention given to the slot. An image of the tensioner clamp interior clamp half can be seen in

Figure 84.

Figure 84: Interior clamp half.

3.2.6.3 Tensioner Wheel Assembly

Like the drive and idler wheels, the tensioner wheels were 3D printed. The same over process was used, a .STL file was created and the tensioner wheels were clean and then the interior hub was sanded. Once the interior hub was smoothed, the bushings were pressed into place. To help ensure that the tensioner wheel would align properly with the drive and idler wheels, the bushings were pressed deeper than initially intended to create a recess on both faces of the tensioner wheels. Figure 85 shows the tensioner wheel with the bushings inserted.

Figure 85: Tensioner wheel with the bushings in place.

3.2.6.4 Tensioner Shaft

The process of machining of the tensioner shafts was very similar to that of the process used for the drive and idler shafts. Stock steel rod was cut rough cut to length on a steel chop saw. The resulting blanks were then chucked in a lathe and the exterior portion of the shaft was turned down using a carbide tool. A slot for the retaining ring was cut near the tip of the shaft using a parting tool and then the end of the shaft was faced. The shafts were then flipped in the lathe and a parting too was used to cut the end of the shaft to length. The end of the shaft was then turned down to form the stud which would be inserted into the exterior clamp half. The shaft was then welded into place in the exterior clamp half. An image of the tensioner shaft welded in place can be seen in Figure 86.

Figure 86: Tensioner shaft after it was welded to the exterior clamp half.

3.2.7 Tread Manufacturing

The tread was manufactured by F.N. Sheppard based on the designs sent to them. The following description

of the manufacturing process was provided by an F.N. Sheppard employee. The timing belt portion of the

tread was first cut to length. The teeth in the center of the belt were ground flat and the low friction fabric

was glued into place. The neoprene backing was then cut to length and adhered to the timing belt and the

adhesive was allowed to dry. The hole pattern was then drilled into the tread using a CNC process. Then

ends of the tread were then welded together to form a continuous loop. Figure 87 contains an image of the

left tread. The final weight of the treads was 0.56 lbf each.

Figure 87: Vehicle tread.

Several modifications were made to the treads over the course of the project. The first of these

modifications was the removal of the low friction fabric where it bunched at the teeth of the tread. The

bunched fabric caused the surface of the channel to be uneven which in turn prevented the manifold from lying flat on the tread. Once the fabric was removed the manifold ran smoothly in the treads.

The next modification made to the treads was the application of silicone sealant over the low friction fabric in an effort to improve the seal between the manifold and the tread. The sealant was carefully aliped and smoothed to create a flat surface for the manifold to slide on and to fill in the gaps in the low friction fabric. Figure 88 shows the fabric before the sealant was applied and Figure 89 shows the fabric after the sealant was applied.Special care was taken to clear each of the tread holes so as not to clog them with the sealant. The results of the application of the sealant to the treads are discussed in Chapter 4.
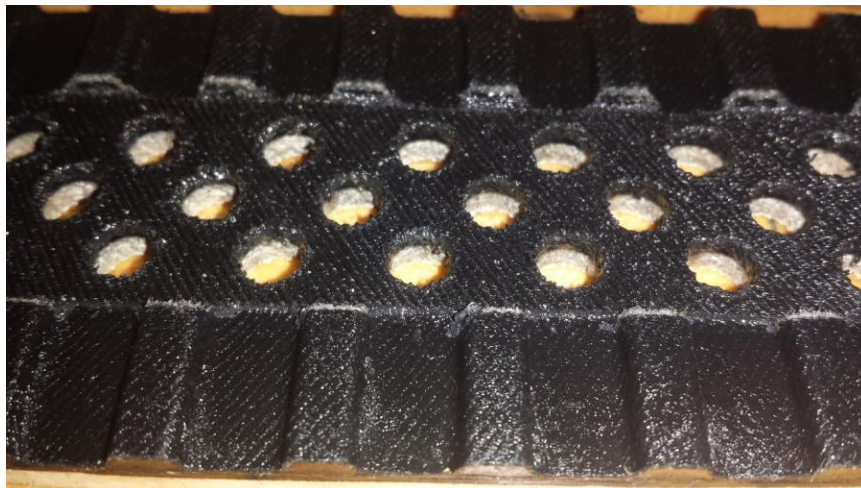
Figure 88: Low friction fabric before the application of the silicone sealant.

Figure 89: Low friction fabric after the application of the silicone sealant.

Finally, the same silicone sealant that was applied to the low friction fabric on the interior of the tread was applied to the exterior of the tread in an effort to increase the coefficient of friction between the wall and the tread. The sealant was carefully applied to the outer surface of the tread and smooth. Figure 90 shows the tread backing before the sealant was applied and Figure 91 shows the tread backing after the sealant was applied. Again, each hole was cleared to prevent clogging. The results of the application of the sealant to the treads are discussed in Chapter 4.

Figure 90: Tread backing before sealant was applied.

Figure 91: Tread backing after the silicone sealant was applied.

3.3 Assembly

This section gives brief overview of the assembled vehicle. It shows the placement of each of the subsystems within the actual vehicle. The final weight of the vehicle was 13.6 lbf. Figure 92 shows the

entire assembled vehicle and Figure 93, Figure 94, Figure 95 and Figure 96 shows the different subsystems in place in the vehicle.
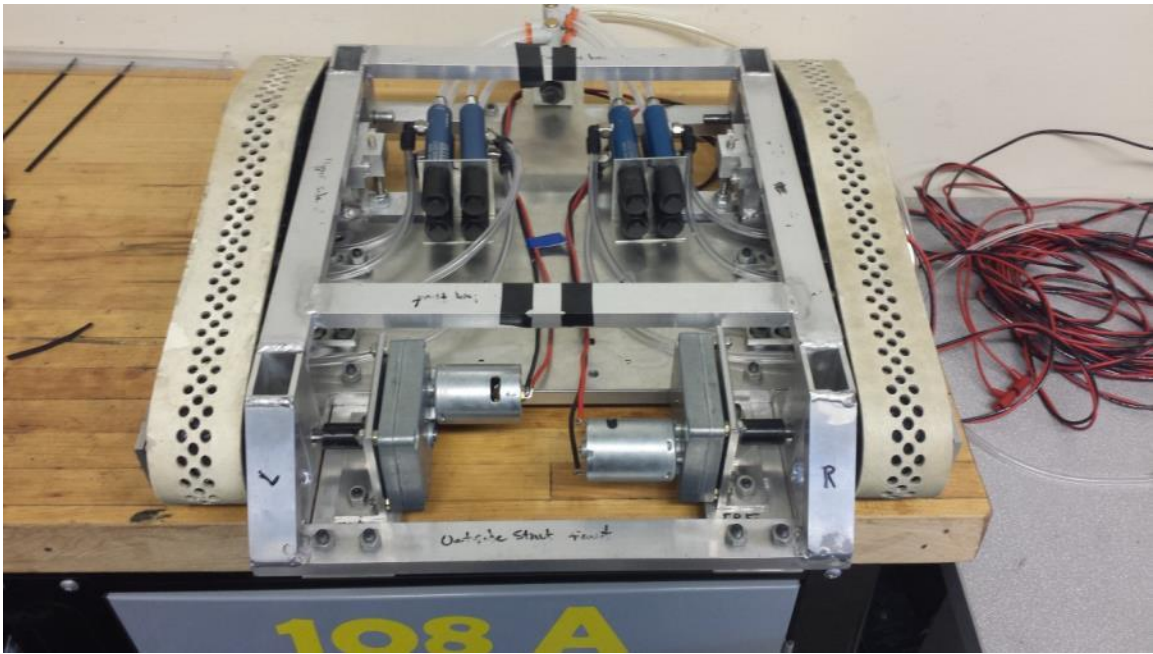
Figure 92: Fully assembled vehicle.
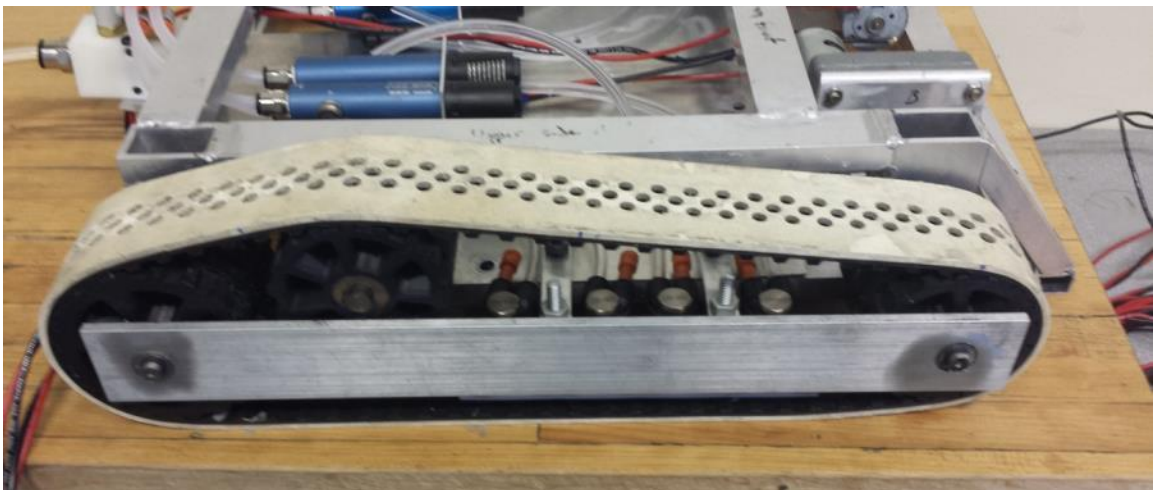
Figure 93: Wheel assembly and manifold on vehicle.

Figure 94: Motor subsystems.

Figure 95: Manifolds from the inside of the vehicle.
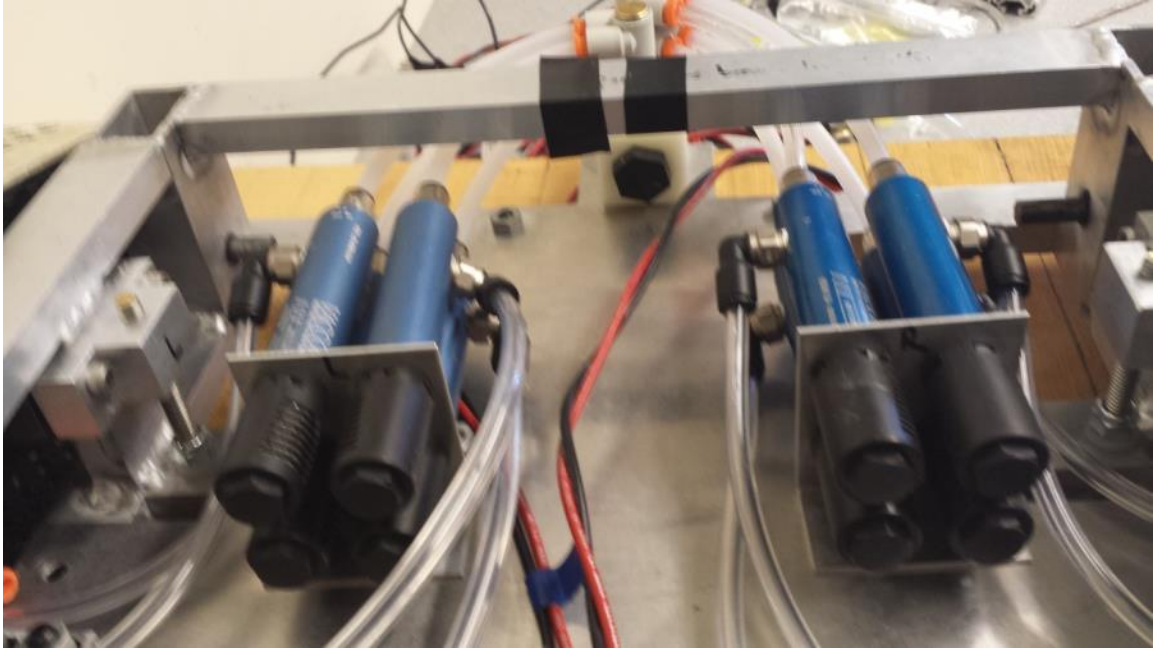
Figure 96: Vacuum system installed in the vehicle.

Chapter 4: Testing

This chapter discusses the testing which was performed on the final vehicle. Additional test data can be found in Appendix D.

4.1 Pressure System Testing

This section covers a series of tests done to gain insight into the vacuum system and how it performed under different conditions. This includes the assessment of the venturi's performance, the verification that each manifold section is independent from the others and how the manifolds act under different vehicle conditions.

The basic procedure for each of the tests conducted was very similar. A vacuum gauge, seen in Figure 97, was attached to the manifold section or venturi being tested and the vacuum pressure was measured. The following subsections give more detailed descriptions of specific tests which were conducted. To eliminate variations in the tread surface from effecting the testing, each test was conducted on the same section of the left and right treads.

Figure 97: Vacuum gauge used during the pressure system testing.

A general procedure for the manifold testing, referred to as the general manifold testing scheme, was developed to keep the tests consistent. The scheme is as follows:

1. The vacuum in the manifold being tested was engaged with all sections closed to the atmosphere.

2. The first manifold section to be tested was connected to the vacuum gauge.

3. The vacuum pressure was recorded.

4. The section closest to the front of the vehicle not being tested was exposed to the atmosphere by removing its plug and the pressure in the section being tested was recorded.

5. Repeat step 4 for each closed section until all sections are open except the one being tested.

6. The vacuum gauge was then moved to the next section to be tested and all open sections were closed.

7. Repeat steps 3-6 until each vacuum section has been tested.

This scheme also included the testing of each section before and after each test to determine if anything untoward occurred during the testing, such as a section becoming clogged. This was done by measuring the pressure in each section sequentially with all the other sections on the manifold closed.

4.1.1 Venturi Reliability

4.1.1.1 Procedure

This test was conducted by measuring the vacuum pressure that was produced by each venture and to determine if it was consistent and to determine the likelihood of clogging. Before each of the other tests in this section were run, the vacuum force produced by each venturi was measured and recorded by attaching the vacuum gauges directly to the venturi's outlet.

4.1.1.2 Results

The results of the venturi reliability testing can be found in Table 45. No venturi clogging was seen during the pressure system testing.

Table 45: Average measured ventuir vacuum pressure versus predicted vacuum pressure.

Venturi Bank	Average Measured Pressure	Ideal Pressure	% Difference
Right	13.16 psi	13.75 psi	4.3 %
Left	13.33 psi	13.75 psi	3.1 %
Total	13.25 psi	13.75 psi	3.6 %

4.1.1.3 Discussion

The venturis proved to be extremely reliable. The average vacuum pressure produced by the banks is very close to the expected outputs. The discrepancies between the expected and measured values can be explained by minor losses in the fittings used on the venturis and the vacuum gauge or by losses in the tubing. No clogging of the venturis was observed during the entirety of the pressure system testing.

4.1.2 Manifold Section Independence

4.1.2.1 Procedure

This test was conducted to determine if the sections of each manifold were independent of each other internally and to determine the pressure losses in the manifolds to the atmosphere. To do this, each manifold was placed on a sheet of silicon rubber, as shown in Figure 98 and the vacuum was engaged. The general manifold section testing scheme was then used to test the manifolds.
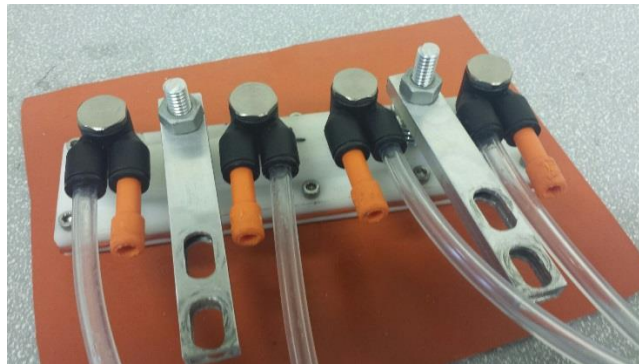
Figure 98: A manifold on the silicone sheet.

4.1.2.2 Results

The results of the manifold section independence testing can be found in Table 46 and Table 47.

Table 46: Right side venturi section independence results.

Section	Average Measured Pressure	Average Venturi Pressure	% Difference
1	12.83 psi	13.01 psi	1.4 %
2	12.91 psi	13.50 psi	4.4 %
3	12.85 psi	13.38 psi	4.0 %
4	12.89 psi	13.38 psi	3.7 %
Average	12.89 psi	13.32 psi	3.4 %

Table 47: Left side venturi section independence results.

Section	Average Measured Pressure	Average Venturi Pressure	% Difference
1	13.24 psi	13.50 psi	1.9 %
2	13.18 psi	13.26 psi	0.6 %
3	13.01 psi	13.50 psi	3.6 %
4	12.95 psi	13.38 psi	3.2 %
Average	13.10 psi	13.41 psi	2.3 %

4.1.2.3 Discussion

The sections in the right and left manifolds proved to be completely independent from one another. The data in Appendix D shows that even when all other sections in a given manifold are open, the measured section maintains its initial pressure. This implies that the manifold gasket provides sufficient seal to prevent all interaction between the sections and that the manifolds themselves are well sealed with few to no defects.

When the measured venturi pressure for a given section taken at the start of the test was compared to the pressure in the section only minor losses are found. These losses are likely due to minute losses in the manifold at the gasket and the inlet fitting.

4.1.3 Tread Installation Effect and Fixed Manifold Testing

4.1.3.1 Procedure

This test was conducted to determine if the treads being installed on the vehicle had any effect on the performance of the manifolds. To do this, each manifold was placed on its respective tread after the treads had been removed from the vehicle. The general manifold testing scheme was then used on each manifold. The treads were then placed onto the wheel system and the manifolds were placed onto the tread. The general manifold testing scheme was used on each manifold. Finally the manifolds were fixed to the vehicle and then tested using the general manifold testing scheme.

4.1.3.2 Results

Table 48 and Table 49 contain the results from the tread installation and fixed manifold testing for the right and left sides of the vehicle respectively.

Table 48: Right side tread and manifold condition testing results.

	Tread Off Vehicle			
Tested Section	All Sections Closed	1 Section Open	2 Sections Open	3 Sections Open
1	7.37 psi	3.44 psi	1.47 psi	7.86 psi
2	12.28 psi	12.28 psi	11.79 psi	9.82 psi
3	12.28 psi	11.79 psi	11.05 psi	7.37 psi
4	12.28 psi	12.28 psi	12.28 psi	10.31 psi
	Tread On Vehicle			
Tested Section	All Sections Closed	1 Section Open	2 Sections Open	3 Sections Open
1	9.82 psi	7.37 psi	6.38 psi	9.82 psi
2	12.28 psi	12.28 psi	10.80 psi	10.56 psi
3	11.79 psi	11.79 psi	11.79 psi	9.33 psi
4	12.28 psi	12.28 psi	12.28 psi	10.80 psi
	Fixed Manifold			
Tested Section	All Sections Closed	1 Section Open	2 Sections Open	3 Sections Open
1	8.84 psi	3.93 psi	2.95 psi	5.65 psi
2	12.28 psi	11.79 psi	10.80 psi	10.56 psi
3	11.79 psi	11.79 psi	11.79 psi	10.56 psi
4	12.28 psi	12.28 psi	12.28 psi	11.79 psi

Table 49: Left side tread and manifold condition testing results.

	Tread Off Vehicle			
Tested Section	All Sections Closed	1 Section Open	2 Sections Open	3 Sections Open
1	10.31 psi	9.33 psi	8.84 psi	8.84 psi
2	9.82 psi	8.59 psi	4.91 psi	1.47 psi
3	9.33 psi	8.84 psi	4.91 psi	0.98 psi
4	12.28 psi	12.28 psi	12.28 psi	10.80 psi
	Tread On Vehicle			
Tested Section	All Sections Closed	1 Section Open	2 Sections Open	3 Sections Open
1	8.35 psi	4.91 psi	1.96 psi	6.88 psi
2	10.31 psi	9.82 psi	4.91 psi	0.98 psi
3	9.33 psi	9.33 psi	4.42 psi	0.49 psi
4	11.30 psi	11.30 psi	10.80 psi	9.82 psi
	Fixed Manifold			
Tested Section	All Sections Closed	1 Section Open	2 Sections Open	3 Sections Open
1	8.35 psi	6.88 psi	5.89 psi	10.31 psi
2	10.80 psi	10.31 psi	7.37 psi	3.68 psi
3	10.31 psi	9.82 psi	6.38 psi	1.96 psi
4	11.79 psi	11.79 psi	11.30 psi	9.82 psi

4.1.3.3 Discussion

There were several different insights which were gained during this portion of the pressure testing. Each of these insights is critical to the robot's ability to function and can be used to improve the performance of future robots significantly.

The first of these insights, and perhaps the most important, is that the geometries of the manifold are critical to its ability to form a seal with the treads. In every test case pressure drops were seen in the section being measured as the sections next to it were opened. This is best seen in the raw data in Appendix D. Additionally, the vacuum pressure in the first and last sections of the manifolds is to some extent dependent on the pressure in the section that is the furthest away from it, again best illustrated in the raw data. Both of these phenomena imply that the manifolds do not lie flat against the treads. This is clearly the case as seen in Figure 99.
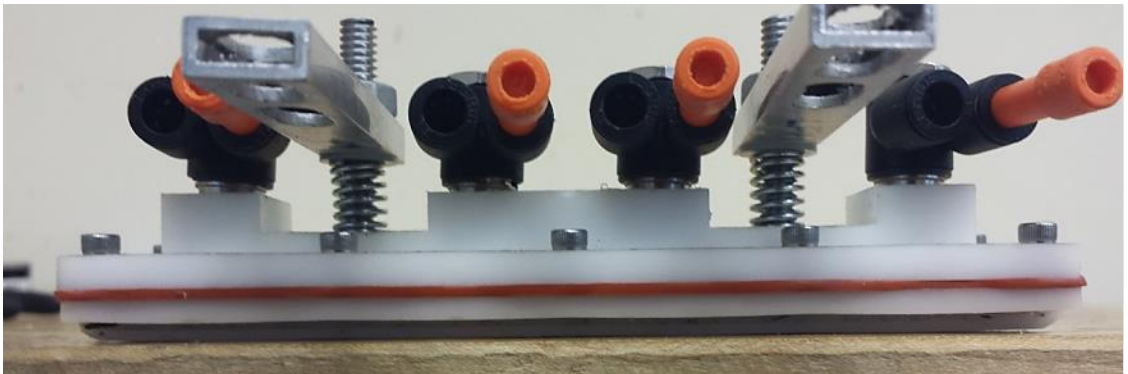
Figure 99: Warpage of the lower half of the manifold.

Another interesting insight is that the magnitudes of the forces seen when all sections are closed is very similar for each of the test cases. This indicates that neither the treads being installed on the wheels nor the manifold being fixed in place cause any impediment to the initial seal formed by the manifold. This is not the case as the manifold sections lose suction. The fixed manifold testing seems to indicate that the manifolds being fixed in place can improve a sections ability to retain its vacuum as the other sections are opened. This is most likely a consequence of both the spring suspension pushing the manifold onto the tread and the manifold's supports preventing the manifold from shifting its position on the tread as sections are opened.

4.1.4 Vertical Surface Testing

4.1.4.1 Procedure

This test was conducted to determine the performance of the manifold system's when the vehicle was adhered to a vertical surface. This was done by adhering the vehicle to a wall and then measuring the pressure in each manifold section sequentially. The general manifold testing scheme was not used as the vehicle could not keep itself adhered to the wall with one manifold not producing an adhering force. Figure 100 shows the vehicle on a vertical surface.
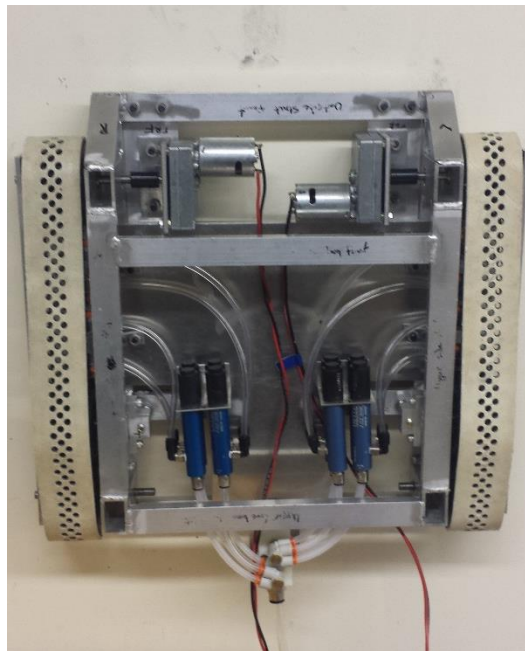
Figure 100: The vehicle on a vertical surface.

4.1.4.2 Results

The results of the vertical surface testing of the pressure system for the right and left sides of the vehicle can be found in Table 50 and Table 51 respectively.

Table 50: On wall results of the vertical surface testing.

Section	Right Side		Left Side	
	Average	Standard Dev.	Average	Standard Dev.
1	0.49 psi	0.69	6.38 psi	4.17
2	10.61 psi	1.86	10.90 psi	0.73
3	12.08 psi	0.27	10.21 psi	1.06
4	12.28 psi	0.00	4.17 psi	3.98
Total	8.86 psi	5.63	7.92 psi	3.19

Table 51: Off wall results of the vertical surface testing.

	Right Side		Left Side	
Section	Average	Standard Dev.	Average	Standard Dev.
1	8.69 psi	4.09	11.15 psi	0.33
2	12.57 psi	0.27	10.26 psi	0.96
3	12.28 psi	0.00	10.66 psi	0.81
4	9.28 psi	3.20	10.26 psi	1.18
Total	10.71 psi	2.00	10.58 psi	0.42

4.1.4.3 Discussion

The vertical surface testing of the vehicle revealed several different insights into the behavior of both the vehicle as whole and the manifold system itself. Firstly, the front section of the right side manifold was completely exposed to the atmosphere during each of the tests. This seems to have been the result of the vehicles frame being misaligned which cause the right corner of the vehicle to rise off of the wall. This in turn caused the tread to lift slightly which broke the seal between the wall and tread. This implies that the frames alignment is critical to the proper functioning of the manifold system.

The left hand manifolds performance during the testing was erratic, with the pressure in the front and rear sections varying dramatically between tests. This seems to have been the result of the front threaded upright consistently loosening during the testing. This allowed the manifold to shift more than it otherwise would have been able to.

4.1.5 Clogged vs Unclogged Performance

4.1.5.1 Procedure

There were several observed incidents during the testing of the manifolds lower chambers filling with the vacuum grease. This series of tests was done to determine if this had a direct effect on the manifolds ability to maintain a seal or would cause clogging in the vacuum system. Each tread was run continuously while grease was applied to the surface of the manifold channel until a large amount of grease had built up in the manifold. Figure 101 and Figure 102 shows the clogged and the unclogged manifolds respectively for comparison. The clogged manifolds were then run through the section independence, tread installation effect and fixed manifold testing regimes. A vertical surface test was not conducted as the clogged manifolds could not safety hold the vehicle on the wall while it was being tested.
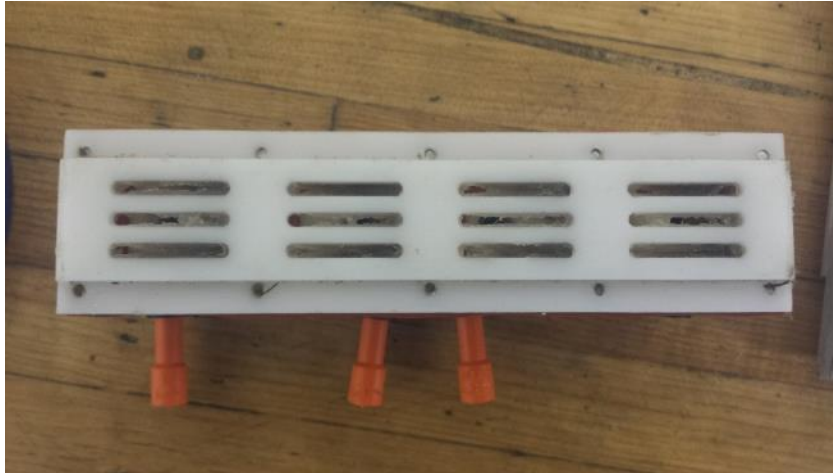
Figure 101: Clogged manifold.
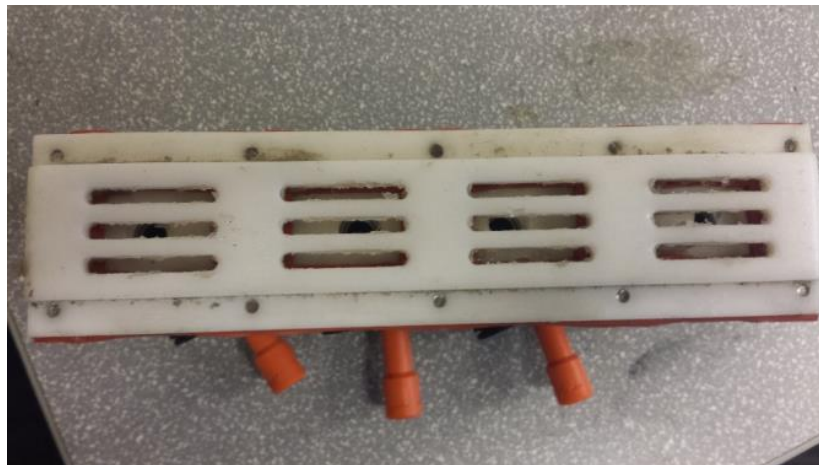
Figure 102: Cleared manifold.

4.1.5.2 Results

The results of the clogged versus unlogged testing can be found in Table 52 and Table 53.

Table 52: Cumulative results of the clogged versus unclogged testing for the right manifold.

Section	Clogged	Unclogged	% Difference
1	8.88 psi	8.92 psi	0.46%
2	12.20 psi	12.28 psi	0.67%
3	11.87 psi	12.03 psi	1.4%
4	11.46 psi	12.11 psi	5.4%

Table 53: Cumulative results of the clogged versus unclogged testing for the left manifold.

Section	Clogged	Unclogged	% Difference
1	7.41 psi	9.29 psi	20%
2	11.01 psi	10.64 psi	3.5%
3	10.39 psi	10.03 psi	3.6%
4	9.78 psi	11.87 psi	17%

4.1.5.3 Discussion

No major discrepancies were seen between the vacuum pressures in the clogged manifold versus the

manifold which had been cleared. This shows that the grease was not being pulled into the manifolds

fittings and causing blockages in the section itself. The real effect that clogging had on the vehicle was the

loss of vacuum force due to tread holes being cut off from the vacuum. This resulted in extremely low

adhesion forces between the vehicle and the surfaces which it was adhering to.

4.1.6 Split Manifold Testing

4.1.6.1 Procedure

To determine if the bowing observed in the manifolds was preventing all of the manifold sections from

engaging at one time, the right side manifold was cut in half as shown in Figure 103. To determine the

effect that this had on the performance of the right side manifold it was tested for section independence, off

wheel tread effects, fixed manifold and vertical surface testing.
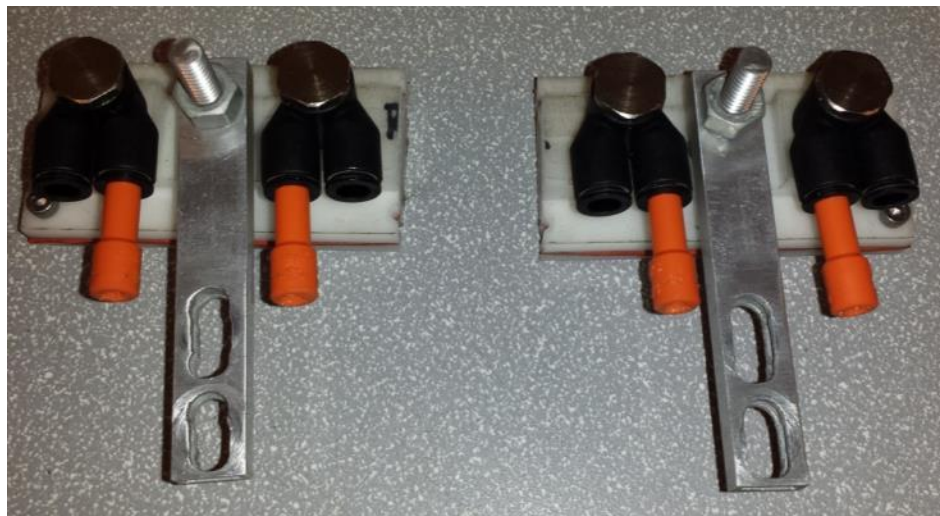
Figure 103: Split right manifold.

The results of the initial vertical surface test prompted a modified vertical surface test to be performed. In

this test the vehicle was adhered to the wall as before. A known force was then applied to the right side of

the frame near the drive wheel as seen in Figure 104. This forced the right hand tread to lay flat on the wall.

Figure 105 shows the right hand tread before and after the tread was forced flat. The vacuum pressure was

then measured as it was in the original vertical surface testing scheme.
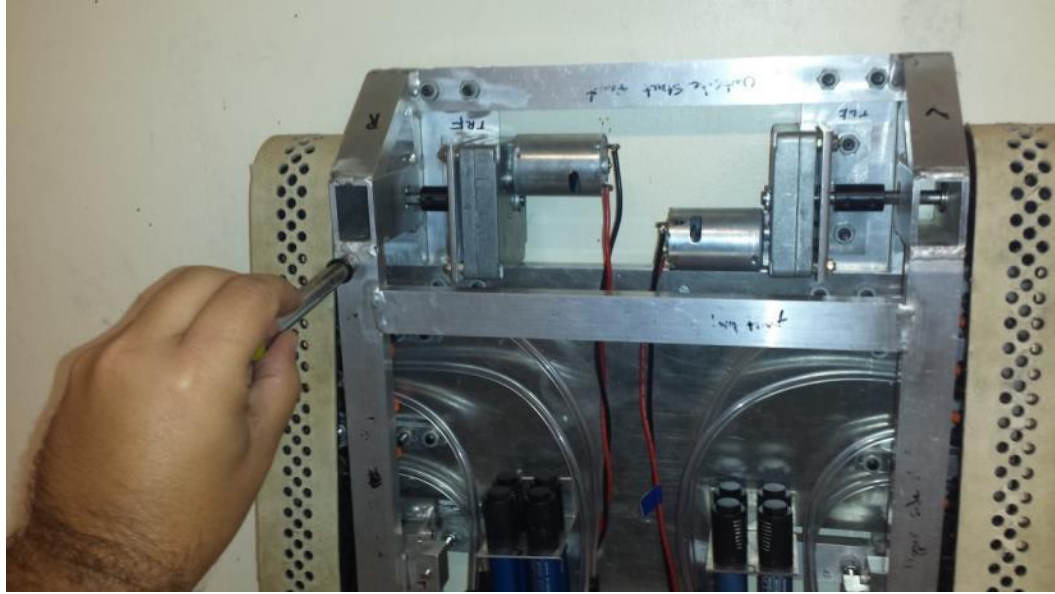
Figure 104: Force being applied to the right corner of the vehicle.

Figure 105: (Left) the right tread after it was pressed onto the wall. (Right) the right tread before it was pressed onto the wall.

4.1.6.2 Results

The raw data from the split right manifold testing can be found in Appendix D. The results of the right split manifold section independence test and the comparison of these results to the whole right manifold section independence test can be found in Table 54. The results of the right split manifold on vehicle tread test and the comparison of these results to the whole right manifold on vehicle tread test can be found in Table 55. Table 56 and Table 57 gives a comparison between the fixed manifold testing results for the split right manifold and the whole right manifold.

Table 54: Performance of the split right manifold versus the whole right manifold for the section independence test.

Section	Right Manifold Pressure Split	Right Manifold Pressure Whole	% Difference
1	12.77 psi	12.83 psi	0.46%
2	13.01 psi	12.91 psi	0.77%
3	12.77 psi	12.85 psi	0.62%
4	12.77 psi	12.89 psi	0.93%
Average	12.83 psi	12.87 psi	0.16%

Table 55: Performance of the split right manifold versus the whole right manifold for the vehicle tread test.

Section	Right Manifold – Split	Right Manifold - Whole	% Difference
1	11.30 psi	7.37 psi	53%
2	11.79 psi	12.28 psi	4.0%
3	11.79 psi	11.79 psi	0.0%
4	10.31 psi	12.28 psi	16%
Average	11.30 psi	10.93 psi	3.4%

Table 56: Performance of the split right manifold versus the whole right manifold for the fixed manifold test.

Section	Right Manifold - Split	Right Manifold – Whole	% Difference
1	8.59 psi	9.33 psi	7.9%
2	12.77 psi	12.28 psi	4.0%
3	11.30 psi	12.28 psi	8.0%
4	10.80 psi	12.28 psi	12%
Average	10.87 psi	11.54 psi	5.9%

Table 57: Performance of the split right manifold versus the whole right manifold for the fixed manifold test.

Split Right Manifold				
Tested Section	All Sections Closed	1 Section Open	2 Sections Open	3 Sections Open
1	10.31 psi	8.10 psi	7.86 psi	7.86 psi
2	12.28 psi	11.79 psi	11.30 psi	11.30 psi

3	10.31 psi	10.31 psi	9.82 psi	7.86 psi
4	9.33 psi	8.84 psi	8.84 psi	7.37 psi
Whole Right Manifold				
Tested Section	All Sections Closed	1 Section Open	2 Sections Open	3 Sections Open
1	8.84 psi	3.93 psi	2.95 psi	5.65 psi
2	12.28 psi	11.79 psi	10.80 psi	10.56 psi
3	11.79 psi	11.79 psi	11.79 psi	10.56 psi
4	12.28 psi	12.28 psi	12.28 psi	11.79 psi

Table 58 shows the comparison between the results of the split right manifold vertical surface testing and the whole right manifold vertical surface test. The results of the no force versus applied force vertical surface testing for the split right manifold and the left manifold can be found in Table 59 and Table 60 respectively.

Table 58: Performance of the split right manifold versus the whole right manifold for the vertical surface test.

Section	Right Manifold - Split	Right Manifold - Whole	% Difference
1	0.00 psi	5.89 psi	100%
2	0.00 psi	11.30 psi	100%
3	9.82 psi	9.82 psi	0.0%
4	12.3 psi	7.37 psi	66 %
Average	5.53 psi	8.60 psi	36 %

Table 59: Results of the applied force test for the right manifold. Applied load was 14 lbf.

Section	No Applied Load	Applied Load	% Difference
1	0.00 psi	10.80 psi	100 %
2	0.00 psi	12.28 psi	100 %
3	9.82 psi	9.82 psi	0.00
4	10.80 psi	11.30 psi	4.4 %
Average	5.16 psi	11.1 psi	53 %

Table 60: Results of the applied force test for the left manifold. Applied load was 14 lbf.

Section	No Applied Load	Applied Load	Difference
1	10.8 psi	9.82 psi	10 %
2	12.3 psi	0.00 psi	100 %
3	9.82 psi	0.00 psi	100 %
4	11.3 psi	0.00 psi	100 %
Average	11.1 psi	2.46 psi	350 %

4.1.6.3 Discussion

The section independence testing was completely successful. Each section was independent from its neighbor and each was fully sealed from the atmosphere. The off wheel testing was also successful with the

average vacuum pressure in the split manifold increasing when compared to the whole manifold off wheel testing.

The fixed manifold testing had mixed results. The average vacuum pressure in the split manifold was slightly lower than the than pressure observed in the whole manifold. This could be the result of the misalignment in the tread or the manner in which the manifolds were fixed in place. The splitting of the manifolds did seem to reduce the effect that the front two and back two sections had on each other, especially at front section of the manifold.

The splitting of the right manifold drastically reduced the effectiveness of the manifold when it was adhered to vertical surfaces. The front half of the manifold did not engage at all, and the effectiveness of the first section on the back half was reduced. This was a direct result of the misalignment of the frame, which caused the front of the right tread to lift off the surface. When the manifold was whole and supported by two struts, this only caused the front section of the manifold to fail. Because the two halves of the manifold only had a single support system, the manifold halves were much easier to shift, allowing the tread to push the front manifold half out of position.

The misalignment in the frame was further highlighted when the modified vertical surface testing was performed. When a load was applied to the right front corner of the vehicle, forcing the right tread flat against the surface, an increase in the section pressure in the two right manifold halves was seen. The application of the force to the front right corner of the vehicle caused all but the first section of the left manifold to fail completely. This implies that as the front right corner of the vehicle was pushed down the back left corner was lifted when the force was applied.

4.1.7 Vacuum Force Testing

4.1.7.1 Procedure

This testing was done to determine the vacuum force developed between the wall and the vehicle. The information gathered during the test was used to validate the tread hole engagement calculation performed in Appendix A. The first step taken during this testing was the determination of the number of tread holes

that were engaged during the testing. This was done by simply counting the tread holes which were

exposed to the slots in the manifolds as shown in Figure 106.
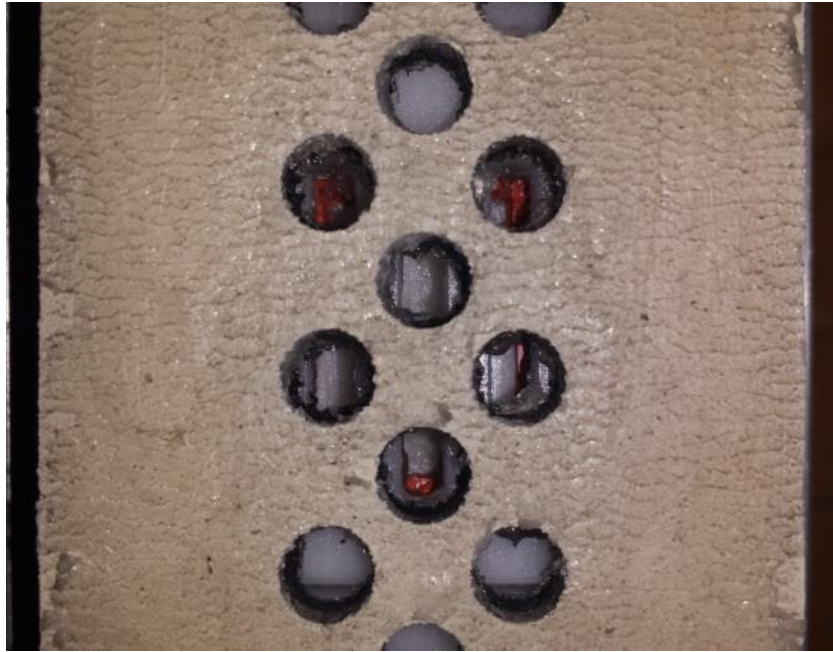
Figure 106: A section of the manifold and the tread holes which it engages.

A series of zip ties, show in Figure 107, were then used to create an attachment point over the center of

gravity of the vehicle. This was done to minimize the effects that the mass of the vehicle would have on the

testing.
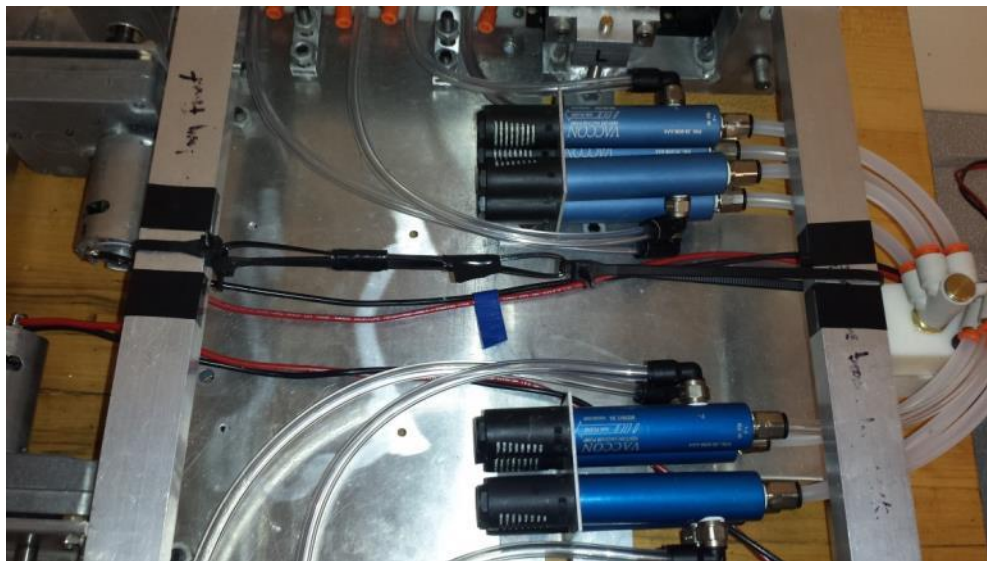
Figure 107: The zip tie suspension system used to perform the pull tests.

The testing was conducted while the vehicle was both on both a horizontal and vertical surface. For both test cases the vehicle was adhered to the surface and the vacuum pressure in each of the manifold sections. A dial force gauge, shown in Figure 108, was then inserted into the attachment point and then pulled perpendicular to the surface as seen in Figure 109. The force when the vehicle began to leave the surface was recorded.

Figure 108: Force gauge used in the pull testing.
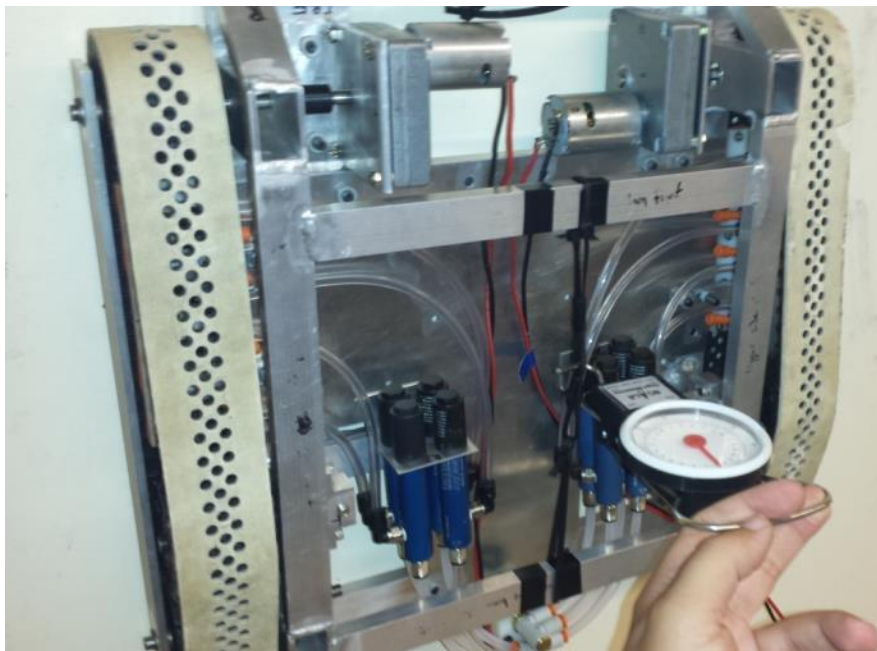
Figure 109: Vertical wall pull test example.

The results of the initial horizontal testing prompted a modified version of the horizontal test to be conducted. Pull-off forces of known magnitude were applied to the vehicle. The vacuum pressure of each manifold section was measured as the force was applied until the vehicle left the surface.

4.1.7.2 Results

The complete data gathered during the vacuum force testing can be found in Appendix D. The number of holes engaged with each manifold section during the pull-off force testing can be found in Table 61. This was important information that was used in the calculation of the predicted pull-off force for the vehicle.

Table 62 gives the average values for the pull-off force of both tests and the average pressure in the manifolds during the tests.

Table 61: Holes engaged during the pull force testing.

Section Number	Right Manifold	Left Manifold
1	8	6
2	6	8
3	7	6
4	6	7
Total	27	27

Table 62: Average pull off force and manifold pressure for the horizontal and vertical tests.

Test Case	Average Pull -Off Force	Average Manifold Pressure
Vertical Surface	17 lbf	7.27 psi
Horizontal Surface	24.5 lbf	10.7 psi

Table 63 and Table 64 contain the predicted and actual pull-off forces for the horizontal and vertical surface tests respectively. Note that the predicted values in Table 65 include the weight of the vehicle. The predicted values were obtained by multiply the number of holes engaged for a given section with the vacuum pressure measured in that section and the area of a single tread hole. Table 66 contains the results from the manifold pressure test and Figure 110 and Figure 111 show plots for the right and the left manifold respectively. Table 67 contains the predicted and actual pull-off forces for the horizontal surface test with the weight of the vehicle excluded from the predictions.

Table 63: Predicted versus actual pull off force for the horizontal test with the mass included in the predicted value.

Test Number	Predicted Pull-Off Force	Actual Pull-Off Force	% Difference
1	39.7 lbf	25.0 lbf	37 %
2	40.3 lbf	24.5 lbf	39 %
3	42.0 lbf	23.0 lbf	45 %
4	41.4 lbf	24.0 lbf	42 %
Average	40.9 lbf	24.1 lbf	41 %

Table 64: Predicted versus actual pull off force for the vertical test.

Test Number	Predicted Pull-Off Force	Actual Pull-Off Force	% Difference
1	18.8	19	1.1 %
2	19.5	17	12 %
3	18.5	15	18 %
4	19.4	16	18 %
5	19.3	20	3.6 %
Average	19.1	17.4	8.9 %

Table 65: Pressure in the right and left manifold sections at different pull off force values.

Right Manifold				
Pull Force	Section 1	Section 2	Section 3	Section 4
0 lbf	10.31 psi	12.28 psi	10.31 psi	10.31 psi
10 lbf	8.84 psi	12.28 psi	9.82 psi	10.31 psi
15 lbf	8.84 psi	11.79 psi	8.84 psi	10.31 psi
20 lbf	7.86 psi	11.79 psi	8.84 psi	9.33 psi
Left Manifold				
Pull Force	Section 1	Section 2	Section 3	Section 4
0 lbf	11.79 psi	10.80 psi	9.82 psi	10.31 psi
10 lbf	11.79 psi	10.80 psi	8.84 psi	10.31 psi
15 lbf	11.79 psi	10.31 psi	8.35 psi	9.82 psi
20 lbf	11.79 psi	10.31 psi	8.35 psi	7.86 psi
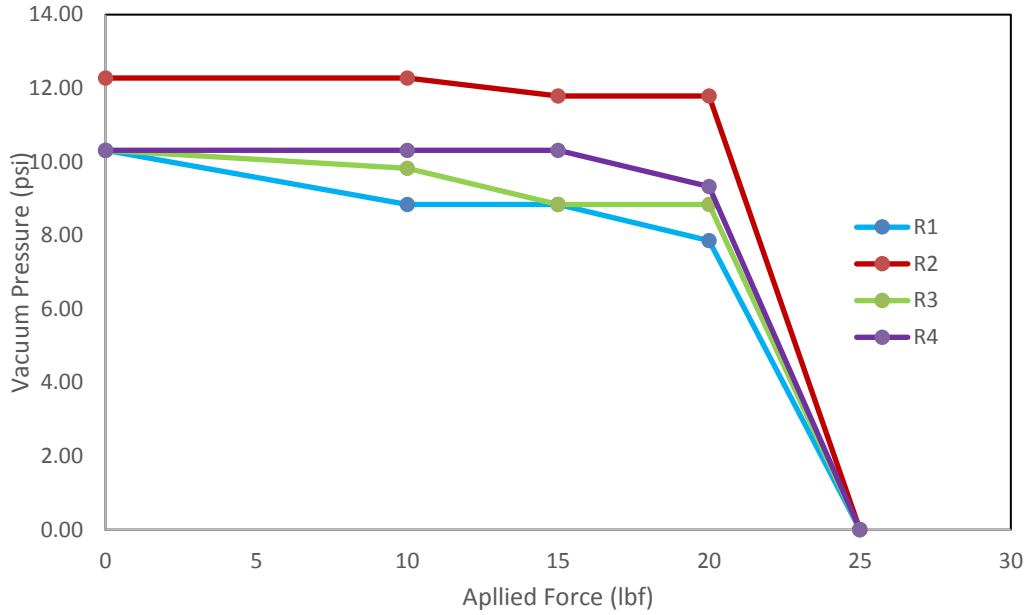
Figure 110: Right side manifold pressure as load was applied.
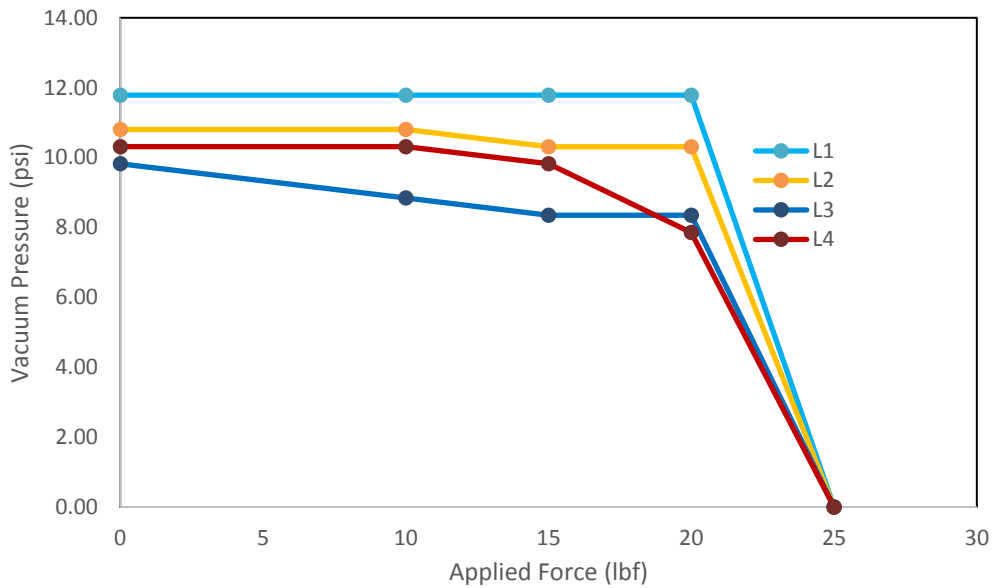
Figure 111: Left side manifold pressure as load was applied.

Table 66: Predicted versus actual pull off force for the horizontal test without the mass included in the predicted value.

Test Number	Predicted Pull-Off Force	Actual Pull-Off Force	% Difference
1	27.3 lbf	25.0 lbf	8.4 %
2	27.8 lbf	24.5 lbf	12 %
3	29.5 lbf	23.0 lbf	22 %

| 4 | 28.9 lbf | 24.0 lbf | 17 % |
| Average | 28.4 lbf | 24.1 lbf | 15 % |

4.1.7.3 Discussion

The discrepancies between the actual and predicted pull-off forces for both of the test cases that were investigated could have several different possible explanations. If the pull-off forces were applied to the vehicle at an angle relative to the testing surface, the uneven loading could cause the development of moments. These moments could initiate premature separation between the treads and the testing surface and cause a loss of pressure. Another possible explanation could be that the pull-off force causes the manifolds to shift. This shifting could then result in the seal between the manifolds and the treads to begin to fail. Finally, the motion of the vehicle being lifted away from the surface could cause the portions of the tread not under the manifold to lift. This lifting of the tread around the manifold could have both opened gaps between the tread and the wall and caused the manifolds to lift at their ends, both of which would cause a premature loss of suction.

The results of the vertical surface testing were very encouraging. The discrepancies between the predicted and actual pull-off force values, while significant, do not preclude the prediction method used for being employed in future works. Further refinement of the method is necessary, but it could be used to estimate the expected force between a vertical surface and the vehicle.

The horizontal testing proved to be much more interesting than the vertical testing. Initially, the mass of the vehicle was included in the predicted pull-off force. When the conducted testing was performed, the discrepancies between the predicted values and the measured values were extremely high. When the weight of the vehicle was removed from the prediction, the discrepancy between the predicted and actual pull-off force dropped considerably.

This observation prompted two new sets of testing to be performed. The first test involved observing the pressure in each section at different applied pull-off forces. This was to determine if the pull-off forces was causing premature loss of seal at the manifolds or the treads. The second test was adding weight to vehicle to determine what effect the additional weight had on the pull-off force.

While some loss in seal was seen as the pull-off force was applied in the pressure system testing, the drop off was not dramatic until the maximum pull-off force was approached. At this point each manifold section lost pressure rapidly and the vehicle left the surface. This seemed to indicate that either the

This result can be interpreted in two different ways to get two distinct scenarios. The first scenario is that the force gauge was measuring the weight of the vehicle and the pull-off force for the entire test. The lowered force between the surface and the vehicle could be the result of tread deformation or the manifolds being shifted. This implies that the predicted force between the surface and the vehicle is much lower than the actual force, but the results of the vertical surface testing seems to contradict this.

The other possible scenario is that the force gauge is measuring the vacuum force between the surface and the vehicle, and only after this force has been overcome does the gauge measure the weight of the vehicle. This is analogous to pre-tension in bolts, where the pre-load must be overcome before the bolt begins to carry any of the loading placed on the members it is attaching. This scenario seems to be supported by the results of the vertical surface testing and the manifold section testing, which indicates that the loss in pressure in the manifold sections is very gradual until a critical point is reached. Further testing should be conducted to confirm which scenario is correct, as the results will have serious implications about future vehicles abilities to adhere to ceilings.

The measured pull-off forces are far from the desire pull-off forces which the vehicle was designed for. This can be directly attributed to the inability of the manifolds to maintain a perfect seal across all sections when the vehicle is on a vertical surface. This will need to be addressed in future iterations of the project.

4.2 Other Testing

4.2.1 Motor Torque Testing

This testing was done in order to determine the torque required drive the vehicle under different conditions. The information gathered from this was used to validate the model used to determine the theoretical torque requirements of the motors.

4.2.1.1 Procedure

The procedure used to determine the motor torque relatively simple. The motors were run during for several different test case, such as when the motors had no load applied to them and when the vehicle was run on a horizontal surface with no vacuum applied. The vehicle was allowed to reach steady state when possible and the current draw from the power supply of the test cases was recorded.

4.2.1.2 Results

The first step was to determine the no load current draw for the motors. This was done by disconnecting the motors from the drive wheels and running them. Because the stall torque was given as fifty inch pounds of torque, the current vs torque relationship could be established. Figure 112 shows the plot that was used to determine the relationship between torque and current for the motors.
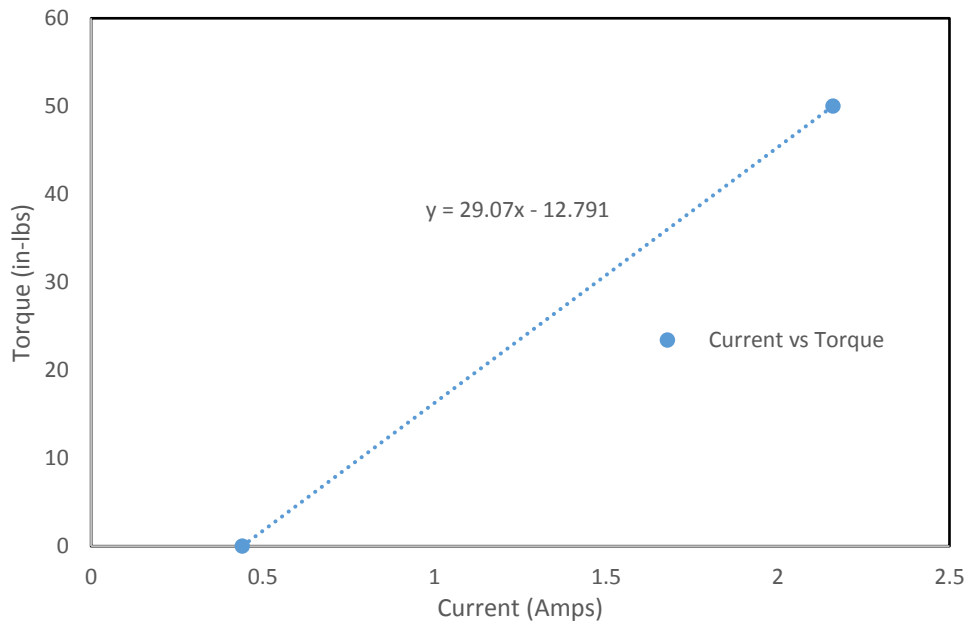
Figure 112: Current versus torque plot.

The current draw of the motors for several different test cases were then measured and recorded. The motor torque for each case was then calculated using the equation from Figure 112. Table 67 contains the current draw for each test case and the corresponding torque produced by the motors and Figure 113 shows a plot of the torque current relationship.

Table 67: Current values measured during different test cases and the corresponding torque values.

Test Case Number	Case Description	Current	Torque
1	Vertical Surface Before Failure	1.55 A	32.27 in-lbf
2	Vertical Surface after Failure	1.22 A	22.67 in-lbf
3	Table Top w/ Vacuum	1.00 A	16.28 in-lbf
4	Table Top w/o Vacuum	0.83 A	11.34 in-lbf
5	Table Top w/ Manifolds Removed	0.65 A	6.10 in-lbf
6	Not on Surface w/ Manifold	0.60 A	4.65 in-lbf
7	Not on Surface w/o Manifold	0.60 A	4.65 in-lbf
8	No Load	0.44 A	0.00 in-lbf
9	Stall Torque	2.16 A	50.00 in-lbf
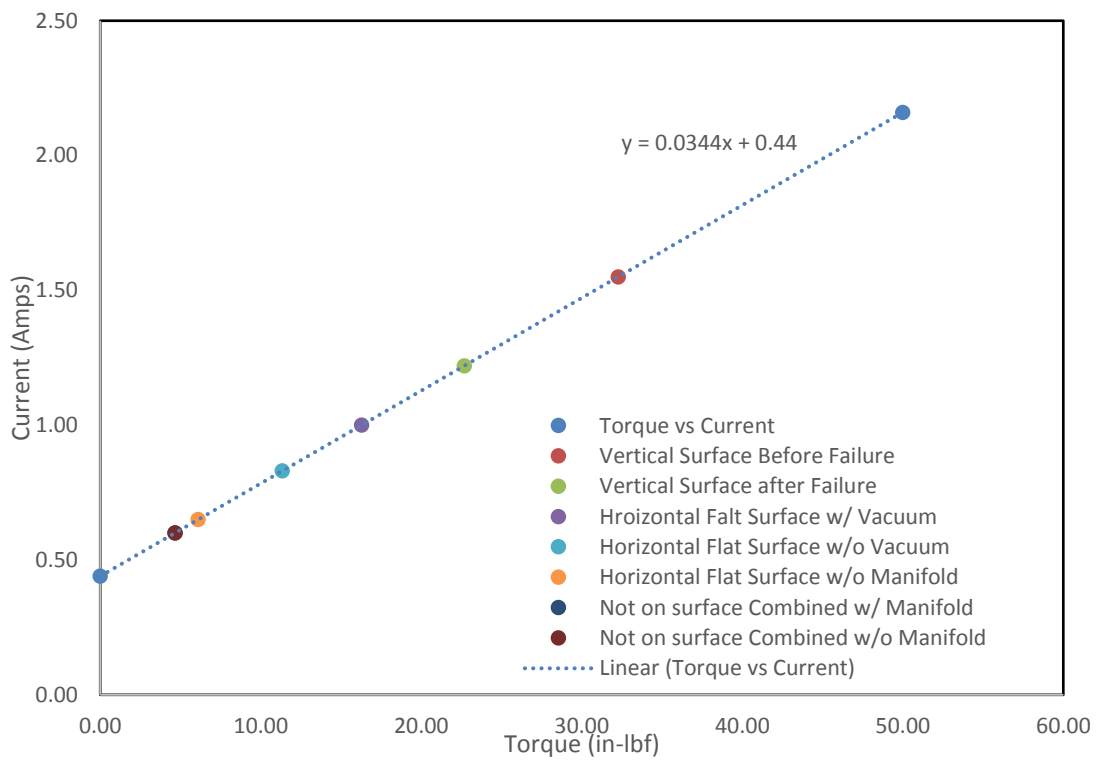
Figure 113: Torque versus current plot showing each test cases torque and current value.

Using the torque values for the different test cases, the contribution of different elements to the motor torque can be estimated. For instance the test case were the vehicle was run on a table top with the manifold removed gives an estimated of the losses in the wheel system when the vehicle is on a surface. Table 68 contains the estimates of the contribution of several different elements of the design to the motor torque and what test cases were used to calculate them. contains a comparison between the calculated and estimated torque contributions and the measured torque. Table 69 contributions of different elements of the vehicle.

Table 68: Calculated values for different motor torque contributors.

Motor Torque Contributor	Test Cases Used	Torque Contribution
Wheel Losses Off Surface	(7)	4.65 in-lbf
Wheel Losses Due to Being on a Surface	(6 − 7)	1.45 in-lbf
Friction Between Manifold/ Tread Due to Vacuum	(3 − 4)	4.94 in-lbf
Friction Between Manifold/Tread Due to Weight and Spring Forces	(4 − 5)	5.23 in-lbf
Total friction Loss Between Treads and Manifolds	(3 − 5)	10.17 in.-lbf
Weight	(1 − 3)	15.99 in-lbf

Table 69: Calculated versus measured values of the motor torque contribution of different elements of the design.

Motor Torque Contributor	Calculated or Estimated Value	Measured Value	% Difference
Losses in Wheel/Tread System	5.00 in-lbf	6.10 in-lbf	18 %
Due to Manifold Friction	10.64 in-lbf	10.17 in.-lbf	4.6 %
Due to Acceleration/Weight	11.13 in.-lbf	15.99 in-lbf	30 %
Total	26.77 in-lbf	32.27 in-lbf	17 %

4.2.1.3 Discussion

The measured torque contributions of the different design elements were relatively close to the values which were calculated in Appendix A. Because of the complexity of the wheel system and its interaction with the tread, the value for the losses in the system was estimated. Since the value was estimated and not calculated, it was expected that there would some difference between the measured and predicted value.

Overall, the vehicle required about seventeen percent more torque than was initially calculated. The major contributor to this discrepancy was the torque contribution of the weight and the acceleration of the vehicle. The contribution of the acceleration and the weight of the vehicle were difficult to separate because it was unknown if the vehicle reached a constant velocity before it slipped from the wall. This meant that measured current during the vertical testing was a lumped value and so when it was compared to the calculated weight and acceleration contributions, these values had to be lumped as well. The discrepancies between measured and calculated values were relatively large. This is likely due to the idealized nature of the calculations used to determine the weight and accelerations values. Further investigation should be conducted to determine the root cause of this in future iterations of the design.

4.2.2 Wheel Alignment

This test was used to determine how well the drive, idler and tensioner wheels were aligned. Misalignment of the wheels in the system could have significant effects on the performance of the belt system and the life time of the tread. The method used was relatively simple and was found in the SDP/SI timing belt design guide.

4.2.2.1 Procedure

To measure the relative misalignments between the wheels one end of a ruler was pressed flush against the face of each wheel. The other end of the straight edge was then positioned over one of the other wheels in the system, as seen in Figure 114, and the distance between the straight edge and the face of the second wheel was measured. This gave the parallel misalignment for each pair of wheels. If the straight edge was not parallel with the face of the wheel, then the angle between the straight edge and the second wheel was determined. An example of angular misalignment can be seen in Figure 115.
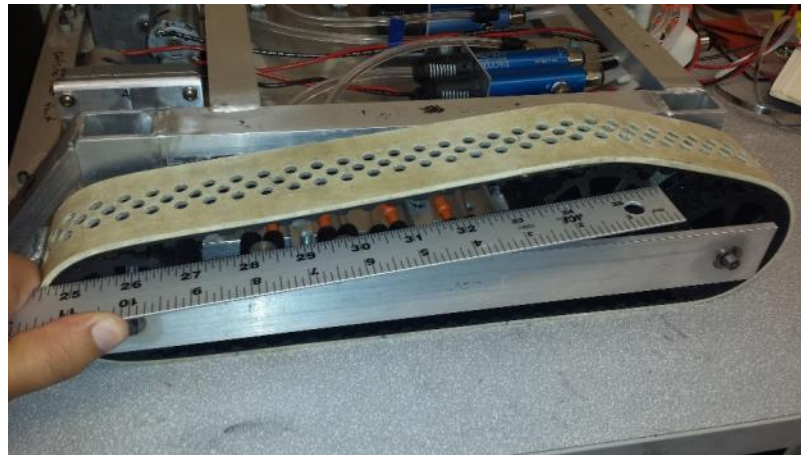
Figure 114: Straight edge going between the drive and tensioner wheels on the right side of the vehicle.

Figure 115: Angular misalignment of the tensioner wheel on the right side of the vehicle.

The angle between the wheels and the surface that the vehicle was resting on was also measured. The

vehicle was place on a flat smooth surface and the straight edge was place flush against it. The straight

edge was then moved into contact with the wheel and the angle between the face of the wheel and the

straight edge was measured. To measure the angular misalignment of the tensioner wheel with ground, the

braces on each side were check for their perpendicularity with the ground, as shown in Figure 116. The

alignment between the top of the brace and the tensioners was then measured as shown in Figure 117.

Figure 116: Straight edge against the brace.

Figure 117: Angular misalignment between the brace and the tensioner wheel on the right side of the vehicle.

4.3.2.2 Results

The parallel and angular misalignments measured for the right and left sides of the vehicle can be seen in

Table 70 and Table 71 respectively. The angular misalignment between the wheels on the right and left

sides of the vehicle compared to a flat surface can be found in Table 72 and Table 73 respectively.

Table 70: Angular and parallel misalignment between wheels on the right side of the vehicle.

Test Case	Parallel Misalignment	Angular Misalignment
Drive – Tensioner	0.0 in.	0.5°
Drive – Idler	0.0 in.	0.0°
Idler – Tensioner	0.0 in.	0.5°

Table 71: Angular and parallel misalignment between wheels on the left side of the vehicle.

Test Case	Parallel Misalignment	Angular Misalignment
Drive – Tensioner	0.0 in.	0.5°
Drive – Idler	0.0 in.	0.41°
Idler – Tensioner	0.0 in.	0.5°

Table 72: Angular misalignment between wheels on the right side of the vehicle a flat surface.

Test Case	Angular Misalignment
Drive Wheel	0.0°
Idler Wheel	0.0°
Tensioner	0.5°

Table 73: Angular misalignment between wheels on the left side of the vehicle a flat surface.

Test Case	Angular Misalignment
Drive Wheel	0.25°
Idler Wheel	0.25°
Tensioner	0.46°

4.2.2.3 Discussion

The method used to determine wheel alignment was very difficult to perform. This was mostly due to the fact that the misalignments were extremely small, with the measurable misalignment being no greater than twenty thousandths of an inch, and occurred over a small distance. The geometries of the wheel system made taking some of the measurements awkward. Despite these difficulties, estimates of the angular and parallel misalignments in the wheels systems were taken.

No parallel misalignment was seen between the wheels on either side of the vehicle was observed. This indicates that the spacing system for the drive, idler and tensioner wheels was successful and the frames wheel support struts where very close to parallel.

The angular misalignment between the tensioner wheels and idler and drive wheels was expected. This is because the tensioner struts were not very well aligned with the rest of the frame. The braces were found to be parallel with the ground, and so the angular misalignment between the tensioner wheel and the ground could be estimated. The angular misalignment between the ground and the tensioner wheel was expected as the tensioner struts were not well aligned with the ground.

The right side of the vehicle was generally well aligned. The drive and idler wheels had no discernable misalignment with each other and with the ground. This was not the case with the left side of the vehicle, which had misalignment between the drive and idler wheel and the ground. This misalignment was likely due to the slop between the shafts of the wheels and the bearings, as well as angular misalignment between the frame struts.

Despite the angular misalignment seen the wheel systems of the robot the tread wheel system worked well during the other testing conducted. This indicates that the system can tolerate small misalignments and still operate properly, but may have reduced lifetime. Future iterations of the design should strive to eliminate

measurable misalignment in the wheel system, as this will increase the life span of the treads and will likely reduce the losses in the wheel system.

4.2.3 Belt Tension Determination

This test was meant to determine the static tension which was developed in the treads after they had been tensioned. The following section covers the procedure used to determine the belt tension and the results of the testing.

4.2.3.1 Procedure

The procedure used to determine the belt tension was relatively straight forward and was found in SPD/SI's timing belt design guide manual. The method used to determine the belt tension is as follows. The belt was deflected by 1/64 in. for each inch of the span where the belt was being tested and the force required to achieve the deflection was recorded. The deflection and force measurement were performed using a belt tension gauge and can be seen in Figure 118. Figure 119 shows the deflection force being measured using the belt tension gauge.

Figure 118: The force gauge used to determine the tread tension.

Figure 119: The tension in the left tread being measured.

4.2.3.2 Results

Equation 4.1 was used to calculate the static tension that was developed in the belt. Table 74 gives an explanation of the variables found in Equation 4.1. The constant Y was calculated using a similar method to that used to determine the mass factor for the tread in Appendix A. The results for the right and left side treads can be found in Table 75 and Table 76 respectively. Table 77 compares the desired tread tension value with the estimated actual tread tension value.

$$T_{st} = \frac{16 * DF - \frac{t}{L} * Y}{1.1} \qquad (4.1)$$

Table 74: Variables used in Equation 4.1.

Symbol	Units	Description
DF	lbf	Force required to deflect the tread 1/64 in. per in of span length.
t	in.	Length of span where the measurement was taken.
L	in.	Pitch length of the tread.
Y	lbf	Constant from SPD/SI.
T_{st}	lbf	Static tension developed in the tread.

Table 75: Predicted tension in the left tread and the values used to calculate it.

Input Variable	Value
DF	4 lbf
t	9.0625 in.
L	34 in.
Y	27 lbf
Output Variable	Value
T_{st}	51.6 lbf

Table 76: Predicted tension in the right tread and the values used to calculate it.

Input Variable	Value
DF	4 lbf
t	9.125 in.
L	34 in.
Y	27 lbf
Output Variable	Value
T_{st}	58.91 lbf

Table 77: A comparison between the measured and desired tread tension values.

	Measured Value	Desired Value	% Difference
Right	58.9 lbf	46.3 lbf	27 %
Left	51.6 lbf	46.3 lbf	11 %

4.2.3.3 Discussion

The belt tension testing provided several important insights into not only the tension developed in the treads when installed on the vehicle, but also how belt tension effects the performance of the tread and the vehicle as a whole. The measured belt tension in both treads was higher than the minimum desired value calculated in Appendix A. This validates the design of the tensioning system. It also demonstrates that the losses in the wheel system are minimal if the treads are tensioned above the minimum desired belt tension. Because the tensioning system could not be raised further higher belt tensions and their effects on the vehicles performance could not be tested.

The testing procedure also gave insight into improvements which would be made to future iterations of the design. While the treads were tensioned to the minimum recommended belt tension, the span on which the manifolds rested was relatively loose and several instances of the treads slumping away from the manifolds when the vehicle was lifted were noted. Additionally, the fact that the span deflected as much as it did could likely have contributed to the reduction in the vacuum pressure in the manifolds. The test procedure used in calculating the belt tension seems to indicate that span length and belt tension directly affect the

amount the treads can deflect. By reducing the effective span length around the manifolds in future designs and increasing the belt tension, the amount of deflection in the tread can be reduced.

4.3 Vehicle Operation Observations

This section gives an overview of performance of the vehicle as a whole and of the observations that were made during process of making vehicle operational which are salient to future iterations of the project. It also gives an overview of the different changes which were made to the vehicle as the operational testing was conducted. Videos of the vehicle operating can be found in the attached files that accompany this report.

4.3.1 Initial Vertical Vehicle Adhesion and Testing

4.3.1.1 Creating the Manifold-Tread Seal

The first step taken to get the vehicle operation was to statically adhere the vehicle to a vertical surface. This was initially impossible as the low friction fabric on the treads was ridged which prevented the manifolds from sealing to the treads. To solve this issue, Dow Corning high-vacuum grease was purchased. The grease had very low volatility and would be stable when subjected to the vacuum. The purpose of the grease was to fill in the gaps in the low friction fabric and to help further reduce the friction between the treads and the manifolds. The grease was liberally applied to fabric and the manifolds were able to form a seal with treads. Figure 120 shows an image of one of the treads being adhered to wall with the manifolds.

Figure 120: A tread being adhered to the wall with a manifold.

4.3.1.2 Vehicle Static Adhesion

Once the manifold-tread seal was successfully created and both treads had been coated by the vacuum grease, the vehicle was fully assembled. The vehicle was then placed on a horizontal surface and the vacuum system was turned on and the vehicle was adhered to the surface. This was done to ensure that the assembly process had not adversely affected the vacuum system. Once it had been confirmed that the vehicle adhered to the horizontal surface, it was moved on to a vertical surface. Figure 121 shows the vehicle when it had been adhered to a vertical surface successfully.
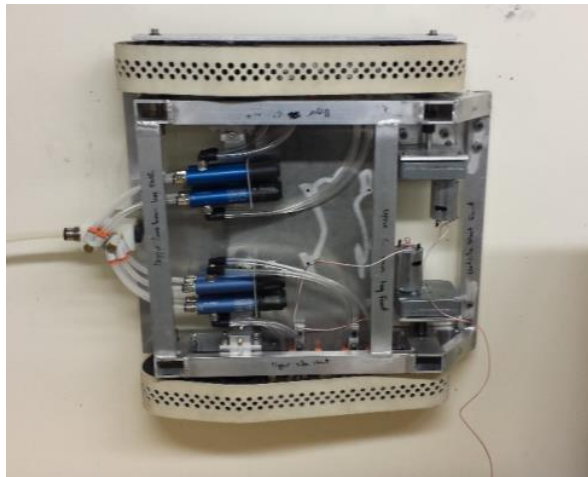
Figure 121: The vehicle being adhered to a vertical surface.

To determine if the vertical adhesion was repeatable the vehicle was removed and replaced on the vertical surface several different times. While the vehicle adhered to the wall successfully most of the time, it was noted that the process of removing the vehicle from the wall caused the manifolds to shift which prevented re-adhesion until the manifold was re adjusted.

Initially, the manifold springs had relatively low spring force, about four pounds at maximum compression, and it was found that they did not provide enough force to push the manifolds back into place. An attempt at fixing the manifolds completely, i.e. holding them in place by using a nut on either side of the support strut, was attempted, but was found to only exacerbate the problem. Stiffer springs which could provide much higher forces, approximately eleven pounds, were purchased and installed. These springs proved to be sufficient, and the adhesion and re-adhesion of the vehicle became much more reliable.

4.3.2 Powered Testing

4.3.2.1 Horizontal Surface Testing

Before the vehicle was placed on the wall and driven under its own power, some horizontal operational testing was performed. This was done by setting the vehicle onto a flat horizontal surface and powering the motors. This was done with the vacuum system engaged and disengaged. The main purpose for this step was to determine if the vehicle would drive in a straight line without using the controller. This testing was successful and so the vertical surface powered testing began.

4.3.2.2 Initial Vertical Surface Testing

The initial vertical powered testing did not go well. Immediately after the motors were powered one of the vehicles treads would slip and the vehicle would begin to fall. Although both treads slipped, the right side slipped much more often than the left. To correct this problem, or to at least diagnosis its cause, several different adjustments to the vehicle were made. For instance, the vehicle was placed sideways on the wall so that its travel path was parallel with the ground rather than perpendicular to it. The manifold suspension system was both loosened and tightened in an attempt to ensure that the manifolds remained in contact with the treads. Finally, large amounts of the vacuum grease were added to the treads as it was noticed that the treads were becoming degreased as the vehicle operated. None of these attempts were successful and seemed to make little to no difference in the vehicles performance.

It was also noted that after the vehicle was run, it became very difficult to re-adhere it to the wall. The cause of this seemed to be the loss of the grease on the tread when the vehicle was run. This loss of grease was caused by two distinct phenomena. The first of these phenomena was the buildup of grease in the vacuum chambers of the manifolds. Figure 122 shows the inside of one of the manifolds after this problem was identified. The second phenomena was the grease being squeezed into the treads hole as the tread passed around the wheels. Interestingly, this did not cause a blockage of the tread holes as the grease remained on the wheels as seen in Figure 123. Channels were cut in the drive and idler wheels to prevent the grease from being squeezed and while this did improve the grease distribution on the tread, it did not solve the vehicles inability to maintain suction after repeated runs.
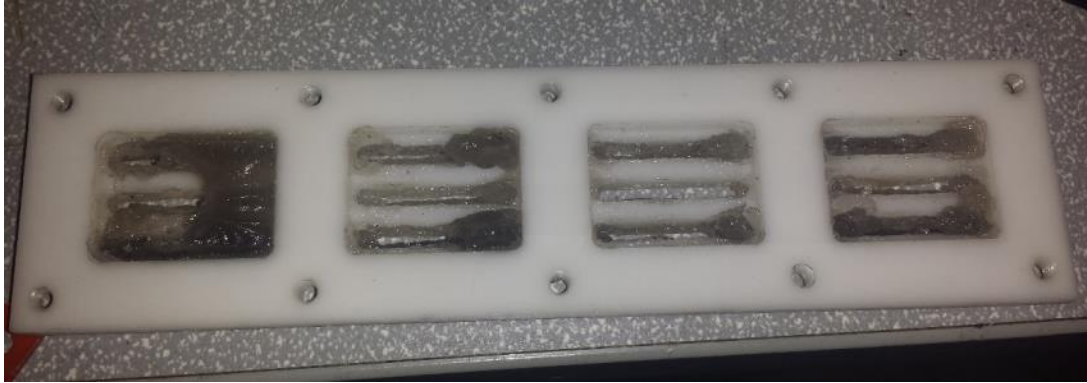
Figure 122: Interior of a manifold after it had become clogged.

Figure 123: Grease spikes which were squeezed into the tread holes during operation.

4.3.2.3 Final Vertical Surface Testing

Because the treads were losing grease and therefore suction, a more permanent solution was sought out to

create the seal between the manifolds and the treads. Ultimately, silicone sealant gel was chosen as the

coating for the inside of the treads as it was readily available and easy to work with. The treads were

cleaned and degreased and the silicone gel was applied to the low friction fabric and allowed to dry. Figure

124 shows the tread after the silicone sealant was applied and allowed to dry. A small amount of grease

was then reapplied to the inside of the treads as the friction between the manifolds and the silicone gel was

relatively high. The vehicle was then reassembled and tested.

Figure 124: Low friction fabric after the silicone sealant had been applied.

The slipping problem seen in the earlier testing was still occurring, but the vehicle was able to travel further than it had during the grease only testing. While the grease only testing failed immediately upon motor startup, the vehicle was able to travel approximately six inches to a foot before slipping occurred. It should also be noted that the adhesion of the vehicle became much more reliable after the silicone was applied as the silicone remained intact and in place as the vehicle operated.

Because the silicone sealant had worked well for the inside of the treads, the outer surface of the tread, which was surprisingly slick, was coated in the sealant. This was done to increase the coefficient of friction between the tread and the wall. The sealant was applied in a thin coat and allowed to dry. The application of sealant to the outer portion of the tread had a marginal effect on the performance of the vehicle, though it still slipped after a short distance.

Up until this point in the attempts to get the vehicle fully operational, the current and voltage supplied to the motors was the maximum allowable values. This meant that the vehicle was accelerated very quickly which could have caused shifting in the frame and the release of the manifolds. To test this theory the voltage supplied to the motors was halved and the maximum current limit on the power supply was lowered slightly. This would prove to be the final operation test that was performed on the vehicle because during the test the drive shafts on both sides of the vehicle stripped the interior of their drive wheels, meaning the drive shafts spun but the wheels did not. This meant that the vehicle was no longer capable of climbing and so operational testing had to be ended.

Chapter 5: Recommendations for Future Work and Conclusion

5.1 Recommendations for Future Work

There are several improvements which can be made to improve the design of this wall climbing robot. This section presents and discusses these improvements.

5.1.1 Tread

There are several modifications which can be made to the tread to improve vehicle performance. The most significant of these is simply to leave the bottoms of the manifold channels as rubber. This would ensure that the interface between the manifold and the tread has a consistent seal which will not degrade over time. Small amounts of the vacuum grease can be applied to the tread to reduce the friction between the manifolds and the tread, but a low-friction, dry interface is preferred.

The next modification would be the use of super high friction and highly compliant material as the backing of the tread. This would help to compensate for any losses in manifold pressure by increasing the coefficient of friction between the tread and the wall. The greater compliance would also allow the vehicle to operate on rougher surfaces. Natural rubber might be a good option for this material, but testing should be done to identify an ideal material.

5.1.2 Wheel System

A suspension system should be added to the wheel system. This would allow the wheels to push flat against the wall and help to compensate for the moment that the vehicle creates as it sits on the wall. This would also help prevent the vehicle from peeling off the wall when it is accelerated.

To prevent the drive wheels from being stripped by the drive shafts over time, the drive wheels should be constructed from aluminum and the shafts should be splined or keyed to assure torque transfer. This would also allow for the wheels to be easily removed from the vehicle if modifications were needed. While this would increase the price of the wheels significantly, it would also increase long term vehicle reliability.

5.1.3 Manifold

The manifolds should be constructed from aluminum because the delrin used in this project, while easy to machine, was prone to warping after machining was complete. Having the manifolds constructed from aluminum would also help to ensure that the manifold suspension system did not strip the manifold threads over time.

The manifold should consist of physically independent floating sections, which have their own suspension system. This suspension system should allow the manifolds to shift with the tread, but should keep them in constant contact. This would help to eliminate the interactions between sections that were observed during this project.

The manifold should also extend over a larger section of the tread. This serves two purposes, it will help to reduce the effect that changes at one end of the vehicle have on the manifold sections at the back and will allow for greater vacuum forces to be generated.

5.1.4 Vacuum Systems

The vacuum system for the project performed well overall, so only minor modifications to the system need to be considered. If smaller venturis could be found then the weight contribution and foot print of the vacuum system in the vehicle could be reduced. An active or passive control system should also be considered for the vacuum system which would allow the vacuum force to be varied as the vehicle moves.

5.1.5 Frame System

The frame should be made generally smaller and lighter. It should also be very low profile relative to the wall to help reduce the distance between the vehicles center of mass and the wall. This would reduce the peel off force produced by the vehicle's center of mass. The frame should also be optimized for the expected loading to reduce its weight without sacrificing frame stiffness.

5.1.6 Motor System

The motors for future projects should be smaller both physically and dimensionally. This would help to reduce the overall weight of the vehicle and reduce the vehicles overall size. The selected motors should

also include encoders to eliminate the need for an external motor speed tracking system. It would also be good to select several motors of similar dimensions, but different maximum torque ratings so that once the vehicle has been built and tested, its motor system can be optimized.

5.1.7 Tensioner System

The third wheel tensioner system should be abandoned. While this system worked, it prevented the manifold from extending further along the tread and increased the height of the frame. It also did not allow for high tread tension values to be attained and prevented the effect that belt tension had on the systems performance from being determined. As an alternative to the third wheel tensioner system, the idler wheel could double as the tensioner.

5.1.8 General Vehicle Improvements

The weight and size of future vehicles should be reduced as much as possible. This would make testing the vehicle much easier and would reduce the risk of injury if the vehicle losses adhesion. Components that are critical to the design of the future project should be professionally machined. This would serve a dual purpose: it would allow for much tighter tolerances to be specified for the vehicles design: and would help to eliminate the misalignments seen in this project.

In addition to reducing the weight of the vehicle, its center of gravity should also be moved closer to the wall to reduce the moment it creates on the vehicle. The center of gravitie's moment could also be compensated for through the addition of a tail to the vehicle. This tail would push on the wall and lift the vehicle rear end slightly, thereby preventing the front of the vehicle from rocking away from the wall. This tail would also help to eliminate any rocking that the vehicle would experience while it was accelerating. However, a fixed tail could make matters worse when traversing down the wall!

5.2 Conclusion

Despite the inability of the vehicle, as designed and manufactured in this project, to climb reliably for any great distance, a great deal of insight was gained into the vacuum tread concept. This information can be used to develop future embodiments of the design and more convincingly demonstrate the concepts viability. Ultimately, this project showed that the concept should be pursued further.

BIBLIOGRAPHY

[1]   G. La Rosa, M. Messina, G. Muscato and R. Sinatra, "A low-cost lightweight climbing robot for the inspection of vertical surfaces," *Mechatronics,* no. 12, pp. 71-96, 2002.

[2]   K. Berns, C. Hillenbrand and T. Luksch, "Climbing Robots for Commercial Applications – a Survey," University of Kaiserslautern, Kaiserslautern, Germany, 2011.

[3]   D. Schmidt and K. Berns, "Climbing robots for maintenance and inspections of vertical structures—A survey of design aspects and technologies," *Robotics and Autonomous Systems,* no. 61, pp. 1288-1305, 2013.

[4]   H. Kim, D. Kim and H. Yang, "A wall climbing robot with vacuum caterpillar wheel system operated by mechanical valve," in *Proceedings of the 9th International Conference on Climbing and Walking Robots*, Brussels, Belgium, 2006.

[5]   B. Hu, L. Wang, Y. Zhao and Z. Fu, "A miniature wall climbing robot with biomechanical suction cups," *Industrial Robot: An International Jounral,* vol. 36, no. 6, pp. 551-561, 2009.

[6]   S. Liu, X. Gao, K. Li, J. Li and X. Duan, "A Small-sized Wall-climbing Robot for Anti-terror Scout," in *IEEE International Conference on Robotics and Biomimetics*, Sanya, China, 2007.

[7]   T. Akinfiev, M. Armada and S. Nabulsi, "Climbing cleaning robot for vertical surfaces," *Industrial Robot: An International Journal,* vol. 36, no. 4, pp. 352-357, 2009.

[8]   A. Leibbrandt, G. Caprari, Angst and Ueli, "Climbing Robot for Corrosion Monitoring of Reinforced Concrete Structures," in *2nd International Conference on Applied Robotics for the Power Industry*, Zurich, Switzerland, 2012.

[9]   M. Taylor, X. Chen, M. Lang, T. McKee, J. Robertson and S. Aston, "TigBot - A Wall Climbing Robot for TIG Welding of Stainless Steel Tanks," in *15th International conference on*

Mechatronics and Machine Vision in Practice, Auckland,New-Zealand, 2008.

[10]   J. C. Grieco, M. Prieto, M. Armada and P. Gonzalez de Santos, "A SIX-LEGGED CLIMBING

ROBOT FOR HIGH PAYLOADS," in *1998 IEEE International Conference on Control*

Applications, Trieste, Italy, 1998.

[11]   D. Longo and G. Muscato, "The Alicia Climbing Robot," *IEEE Robotics & Automation Magazine,*

pp. 42-50, 2006.

[12]   H. X. Zhang, W. Wang and J. W. Zhang, "High Stiffness Pneumatic Actuating Scheme and

Improved Position Control Strategy Realization of a Pneumatic Climbing Robot," in *IEEE*

International Conference on Robotics and Biomimetics, Bangkok, Thailand, 2008.

[13]   F. XU, D. XIA and G. JIANG, "Initial Design and Analysis of a Helix Cable Detecting Robot," in

32nd Chinese Control Conference, Xi'an, China, 2013.

[14]   F. ROCHAT, P. SCHOENEICH, O. TRUONG-DAT NGUYEN and F. MONDADA,

"TRIPILLAR: MINIATURE MAGNETIC CATERPILLAR CLIMBING ROBOT WITH PLANE

TRANSITION ABILITY," Ecole polytechnique fédérale de Lausanne, Lausanne, Switzerland.

[15]   W. Shen, J. Gu and Y. Shen, "Permanent Magnetic System Design for the Wall-climbing Robot,"

in *IEEE International Conference on Mechatronics & Automation*, Niagara Falls, Canada, 2005.

[16]   M. Spenko, G. Haynes, J. Sanders, M. Cutkosky and A. Rizzi, "Biologically Inspired Climbing

with a Hexapedal Robot," *Journal of Field Robotics,* vol. 25, no. 4-5, pp. 223-242, 2008.

[17]   T. Lun Lam and Y. Xu, "Tree Climbing Robot - Design, Kinematics and Motion PLanning,"

Springer Tracts in Advanced Robotics, vol. 78, 2012.

[18]   G. L. K. Cui and J. Guo, "Design of a Climbing Robot Based on Electrically Controllable

Adhesion Technology," in *2012 International Conference on Solid State and Materials*, 2012.

[19]   "A gecko-inspired electroadhesive wall-climbing robot," *IEEE Potentials,* pp. 15-19, 2015.

[20]   Y. Yoshida and S. Ma, "Design of a Wall-Climbing Robot with Passive Suction Cups," in *IEEE International Conference on Robotics and Biomimetics*, Tianjin, China, 2010.

[21]   M. Guimaraes and J. Lindberg, "REMOTE CONTROLLED VEHICLE FOR INSPECTION OF VERTICAL CONCRETE STRUCTURES," *IEEE,* vol. 14, 2014.

[22]   A. Fallah, M. Rezasoltani and A. M. H. Riasi, "Numerical Analysis of a Non-Contact Surface Adhesion System based on Vortex Cup for Wall Climbing Robots," in *RSIIISM International Conference on Robotics and Mechatronics*, Tehran, Iran, 2013.

[23]   R. Budynas and K. Nisbett, Shigley's Mechanical Engineering Design, New York: McGraw-Hill, 2011.

[24]   NYU Tandon School of Engineering, "NYU Tandon School of Engineering," [Online]. Available: http://engineering.nyu.edu/gk12/Information/Vault_of_Labs/Physics_Labs/static%20and%20kineti c%20friction.doc.. [Accessed 26 May 2016].

[25]   SDP/SI, "SDP/SI Technical Section," [Online]. Available: http://www.sdp-si.com/D265/HTML/D265T050.html. [Accessed 27 5 2016].

[26]   Smalley Steel Ring Company, "Load Capacity," 2016. [Online]. Available: http://www.smalley.com/ring-design/load-capacity. [Accessed 27 5 2016].

Appendix A - **Simulations and Calculations**

A.1 Symbolic Calculation of Motor Torque

A.1.1 Calculation Description

The purpose of this calculation was to create a set of equations which could be used to calculate the required drive motor torque. Because the vehicle is symmetrical about its longitudinal axis, the torque of a single motor was calculated for half of the vehicle.

A.1.2 Assumptions

- Losses in the wheel system due to friction can be lumped at the drive wheel.

- The inertia of all the wheels can be lumped at the drive wheel.

- The Idler wheel does not support any dynamic load during forward motion.

- Tread is rigid along its longitudinal axis.

- Tread does not slip at the wall.

- Frame and Manifold move relative to Tread and Wall.

- Vehicle is symmetrical and the solution for the required motor torque can be found by looking at half of the vehicle.

A.1.3 Free Body and Mass Acceleration Diagrams
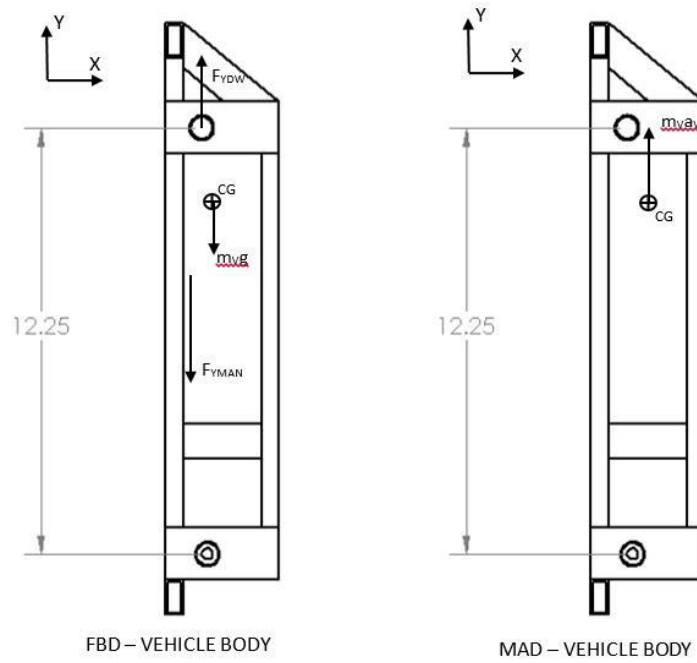
Figure 125: Free body and mass acceleration diagrams for the body of the vehicle.
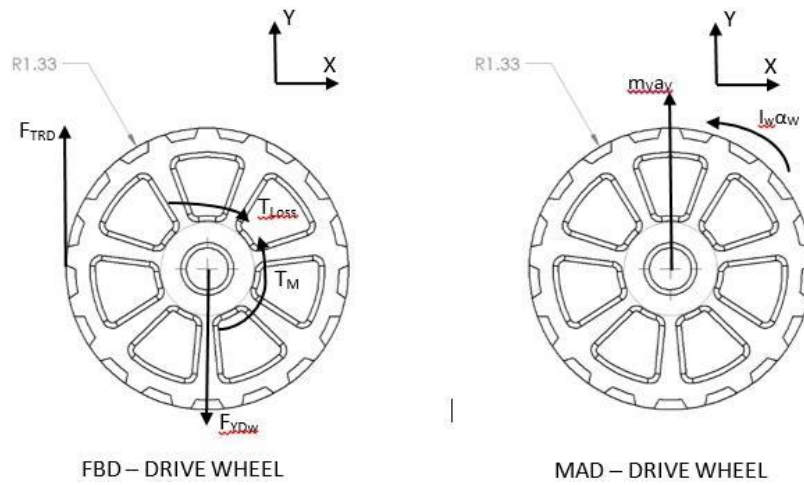
Figure 126: Free body and mass acceleration diagrams for the drive wheel.
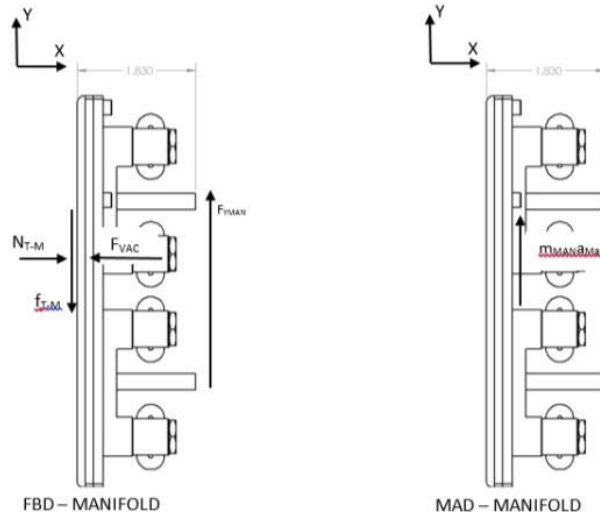
Figure 127: Free body and mass acceleration diagrams for the manifold.
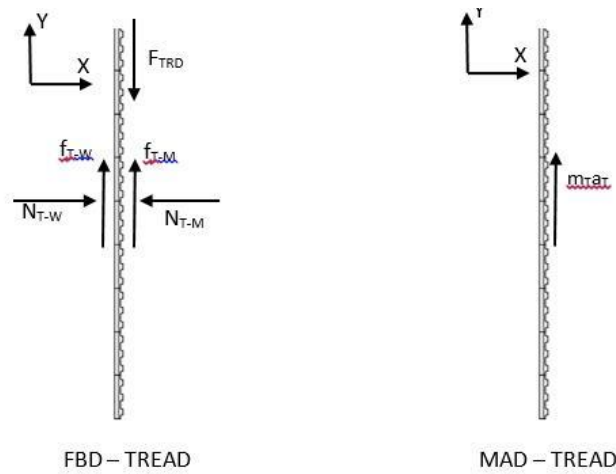
Figure 128: Free body and mass acceleration diagrams for the tread.

A.1.4 Variable Definitions

The variables used in the motor torque calculator can be found in Table 78.

Table 78: Variable symbols, units and descriptions for the symbolic motor torque calculator.

Symbol	Units	Description
m_V	SLUG	Mass of the Vehicle
F_{YDW}	LBF	Force in the Y Direction on the Drive Wheel
F_{VMAN}	LBF	Force Produced by Manifold on Main Vehicle
a_V	FT/S^2	Acceleration of the Vehicle
F_{TRD}	LBF	Force Between Drive Wheel and Tread
T_M	IN - LBF	Torque Produced by Motors
T_{Loss}	IN - LBF	Lumped Losses in the Rotation of the Wheels

146

I_W	LBM*IN^2	Lumped Rotational Inertia of The Wheels and Shafts
α_W	RAD/S^2	Angular Acceleration of Drive Wheel
R_{DW}	IN	Radius of Drive Wheel.
N_{T-W}	LBF	Normal Force Between the Tread and the Wall
f_{T-W}	LBF	Friction Force Between tread and Wall
μ_{T-W}	UNITLESS	Static Coefficient of Friction between Tread and Wall
N_{T-M}	LBF	Normal Force between the Tread and the Manifold
f_{T-M}	LBF	Friction Force between Tread and Manifold
μ_{T-M}	UNITLESS	Static Coefficient of Friction between Tread and Manifold
F_{VAC}	LBF	Vacuum Force Produced by Manifold
m_t	SLUG	Mass of the Tread
a_T	FT/S^2	Acceleration of Tread. Assumed equal to Zero.
m_{Man}	SLUG	Mass of Manifold. Assume accounted for in m_v.
a_{Man}	FT/S^2	Acceleration of Manifold. Assumed Equal to a_V.

A.1.5 Symbolic Manipulation

Begin by summing forces and accelerations for the vehicle body, given in Equation A.1.1 and solving for

F_{YDW} which yields Equation A.1.2.

$$F_{YDW} - m_V g - F_{VMAN} = m_V a_V \tag{A.1.1}$$

$$F_{YDW} = m_V g + F_{VMAN} + m_V a_V \tag{A.1.2}$$

Next, sum forces on the drive wheel, yielding Equation A.1.3. Also, sum moment about the center of the

drive wheel to get Equation A.1.4.

$$F_{TRD} - F_{YDW} = m_V a_V \tag{A.1.3}$$

$$T_M - T_{Loss} - R_{DW} F_{TRD} = I_W \alpha_W \tag{A.1.4}$$

Use the relationship between angular acceleration and linear acceleration to find α_W in terms of a_V as seen

in Equation A.1.5. Solve for F_{TRD} in Equation A.1.4 to yield Equation A.1.6.

$$\alpha_W = \frac{a_V}{R_{DW}} \tag{A.1.5}$$

$$F_{TRD} = \frac{T_M}{R_{DW}} - \frac{T_{Loss}}{R_{DW}} - \frac{I_W \alpha_W}{R_{DW}} \tag{A.1.6}$$

Substitute Equation A.1.5 and Equation A.1.6 into Equation A.1.3 and manipulate to solve for T_M to yield

Equation A.1.7.

$$T_M = T_{Loss} + \frac{I_W a_V}{R_{DW}} + R_{DW} F_{YDW} + R_{DW} m_V a_V \qquad \text{(A.1.7)}$$

Sum forces in the x-direction on the manifold to relate F_{VAC} and N_{T-M} in Equation A.1.8. Sum forces in the

y-direction to find Equation A.1.9 and substitute in the relationship between normal force and frictional

force to find Equation A.1.10.

$$N_{T-M} = F_{VAC} \qquad \text{(A.1.8)}$$

$$F_{VMAN} = f_{T-M} \qquad \text{(A.1.9)}$$

$$F_{VMAN} = \mu_{T-M} F_{VAC} \qquad \text{(A.1.10)}$$

Sum forces on the x-direction on the tread to yield Equation A.1.11. The friction between the wall and the

tread must be greater than both the friction between the manifold and the tread and the weight of the

vehicle, this is expressed in Equation A.1.12 and Equation A.1.13 respectively.

$$N_{T-M} = N_{T-W} \qquad \text{(A.1.11)}$$

$$f_{T-W} > f_{T-M} \qquad \text{(A.1.12)}$$

$$f_{T-W} > m_V g \qquad \text{(A.1.13)}$$

Solve for T_M by substituting Equation A.1.2 and Equation A.1.10 into Equation A.1.7 to find Equation

A.1.14. Simplify to find Equation A.1.15.

$$T_M = T_{Loss} + \frac{I_W a_V}{R_{DW}} + R_{DW}(m_V g + \mu_{T-M} F_{VAC} + m_V a_V) + R_{DW} m_V a_V \qquad \text{(A.1.14)}$$

$$T_M = T_{Loss} + R_{DW} m_V g + R_{DW} \mu_{T-M} F_{VAC} + \left(\frac{I_W}{R_{DW}} + 2 R_{DW} m_V\right) a_V \qquad \text{(A.1.15)}$$

Example of Use

This example represents the final settings used in the calculator to determine the motor torque required for

the project. Table 79 contains the variable values used in the calculator. Table 80 contains the results of the

calculation.

Table 79: Final input variables used in the motor torque calculator.

Variable	Value
m_V	.25 slugs (8 lbs)
a_V	.25 ft/s^2
T_{Loss}	5 in-lbf
I_W	.0421 slug-in^2
R_{DW}	1.33 in

μ_{T-W}	1
μ_{T-M}	.5
F_{VAC}	16 lbf

Table 80: Final outputs from the motor torque calculator.

Solution	Value
T_M	26.77 in-lbf
α_W	2.26 Rad/s^2
F_{YDW}	16.1 lbf
f_{T-W}	16 lbf
f_{T-M}	8 lbf

A.2 Motor RPM Requirement

Calculation Description

This calculation determines the vehicles linear velocity based on a given motor output shaft angular velocity. This is simply the calculation to solve for the linear velocity of a rolling wheel based on the wheels angular velocity which is expressed in Equation A.2.1.

A.2.1 Variables

The variables used in the motor RPM requirements calculation can be found in Table 81.

Table 81: Variable symbols, units and descriptions for the motor RPM requirement calculation.

Symbol	Units	Description
R_{DW}	in.	The radius of the drive wheel.
t_{TRD}	In.	Thickness of the tread.
ω_M	RPM	Motor output shaft angular velocity
v_V	in/s	Vehicle velocity

A.2.2 Equation

$$v_V = (.105\frac{rad * min}{rev * s})R_{DW}\omega_M \qquad (A.2.1)$$

A.2.3 Example

This example uses the angular velocities of the two motors which were considered for the project. Two different drive wheel radiuses were used as well of sizes similar to the estimated drive wheel radius. Table 82 contains the results of this calculation.

Table 82: Results of the motor RPM requirements calculation for different motor and wheel combinations.

Scenario	R_{DW}	ω_M	v_V
17 Tooth Wheel – Molon Motor	1.33 in.	25 RPM	3.5 in/s
17 Tooth Wheel – Maxon Motor	1.33 in.	50 RPM	7.0 in/s
18 Tooth Wheel – Molon Motor	1.43 in.	25 RPM	3.8 in/s
18 Tooth Wheel – Maxon Motor	1.43 in.	50 RPM	7.5 in/s

A.3 Evacuation Rate Calculation

A.3.1 Calculation Description

This calculation was used to determine the time it would take the venturis to evacuate the volume of vacuum system they were attached to. To begin, the volume of the different portions of the vacuum system are estimated and add to get an estimate of the total volume being evacuated. This value is then used in conjunction with the evacuation rates of the different venturis to determine the time it takes to achieve full evacuation.

A.3.2 Volume Estimation

There are four major volume sources that the venturi must evacuate. These are the manifold chamber, the tubing connecting the manifold and the venturi, and the volume of the tread perforations. Equation A.3.1 gives the combined volume calculations based on estimated tube lengths and tread thickness. Table 83 gives an explanation of the different variables found in Equation A.3.1.

$$(l_{cham} * w_{cham} * d_{cham}) + (l_{tube} * (\pi * d_{itube}{}^2)) + \left(\frac{A_{Vac}}{8} * t_{tread}\right) = V_{total} \qquad \text{(A.3.1)}$$

Table 83: Variable symbols, units and descriptions for the evacuation rate calculation.

Symbol	Value	Description
l_{cham}	1 in	Length of a single manifold chamber
w_{cham}	0.75 in	Width of a single manifold chamber
d_{cham}	.1875 in	Depth of a single manifold chamber
l_{tube}	12 in	Estimated length of tube between manifold and venturi
d_{itube}	.2 in	Inner diameter of tubing
A_{Vac}	2.4 in^2	Total wall area exposed to vacuum
t_{tread}	.2 in	Estimated tread thickness
V_{total}	9.4 x 10^{-4} ft^3	Total area evacuated by a single venturi

A.3.3 Evacuation Time

Using the results from Equation A.3.1, the time to evacuate the estimated volume can found using the time to evacuate a cubic foot given by Vaccon. Equation A.3.2 is simply the rate given by Vaccon, $Rate_{Evac}$, multiplied by the estimated volume being evacuated, V_{total}. Table 84 gives evacuation times for each of the venturis considered for the project.

$$V_{total} * Rate_{Evac} = t_{evac} \qquad \text{(A.3.2)}$$

Table 84: The evacuation rate and time to evacuate for each of the venturi models considered for the project.

Venturi Model	Evacuation Rate	Time to Evacuation
JS-60M	28.24 s/ft^3	.027 s
JS-90M	10.05 s/ft^3	.009 s
JS-100M	8.99 s/ft^3	.008 s
JS-150M	4.46 s/ft^3	.004 s

A.4 Minimum Belt Tension Requirement Calculation

A.4.1 Calculation Description

This calculation is used to determine the minimum tension which must be developed in treads for the

vehicle to function properly. This was done by using a timing belt design guide produced by SDP/SI [25].

A.4.2 Equation

Equation A.4.1 was found in the SDP/SI design guide [25]. It solves for the minimum static belt tension per

span required for maximum belt life and smooth belt operation. Table 85 contains a definition for each of

the variables in Equation A.4.1.

$$T_{st} = \frac{.821 * DQ}{d} + m * (\frac{d * DR}{3820})^2 \qquad (A.4.1)$$

Table 85: Variable symbols, units and descriptions for the minimum belt tension requirement calculation.

Symbol	Units	Description
T_{st}	lbf	Static Tension per Span
DQ	in-lbf	Driver Design Torque
d	in.	Driver Pitch Diameter
DR	RPM	Driver Angular Velocity
m	Unit Less	Belt Mass Factor

A.4.3 Calculating Mass Factor

SDP/SI's design guide does not contain the mass factor for the H-type belt. To estimate it, two families of

belt which SDP/SI did provide data for were analyzed. The belts within these families shared basic tooth

geometries with each other. The two families were the GT2 type belts which had rounded teeth and the XL

family which has trapezoidal teeth. The H-Type belts fall within the XL family. The following method was

used to estimate the mass factor of the tread.

First, the linearity of the mass factor vs belt width was established by plotting the given mass factor vs belt

width data for several different types of belts. Table 86 contains the data provided by SDP/SI for two

different families of belts. The data for each family was plotted and shown to be linear as seen in Figure

129 and Figure 130.

Table 86: Belt family data from SDP/SI.

Belt Type	Belt Width	m	Pitch Length
2mm GT2	4 mm	0.026	2 mm
	6 mm	0.039	2 mm
	9 mm	0.058	2 mm
	12 mm	0.077	2 mm
3mm GT2	6 mm	0.077	3 mm
	9 mm	0.120	3 mm
	12 mm	0.150	3 mm
	15 mm	0.190	3 mm
5mm GT2	9 mm	0.170	5 mm
	15 mm	0.280	5 mm
	20 mm	0.380	5 mm
	25 mm	0.470	5 mm
MXL	.125 in.	0.003	0.08 in.
	.1875 in.	0.004	0.08 in.
	.25 in.	0.005	0.08 in.
XL	.25 in	0.010	0.2 in
	.375 in.	0.015	0.2 in
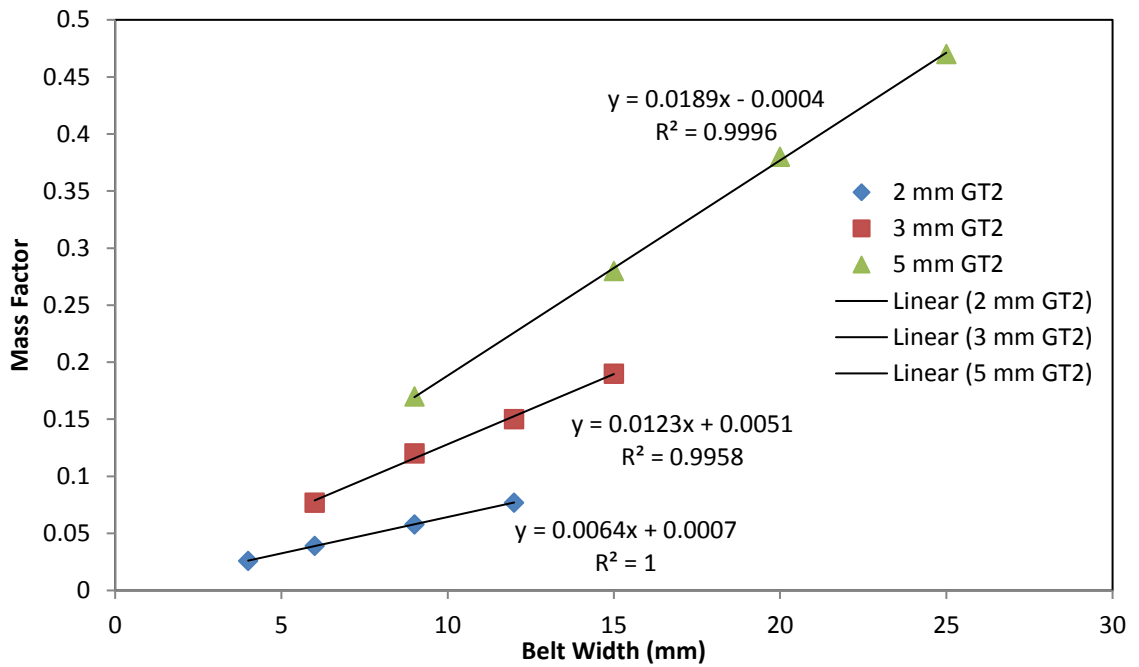
Figure 129: Mass factor versus belt width for the GT2 belt family.
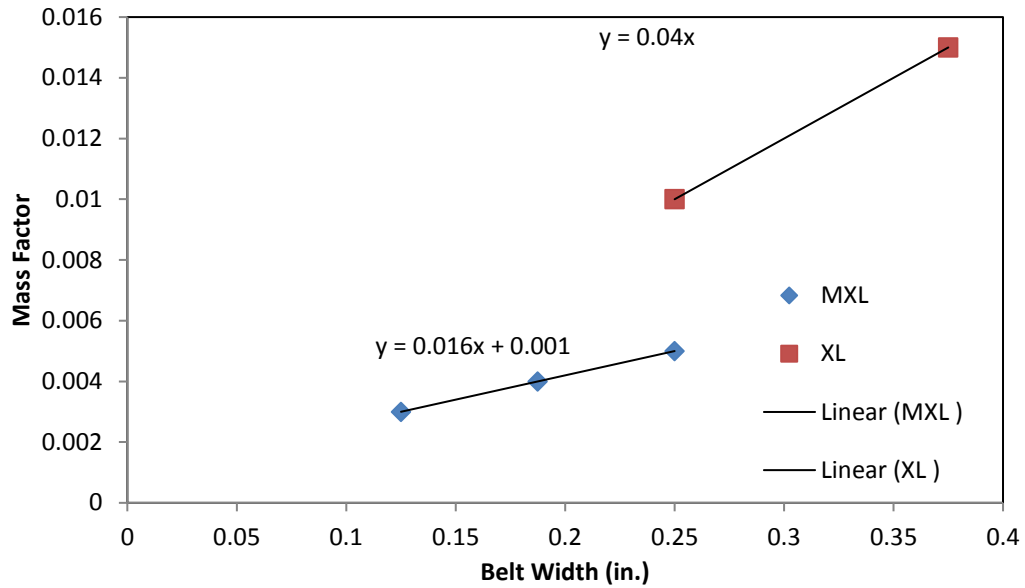
Figure 130: Mass Factor versus belt width for the trapezoidal tooth family.

The next step was to determine if there was a linear relationship between the pitch of the belts in each

family and the ratio of mass factor vs belt width. To do this, the slopes from the GT2 family were plotted

against their respective pitch lengths and this plot can be seen in Figure 131. The relationship was not

perfectly linear, but was close enough that an estimate of the mass factor the tread could be found.
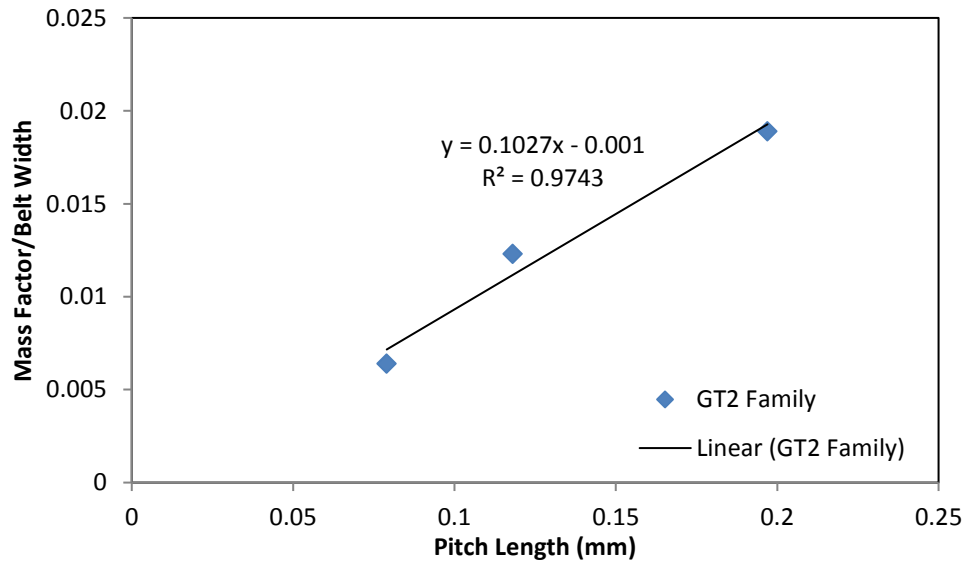
Figure 131: Mass factor per belt width versus pitch length for the GT2 belt family.

By plotting the trapezoidal family relationship of pitch length to the ratio of mass factor to belt width an

equation can be found which will solve for the ratio of mass factor to belt width for the H-type belt. This

ratio can then be multiplied by the width of the belt to get the mass factor estimate for the tread. Figure 132 shows the plot and equation generated from relationship of pitch length to the ratio of mass factor to belt width. Table 87 gives the mass factor to belt width ratio for the H-Type belt, as well as the mass factor for the tread.
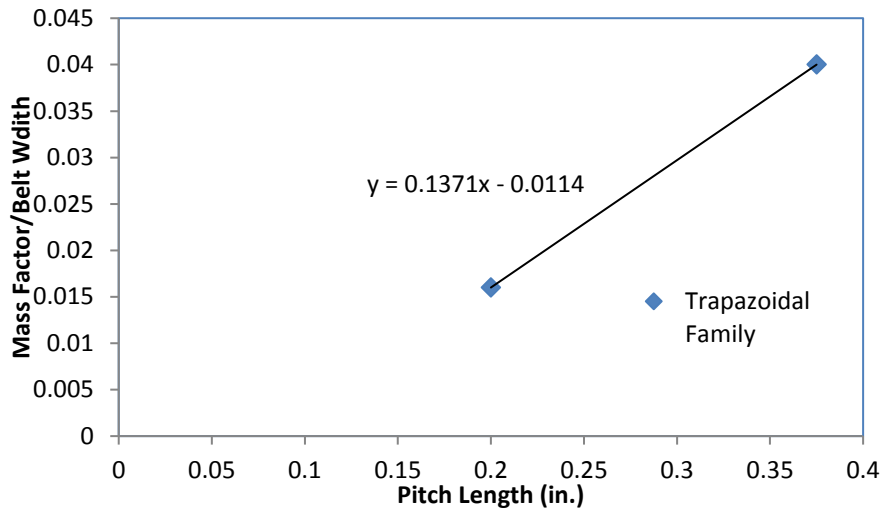
Figure 132: Mass factor per belt width versus pitch length for the trapezoidal tooth belt family.

Table 87: The estimated mass factor per belt width and estimated mass factor for the H-Type belt used for the tread.

Parameter	Value
Mass Factor to Belt Width Ratio	0.057
Estimated Mass Factor for H-Type Belt	0.12

Solving for Minimum Tread Static Tension

With an estimate for the mass factor, the minimum belt tension for single span can be solved. Table 88 contains the values input into Equation A.4.1 and the resulting tension per span and the total tension for all three spans.

Table 88: The input variables used to estimate the minimum belt tension required and the results of the calculation.

Input Variable	Value
DQ	50 in-lbf
d	2.66 in.
DR	25 RPM
m	0.12
Output Variable	**Value**
T_{st}	17.43 lbf
$3 * T_{st}$	46.3 lbf

156

A.5 Tread Factor of Safety Estimation

A.5.1 Calculation Description

This calculation was used to estimate the maximum tension force that the tread could be subjected to before

failure. The results were then compared to the desired belt tension and a factor of safety was found.

A.5.2 Solution

Table 89 contains the variables used to calculate the maximum allowable tread tension. It was assumed that

the steel cables imbedded in the tread would carry all of the tension loading and that tread failure occurred

only when the cables failed

Table 89: Variables and their values used to calculate the maximum allowable tread tension.

Symbol	Value	Description
Y_S	36,000 psi	Yield Strength of Steel
D_C	0.0625 In.	Cable Diameter
N_C	8	Number of cables in the tread

Equation A.5.1 solves for the maximum tread tension allowable.

$$T_{max} = Y_S * N_C * \frac{\pi}{4} * D_C \tag{A.5.1}$$

Table 90 gives the maximum tread tension, the desired tread tension and the factor of safety of the tread.

Table 90: Results of the tread factor of safety calculation.

Max Allowable Tension	Desired Tension	Factor of Safety
883 lbf	55 lbf	16

A.6 Total Tread Perforation Area Calculation

A.6.1 Calculation Description

This calculation was used to determine the total area of tread perforation required to generate the force required to hold the vehicle on the wall given a maximum vacuum pressure obtainable from the venturis selected. The force value used in this calculation was found in vacuum force requirements calculation.

A.6.2 Solution

Equation A.6.1 is simply the relationship between pressure and force solved for the area. Equation A.6.2 gives the numerical solution to the problem.

$$\frac{F_{VAC}}{P_{Ven}} = A_{Perf} \tag{A.6.1}$$

$$\frac{33\ lbf}{13.75\ \frac{lbf}{in^2}} = 2.4\ in^2 \tag{A.6.2}$$

A.7 Vacuum Force Requirements

A.7.1 Calculation Description

This calculation was used to determine the force which would be required to hold the vehicle to a vertical wall and the ceiling. This was done using the maximum desired system mass plus the desired payload mass and by estimating the friction coefficient between the wall and the tread.

A.7.2 Equations and Variables

Equation A.7.1 gives the minimum vacuum force which prevents slipping with a desired factor of safety. Equation A.7.2 gives the minimum vacuum force which will hold the vehicle to the ceiling with a desired factor of safety.

Table 91 contains a list of the variables used in Equation A.7.1 and Equation A.7.2.

$$\frac{w_V FS_{wall}}{\mu_{T-W}} = F_{wall} \tag{A.7.1}$$

$$FS_{ceil} w_V = F_{ceil} \tag{A.7.2}$$

Table 91: Variable symbols, units and descriptions for the vacuum force requirements calculation.

Symbol	Units	Description
w_V	lbf	Weight of the vehicle plus payload
μ_{T-W}	Unit less	Estimated coefficient of friction between the tread and the wall.
FS_{wall}	Unit less	Wall Factor of Safety
FS_{ceil}	Unit less	Ceiling Factor of Safety
F_{wall}	lbf	Required vacuum force on wall
F_{ceil}	lbf	Required vacuum force on ceiling

A.7.3 Solution

The input variables and the results of the vacuum force requirements can be found in Table 92.

Table 92: Input values for the vacuum force requirements calculation and the results.

Input Variable	Value
w_V	16.5 lbf
μ_{T-W} [24]	1
FS_{wall}	2
FS_{ceil}	2
Output Variable	**Value**
F_{wall}	33 lbf
F_{ceil}	33 lbf

A.8 Final Tread Hole Pattern and Manifold Slot Length Calculation

A.8.1 Calculation Description

This calculation was used to determine if the tread hole pattern and manifold slot length chosen would provide sufficient wall area exposed to vacuum as the manifold moved along the tread. This was done by determining the number of tread holes which were exposed to vacuum for any given manifold position along the tread. This calculation only determines the wall area exposed for a single tread and the results of the calculation can simply be multiplied by two to obtain the total are for both treads.

A.8.2 Process

The process used to determine the number of tread holes exposed to each vacuum section of the manifold was relatively straight forward. An assembly was created in Solidworks which contained a length of tread and the lower half of the manifold. The manifold was positioned at the edge of the tread, as seen in Figure 133, using a distance mate. The number of holes exposed to each vacuum section of the manifold was then counted by looking at the bottom of the tread. The manifold was then incremented along the tread fifty thousandths of an inch and the process was repeated for a total displacement of one and a half inches. Figure 134 shows the tread holes which were exposed in the zero position and the Figure 135 shows the tread holes exposed after the manifold had been moved a tenth of an inch along the tread.
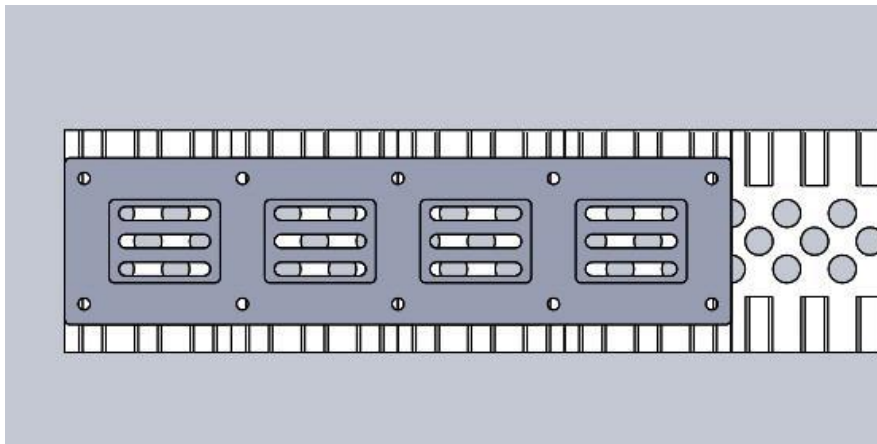
Figure 133: A top view of the model used to determine the tread hole engagement.
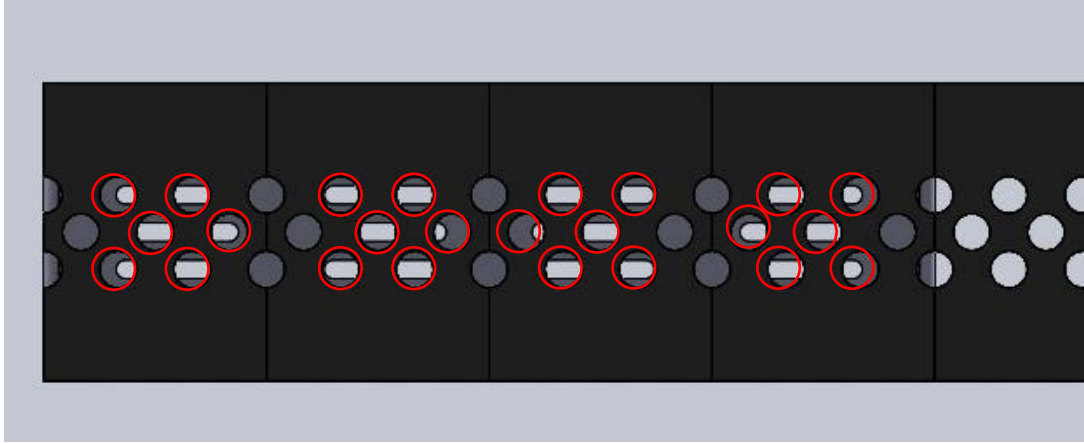
Figure 134: Tread holes engaged with the manifold sections with the manifold at zero displacement.
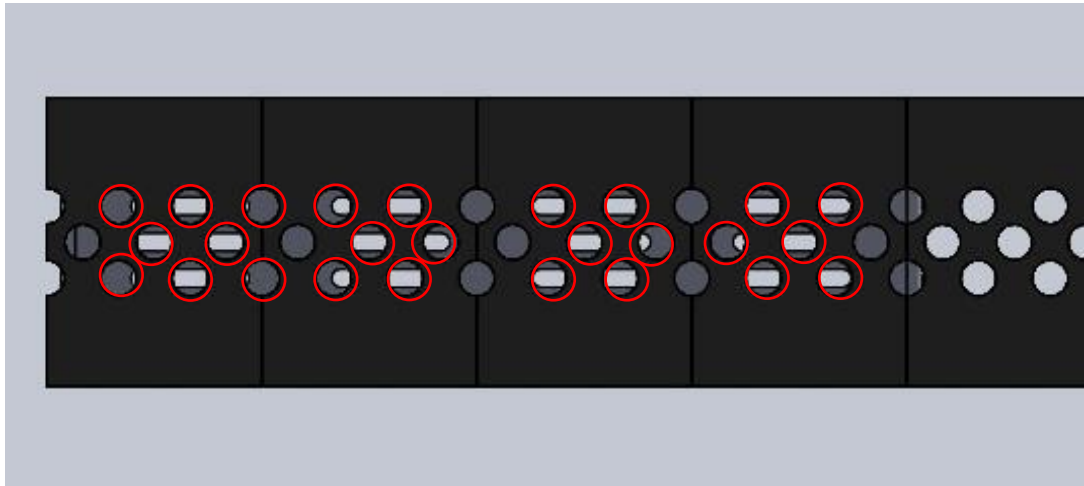
Figure 135: Tread holes engaged with the manifold sections with the manifold at a tenth of an inch of displacement.

A.8.3 Results

Two different conditions were placed on what would be considered engagement of a tread hole. These were the any engagement condition and the major engagement condition. The any engagement condition considered any tread hole exposed to be fully engaged. Table 93 contains the tabulated results of the any engagement condition interpretation of the data collected. The major engagement condition would only consider a tread hole engaged if the hole was exposed over approximately a quarter of its diameter. Figure 136 shows the hole exposure which was and was not considered in the major engagement condition. Table 94 contains the tabulated results of the major engagement condition interpretation of the data collected.

Figure 136: (Left) A hole which would be disregarded in the major engagement condition. (Right) A hole which would be considered engaged for the major engagement condition.

Table 93: Data for the any engagement condition.

Displacement (in.)	First Section	Second Section	Third Section	Fourth Section	Total Engaged
0	6	6	6	6	24
0.05	6	6	7	6	25
0.1	8	6	6	6	26
0.15	6	6	6	7	25
0.2	6	8	6	6	26
0.25	6	6	6	6	24
0.3	6	6	8	6	26
0.35	7	6	6	6	25
0.4	6	6	6	8	26
0.45	6	7	6	6	25
0.5	6	6	6	6	24
0.55	6	6	7	6	25
0.6	8	6	6	6	26
0.65	6	6	6	7	25
0.7	6	8	6	6	26
0.75	6	6	6	6	24
0.8	6	6	8	6	26
0.85	7	6	6	6	25
0.9	6	6	6	8	26
0.95	6	7	6	6	25
1	6	6	6	6	24
1.05	6	6	7	6	25
1.1	8	6	6	6	26
1.15	6	6	6	7	25
1.2	6	8	6	6	26
1.25	6	6	6	6	24
1.3	6	6	8	6	26
1.35	7	6	6	6	25
1.4	6	6	6	8	26
1.45	6	7	6	6	25
1.5	6	6	6	6	24

Table 94: Data for the major engagement condition.

Displacement (in.)	First Section	Second Section	Third Section	Fourth Section	Total Engaged
0	6	6	6	6	24
0.05	6	6	4	6	22
0.1	4	6	6	6	22
0.15	6	6	6	4	22
0.2	6	4	6	6	22
0.25	6	6	6	6	24
0.3	6	6	4	6	22
0.35	4	6	6	6	22
0.4	6	6	6	4	22
0.45	6	4	6	6	22
0.5	6	6	6	6	24
0.55	6	6	4	6	22
0.6	4	6	6	6	22
0.65	6	6	6	4	22
0.7	6	4	6	6	22
0.75	6	6	6	6	24
0.8	6	6	4	6	22
0.85	4	6	6	6	22
0.9	6	6	6	4	22
0.95	6	4	6	6	22
1	6	6	6	6	24
1.05	6	6	4	6	22
1.1	4	6	6	6	22
1.15	6	6	6	4	22
1.2	6	4	6	6	22
1.25	6	6	6	6	24
1.3	6	6	4	6	22
1.35	4	6	6	6	22
1.4	6	6	6	4	22
1.45	6	4	6	6	22
1.5	6	6	6	6	24

The tabulated data between the two cases were plotted get a visualization of the data. Figure 137shows the plot for the any engagement condition and Figure 138 shows the plot for the major engagement condition.
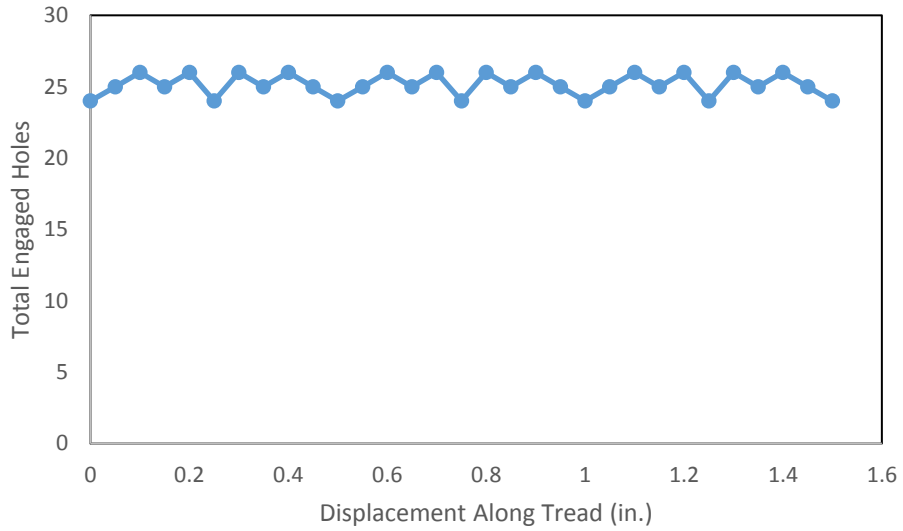
Figure 137: A plot of the total engaged holes versus the manifold displacement for the any engagement condition.
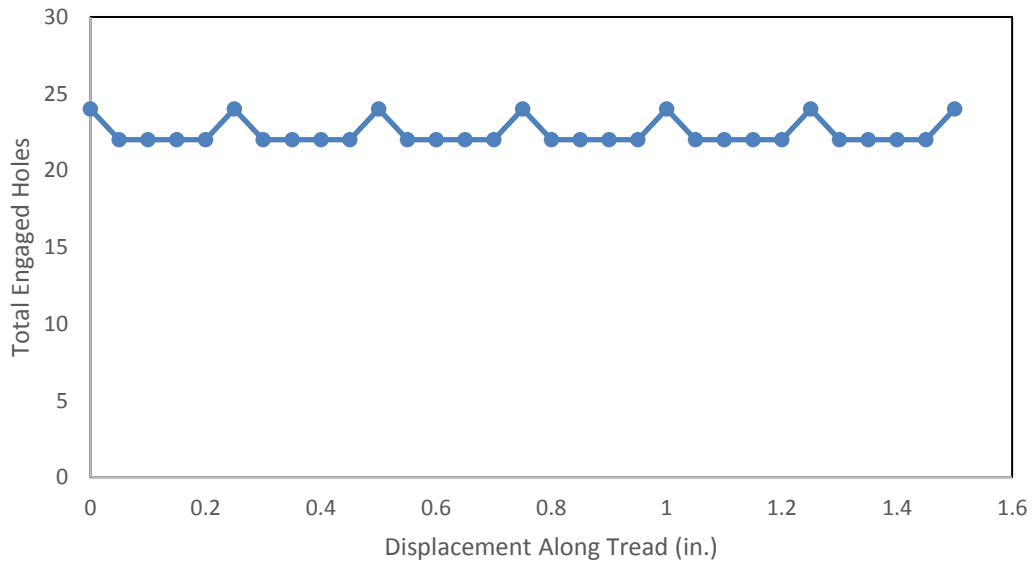
Figure 138: A plot of the total engaged holes versus the manifold displacement for the major engagement condition.

To determine the average vacuum force between the wall and the tread, the average number of holes engaged for each condition was determined. The area of a single tread hole was calculated and then multiplied by the average number of engaged holes. This gave the total area engaged. This value was then multiplied by the nominal vacuum pressure produced by the venturis to yield the average force between the wall and the tread for the given hole pattern. Table 95 contains the results of the any engagement condition

and Table 96 gives the results for the major engagement condition. Because the major engagement

condition is more conservative, the force value yielded was used in the design of the vehicle.

Table 95: The results of the any engagement condition calculation.

Parameter	Value
Area of a Single Hole	.05 in^2
Average Number of Engaged Holes	25.16
Average Area Engaged	1.25 in^2
Maximum Number of Engaged Holes	26
Minimum Number of Engaged Holes	24
Venturi Vacuum Pressure	13.75 psi
Average Vacuum Force	16.98 lbs
Maximum Force Value	17.9 lbs
Minimum Force Value	16.5 lbs

Table 96: The results of the major engagement condition calculation.

Parameter	Value
Area of a Single Hole	.05 in^2
Average Number of Engaged Holes	22.45
Average Area Engaged	1.12 in^2
Maximum Number of Engaged Holes	24
Minimum Number of Engaged Holes	22
Venturi Vacuum Pressure	13.75 psi
Average Vacuum Force	15.15 lbs
Maximum Force Value	16.5 lbs
Minimum Force Value	15.125 lbs

A.9 Skid Steering Calculator

A.9.1 Calculation Description

A symbolic analysis of the vehicle during skid steering was conducted and the resulting calculations were used to create a calculator. This calculator was then used in several later calculations such as the bearing loading calculation.

A.9.2 Assumptions

- The treads slip relative to the wall.

- The tread friction force which resists gravity acts at the geometric center of the vehicle.

- The distributed loading from the tread slipping can be split into three force.

- Assume that the drive force which causes rotation is equal to the dynamic friction between the wall and the tread

A.9.3 Free Body Diagrams
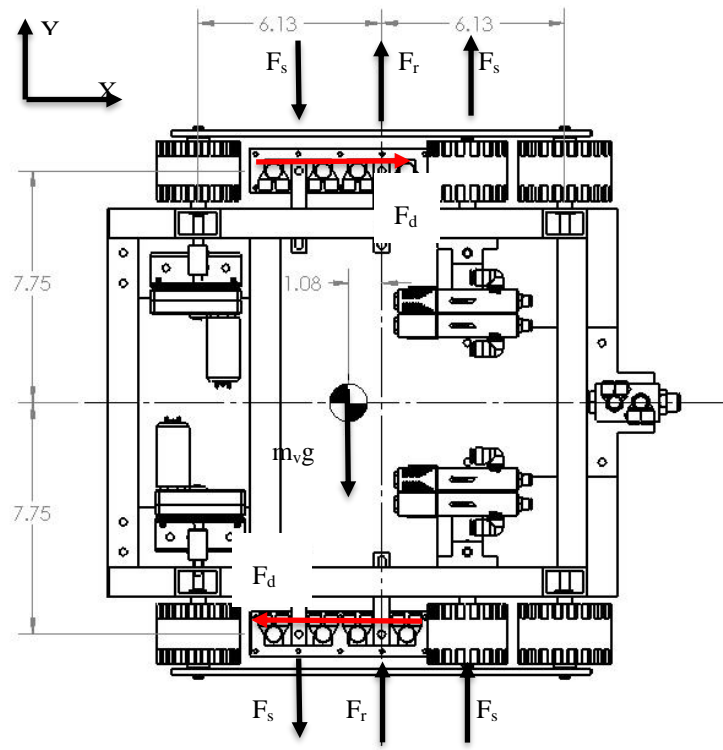
Figure 139: Vehicle Free Body Diagram.
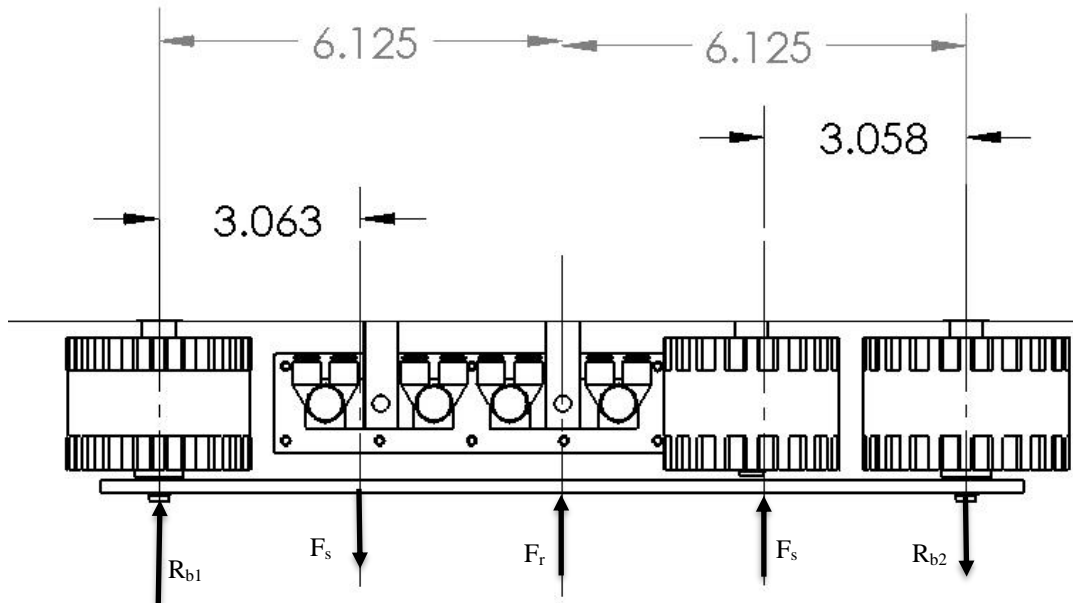
Figure 140: Wheel System Free Body Diagram.

A.9.4 Variables

Table 97: Variable symbols, units and description for the skid steering calculation.

Symbol	Units	Description
m_V	SLUG	Mass of the Vehicle
F_d	LBF	The Tread Drive Force
F_s	LBF	Tread Resistance to Turning
F_R	FT/S^2	The Tread resistance to vehicle weight
R_{b1} - R_{b2}	LBF	Bearing loads
F_{VAC}	LBF	Vacuum Force on Each Tread
μ_k	N/A	Kinetic coefficient of friction between tread and wall

A.9.5 Symbolic Manipulation

Begin by setting the conditions for the friction forces as seen in Equation A.9.1 and Equation A.9.2.

$$\mu_k * F_{VAC} = F_R + F_s \tag{A.9.1}$$

$$\mu_k * F_{VAC} > F_d \tag{A.9.2}$$

Sum moments about the geometric center of the vehicle, yielding Equation A.9.3.

$$2 * F_d * 7.75 \, in. = m_V g * 1.08 \, in. + 4 * F_s * 3.0625 \, in. \tag{A.9.3}$$

Next sum forces in the y-direction on the vehicle, yielding Equation A.9.4. This is then simplified to solve

for F_R which yields Equation A.9.5.

$$2 * F_s + m_V g = 2 * F_R + 2 * F_s \qquad \text{(A.9.4)}$$

$$F_R = 0.5 * m_V g \qquad \text{(A.9.5)}$$

Sum moment about the center of the tread to find Equation A.9.6.

$$R_{b1} * 6.125 \ in. + R_{b2} * 6.125 \ in. = 2 * F_s * 3.0625 \ in. \qquad \text{(A.9.6)}$$

Sum forces in the y-direction on the wheel system to get Equation A.9.7. Simplify to get Equation A.9.8.

$$R_{b1} + F_s + F_R = R_{b1} + F_s \qquad \text{(A.9.7)}$$

$$R_{b2} = R_{b1} + F_R \qquad \text{(A.9.8)}$$

A.9.6 Solution

The input variables and resulting outputs of the skid steering calculation can be found Table 98.

Table 98: The input variables for the skid steering calculation and the results.

Input Variables	Values
F_{VAC}	16 lbf
μ_k [24]	0.8
m_V	.5 Slugs
Output Variables	**Values**
F_d	4.9 lbf
F_s	4.75 lbf
F_R	8.05 lbf
R_{b1}	-1.65 lbf
R_{b2}	6.4 lbf

A.10 Allowable Friction Between The Tread and The Manifold

A.10.1 Calculation Description

This calculation determines the maximum allowable friction force and coefficient of friction between the tread and the manifold. The criterion these values must satisfy is that the maximum friction force be twenty percent of the maximum motor torque.

A.10.2 Solution

The contribution that the friction contributes to the required motor torque is given by Equation A.10.1, which was determined in the symbolic motor torque calculation. Manipulating Equation A.10.1 yields Equation A.10.2, which solves for the maximum coefficient of friction between the tread and manifold. Table 99 gives a description of the variables found in Equation A.10.1 and Equation A.10.2.

$$R_{DW} * \mu_{T-M} * F_{VAC} = T_{friction} \qquad\qquad (A.10.1)$$

$$\frac{T_{friction}}{R_{DW} * F_{VAC}} = \mu_{T-M} \qquad\qquad (A.10.2)$$

Table 99: The variable symbols, units and description for the allowable tread/manifold friction calculation.

Symbol	Units	Description
R_{DW}	in	Drive wheel radius
μ_{T-M}	Unit Less	Coefficient of Friction between the tread and the manifold
F_{VAC}	lbf	Vacuum Force between the manifold and the tread
$T_{friction}$	In-lbf	Torque contribution of the tread-manifold friction

Since the maximum torque of the motor is 50 in-lbf, the allowable torque contribution from friction is 10 in-lb. inserting this value, the drive wheel radius and the vacuum force into Equation A.10.2 yields the maximum allowable coefficient of friction. Table 100 contains this maximum value and the resulting maximum allowable friction between the tread and the manifold.

Table 100: The results of the allowable tread/manifold friction calculation.

Parameter	Value
Max μ_{T-M}	0.5
Max f_{T-M}	10.5 lbf

A.11 Frame Simulation

A.11.1 Simulation Description

This simulation was used to validate the design of the vehicles frame. The simulation was performed in Solidworks simulation package. It describes the boundary conditions and loading conditions that were applied to the frame and how those conditions were determined. It reports the factor of safety, maximum Von Mises stress and the deflection of the bracket. The material for the entire frame was chosen to account for the degradation in strength of the frame due to welding.

A.11.2 Boundary Conditions

The boundary conditions of the frame were difficult to determine as the frame is not fixed. To simulate the inside holes of the drive and idler uprights were fixed as shown in Figure 141.
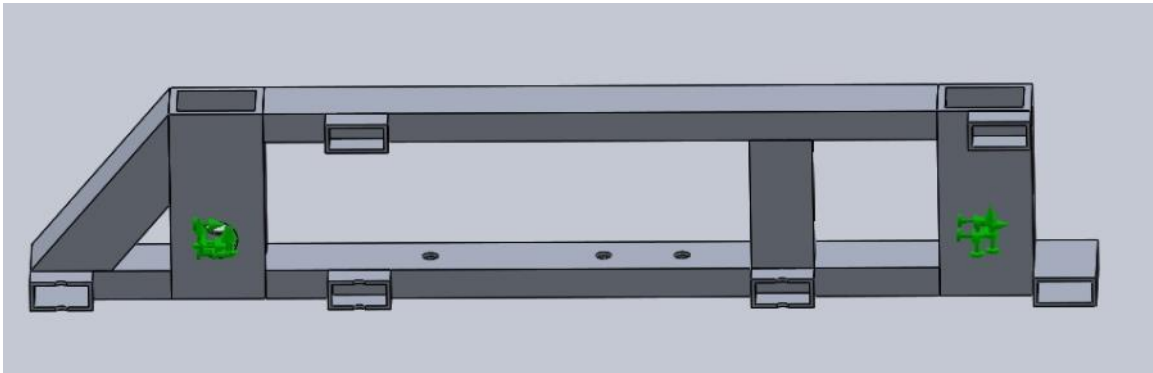
Figure 141: The fixed locations of the frame.

A.11.3 Loading Conditions

The loading conditions of the frame were assumed to be symmetrical about its midline. Three different sets of loads were applied to the vehicle. These were the bearing loading, the tensioner moment and the motor plate loading which can be seen in Figure 142, Figure 143 and Figure 144 respectively. Table 101 gives the values of the loading conditions applied to the frame. The loading was symmetrical about the center of the vehicle so only one side is shown.

Table 101: Loading conditions of the Frame.

Load	Magnitude	Direction
Tread Tension – Idler	55 lbf	Negative X
Bearing Load – Idler	6.4 lbf	Positive Z

Tread Tension – Driver	55 lbf	Positive X
Bearing Load – Driver	6.4 lbf	Negative Z
Tensioner Moment	90 lbf	Positive About X Axis
Forward Plate Force	16 lbf	Negative Y
Rear Plate Force	18 lbf	Positive Y

Figure 142: Tread tension and bearing loading conditions.
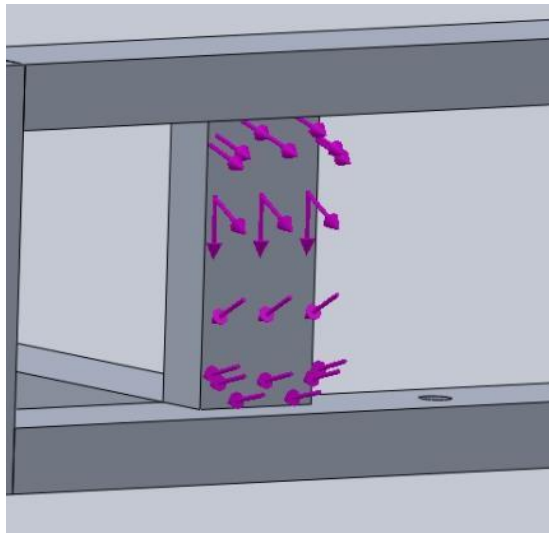
Figure 143: Torque produced by the tensioner assembly on the frame.
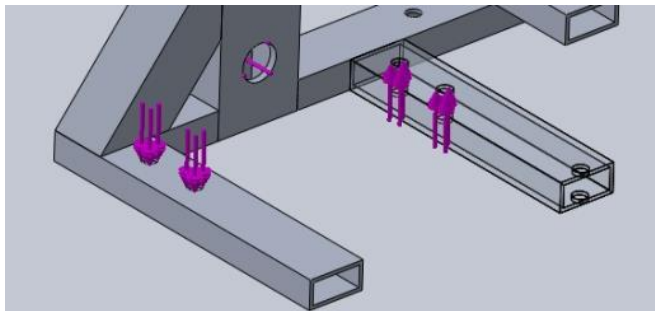
Figure 144: Forces produced by the motor plate.

A.11.4 Mesh

The mesh of the frame was generated by Solidworks. Figure 145 shows the meshed frame.
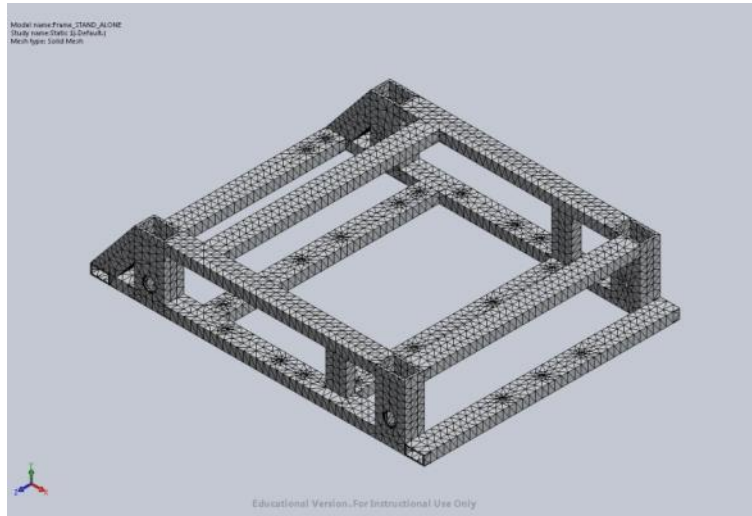
Figure 145: Meshed frame.

A.11.5 Simulation Results

The results of the simulation were promising. The resultant deflection, resultant stresses and factor of safety were well within acceptable bounds. Table 102 lists the results of the simulation. Figure 146, Figure 147 and Figure 148 show plots of the resultant deflection, resultant stresses and factor of safety respectively.

Table 102: Results of the motor bracket simulation.

Parameter	Value
Maximum Von Mises Stress	4436.5 psi
Maximum Displacement	0.002 in.
Minimum Factor of Safety	7.4
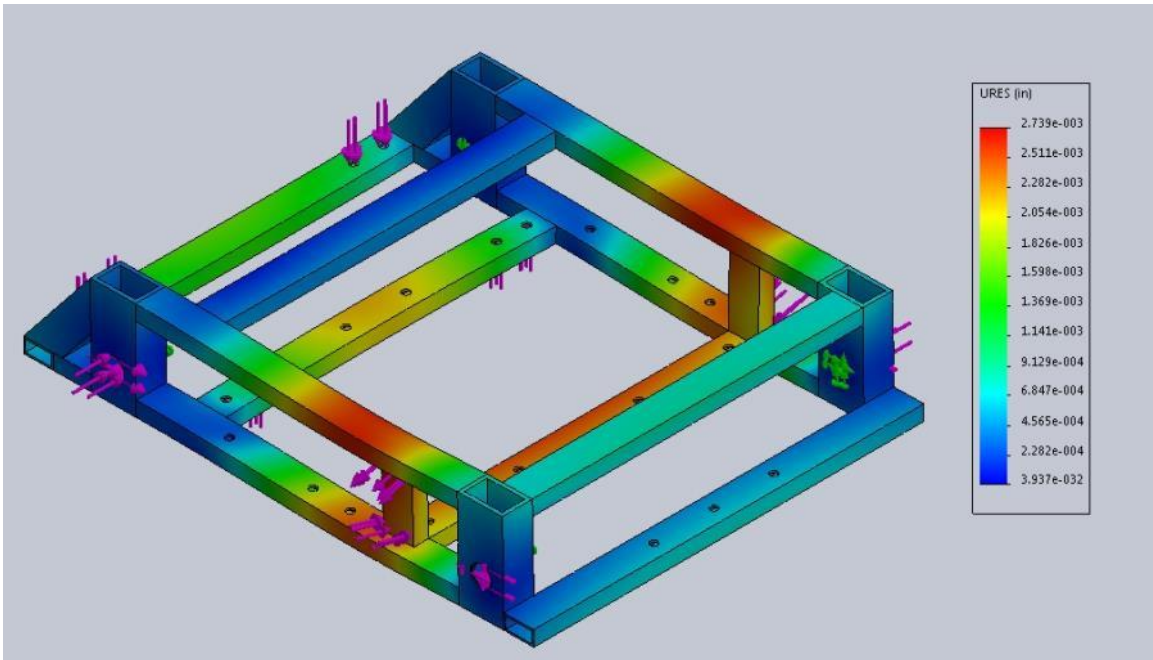
Figure 146: Displacement plot of the frame.
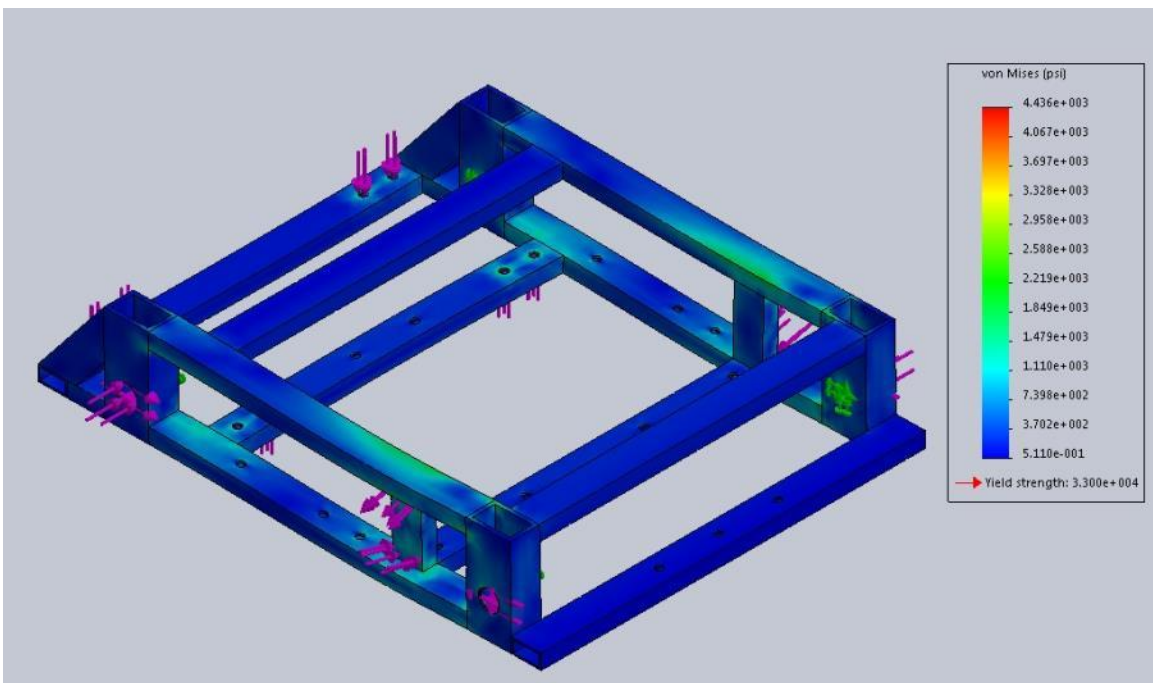
Figure 147: Von Mises stress plot of the frame.
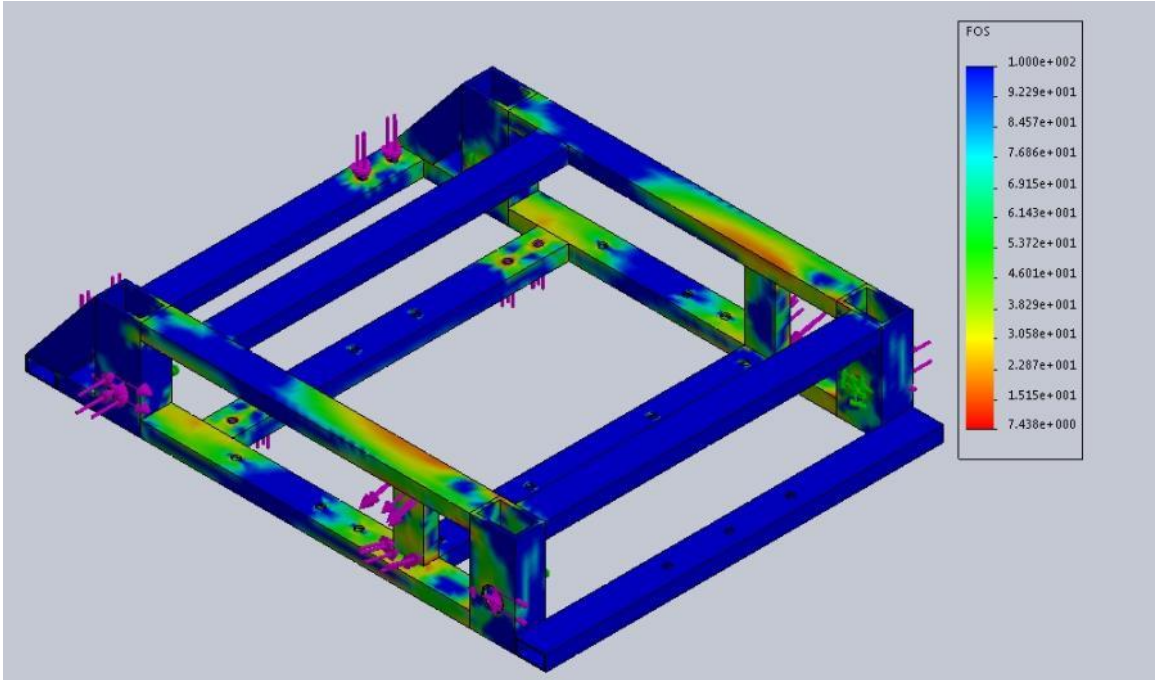
Figure 148: Factor of safety plot of the frame.

A.12 Motor Bracket Simulation

A.12.1 Simulation Description

This simulation was used to validate the design of the motor mounting brackets. The simulation was performed in Solidworks simulation package. It describes the boundary conditions and loading conditions that were applied to the bracket and how those conditions were determined. It reports the factor of safety, maximum Von Mises stress and the deflection of the bracket.

A.12.2 Boundary Conditions

To simulate the mounting bracket being rigidly attached to the motor mounting plate the faces of the bolt holes in the lower leg of the bracket were fixed in all directions. Figure 149 shows the fixture locations used in the simulation.
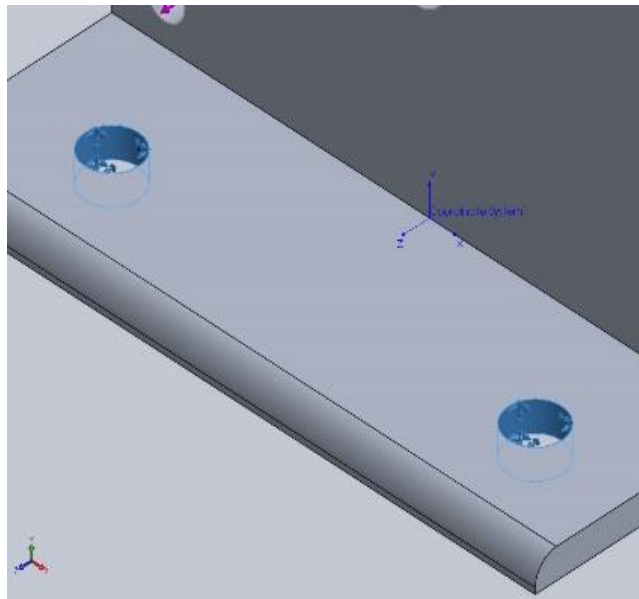
Figure 149: Fixtures used in the motor bracket simulation.

A.12.3 Loading Conditions

Two different sets of loads were applied to the bracket. One was meant to simulate the moment created by the weight of the motor hanging on bracket. The other was the bracket's resistance to the torque produce by the motor during operation.

A simple hand calculation was used to determine the magnitudes and directions of reaction forces at the motor mounting holes due to the motor weights. The magnitude of the individual forces was found to be 0.51 lbf. The forces at the top of the bracket pointed in the negative z-direction and those at the bottom pointed in the positive z-direction. These forces were inserted into the simulation as force loads on the inside faces of the motor mounting holes in the bracket. Figure 150 shows the loading condition due to the motor mass.
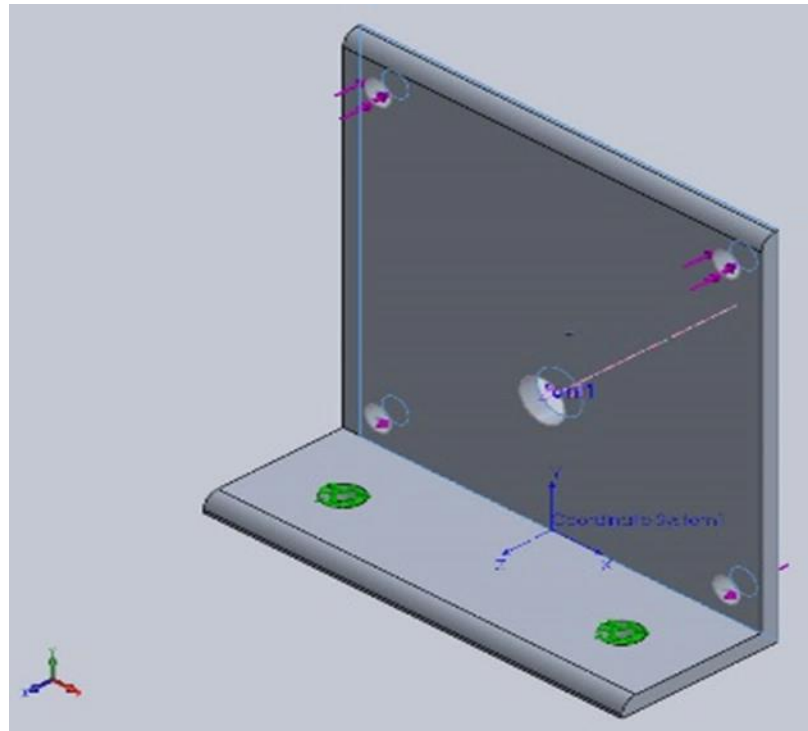
Figure 150: The loading on the motor bracket due to the mass of the motor.

It was assumed for the purposes of the determining the torque that the motor was operating at its full load capacity. This gave the torque applied to the bracket a magnitude of 50 in-lbf. It was also assumed that the vehicle was moving forwards which gave the torque applied to the bracket a counter-clockwise direction. The torque was centered on the axis of the trough hole for the motor shaft. The torque was applied to the back face of the bracket. Figure 151 shows the torque load applied to the motor bracket during the simulation.
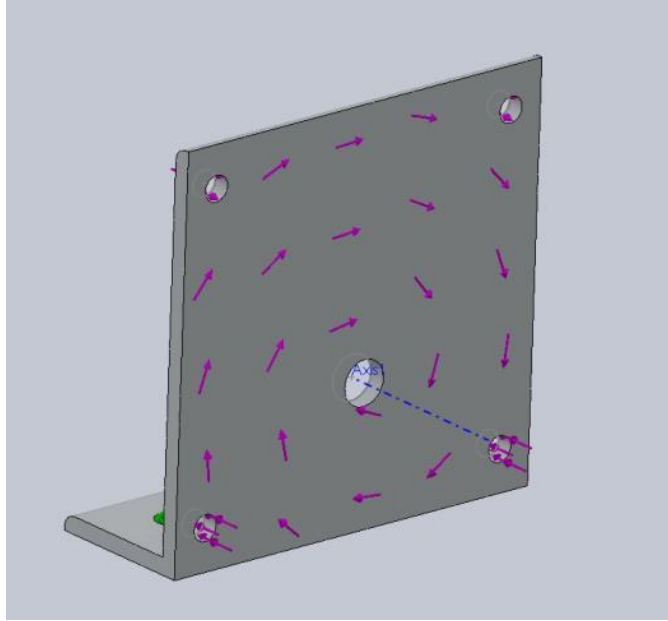
Figure 151: Torque load simulation the motor.

A.12.4 Simulation Results

The results of the simulation were promising. The resultant deflection, resultant stresses and factor of safety were well within acceptable bounds. Table 103 lists the results of the simulation. Figure 152, Figure 153 and Figure 154 show plots of the resultant deflection, resultant stresses and factor of safety respectively. Figure 155 shows the reaction forces at the fixed locations on the bracket. These reactions would be used in the motor plate validation simulation.

Table 103: Results of the motor bracket simulation.

Parameter	Value
Maximum Von Mises Stress	6390 psi
Maximum Displacement	0.0035 in.
Minimum Factor of Safety	6.2
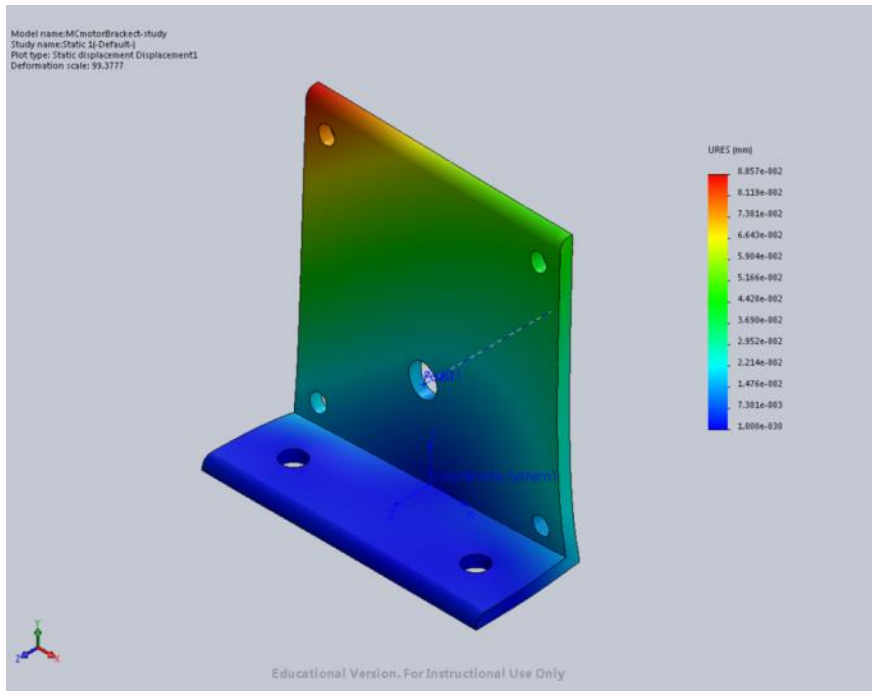
Figure 152: Deflection plot of the motor bracket.
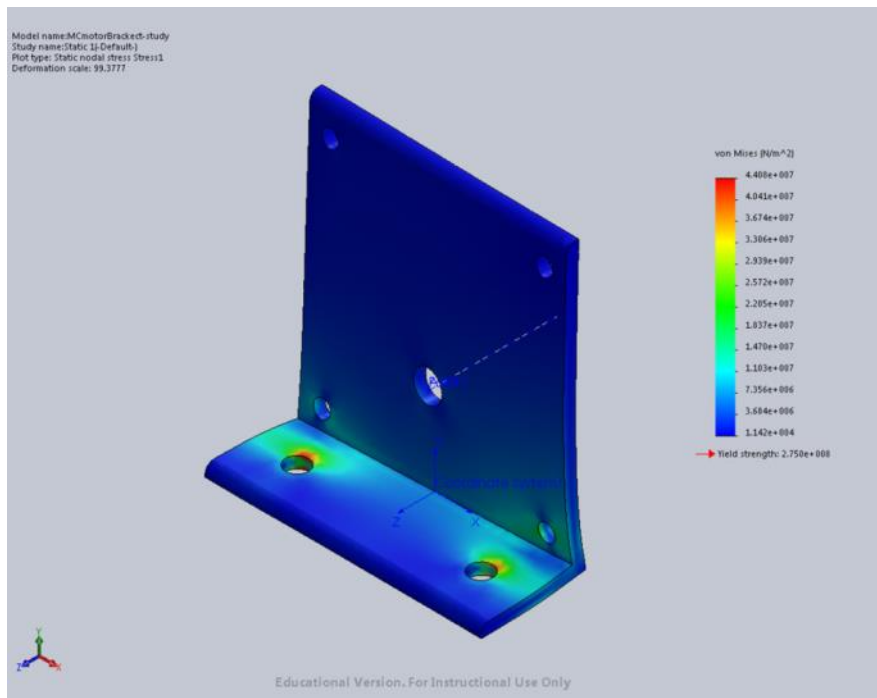
Figure 153: Von Mises stress plot of the motor bracket.
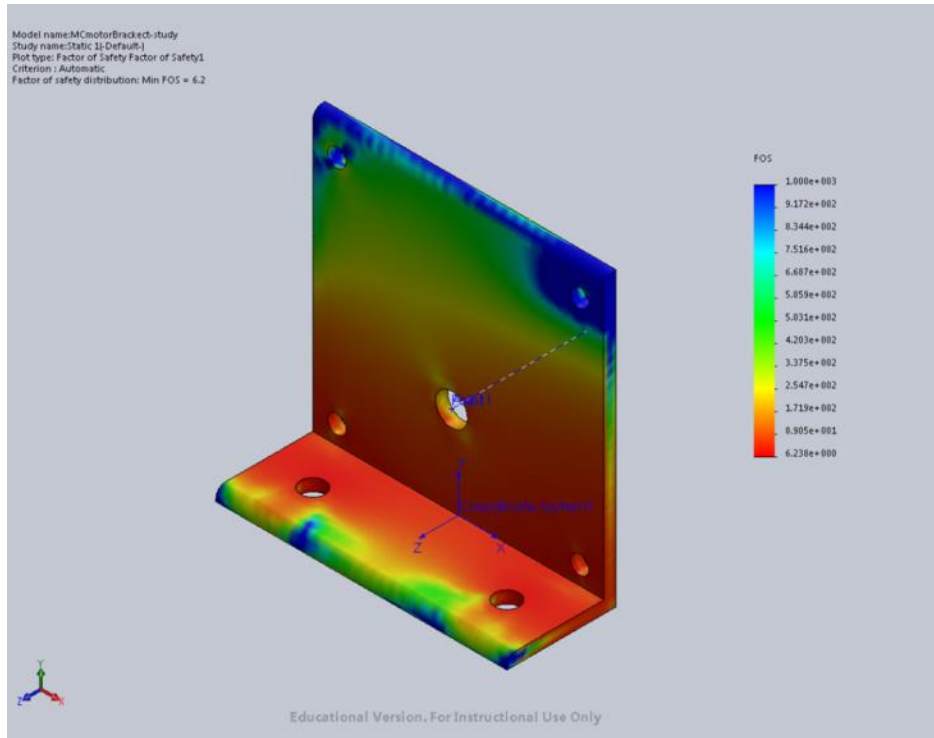
Figure 154: Factor of safety plot of the motor bracket.
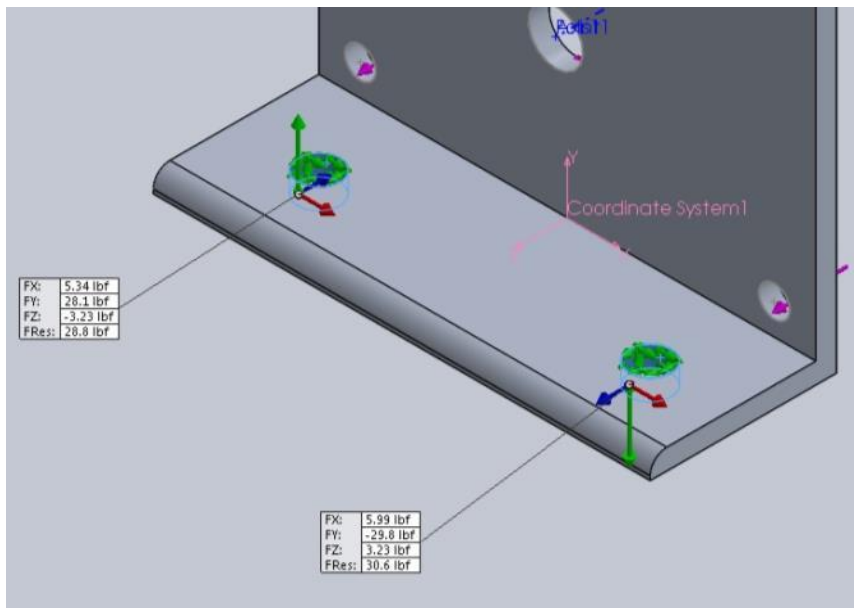
Figure 155: Reactions at the fixed holes of the motor bracket.

A.13 Motor Plate Validation

A.13.1 Simulation Description

This simulation was used to validate the design of the motor base plates. The simulation was performed in Solidworks simulation package. It describes the boundary conditions and loading conditions that were applied to the plates and how those conditions were determined. It reports the factor of safety, maximum Von Mises stress and the deflection of the bracket.

A.13.2 Boundary Conditions

The plate was fixed in all directions at the four outer holes on the plate. This was done to simulate the rigid attachment of the plates to the fame. Figure 156 shows the fixture location used in the simulation.
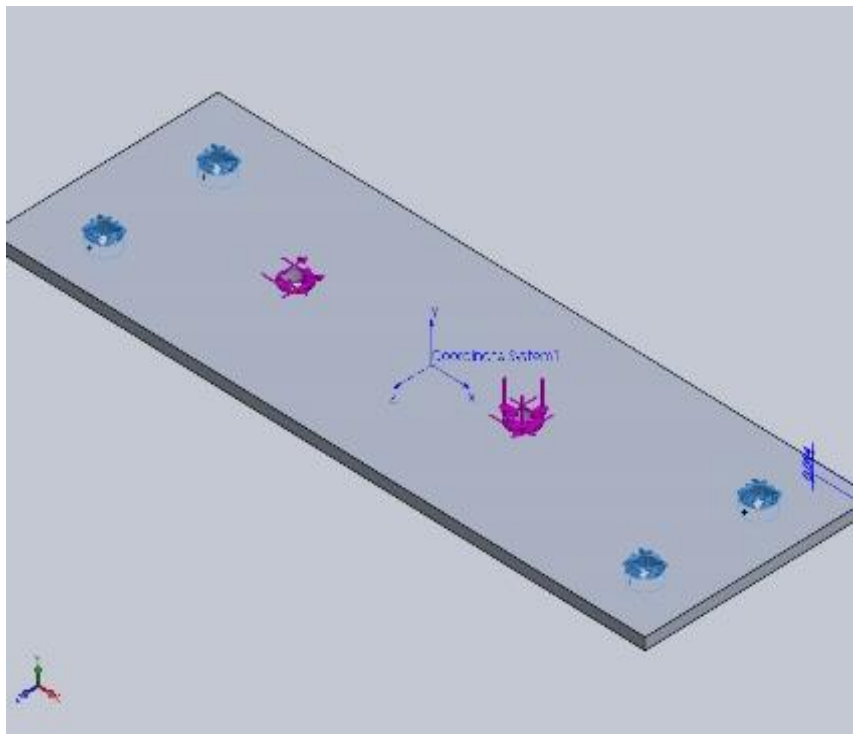
Figure 156: Fixtures used in the motor plate simulation, Highlighted in blue.

A.13.3 Loading Conditions

The loading conditions for the plates were taken directly from the reaction forces found during the simulation of the motor bracket. They were taken to act on the on the bolt holes which attached the motor plates to the motor brackets. Table 104 contains the magnitudes and directions of the loading conditions

used in the plate simulation. Note that the direction of the forces is flipped relative to their counter parts on

the motor bracket. Figure 157 shows the loading conditions applied to the plate.

Table 104: Loading conditions applied to the motor plate.

Forward Hole	Value
x - direction	-5.34 lbf
y-direction	-28.1 lbf
z-direction	3.23 lbf
Rear Hole	Value
x - direction	-5.99 lbf
y-direction	29.8 lbf
z-direction	-3.23 lbf
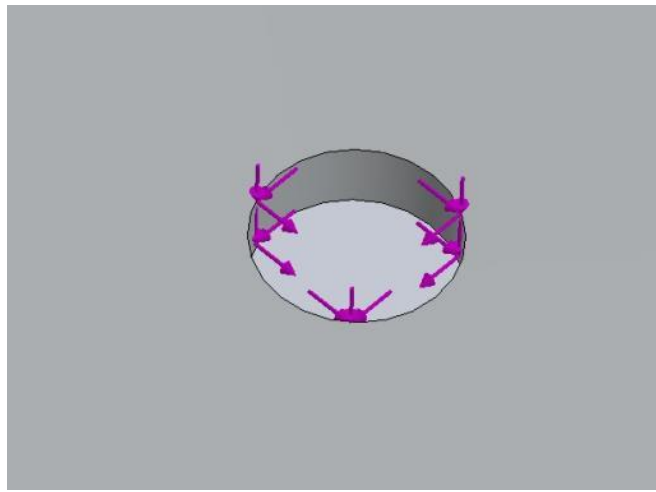
Figure 157: An image of the rear hole showing the loading conditions.

A.13.4 Mesh

The mesh for the motor plate was auto generated by Solidworks. A fine mesh was chosen to increase the accuracy of the results. Figure 158 shows the meshed motor plate.

Figure 158: Meshed motor plate.

A.13.5 Simulation Results

The resultant deflection, resultant stresses and factor of safety were well within acceptable bounds. Table 105 lists the results of the simulation. Figure 159, Figure 160 and Figure 161 show plots of the resultant deflection, resultant stresses and factor of safety respectively. Figure 162 shows the reaction forces at the fixed locations on the motor plate. These reactions were used in the simulation of the frame.

Table 105: Results from the motor plate simulation.

Simulation Result	Value
Maximum Von Mises Stress	11,525 psi
Maximum Displacement	0.005 in.
Minimum Factor of Safety	3.5
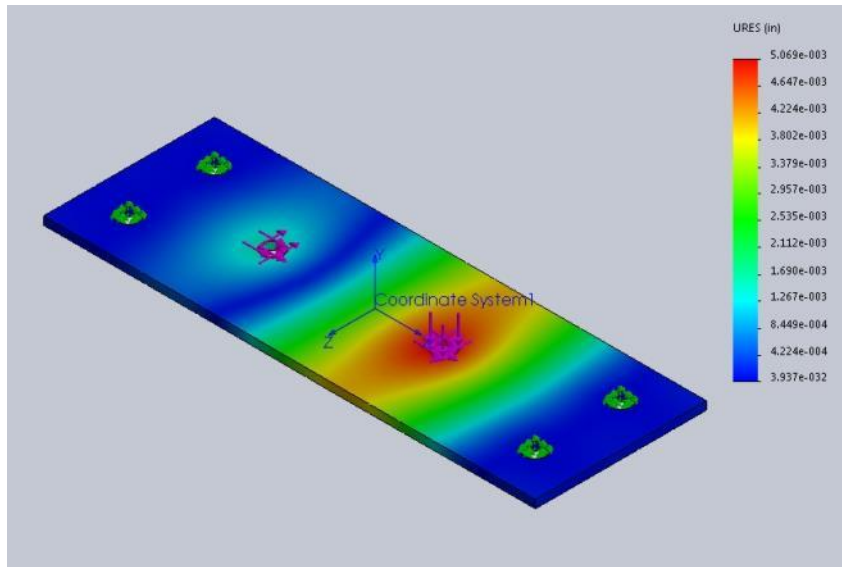
Figure 159: Deflection plot of the motor plate.
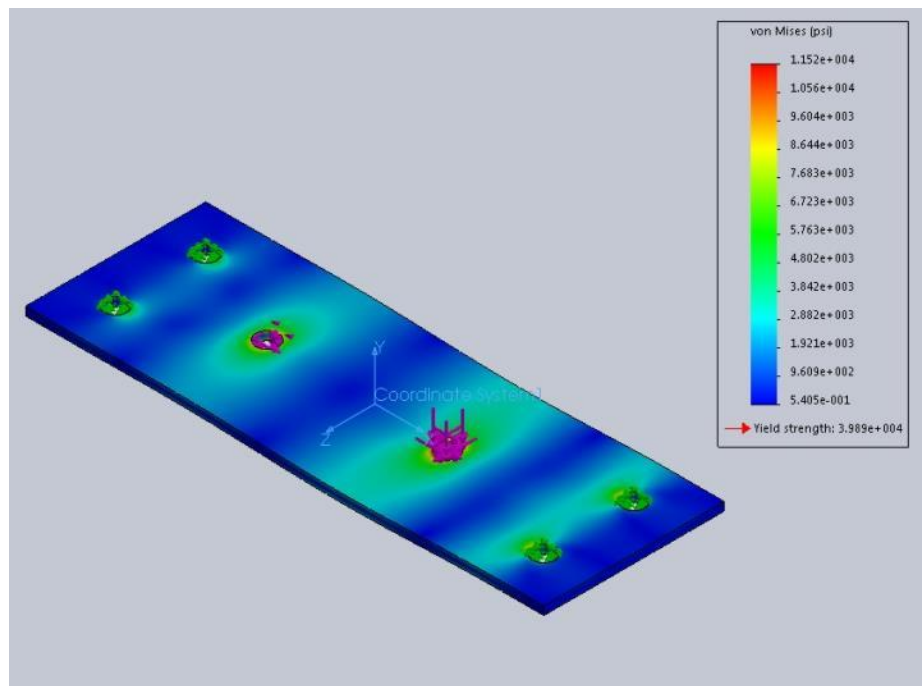
Figure 160: Von Mises Stress plot of the motor plate.
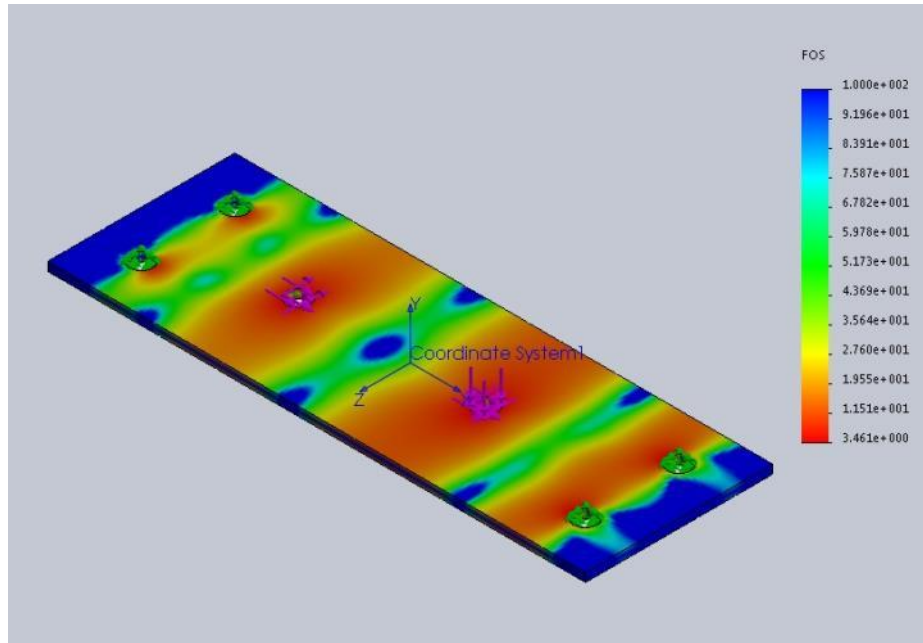
Figure 161: Factor of safety plot of the motor plate.
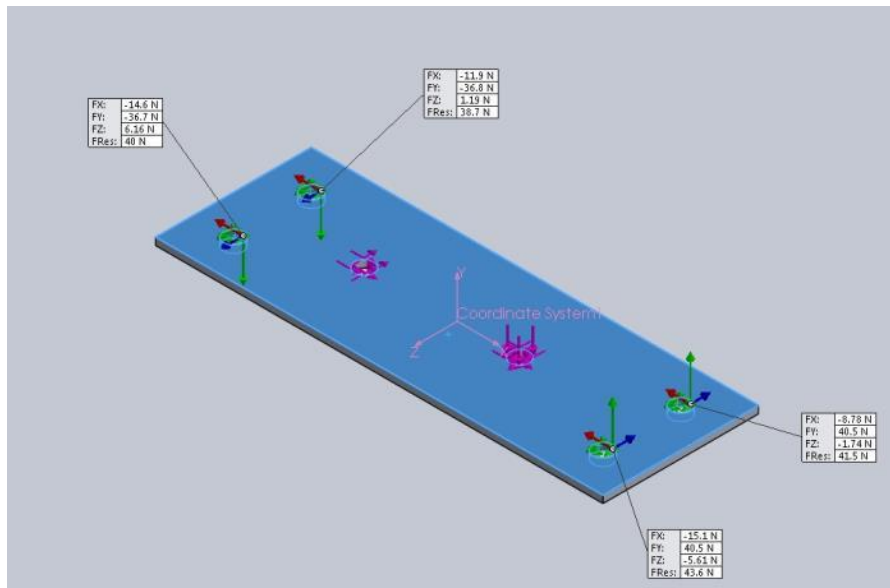
Figure 162: Reactions of the motor plate at the fixed holes.

A.14 Manifold Mounting Strut Validation

A.14.1 Simulation Description

This simulation was used to validate the design of the manifold mounting struts. The simulation was performed in Solidworks simulation package. It describes the boundary conditions and loading conditions that were applied to the struts and how those conditions were determined. It reports the factor of safety, maximum Von Mises stress and the deflection of the bracket.

A.14.2 Boundary Conditions

The mounting strut was fixed in place at the frame mounting holes. Figure 163 shows the fixed locations of the mounting struts.
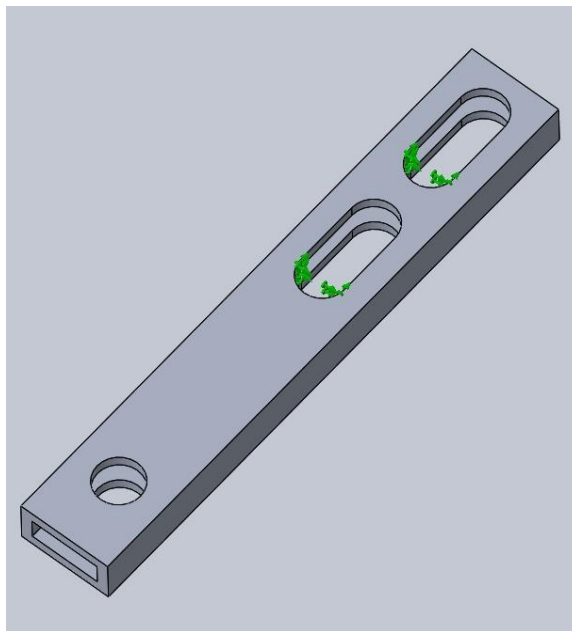
Figure 163: Fixed locations on the mounting strut.

A.14.3 Loading Conditions

The loading conditions of the strut were simple to determine. A load perpendicular to the bottom face of the strut was applied at the manifold mounting hole to simulate the spring force from the suspension. A

horizontal load simulating the manifold friction was also applied. Table 106 contains the magnitudes of the applied loads and Figure 164 shows their location and direction.

Table 106: Magnitudes of the loads applied to the strut.

Load	Magnitude
Spring Force	11 lbf
Manifold Friction	10 lbf
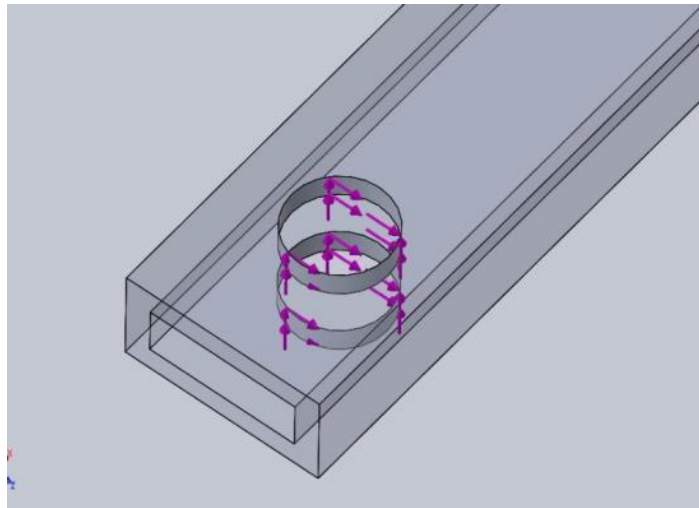
Figure 164: Loading conditions for the strut simulation.

A.14.4 Mesh

The mesh for the motor plate was auto generated by Solidworks. A fine mesh was chosen to increase the accuracy of the results. Figure 165 shows the strut.

Figure 165: Meshed support strut.

A.14.5 Simulation Results

Table 107 lists the results of the simulation. Figure 166, Figure 167 and Figure 168 show plots of the resultant deflection, resultant stresses and factor of safety respectively.

Table 107: Results from the motor plate simulation.

Simulation Result	Value
Maximum Von Mises Stress	11,550 psi
Maximum Displacement	0.004 in.
Minimum Factor of Safety	3.5
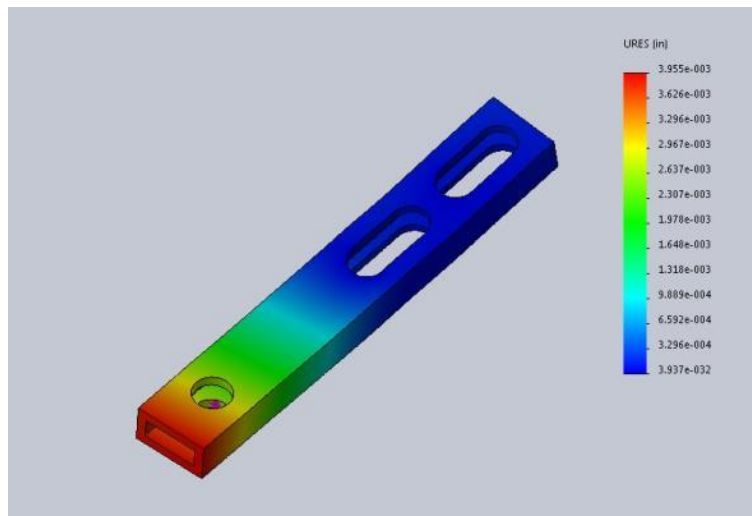
Figure 166: Deflection plot of the strut.
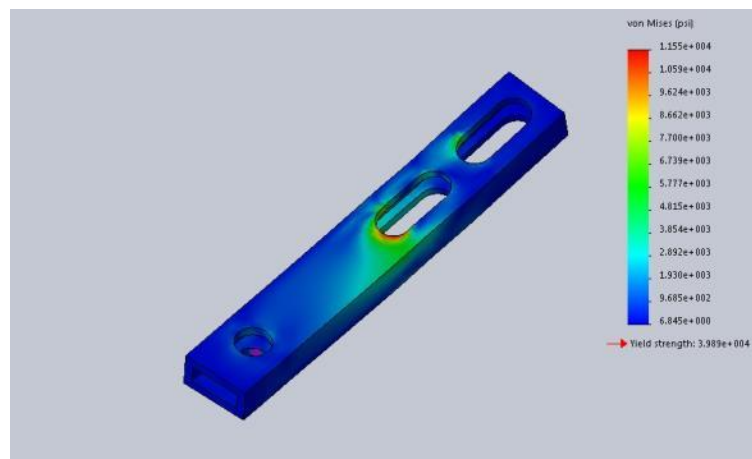
Figure 167: The Von Mises Stress plot of the strut.
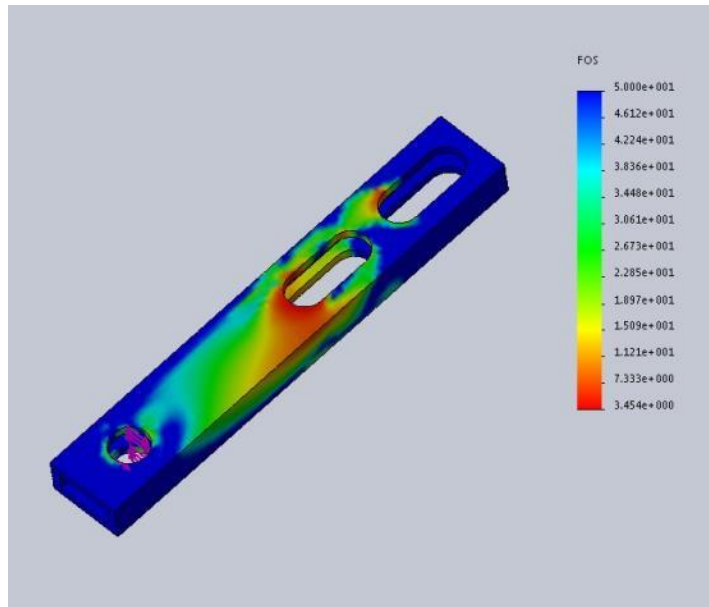
Figure 168: Factor of safety plot of the strut.

A.15 Bearing Loading Calculation

A.15.1 Calculation Description

This calculation was used to determine maximum loading which the bearings in the vehicle would carry during operation.

A.15.2 Assumptions

- The tread tension load is distributed equally between the frame and brace bearings.

- The vehicle is parallel the ground.

- The weight of the vehicle is carried by only two of the bearings

A.15.3 Solution

Table 108 gives the variables and their values used to calculate the bearing loading.

Table 108: Force values which are applied across two bearings.

Symbol	Description	Value
T_T	Tread Tension	110 lbf
w_V	Weight of the vehicle	16 lbf

The load on a single bearing is equal to half of the tension in the tread plus half of the weight of the vehicle, as seen in Equation A.15.1.

$$F_B = .5 * T_T + .5 * w_V \qquad \text{(A.15.1)}$$

The results of this calculation can be found in Table 109.

Table 109: Results of the bearing loading calculation.

Predicted Bearing Load	Max Bearing Load	Safety Factor
63 lbf	280 lbf	4.44

A.16 Drive Shaft Simulation

A.16.1 Simulation Description

This simulation was used to validate the design of the drive shaft wheel and to determine the diameter and the material used to construct it. The simulation was performed in Solidworks simulation package. It describes the boundary conditions and loading conditions that were applied to the shaft and how those conditions were determined. It reports the factor of safety, maximum Von Mises stress and the deflection of the bracket.

A.16.2 Boundary Conditions

The end of the shaft which couples to the motor was fixed to simulate the stalling of the motor. The locations where the bearings contact the shafts was fixed radially and axially to prevent the shaft from shifting at these locations but still allowing for rotation. Figure 169 shows the locations of the shaft fixtures.
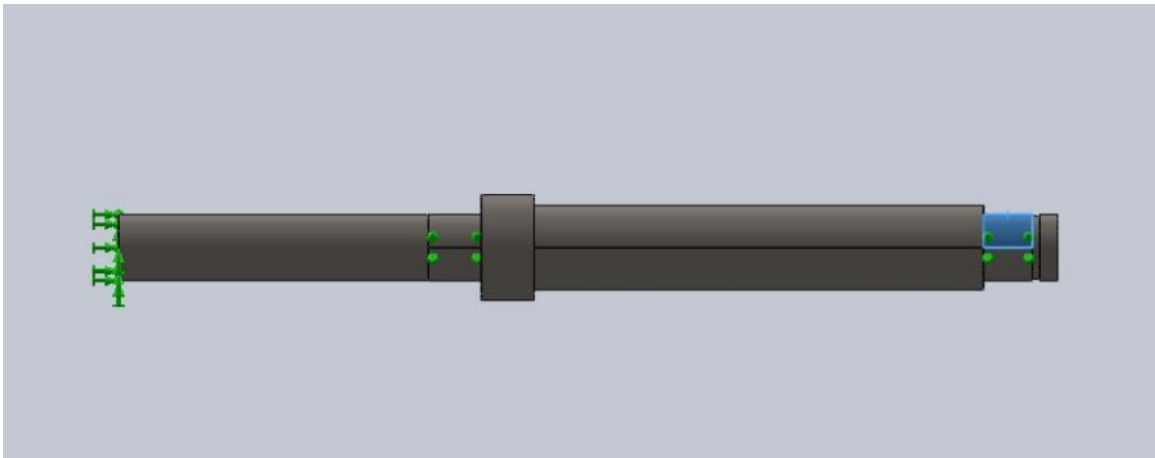
Figure 169: Fixed locations on the shaft.

A.16.3 Loading Conditions

Two loads were applied to the brace at the shaft. The first was the motor torque load and the second was the tread tension load. Table 110 gives the magnitudes of these loads and their location and directions can be seen in Figure 170.

Table 110: Magnitudes of the loads applied to the brace.

Load	Magnitude
Tread Tension	110 lbf
Motor Torque	50 in-lbf
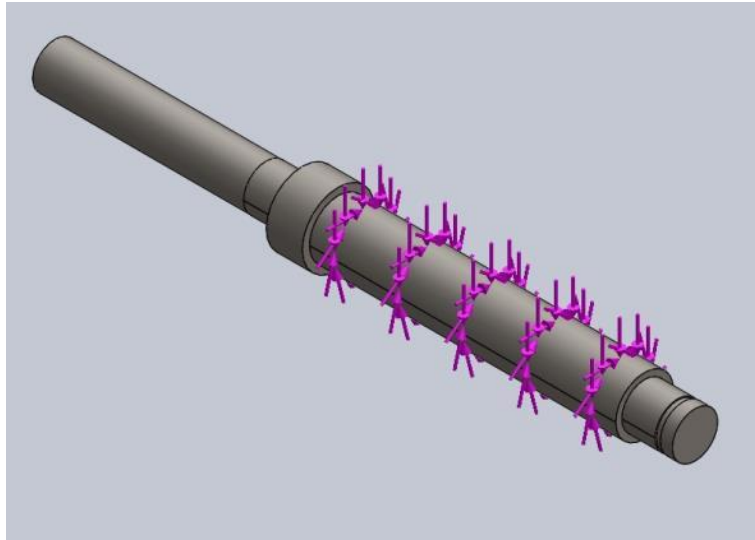
Figure 170: Locations of the loads applied to the brace.

A.16.4 Mesh

The mesh for the brace was auto generated by Solidworks. A fine mesh was chosen to increase the accuracy of the results. Figure 171 shows the meshed brace.
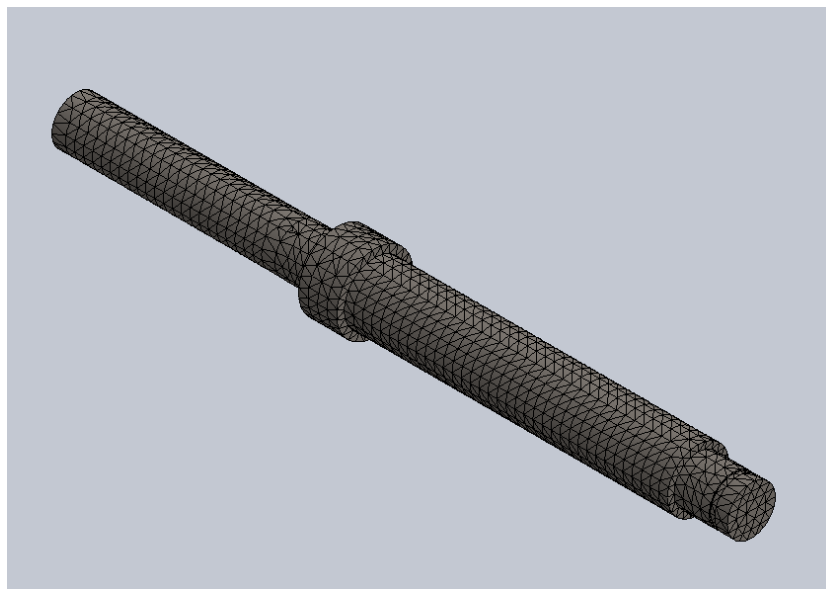
Figure 171: Meshed drive shaft.

A.16.5 Simulation Results

The 0.4 in. diameter steel shaft was chosen. Table 111 lists the results of the simulation for each material

type and diameter that was simulated. Figure 172, Figure 173 and Figure 174 show plots of the resultant

deflection, resultant stresses and factor of safety respectively for the chosen shaft diameter and material.

Table 111: Results from the different shaft simulations.

Simulation Diameter and Material	Maximum Displacement	Maximum Von Mises Stress	Minimum Factor of Safety
0.45 in. Steel	0.002 in.	17,440 psi	4.4
0.45 in. Aluminum	0.007 in.	17,610 psi	2.3
0.4 in. Steel	0.002 in.	17,960 psi	4.3
0.4 in. Aluminum	0.006 in.	17,615 psi	2.3
0.35 in. Steel	0.002 in.	19,130 psi	4.0
0.35 in. Aluminum	0.007 in.	19,050 psi	2.0
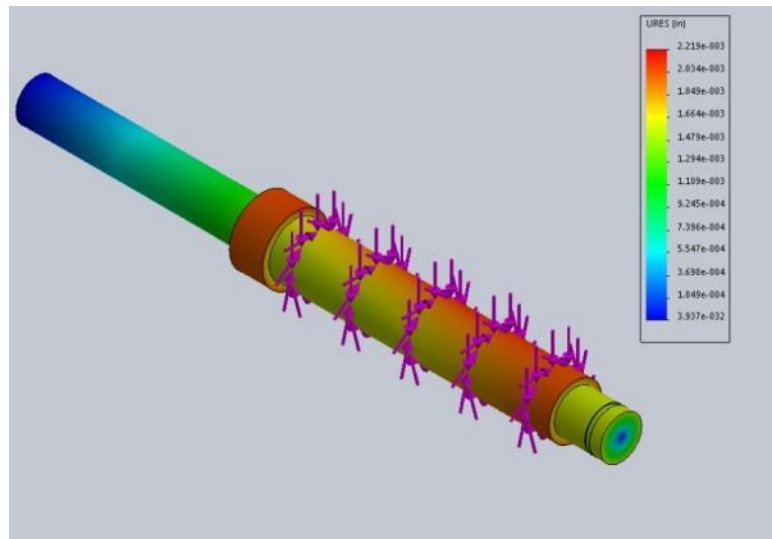
Figure 172: Deflection plot of the drive shaft.
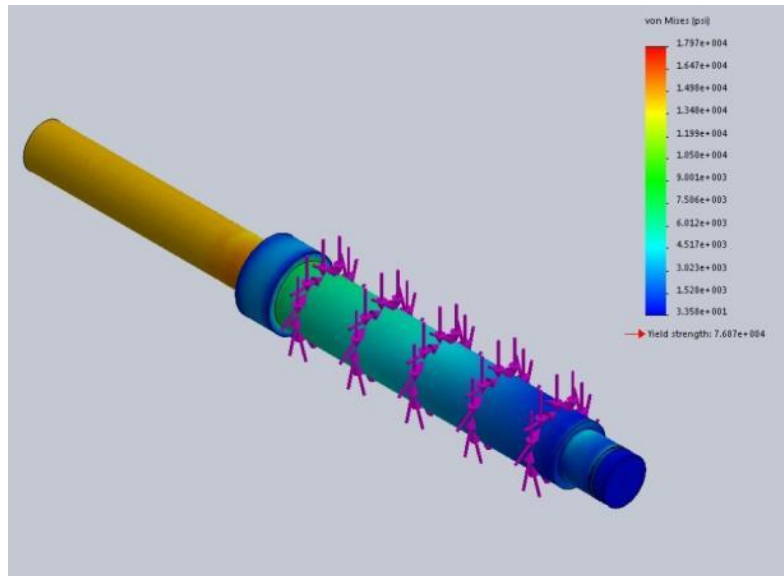
Figure 173: The Von Mises Stress plot of the drive shaft.
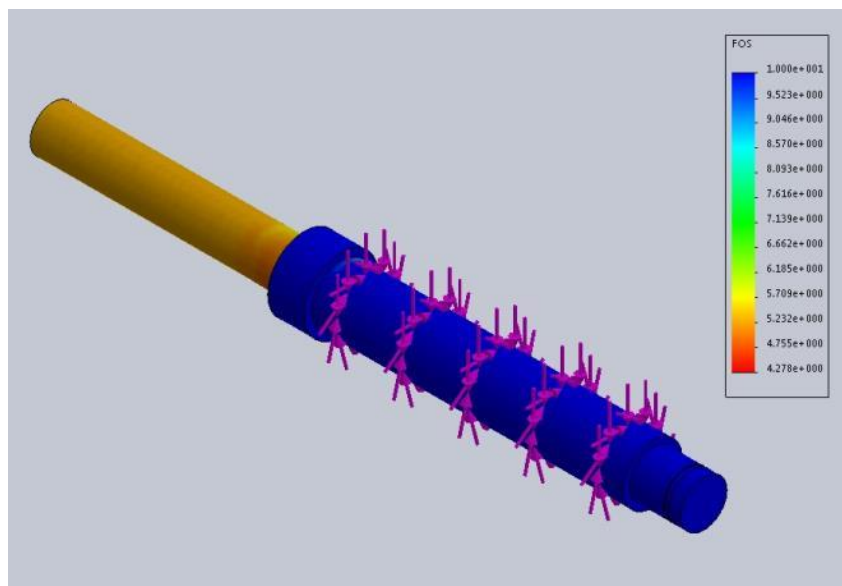
Figure 174: The Factor of safety plot of the drive shaft.

A.17 Retaining Ring Calculation

A.17.1 Calculation Description

This calculation serves as the verification that the snap rings chosen for the project would be capable of withstanding the operating loads they were subjected to.

A.17.2 Equations and Variable Descriptions

Two equations are used. Equation A.17.1 calculates the maximum allowable thrust load which can be applied to the retaining rings before the rings shear. Equation A.17.2 calculates the maximum allowable thrust load which can be applied to the retaining rings before the groove in the shaft yields. Both equations used in this section were found on Smalley's website [26].

$$P_R = \frac{DTS_s\pi}{K} \tag{A.17.1}$$

$$P_G = \frac{DdS_Y\pi}{K} \tag{A.17.2}$$

Table 112: Ring shear variable symbols and descriptions.

Symbol	Description
P_R	Allowable Thrust Load Based on Ring Shear (lb)
D	Shaft Diameter (in)
T	Ring Thickness (in)
S_s	Ring Material Shear Strength (psi)
K	Factor of Safety

Table 113: Slot yielding variable symbols and descriptions.

Symbol	Description
P_G	Allowable Thrust Load Before Groove Deformation (lb)
D	Shaft Diameter (in)
d	Groove Depth (in)
S_Y	Groove Material Yield Strength (psi)
K	Factor of Safety

A.17.3 Values and Results

The results of the drive and idler retaining ring calculations can be found in Table 114. The results of the

tensioner shaft retaining ring calculation can be found in Table 115.

Table 114: Input variable values for the drive and idler shaft retaining rings and the results of the calculation.

Input Variable	Value
D	0.315 in
T	0.032 in
S_s	45 kpsi
d	0.008 in
S_Y	45 kpsi
K	3
Output Variable	**Value**
P_R	473 lbf
P_G	118 lbf

Table 115: Input variable values for the tensioner shaft retaining rings and the results of the calculation.

Variable	Value
D	0.375 in
T	0.025 in
S_s	45 kpsi
d	0.012 in
S_Y	45 kpsi
K	3
Output Variable	**Value**
P_R	441 lbf
P_G	211 lbf

A.18 Drive Wheel Press Fit Calculation

A.18.1 Calculation Description

This calculation was used to determine the required press fit to fix the drive wheel onto the drive shaft. It begins by determining the force required to hold the drive wheel in place. That force is then converted into a pressure and that is used to determine the required interference between the drive wheel and the drive shaft. It was assumed that these values would also be applicable to the idler wheel. All equations used for this calculator were obtained from [23].

A.18.2 Required Pressure Calculation

The first step was determining the friction force required to hold the drive wheel in place. Equation A.18.1 shows the calculation used.

$$F_r = \frac{2}{D_{DS}} * T_m * FS \qquad (A.18.1)$$

This force value was then used to determine the required normal force in Equation A.18.2.

$$N_{DW} = \frac{F_r}{\mu_{W-S}} \qquad (A.18.2)$$

This normal force was then converted to a pressure force using the area of the shaft as seen in Equation A.18.3.

$$P_I = \frac{N_{DW}}{(\pi * D_{DS} * w_{dw})} \qquad (A.18.3)$$

Table 116 contains the variables and their values used to calculate the require interference pressure. Table 117 contains the results of this calculation.

Table 116: The input variable symbols, descriptions and values used to calculate the required press fit pressure.

Symbol	Description	Value
D_{DS}	Drive Shaft Diameter	0.4 in.
T_m	Motor Torque	50 in-lbf
FS	Desired Safety Factor	2
μ_{W-S}	Friction between drive shaft and drive wheel	0.35
w_{dw}	The Width of the Drive wheel	2 in

Table 117: The output variable symbols, descriptions and values from the required press fit pressure calculation.

Symbol	Description	Value
F_r	Force required to resist the motor torque	500 lbf
N_{DW}	Normal Force Between the Drive wheel and the drive shaft	1430 lbf
P_I	The Required Interference Pressure	570 psi

A.18.3 Required Interference Calculation

Using Equation A.18.4, the required interference fit between the drive wheel and the drive shaft can be found.

$$\delta = P_I * R_{DS} * [\frac{1}{E_{DW}} * \left(\frac{r_{dw}^2 + R_{DS}^2}{r_{dw}^2 - R_{DS}^2} + v_{DW} \right) + \frac{1}{E_{DS}} * \left(\frac{R_{DS}^2}{R_{DS}^2} - v_{DS} \right) \qquad \text{(A.18.4)}$$

Table 118 contains the variables used in the calculation and the resulting interference required.

Table 118: Input variable symbols, descriptions and values used to calculate the required interference and the resulting interference.

Variable	Description	Value
P_I	The Required Interference Pressure	570 psi
R_{DS}	Radius of the Drive Shaft	0.2 in.
E_{DW}	The Youngs modulus of ABS	320 ksi
r_{dw}	The outer radius of the drive wheel	1.33 in.
v_{DW}	Poisons Ratio for ABS	0.35
E_{DS}	The Youngs modulus of steel	29.9 Msi
v_{DS}	Poisons ratio for Steel	0.29
δ	The Required Interference	0.001 in.

A.19 Drive Wheel Validation

A.19.1 Simulation Description

This simulation was used to validate the design of the drive wheel. The simulation was performed in Solidworks simulation package. It describes the boundary conditions and loading conditions that were applied to the wheel and how those conditions were determined. It reports the factor of safety, maximum Von Mises stress and the deflection of the bracket.

A.19.2 Boundary Conditions

The wheel was fixed at the tooth locations to simulate the engagement between the tread and the drive wheel. 8 sets of teeth were fixed as this was the estimated tooth engagement between the tread and the wheel. Figure 175 shows the location of the fixtures.
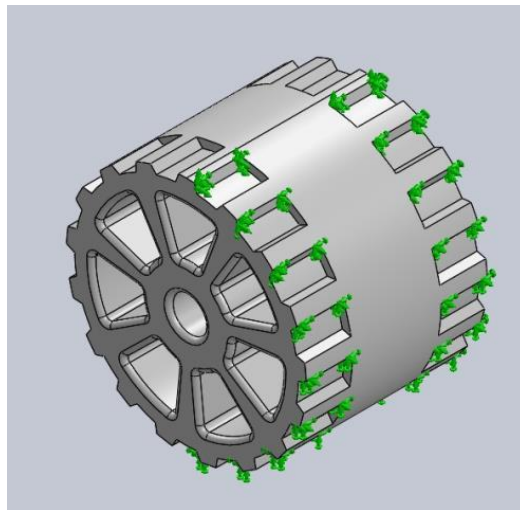
Figure 175: Fixed locations of drive wheel.

A.19.3 Loading Conditions

Three loads were applied to the wheel in the simulation. They were the pressure load due to press fitting the wheel onto the shaft, the motor torque and the belt tension. Table 119 gives the magnitudes of these loads and their location and directions can be seen in Figure 176.

Table 119: Magnitudes of the loads applied to the drive wheel.

Load	Magnitude
Tread Tension	110 lbf
Press Fit Pressure	500 psi
Motor Torque	50 in-lbf
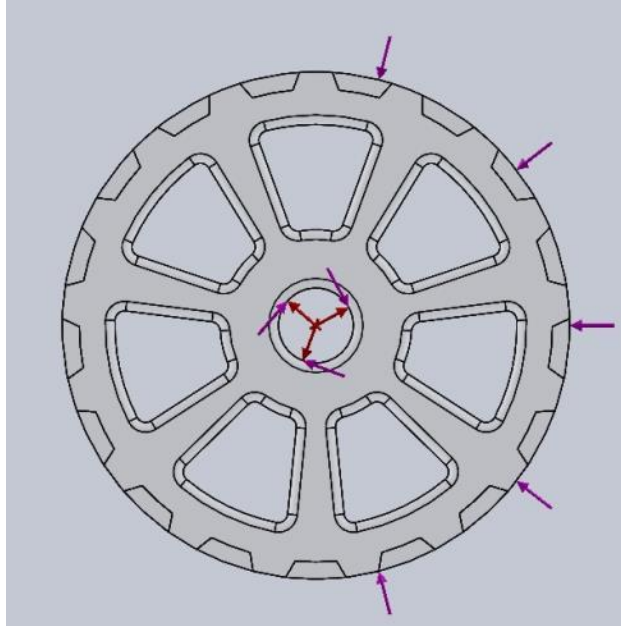
Figure 176: Locations of the loads applied to the drive wheel.

A.19.4 Mesh

The mesh for the wheel was auto generated by Solidworks. A fine mesh was chosen to increase the accuracy of the results. Figure 177 shows the meshed wheel.
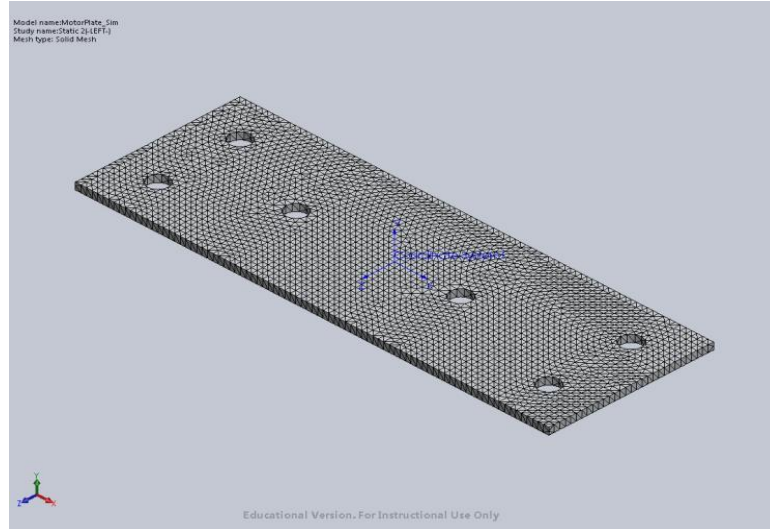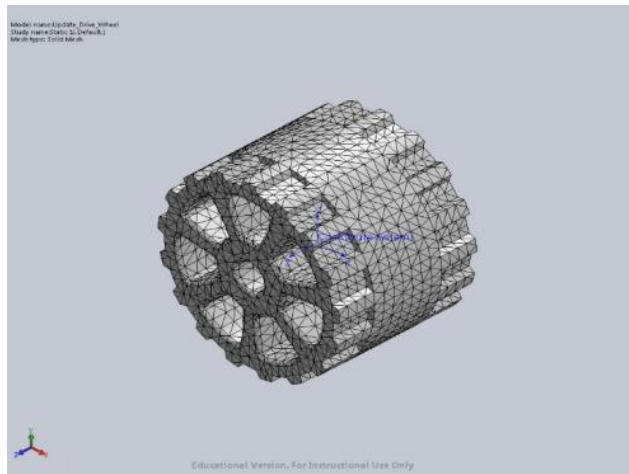

Figure 177: Meshed drive wheel.

A.19.5 Simulation Results

Table 120 lists the results of the simulation. Figure 178, Figure 179 and Figure 180 show plots of the resultant deflection, resultant stresses and factor of safety respectively.

Table 120: Results from the drive wheel simulation.

Simulation Result	Value
Maximum Von Mises Stress	1030 psi
Maximum Displacement	0.001 in.
Minimum Factor of Safety	4.5
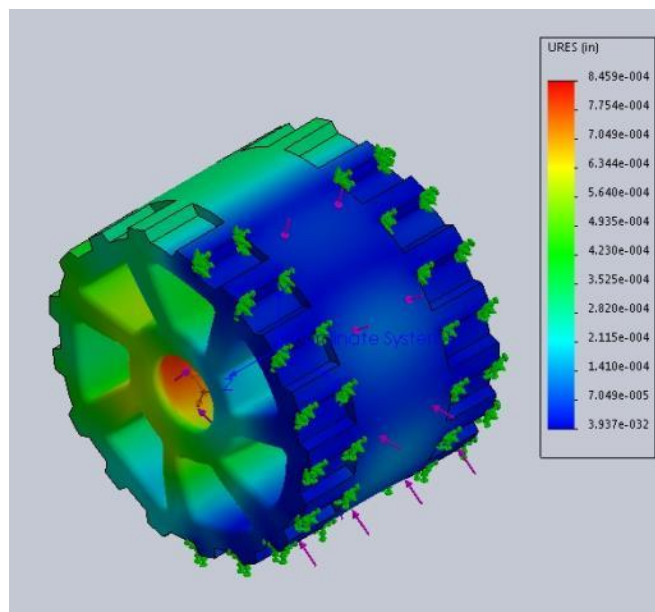
Figure 178: Deflection plot of the drive wheel.
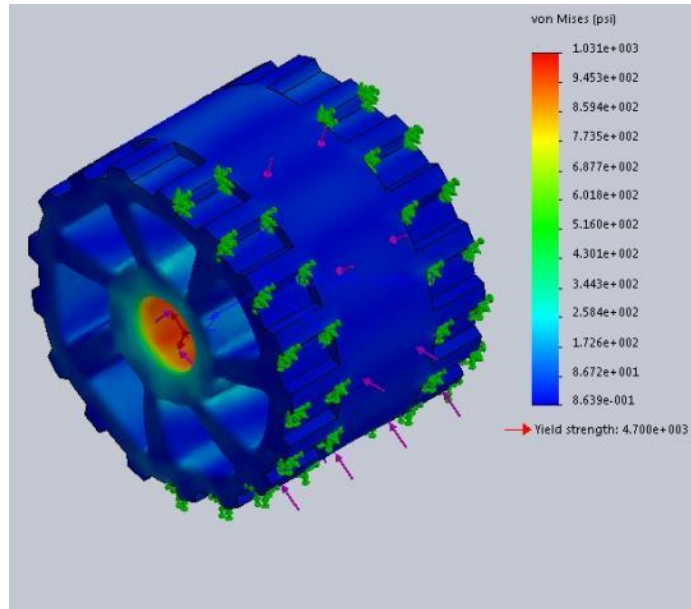
Figure 179: The Von Mises Stress plot of the drive wheel.
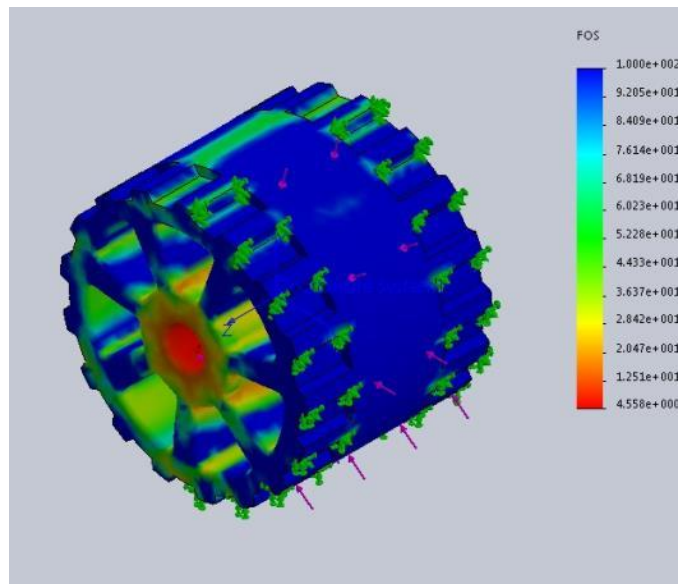
Figure 180: The Factor of safety plot of the drive wheel.

A.20 Brace Validation Simulation

A.20.1 Simulation Description

This simulation was used to validate the design of the wheel stiffening brace. The simulation was performed in Solidworks simulation package. It describes the boundary conditions and loading conditions that were applied to the brace and how those conditions were determined. It reports the factor of safety, maximum Von Mises stress and the deflection of the bracket.

A.20.2 Boundary Conditions

The brace was fixed at the edges of bearing mounting holes. Figure 181 shows the fixed locations on the frame.

Figure 181: Fixed locations of the brace.

A.20.3 Loading Conditions

Two loads were applied to the brace at the bearing mounting holes. The first was the tread tension force which pointed at the center of the brace. The second were the bearing thrust loads which pointed towards the brace. Table 121 gives the magnitudes of these loads and their location and directions can be seen in Figure 182.

Table 121: Magnitudes of the loads applied to the brace.

Load	Magnitude
Tread Tension	55 lbf
Bearing Thrust load	6.4 lbf

Figure 182: Locations of the loads applied to the brace.

A.20.4 Mesh

The mesh for the brace was auto generated by Solidworks. A fine mesh was chosen to increase the accuracy of the results. Figure 183 shows the meshed brace.
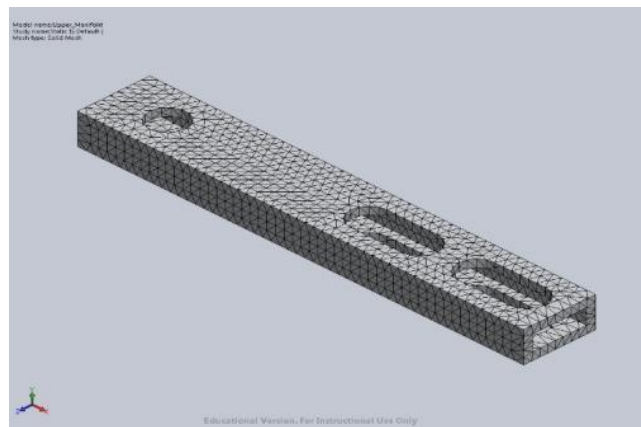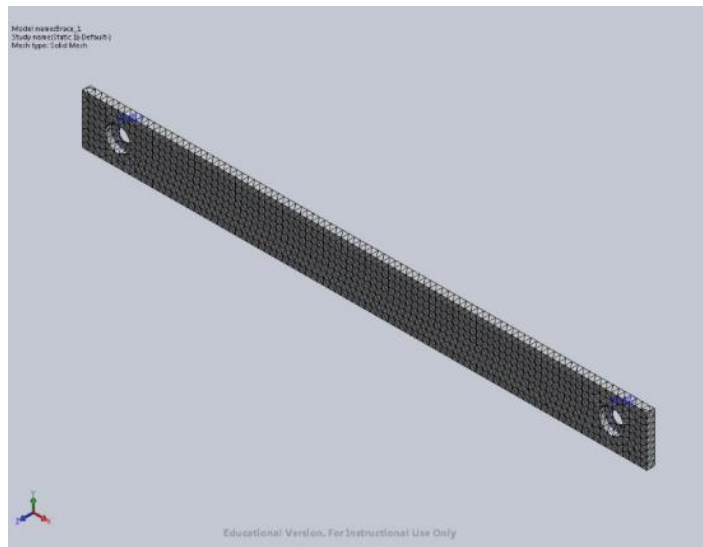

Figure 183: The meshed brace.

A.20.5 Simulation Results

Table 122 lists the results of the simulation. Figure 184, Figure 185 and Figure 186 show plots of the resultant deflection, resultant stresses and factor of safety respectively.

Table 122: Results from the motor plate simulation.

| Simulation Result	Value
Maximum Von Mises Stress	4,319 psi
Maximum Displacement	0.002 in.
Minimum Factor of Safety	9.2
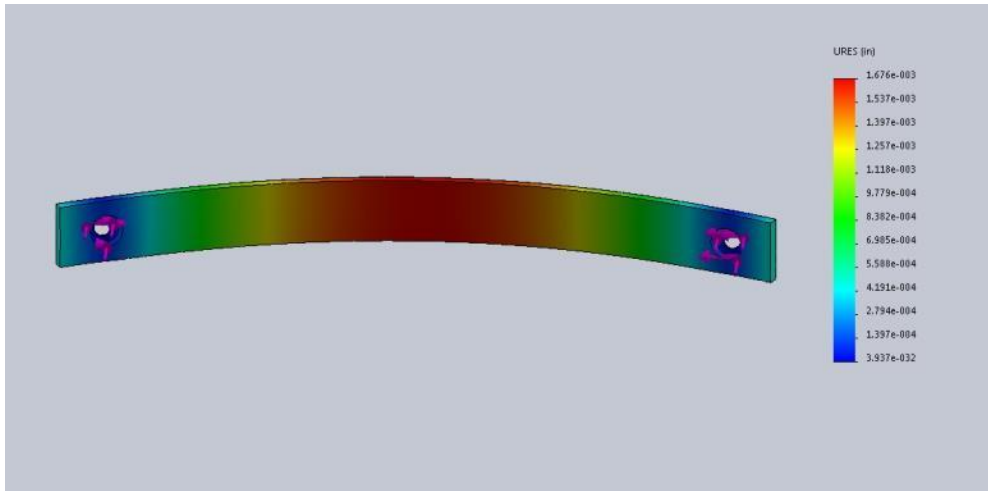
Figure 184: Deflection plot of the brace.
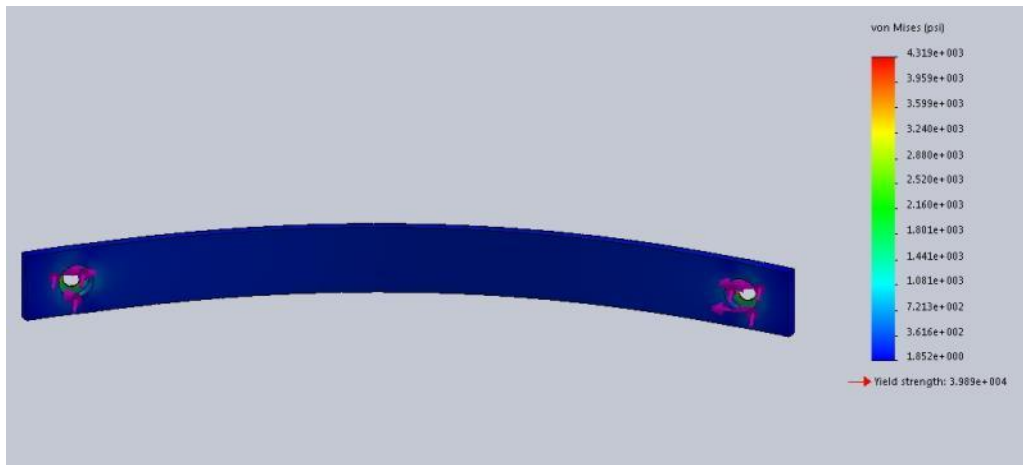
Figure 185: The Von Mises Stress plot of the brace.
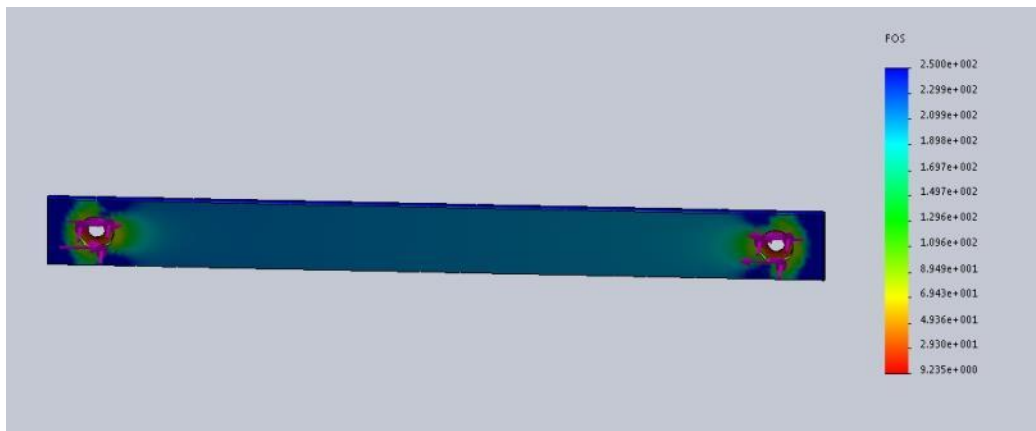
Figure 186: The Factor of safety plot of the brace.

A.21 Brace Buckling

A.21.1 Calculation Description

This calculation checks the wheel brace for buckling. The results are used to justify the design of the brace.

A.21.2 Solution

Table 123 gives the known variables used in this calculation. The brace is assumed to have the both ends pivoted.

Table 123: Values used to calculate the buckling condition and factor of safety for the brace.

Symbol	Description	Value
b	The base dimension of the brace	0.1875 in.
h	The height dimension of the brace	1.5 in.
l	The length of the beam	12.25 in.
C	The constant used for the end conditions of the brace	1
E	The elastic modulus of aluminum 6061-t6	10 Msi
S_y	The yield strength of aluminum 6061-T6	45 ksi
P_a	The applied loading on the brace	110 lbf

The first thing that must be calculated is the radius of gyration of the brace, this is given by Equation A.21.1 were I_b is the area moment of inertia of the brace and A_b is the area of the brace.

$$k = \sqrt{\frac{I_b}{A_b}} = 0.433 \; in. \tag{A.21.1}$$

The next step is to determine the slenderness ratio of the brace, which is given by Equation A.21.2.

$$\frac{l}{k} = 28.3 \tag{A.21.2}$$

The next step is to determine if the brace can be treated as an Euler column. This is done by calculating a minimum slenderness ratio and comparing that to the actual slenderness ratio. Equation A.21.3 gives the calculated minimum slenderness ratio.

$$\left(\frac{l}{k}\right)_1 = \sqrt{\frac{2 * \pi^2 * C * E}{S_y}} = 66.2 \tag{A.21.3}$$

Since the actual slenderness ratio is less than the minimum slenderness ratio, the brace must be treated as

an intermediate length column. Equation A.21.4 solves for the critical load for the brace.

$$P_{cr} = \left(S_y - \left(\frac{S_y}{2 * \pi} * \frac{l}{k}\right)^2 * \frac{1}{C * E}\right) * A_b = 12{,}600 \; lbf \tag{A.21.4}$$

The safety factor of the brace for buckling can be found by comparing the expected brace load with the

critical load as seen in Equation A.21.5.

$$F.S. = \frac{P_{cr}}{P_a} = 114 \tag{A.21.5}$$

A.22 Tensioner Shaft and Exterior Clamp Half Simulation

A.22.1 Simulation Description

This simulation was used to validate the design of the tensioner shaft and exterior clamp half. The

simulation was performed in Solidworks simulation package. It describes the boundary conditions and

loading conditions that were applied to the shaft and clamp half and how those conditions were determined.

It reports the factor of safety, maximum Von Mises stress and the deflection of the bracket.

A.22.2 Boundary Conditions

The model was fixed in two locations. Each of the threaded holes which attach the exterior and interior

clamp halves were fixed. The back plate of the clamp half was fixed perpendicular to its surface to simulate

the tensioner upright. Figure 187 shows the fixed locations of the model.
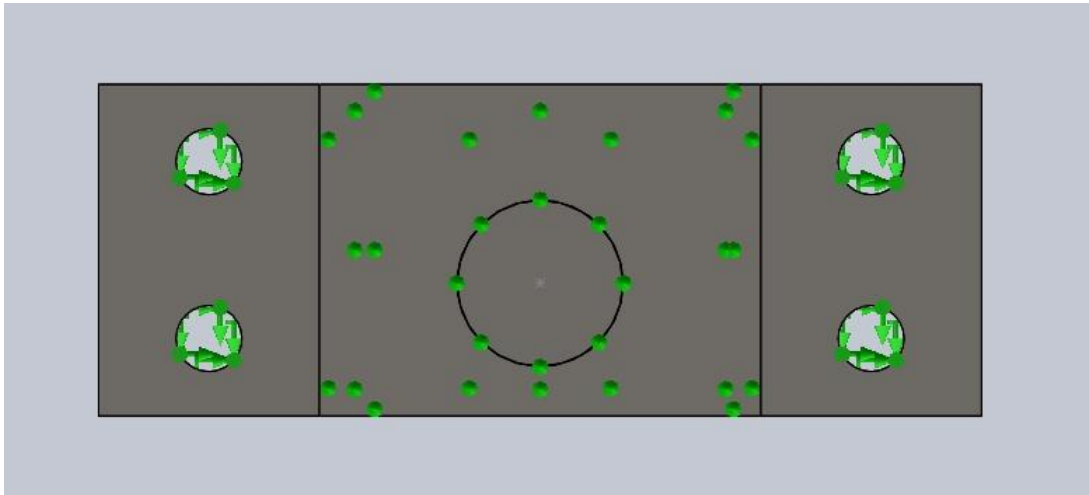
Figure 187: Fixed locations of the model.

A.22.3 Loading Conditions

The only load applied to the model was at the shaft location. This was to simulate the portion of the tension load applied down on the shaft. Its magnitude was determined to be 55 lbf. Figure 188 shows the tension load on the shaft.
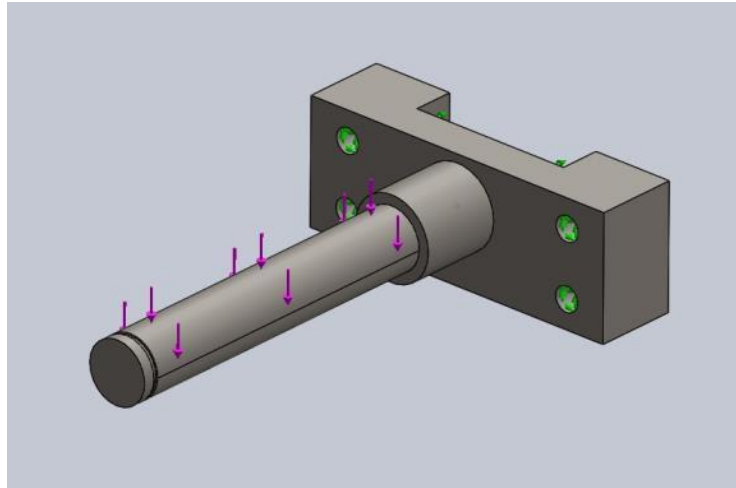
Figure 188: Tensioner shaft and exterior clamp loading.

A.22.4 Mesh

The mesh for the wheel was auto generated by Solidworks. A fine mesh was chosen to increase the accuracy of the results. Figure 189 shows the meshed wheel.
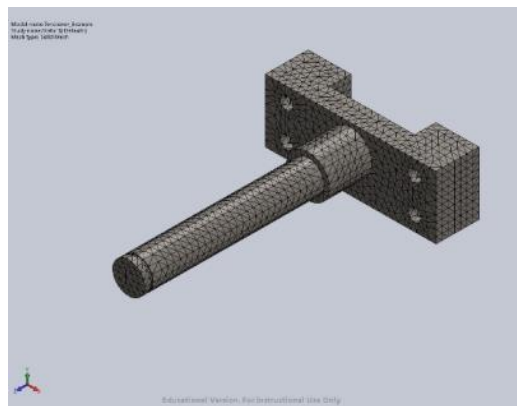

Figure 189: Meshed tensioner shaft and exterior clamp half.

A.22.5 Simulation Results

Table 124 lists the results of the simulation. Figure 190, Figure 191 and Figure 192 show plots of the resultant deflection, resultant stresses and factor of safety respectively.

Table 124: Results from the tensioner shaft and exterior clamp half simulation.

Simulation Result	Value
Maximum Von Mises Stress	11,850 psi
Maximum Displacement	0.003 in.
Minimum Factor of Safety	6.5
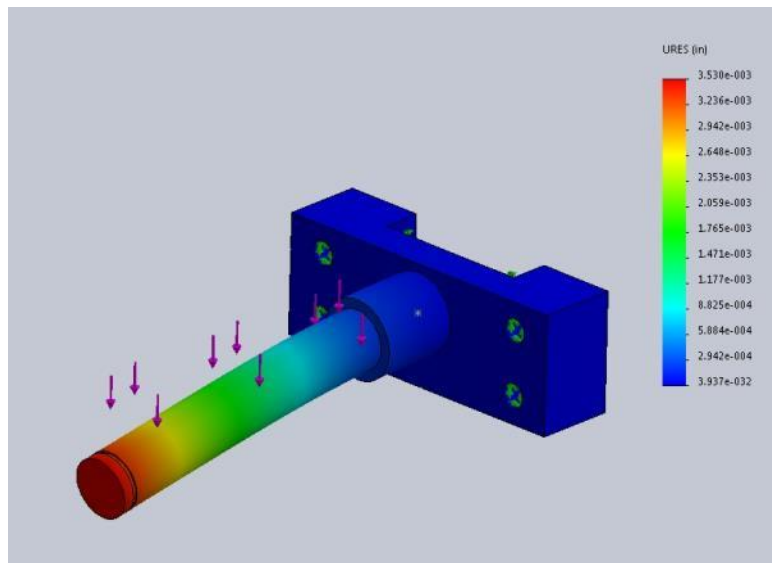
Figure 190: Deflection plot of the tensioner shaft and exterior clamp half.
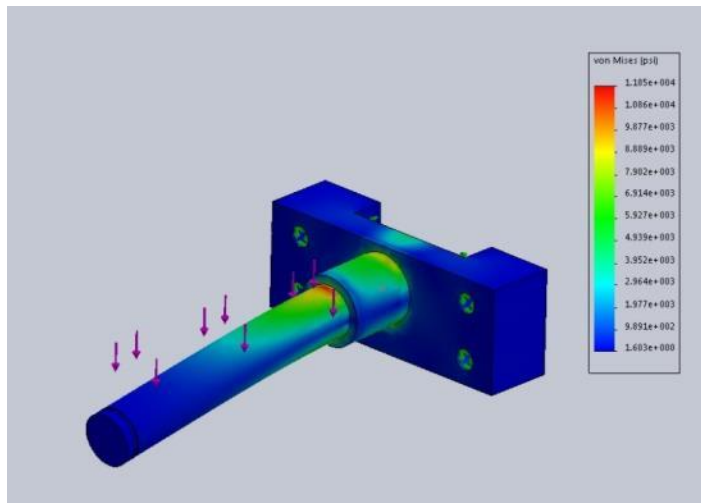
Figure 191: The Von Mises Stress plot of the tensioner shaft and exterior clamp half.
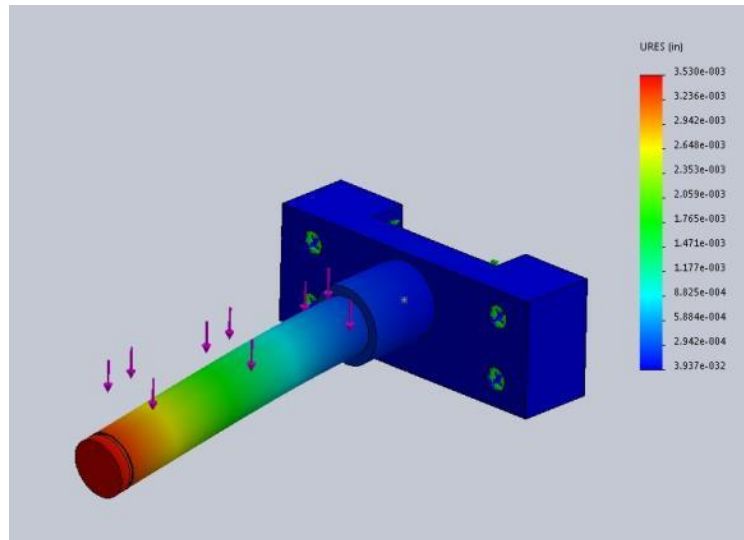
Figure 192: The Factor of safety plot of the tensioner shaft and exterior clamp half.

A.23 Tensioner Design Validation

A.23.1 Calculation Description

This calculation was intended to validate the design of the tensioner system. This was done using Solidworks belt tool. It describes the process used to determine the tension developed in the belt as the tensioner is raised. It reports the tension in the belt.

A.23.2 Procedure

The procedure used to determine the tension in the treads as the tensioner is raised is relatively simple. Since the pitch length and the material composition of the treads is known, the tension in the belt can be estimated by checking the extension of the belt as the tensioner is raised. To do this, a model of the wheel system was created. The Solidworks belt tool was then used to wrap a belt around the drive, idler and tensioner wheels, as shown in Figure 193.
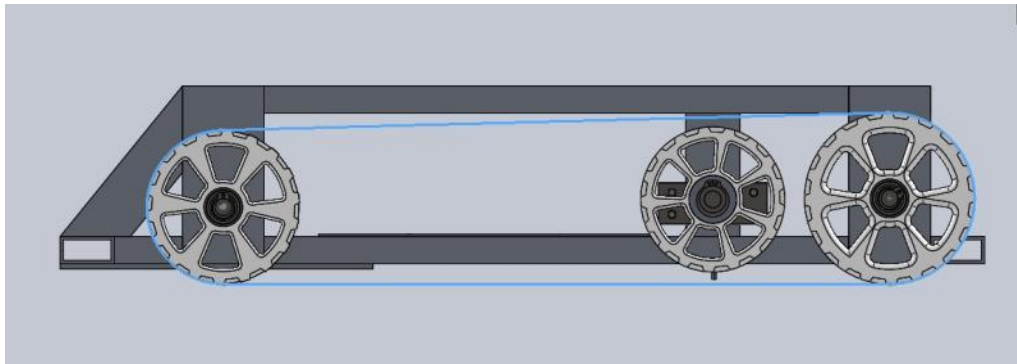
Figure 193: The slack condition of the belt. Belt length 33.83 in.

The tensioner assembly was then raised and the length of the belt was recorded. The actual tread length was then subtracted from this value to determine the strain in the belt. This strain value was then multiplied by the elastic modulus of the belt, which was assumed to be dominated by the modulus of the steel reinforcement cables, to determine the stress in the tread. This stress was then converted into a tension force.

A.23.3 Results

Figure 194 shows the simulation when the tensioner has reached its assumed minimum distance to the top of the vehicle frame. This distance was determined based on the assumed weld bead dimensions, which limits how close the tensioner can get to the top of the vehicle. Table 125 gives the parameters used in the calculation of the developed tension at this height.
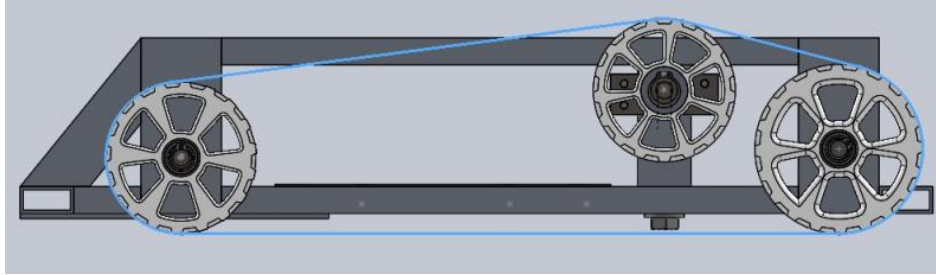
Figure 194: The assumed maximum tensioner height. Belt length 34.01 in.

Table 125: Parameters used to calculate belt tension.

Symbol	Variable Description	Value
d_T	Tensioner distance from Top of frame	0.171 in.
L_{TC}	Calculated Tread Length	34.01 in.
L_{TA}	Actual belt Length	34.00 in.
E_s	Young's Modulus of Steel cables	29 Mpsi
N_C	Number of Cables across width of the belt	8
d_C	Cable Diameter	0.0625 in.

The strain developed in the tread is given by Equation B.22.1.

$$\varepsilon_T = \frac{L_{TC} - L_{TA}}{L_{TA}}$$ (B.22.1)

This strain was then used to calculate the stress in the tread using Equation B.22.2.

$$\sigma_T = E_s * \varepsilon_T$$ (B.22.2)

The tension in the tread was then calculated using Equation B.22.3.

$$T_T = \sigma_T * N_C * \frac{\pi}{4} * d_C^2$$ (B.22.3)

Table 126 contains the results of the calculation.

Table 126: Results of the tensioner design validation calculation.

Symbol	Description	Value
ε_T	Belt Strain	2.9 x 10^-4 in./in.
σ_T	Belt Stress	8529 psi
T_T	Belt Tension	209 lbf

Appendix B - Bill of Materials

This section gives a breakdown of the parts and raw materials used in the project. This includes the cost, supplier and quantity of items purchased for the project. The bill of materials has been broken down by subsystem's which correspond to those found in Chapter 2.

Table 127: Frame raw material supplier, quantity and cost breakdown.

Part Description	Supplier	SKU	Quantity	Cost
1/4"-20 5/8" Low-Profile Alloy Steel SHCS	McMaster	92220A184	(1 Box of 50)	$9.14
1/4"-20 Zinc Aluminum Coated Steel Hex Nut	McMaster	93827A211	(1 Box of 100)	$6.74
18"x18"x0.04" Aluminum 6061 Sheet	McMaster	89015K169	1	$28.80
.5"x1"x3' 0.0625"Thick 6061 Aluminum Tubing	McMaster	6546K51	4	$35.44
1"x1.5"x3' 1/8"Thick 6061 Aluminum Tubing	McMaster	6546K38	1	$21.15
1/4"-20 1/2" Low-Profile Alloy Steel SHCS	McMaster	92220A183	8 (1 Box of 50)	$9.15
1/4"-20 1" Low-Profile Alloy Steel SHCS	McMaster	92220A186	8 (1 Box of 50)	$11.48
3/16"x1.5"x3' 6061 Aluminum Bar	McMaster	8975K588	1	$8.32
Total				$130.22

Table 128: Motor raw material supplier, quantity and cost breakdown.

Part Description	Supplier	SKU	Quantity	Cost
2"x2'x3/32" 6061 Aluminum Plate	McMaster	8975K342	1	$4.83
Compact Square-Face DC Gearmotor	McMaster	6409K26	2	$106.32
3"x2"X2' 3/16 Thick 6061 Aluminum 90^0 Angle	Metals Depot	A332316	1	$17.40
Type 18-8 Stainless Steel Narrow Hex Nut	McMaster	90730A411	8 (1 Box of 100)	$5.92
5/16" ShaftDia. Straight Shaft Coupler	McMaster	6412K12	2	$15.56
Total				$150.03

Table 129: Vacuum raw material supplier, quantity and cost breakdown.

Part Description	Supplier	SKU	Quantity	Cost
Miniature J-Series Fixed Venturi Vacuum Pump	Vaccon	JS-90M-AA4	8	$572
Push-to-Connect Tube Fitting for Air - Straight	McMaster	5779K108	8	$24.64
Push-to-Connect Tube Fitting for Air - Swivel 90^0 Elbow	McMaster	5779K151	8	$24.96
2"x24" 1/16" Thick 6061 Aluminum Sheet	McMaster	89015K181	1	$7.08
Low-Profile Alloy Steel Socket Head Cap Screw	McMaster	92220A178	2	$6.07
Nylon Manifold	McMaster	5253K302	1	$29.75
Hex-Head Polypropylene Plug	McMaster	4515K211	1	$1.03
Push-to-Connect Tube Fitting for Air Straight Adapter	McMaster	5779K117	1	$5.30
Total				$670.83

Table 130: Manifold raw material supplier, quantity and cost breakdown.

Part Description	Supplier	Supplier SKU	Quantity	Cost
White Delrin ® Acetal Resin Rectangular Bar	McMaster	8739K74	1	$70.44
Multipurpose 6061 Aluminum Rectangular Tube	McMaster	6546K47	1	$4.29
Multipurpose 6061 Aluminum Rod	McMaster	8974K22	1	$2.00
Steel Compression Spring 0.375" L	McMaster	9657K265	4 (1 Box of 12)	$10.35
Steel Compression Spring 0.75"	McMaster	9657K288	4 (1 Box of 12)	$10.35
Push-to-Connect Tube Fitting for Air Double 90 Degree Elbow	McMaster	5779K254	8 (1 Box of 100)	$102.24
Black-Oxide Alloy Steel Socket Head Cap Screw	McMaster	91251A144	16	$8.46
Fiberglass Fabric-Reinforced Silicone Rubber	McMaster	8612K51	1	$18.35
Total				$226.48

Table 131: Wheel raw material supplier, quantity and cost breakdown.

Part Description	Supplier	Supplier SKU	Quantity	Cost
.5" Dia. 3' 1045 Medium Carbon Steel Rod	McMaster	8279T27	1	$20.22
8mm Black-Finish Steel External Retaining Ring	McMaster	98541A116	6	$8.00
3/8" Shaft Brass Thrust Bearing	McMaster	7447K3	4	$5.32
Flanged Stainless Steel Ball Bearing - ABEC-5	McMaster	7804K147	8	$57.20
Drive Wheel	Cal Poly	N/A	2	$140.00
Idler Wheel	Cal Poly	N/A	2	$160.00
Total				$390.74

Table 132: Tensioner raw material supplier, quantity and cost breakdown.

Part Description	Supplier	Supplier SKU	Quantity	Cost
1/2"x3/4"x6"Low-Carbon Steel Rectangular Bar	McMaster	8910K693	1	$4.34
1/2"x3/4"x 6" 6061 Aluminum Rectangular Bar	McMaster	8975K618	1	$2.41
1/4"-20 3"High-Strength Steel Cap Screw	McMaster	92620A553	2 (1 Box of 5)	$9.47
3/8" Dia. Steel External Retaining Ring	McMaster	97633A170	2 (1 Box of 100)	$8.74
3/8" Dia. Bronze Flange Bearing	McMaster	9440T54	4	$10.72
Tensioner Wheel	Cal Poly	N/A	2	$120.00
Total				$155.68

Table 133: Tread raw material supplier, quantity and cost breakdown.

Part Description	Supplier	Supplier SKU	Quantity	Cost
Custom Timing Belt	F.N. Sheppard	N/A	2	$574.98

5.3-oz. High-Vacuum Grease	Mcmaster	2966K52		1	$29.19
Silicone Sealant	ACE	1012228		1	$6.99
Total					$611.16

Appendix C - Vehicle Weight Break Down

Table 134: Weight breakdown for left side components.

Component Name	Weight (oz.)	Weight (lbf)
Tread	9	0.56
Wheel Assembly	15.8	0.99
Idler Wheel and Shaft	4.6	0.29
Drive Wheel and Shaft	4.9	0.31
Brace	6.4	0.40
Manifold With Fasteners	8.8	0.55
Venturi Bank	10.5	0.66
Venturi Bracket	0.5	0.03
Tensioner Assembly	9.2	0.58
Interior Clamp Half	1.3	0.08
Screw Assembly	0.65	0.04
Tensioner Shaft and Exterior Clamp Half	3.7	0.23
Tensioner Wheel	3.4	0.21
Motor Assembly	26.6	1.66
Mounting Plate	1.4	0.09
Coupler	0.9	0.06
Mounting Bracket	2.8	0.18
Motor	18.6	1.16

Table 135: Weight breakdown for right side components.

Tread	Weight (oz.)	Weight (lbf)
Wheel Assembly	9.1	0.57
Idler Wheel and Shaft	15.5	0.97
Drive Wheel and Shaft	4.7	0.29
Brace	4.4	0.28
Manifold With Fasteners	6.5	0.41
Venturi Bank	8.8	0.55
Venturi Bracket	10.2	0.64
Tensioner Assembly	0.4	0.03
Interior Clamp Half	9	0.56
Screw Assembly	1.3	0.08
Tensioner Shaft and Exterior Clamp Half	0.7	0.04
Tensioner Wheel	3.7	0.23
Motor Assembly	3.4	0.21
Mounting Plate	26.6	1.66
Coupler	1.4	0.09

	Weight (oz.)	Weight (lbf)
Mounting Bracket	0.9	0.06
Motor	2.9	0.18
Tread	18.6	1.16

Table 136: Weight breakdown for other vehicle components.

Component Name	Weight (oz.)	Weight (lbf)
Inlet Manifold	6.1	0.38
Frame Plate Fastener	52.6	3.29
Plate	6.5	0.41
Frame	45.4	2.84

Table 137: The final weight of the vehicle.

Total weight (oz.)	Total Weight (lbf)	Weight Without Treads
217	13.6	12.5

Appendix D - **Testing Data**

Table 138: Data for Fixed Right Manifold Unclogged Test.

Section	1	2	3	4
Venturi Power	26.5	27	27	27
Section	**1**	**2**	**3**	**4**
All Sections Closed - Initial	19	25	25	25
Section	**1**	**2**	**3**	**4**
All Sections Closed - Final	19	25	25	25
Section	**1**	**2**	**3**	**4**
Pressure in Section 1 (inHg)	18	closed	closed	closed
	8	open	closed	closed
	6	open	open	closed
	11.5	open	open	open
Section	**1**	**2**	**3**	**4**
Pressure in Section 2 (inHg)	closed	25	closed	closed
	open	24	closed	closed
	open	22	open	closed
	open	21.5	open	open
Section	**1**	**2**	**3**	**4**
Pressure in Section 3 (inHg)	closed	closed	24	closed
	open	closed	24	closed
	open	open	24	closed
	open	open	21.5	open
Section	**1**	**2**	**3**	**4**
Pressure in Section 4 (inHg)	closed	closed	closed	25
	open	closed	closed	25
	open	open	closed	25
	open	open	open	24

Table 139: Data for Unfixed Right Manifold Unclogged Test.

Section	1	2	3	4
Venturi Pressure (inHg)	27	27.5	26	26
Section	**1**	**2**	**3**	**4**
All Sections Closed – Initial (inHg)	20	25	25	24
Section	**1**	**2**	**3**	**4**
All Sections Closed – Final (inHg)	20	25	24	25
Section	**1**	**2**	**3**	**4**
Pressure in Section 1 (inHg)	20	closed	closed	closed
	15	open	closed	closed
	13	open	open	closed
	20	open	open	open
Section	**1**	**2**	**3**	**4**
Pressure in Section 2 (inHg)	closed	25	closed	closed
	open	24	closed	closed
	open	22	open	closed
	open	21.5	open	open
Section	**1**	**2**	**3**	**4**
Pressure in Section 3 (inHg)	closed	closed	24	closed
	open	closed	24	closed
	open	open	22.5	closed

	open	open	19	open
Section	**1**	**2**	**3**	**4**
	closed	closed	closed	25
Pressure in Section 4 (inHg)	open	closed	closed	25
	open	open	closed	25
	open	open	open	22

Table 140: Data for the right manifold independence unclogged test.

Section	**1**	**2**	**3**	**4**
Venturi Pressure (inHg)	27.5	28	27.5	27.5
Section	**1**	**2**	**3**	**4**
All Sections Closed – Initial (inHg)	26	25	26	26
Section	**1**	**2**	**3**	**4**
All Sections Closed – Final (inHg)	26.5	25	25	26
Section	**1**	**2**	**3**	**4**
	26	closed	closed	closed
Pressure in Section 1 (inHg)	26	open	closed	closed
	26	open	open	closed
	26	open	open	open
Section	**1**	**2**	**3**	**4**
	closed	26	closed	closed
Pressure in Section 2 (inHg)	open	26	closed	closed
	open	26	open	closed
	open	26	open	open
Section	**1**	**2**	**3**	**4**
	closed	closed	26	closed
Pressure in Section 3 (inHg)	open	closed	26	closed
	open	open	26	closed
	open	open	26	open
Section	**1**	**2**	**3**	**4**
	closed	closed	closed	26
Pressure in Section 4 (inHg)	open	closed	closed	26
	open	open	closed	26
	open	open	open	26

Table 141: Data for the right manifold off vehicle unclogged test.

Section	**1**	**2**	**3**	**4**
Venturi Pressure (inHg)	27	27	26.5	27
Section	**1**	**2**	**3**	**4**
All Sections Closed – Initial (inHg)	16	25	24	24
Section	**1**	**2**	**3**	**4**
All Sections Closed – Final (inHg)	15	25	24	25
Section	**1**	**2**	**3**	**4**
	15	closed	closed	closed
Pressure in Section 1 (inHg)	7	open	closed	closed
	3	open	open	closed
	16	open	open	open
Section	**1**	**2**	**3**	**4**
Pressure in Section 2 (inHg)	closed	25	closed	closed
	open	25	closed	closed

	open	24	open	closed
	open	20	open	open
Section	**1**	**2**	**3**	**4**
	closed	closed	25	closed
Pressure in Section 3 (inHg)	open	closed	24	closed
	open	open	22.5	closed
	open	open	15	open
Section	**1**	**2**	**3**	**4**
	closed	closed	closed	25
Pressure in Section 4 (inHg)	open	closed	closed	25
	open	open	closed	25
	open	open	open	21

Table 142: Data for Fixed Right Manifold Clogged Test.

Section	**1**	**2**	**3**	**4**
Venturi Pressure (inHg)	26.5	26	26.5	26.5
Section	**1**	**2**	**3**	**4**
All Sections Closed – Initial (inHg)	16	25	25	21
Section	**1**	**2**	**3**	**4**
All Sections Closed – Final (inHg)	16.5	26.5	26	23
Section	**1**	**2**	**3**	**4**
	17	closed	closed	closed
Pressure in Section 1 (inHg)	12	open	closed	closed
	9	open	open	closed
	11	open	open	open
Section	**1**	**2**	**3**	**4**
	closed	25	closed	closed
Pressure in Section 2 (inHg)	open	25	closed	closed
	open	23	open	closed
	open	21	open	open
Section	**1**	**2**	**3**	**4**
	closed	closed	25	closed
Pressure in Section 3 (inHg)	open	closed	25	closed
	open	open	23	closed
	open	open	18	open
Section	**1**	**2**	**3**	**4**
	closed	closed	closed	23
Pressure in Section 4 (inHg)	open	closed	closed	23
	open	open	closed	23
	open	open	open	21

Table 143: Data for Unfixed Right Manifold Clogged Test.

Section	**1**	**2**	**3**	**4**
Venturi Pressure (inHg)	27	26.5	26	26.5
Section	**1**	**2**	**3**	**4**
All Sections Closed – Initial (inHg)	19	24	23	23
Section	**1**	**2**	**3**	**4**
All Sections Closed – Final (inHg)	18	24	23	23
Section	**1**	**2**	**3**	**4**
Pressure in Section 1 (inHg)	20	closed	closed	closed

	1	2	3	4
	16	open	closed	closed
	15	open	open	closed
	17.5	open	open	open
Section	**1**	**2**	**3**	**4**
Pressure in Section 2 (inHg)	closed	24	closed	closed
	open	24	closed	closed
	open	21	open	closed
	open	16	open	open
Section	**1**	**2**	**3**	**4**
Pressure in Section 3 (inHg)	closed	closed	24	closed
	open	closed	24	closed
	open	open	20	closed
	open	open	2	open
Section	**1**	**2**	**3**	**4**
Pressure in Section 4 (inHg)	closed	closed	closed	22
	open	closed	closed	23
	open	open	closed	23
	open	open	open	20

Table 144: Data for the right manifold independence clogged test.

Section	**1**	**2**	**3**	**4**
Venturi Pressure (inHg)	26	27	27	27
Section	**1**	**2**	**3**	**4**
All Sections Closed – Initial (inHg)	26	27	27	26.5
Section	**1**	**2**	**3**	**4**
All Sections Closed – Final (inHg)	26.5	26.5	26	26.5
Section	**1**	**2**	**3**	**4**
Pressure in Section 1 (inHg)	26.5	closed	closed	closed
	26	open	closed	closed
	26	open	open	closed
	26	open	open	open
Section	**1**	**2**	**3**	**4**
Pressure in Section 2 (inHg)	closed	27	closed	closed
	open	27	closed	closed
	open	27	open	closed
	open	27	open	open
Section	**1**	**2**	**3**	**4**
Pressure in Section 3 (inHg)	closed	closed	26.5	closed
	open	closed	26.5	closed
	open	open	26.5	closed
	open	open	26.5	open
Section	**1**	**2**	**3**	**4**
Pressure in Section 4 (inHg)	closed	closed	closed	26.5
	open	closed	closed	26.5
	open	open	closed	26.5
	open	open	open	26.5

Table 145: Data for the right manifold off vehicle clogged test.

Section	**1**	**2**	**3**	**4**
Venturi Pressure (inHg)	26.5	27	26.5	27

Section	1	2	3	4
All Sections Closed – Initial (inHg)	20	25.5	24	25
Section	1	2	3	4
All Sections Closed – Final (inHg)	19	24	24	25
Section	1	2	3	4
Pressure in Section 1 (inHg)	20	closed	closed	closed
	15	open	closed	closed
	14	open	open	closed
	20	open	open	open
Section	1	2	3	4
Pressure in Section 2 (inHg)	closed	25	closed	closed
	open	24	closed	closed
	open	23	open	closed
	open	21	open	open
Section	1	2	3	4
Pressure in Section 3 (inHg)	closed	closed	23	closed
	open	closed	23	closed
	open	open	20	closed
	open	open	11	open
Section	1	2	3	4
Pressure in Section 4 (inHg)	closed	closed	closed	25
	open	closed	closed	24
	open	open	closed	24
	open	open	open	24

Table 146: Data for Fixed Left Manifold Unclogged Test.

Section	1	2	3	4
Venturi Pressure (inHg)	27	27	27	27
Section	1	2	3	4
All Sections Closed – Initial (inHg)	18	22	21	24
Section	1	2	3	4
All Sections Closed – Final (inHg)	17	23	21.5	25
Section	1	2	3	4
Pressure in Section 1 (inHg)	17	closed	closed	closed
	14	open	closed	closed
	12	open	open	closed
	21	open	open	open
Section	1	2	3	4
Pressure in Section 2 (inHg)	closed	22	closed	closed
	open	21	closed	closed
	open	15	open	closed
	open	7.5	open	open
Section	1	2	3	4
Pressure in Section 3 (inHg)	closed	closed	21	closed
	open	closed	20	closed
	open	open	13	closed
	open	open	4	open
Section	1	2	3	4
Pressure in Section 4 (inHg)	closed	closed	closed	24
	open	closed	closed	24
	open	open	closed	23
	open	open	open	20

Table 147: Data for Unfixed Left Manifold Unclogged Test.

Section	1	2	3	4
Venturi Pressure (inHg)	27.5	27	27	27
Section	**1**	**2**	**3**	**4**
All Sections Closed – Initial (inHg)	18	23.5	20	23
Section	**1**	**2**	**3**	**4**
All Sections Closed – Final (inHg)	17.5	20	19	23
Section	**1**	**2**	**3**	**4**
Pressure in Section 1 (inHg)	17	closed	closed	closed
	10	open	closed	closed
	4	open	open	closed
	14	open	open	open
Section	**1**	**2**	**3**	**4**
Pressure in Section 2 (inHg)	closed	21	closed	closed
	open	20	closed	closed
	open	10	open	closed
	open	2	open	open
Section	**1**	**2**	**3**	**4**
Pressure in Section 3 (inHg)	closed	closed	19	closed
	open	closed	19	closed
	open	open	9	closed
	open	open	1	open
Section	**1**	**2**	**3**	**4**
Pressure in Section 4 (inHg)	closed	closed	closed	23
	open	closed	closed	23
	open	open	closed	22
	open	open	open	20

Table 148: Data for the left manifold independence unclogged test.

Section	1	2	3	4
Venturi Pressure (inHg)	27	27	27	27.5
Section	**1**	**2**	**3**	**4**
All Sections Closed – Initial (inHg)	27	27	26.5	26
Section	**1**	**2**	**3**	**4**
All Sections Closed – Final (inHg)	27	27	27	26.5
Section	**1**	**2**	**3**	**4**
Pressure in Section 1 (inHg)	27	closed	closed	closed
	27	open	closed	closed
	26.5	open	open	closed
	27	open	open	open
Section	**1**	**2**	**3**	**4**
Pressure in Section 2 (inHg)	closed	27	closed	closed
	open	27	closed	closed
	open	27	open	closed
	open	27	open	open
Section	**1**	**2**	**3**	**4**
Pressure in Section 3 (inHg)	closed	closed	26.5	closed
	open	closed	26	closed
	open	open	26.5	closed
	open	open	26.5	open
Section	**1**	**2**	**3**	**4**

Pressure in Section 4 (inHg)	closed	closed	closed	26
	open	closed	closed	26
	open	open	closed	26
	open	open	open	26

Table 149: Data for the left manifold off vehicle unclogged test.

Section	1	2	3	4
Venturi Pressure (inHg)	27	27	27	27
Section	**1**	**2**	**3**	**4**
All Sections Closed – Initial (inHg)	21	21.5	21	25
Section	**1**	**2**	**3**	**4**
All Sections Closed – Final (inHg)	22	20	20	25
Section	**1**	**2**	**3**	**4**
Pressure in Section 1 (inHg)	21	closed	closed	closed
	19	open	closed	closed
	18	open	open	closed
	18	open	open	open
Section	**1**	**2**	**3**	**4**
Pressure in Section 2 (inHg)	closed	20	closed	closed
	open	17.5	closed	closed
	open	10	open	closed
	open	3	open	open
Section	**1**	**2**	**3**	**4**
Pressure in Section 3 (inHg)	closed	closed	19	closed
	open	closed	18	closed
	open	open	10	closed
	open	open	2	open
Section	**1**	**2**	**3**	**4**
Pressure in Section 4 (inHg)	closed	closed	closed	25
	open	closed	closed	25
	open	open	closed	25
	open	open	open	22

Table 150: Data for Fixed Left Manifold clogged Test.

Section	1	2	3	4
Venturi Pressure (inHg)	27.5	27	27	27.5
Section	**1**	**2**	**3**	**4**
All Sections Closed – Initial (inHg)	15	23.5	22.5	18
Section	**1**	**2**	**3**	**4**
All Sections Closed – Final (inHg)	16.5	23	22.5	17.5
Section	**1**	**2**	**3**	**4**
Pressure in Section 1 (inHg)	16	closed	closed	closed
	11	open	closed	closed
	10	open	open	closed
	16.5	open	open	open
Section	**1**	**2**	**3**	**4**
Pressure in Section 2 (inHg)	closed	23	closed	closed
	open	22.5	closed	closed
	open	22	open	closed
	open	22	open	open

Section	1	2	3	4
Pressure in Section 3 (inHg)	closed	closed	23	closed
	open	closed	22	closed
	open	open	21	closed
	open	open	18	open
Section	1	2	3	4
Pressure in Section 4 (inHg)	closed	closed	closed	18
	open	closed	closed	17.5
	open	open	closed	18
	open	open	open	15

Table 151: Data for Unfixed Left Manifold clogged Test.

Section	1	2	3	4
Venturi Pressure (inHg)	27	27.5	27	27.5
Section	1	2	3	4
All Sections Closed – Initial (inHg)	16	24	22	19
Section	1	2	3	4
All Sections Closed – Final (inHg)	17	24	21	19
Section	1	2	3	4
Pressure in Section 1 (inHg)	16	closed	closed	closed
	13	open	closed	closed
	11	open	open	closed
	20	open	open	open
Section	1	2	3	4
Pressure in Section 2 (inHg)	closed	24	closed	closed
	open	23	closed	closed
	open	23	open	closed
	open	21	open	open
Section	1	2	3	4
Pressure in Section 3 (inHg)	closed	closed	21	closed
	open	closed	21	closed
	open	open	20	closed
	open	open	12	open
Section	1	2	3	4
Pressure in Section 4 (inHg)	closed	closed	closed	19
	open	closed	closed	21
	open	open	closed	19
	open	open	open	16

Table 152: Data for the left manifold independence clogged test.

Section	1	2	3	4
Venturi Pressure (inHg)	28	27	28	27
Section	1	2	3	4
All Sections Closed – Initial (inHg)	27	27	26.5	27
Section	1	2	3	4
All Sections Closed – Final (inHg)	27	27	26.5	27
Section	1	2	3	4
Pressure in Section 1 (inHg)	27	closed	closed	closed
	27	open	closed	closed
	27	open	open	closed

	27	open	open	open
Section	**1**	**2**	**3**	**4**
Pressure in Section 2 (inHg)	closed	26.5	closed	closed
	open	26.5	closed	closed
	open	26.5	open	closed
	open	26.5	open	open
Section	**1**	**2**	**3**	**4**
Pressure in Section 3 (inHg)	closed	closed	26.5	closed
	open	closed	26.5	closed
	open	open	26.5	closed
	open	open	26.5	open
Section	**1**	**2**	**3**	**4**
Pressure in Section 4 (inHg)	closed	closed	closed	26.5
	open	closed	closed	26.5
	open	open	closed	26.5
	open	open	open	26.5

Table 153: Data for the left manifold off vehicle unclogged test.

Section	**1**	**2**	**3**	**4**
Venturi Pressure (inHg)	27	27	27	27.5
Section	**1**	**2**	**3**	**4**
All Sections Closed – Initial (inHg)	13	20	20	23
Section	**1**	**2**	**3**	**4**
All Sections Closed – Final (inHg)	13	20	19	23
Section	**1**	**2**	**3**	**4**
Pressure in Section 1 (inHg)	15	closed	closed	closed
	10	open	closed	closed
	7	open	open	closed
	12.5	open	open	open
Section	**1**	**2**	**3**	**4**
Pressure in Section 2 (inHg)	closed	20	closed	closed
	open	20	closed	closed
	open	12	open	closed
	open	1	open	open
Section	**1**	**2**	**3**	**4**
Pressure in Section 3 (inHg)	closed	closed	20	closed
	open	closed	19	closed
	open	open	13	closed
	open	open	2	open
Section	**1**	**2**	**3**	**4**
Pressure in Section 4 (inHg)	closed	closed	closed	23
	open	closed	closed	23
	open	open	closed	23
	open	open	open	21

Table 154: Vertical surface test and following table top test data test set 1.

Vertical Test				
Section	**1**	**2**	**3**	**4**
Right Side Pressure (inHg)	0	15	24	25

Section	1	2	3	4
Left Side Pressure (inHg)	15	22	20	2.5
Table Top Test				
Section	1	2	3	4
Right Side Pressure (inHg)	20	25	25	18
Section	1	2	3	4
Left Side Pressure (inHg)	23	23	23	22

Table 155: Vertical surface test and following table top test data test set 2.

Vertical Test				
Section	1	2	3	4
Right Side Pressure (inHg)	3	23	24	25
Section	1	2	3	4
Left Side Pressure (inHg)	22	20	18	13
Table Top Test				
Section	1	2	3	4
Right Side Pressure (inHg)	3	25	25	26
Section	1	2	3	4
Left Side Pressure (inHg)	23.5	20	20	17.5

Table 156: Vertical surface test and following table top test data test set 3.

Vertical Test				
Section	1	2	3	4
Right Side Pressure (inHg)	0	24	25	25
Section	1	2	3	4
Left Side Pressure (inHg)	10	23	20	7
Table Top Test				
Section	1	2	3	4
Right Side Pressure (inHg)	23	26	25	24.5
Section	1	2	3	4
Left Side Pressure (inHg)	23	18	20	21

Table 157: Vertical surface test and following table top test data test set 4.

Vertical Test				
Section	1	2	3	4
Right Side Pressure (inHg)	2	22	25	25
Section	1	2	3	4
Left Side Pressure (inHg)	18	24	23	0
Table Top Test				
Section	1	2	3	4
Right Side Pressure (inHg)	22.5	26	25	16
Section	1	2	3	4
Left Side Pressure (inHg)	22	22	23.5	20

Table 158: Vertical surface test and following table top test data test set 5.

Vertical Test				
Section	1	2	3	4

Right Side Pressure (inHg)	0	24	25	25
Section	**1**	**2**	**3**	**4**
Left Side Pressure (inHg)	0	22	23	20
Table Top Test				
Section	**1**	**2**	**3**	**4**
Right Side Pressure (inHg)	20	26	25	10
Section	**1**	**2**	**3**	**4**
Left Side Pressure (inHg)	22	21.5	22	24

Table 159: Split Manifold Testing. All Pressure Value in inHg.

Manifold Section Independence Test				
Section	**Front Half Sections**		**Back Half Sections**	
	1	**2**	**3**	**4**
Right Side Pressure (inHg)	26	26.5	26	26
Section	**Whole Manifold**			
	1	**2**	**3**	**4**
Left Side Pressure (inHg)	26	26	27.5	27
On Tread Off Wheels				
Section	**Front Half Sections**		**Back Half Sections**	
	1	**2**	**3**	**4**
Right Side Pressure (inHg)	23	24	24	21
Section	**Whole Manifold**			
	1	**2**	**3**	**4**
Left Side Pressure (inHg)	18	23	21	24
Fixed Manifold Test				
Section	**Front Half Sections**		**Back Half Sections**	
	1	**2**	**3**	**4**
Right Side Pressure (inHg)	17.5	26	23	22
Section	**Whole Manifold**			
	1	**2**	**3**	**4**
Left Side Pressure (inHg)	17	23	22	20
Vertical Surface Test				
Section	**Front Half Sections**		**Back Half Sections**	
	1	**2**	**3**	**4**
Right Side Pressure (inHg)	0	0	20	25
Section	**Whole Manifold**			
	1	**2**	**3**	**4**
Left Side Pressure (inHg)	12	23	20	15

Table 160: The split manifold vertical surface test data with and without applied load.

No Applied Force				
Section	**Front Half Sections**		**Back Half Sections**	
	1	**2**	**3**	**4**
Right Side Pressure (inHg)	0	0	20	22
Section	**Whole Manifold**			
	1	**2**	**3**	**4**
Left Side Pressure (inHg)	15	23	21	10
With Applied Force – 14 lbf				
Section	**Front Half Sections**		**Back Half Sections**	
	1	**2**	**3**	**4**

Right Side Pressure (inHg)	22	25	20	23
Section	**Whole Manifold**			
	1	**2**	**3**	**4**
Left Side Pressure (inHg)	20	0	0	0

Table 161: Fixed Split Manifold Influence Testing. All Pressure Values in inHg.

Section	**1**	**2**	**3**	**4**
Venturi Pressure (inHg)	27	26.5	27	26
Section	**1**	**2**	**3**	**4**
All Sections Closed – Initial (inHg)	21	20	20	25
Section	**1**	**2**	**3**	**4**
All Sections Closed – Final (inHg)	22	20	19	25
Section	**1**	**2**	**3**	**4**
Pressure in Section 1 (inHg)	21	closed	closed	closed
	19	open	closed	closed
	18	open	open	closed
	18	open	open	open
Section	**1**	**2**	**3**	**4**
Pressure in Section 2 (inHg)	closed	20	closed	closed
	open	17.5	closed	closed
	open	10	open	closed
	open	3	open	open
Section	**1**	**2**	**3**	**4**
Pressure in Section 3 (inHg)	closed	closed	19	closed
	open	closed	18	closed
	open	open	10	closed
	open	open	2	open
Section	**1**	**2**	**3**	**4**
Pressure in Section 4 (inHg)	closed	closed	closed	25
	open	closed	closed	25
	open	open	closed	25
	open	open	open	22

Table 162: Table top pull force data.

Test 1					
Section	**1**	**2**	**3**	**4**	**Pull-Off Force**
Right Side Pressure (inHg)	20	25	24	20	
Section	**1**	**2**	**3**	**4**	25 lbf
Left Side Pressure (inHg)	22	21	19	17	
Test 2					
Section	**1**	**2**	**3**	**4**	**Pull-Off Force**
Right Side Pressure (inHg)	21	25	22.5	21.5	
Section	**1**	**2**	**3**	**4**	24.5 lbf
Left Side Pressure (inHg)	25	22.5	19	15	
Test 3					
Section	**1**	**2**	**3**	**4**	**Pull-Off Force**
Right Side Pressure (inHg)	20	25	22	20	
Section	**1**	**2**	**3**	**4**	23 lbf
Left Side Pressure (inHg)	25	24	24.5	21.5	
Test 4					

Section	1	2	3	4	Pull-Off Force
Right Side Pressure (inHg)	20	25	23.5	22	
Section	1	2	3	4	24 lbf
Left Side Pressure (inHg)	25	23.5	20	19	

Table 163: Vertical surface pull off testing data.

Test 1					
Section	1	2	3	4	Pull-Off Force
Right Side Pressure (inHg)	0	0	23	24	
Section	1	2	3	4	19 lbf
Left Side Pressure (inHg)	15	22	22	11	
Test 2					
Section	1	2	3	4	Pull-Off Force
Right Side Pressure (inHg)	0	0	23	25	
Section	1	2	3	4	17 lbf
Left Side Pressure (inHg)	16	23	20	14	
Test 3					
Section	1	2	3	4	Pull-Off Force
Right Side Pressure (inHg)	0	0	23	22	
Section	1	2	3	4	15 lbf
Left Side Pressure (inHg)	13	25	21	10	
Test 4					
Section	1	2	3	4	Pull-Off Force
Right Side Pressure (inHg)	0	0	24	23	
Section	1	2	3	4	16 lbf
Left Side Pressure (inHg)	15	22	25	12	
Test 5					
Section	1	2	3	4	Pull-Off Force
Right Side Pressure (inHg)	0	0	24	22	
Section	1	2	3	4	20 lbf
Left Side Pressure (inHg)	10	23	24	16	

Table 164: Holes engaged with manifold sections during pull force testing.

Section	1	2	3	4	Sum
Right Side Engaged Holes	8	6	7	6	27
Section	1	2	3	4	Sum
Left Side Engaged Holes	6	8	6	7	27